UNICA

UNIVERSITÀ
DEGLI STUDI
DI CAGLIARI

Ph.D. DEGREE IN
Innovation Science and Technology

Cycle XXXVIII

TITLE OF THE Ph.D. THESIS

Eco-geomorphological and hydrodynamic analysis of Mediterranean microtidal beaches in Southern Sardinia

Scientific Disciplinary Sector(s)

GEOS-03/A

Ph.D. Student:	Antonio Usai
Supervisor	Prof. Sandro Demuro
Co-Supervisor	Prof. Giovanni Coco Dr. Simone Simeone

Final exam. Academic Year 2024/2025
Thesis defence session: February 2026

To Veronica, my parents, my sister and my friends, for their constant presence, support and for always encouraging me to never give up.

‘‘*Writing always means hiding something in such a way that it then is discovered*”

Italo Calvino

ABSTRACT

Global climate change is increasingly having an impact on the marine and coastal environment, with rising sea levels and a growing frequency and intensity of extreme weather and marine events. These phenomena threaten the stability of coastal systems, accelerating beach erosion, damaging infrastructure and exposing ecosystems and economic activities to significant risks. In this context, integrated coastal management strategies become essential, as they play a key role in predicting, mitigating and adapting to potential impacts on coastal areas. Therefore, ensuring the long-term resilience of coastal systems requires strategic planning grounded in robust scientific knowledge. This thesis carries out a multidisciplinary study on the geomorphological, morphometric, hydrodynamic and ecological aspects of the microtidal beaches of Southern Sardinia, Italy (Western Mediterranean Sea). Given the geomorphological variability along this coastal stretch, as well as the differing wave conditions and exposures, an initial morphometric analysis and classification was carried out on 79 microtidal beaches (natural or influenced by the presence of artificial structures), providing an estimation of their level of embaymentisation and the prevailing hydrodynamic circulation in the surf zone. In addition, the spatio-temporal variation of the shorelines was investigated to estimate the accretion and retreat rates for each identified beach. The results highlighted that, over approximately 70 years, changes in shoreline position reflect dynamics associated with the levels of naturalness or human modification of the beach. In fact, some beaches exhibited more pronounced shoreline evolution trends, probably due in part to possible human influence (e.g., construction of artificial structures, damage to the *Posidonia oceanica* meadow, and others). From a hydrodynamic perspective, a further contribution of this thesis was the numerical modelling of currents circulation within the surf zone of embayed beaches (a common beach type along the studied coastlines). Numerical modelling highlighted that wind forcing on the sea surface plays a crucial role in the formation and location of rip currents, as well as in determining their intensity and their longshore and cross-shore extent. Finally, considering the widespread presence of *Posidonia oceanica* meadow along the entire coastline, the role of beach-cast in coastal flooding events was investigated. For this purpose, a coastal video monitoring system, located on a microtidal urban beach (Poetto), and numerical modelling were used to analyse two storm events and their effects on morphodynamic processes, such as the interaction between wave motion and beach-cast (mainly composed of *Posidonia oceanica* and *Arundo donax* remains).

Keywords: *Morphometric analysis; Embayed beaches; Shoreline changes; Hydrodynamic circulation; Numerical modelling; Posidonia oceanica; Seagrass banquettes.*

ACKNOWLEDGEMENTS

I sincerely thank my PhD Supervisor, **Prof. Sandro Demuro**, for his support and availability during my PhD programme. I am also grateful for being included as a member of the **Coastal and Marine Geomorphology Group** (CMGG) at the University of Cagliari and for having access to all the equipment necessary for my research.

I would like to warmly thank my first PhD Co-Supervisor, **Prof. Giovanni Coco**, for his constant guidance throughout my research. I am sincerely grateful to him for welcoming me to the **University of Auckland** during my research abroad and for giving me the opportunity to collaborate with him, introducing me to the numerical modelling of morphodynamic processes. His support has been crucial not only in advancing of my scientific knowledge, but also for my personal and professional growth. Above all, I would like to thank him for sharing with me his vision of scientific research, grounded in deep respect for people and collaboration.

Furthermore, with immense pleasure, I would also like to thank my second PhD Co-Supervisor, **Dr. Simone Simeone**, for believing in me from the beginning of my PhD programme and for his constant support throughout all phases of my research. I am also grateful to him for giving me the opportunity to collaborate with him and his research group, and for welcoming me at his workplace, the **IAS-CNR** (Oristano - Torregrande). Above all, I wish to express my profound gratitude for having transmitted to me the true spirit of scientific research, not only in the dedication to achieving results, but above all in the enthusiasm for discovery, the curiosity in research and the ability to go beyond one's limits.

I would also like to thank the PhD Coordinator, **Prof. Maria Francesca Casula**, for her constant availability and support in helping us PhD students with the various requirements and administrative tasks. This thesis was produced while attending the PhD programme in **INNOVATION SCIENCE AND TECHNOLOGY** at the **University of Cagliari**, Cycle XXXVIII, with the support of a scholarship financed by the Ministerial Decree no. 351 of 9th April 2022, based on the NRRP - funded by the European Union - NextGenerationEU - Mission 4 "Education and Research", Component 1 "Enhancement of the offer of educational services: from nurseries to universities" - Investment 3.4 "Advanced teaching and university skills".

I would like to thank the support provided by the **NEPTUNE 3 Project** (Natural Erosion Prevision Through Use of Numerical Enviroment) (L.R. 7.08.2007, N.7: Promozione della ricerca scientifica in Sardegna e dell'Innovazione tecnologica in Sardegna), which supported me in my research activities, including the collection of topographic and bathymetric data.

I also thank the **Department of Mechanical, Chemical and Materials Engineering** and the **Department of Chemical and Geological Sciences** of the **University of Cagliari**, and the **MEDCOASTLAB** (Mediterranean Geomorphological Coastal and Marine Laboratory).

My thanks also go to the company **SARDEGNA PROGETTA**, for their collaboration and for training and supporting me in activities related to coastal video monitoring systems. In particular, I wish to express my gratitude to **Mariella Pilo** and especially to **Pasquale Pittaluga**, for sharing with me some of his vast knowledge in this field during my training.

I also thank the **Port System Authority of the Sardinia Sea** for their logistical support and the **Municipality of Domus de Maria**, the **ASL 8 Cagliari** and the **Italian Navy** (**Marina Militare Italiana**) for their availability and access to the coastal video monitoring stations.

I would like to sincerely thank my colleagues and friends, **Dr. Daniele Trogu** and **Dr. Marco Porta**, for their continuous encouragement and unwavering support throughout my PhD activities. Their presence and availability were invaluable throughout my research. I am also grateful to **Dr. Andrea Ruju**, **Prof. Angelo Ibba** and **Dr. Salvatore Vacca** for their assistance and availability.

I would like to extend my sincere thanks to my friends and colleagues at the University of Auckland for welcoming me into their activities and for making my stay abroad in New Zealand a truly extraordinary experience. I am especially grateful to **Eduardo Gómez**, **Charline Dalinghaus**, **Édouard Basquin**, **Zhanchao Shao**, **Xin Li** and **Iñaki de Santiago**. I also wish to thank **Dr. Valentina Spano** for her help and support during a significant phase of my PhD research and for becoming a personal point of reference in seeing the world beyond academic life.

My deepest thanks go to **Veronica**, for always believing in me from the beginning of this PhD, for motivating me through challenging times and for encouraging me to never give up. Having her by my side has been truly invaluable. Last but not least, I would like to thank my **parents** and my **sister**, who have always been there for me and supported me through every moment, both the good and the difficult ones. I am equally grateful to my friends for their constant encouragement and support throughout these three years.

Contents

List of Figures

List of Tables

List of Publications

Peer-reviewed articles:

Usai, A.; Simeone, S.; Trogu, D.; Porta, M.; De Muro, S., **2025a**. A morphometric analysis of embayed beaches: southern Sardinia Island. *Geomorphology* 483, 109838. https://doi.org/10.1016/j.geomorph.2025.109838.

Usai, A.; Trogu, D.; Porta, M.; Demuro, S.; Simeone, S., **2025b**. 70 years of shoreline changes in southern Sardinia (Italy): Retreat and accretion on 79 Mediterranean microtidal beaches. *Water 17* (17), 2517. https://doi.org/10.3390/w17172517.

Chatzipavlis, A.; Trogu, D.; Ruju, A.; Montes, J.; Usai, A.; Porta, M.; Coco, G.; De Muro, S.; Ciavola, P., **2025**. Development and validation of an early warning system for coastal flooding on a Mediterranean urban beach. *EGUsphere* [preprint]. https://doi.org/10.5194/egusphere-2025-2292.

Conference papers:

Usai, A.; Simeone, S.; Trogu, D.; Porta, M.; De Muro, S., **2024**. Morphometric analysis and classification of the embayed beaches on the southern coast of Sardinia Island (Western Mediterranean Sea). In: *Coastlines under change: Proceedings from the International Coastal Symposium (ICS) 2024 (Doha, Qatar)*; Phillips, M.R., Al-Naemi, S., Duarte, C.M., Eds.; *J. Coast. Res.* 113, 748-752. https://doi.org/10.2112/JCR-SI113-147.1.

Trogu, D.; Simeone, S.; Usai, A.; Porta, M.; De Muro, S., **2024**. On the role of wood and seagrass rests in coastal flooding events in Mediterranean microtidal beaches. In: *Coastlines under change: Proceedings from the International Coastal Symposium (ICS) 2024 (Doha, Qatar)*; Phillips, M.R., Al-Naemi, S., Duarte, C.M., Eds.; *J. Coast. Res.* 113, 115-119. https://doi.org/10.2112/JCR-SI113-023.1.

Chapter 1: INTRODUCTION

Coastal areas are among the highest dynamic and complex natural environments on the planet, continuously changing over time and space (Benavente et al., 2023; Chowdhury et al., 2023). As transitional zones between marine and terrestrial environments, they play a crucial ecological, economic, and social role (Wright et al., 2019; Gleason et al., 2023). Due to the high population density and intense human activity along coastal regions (Small and Nicholls, 2003; McGranahan et al., 2007; Bird, 2008), these areas have been subjected over time to significant anthropogenic pressures (Williams et al., 2022), including commercial activities and the construction of coastal infrastructures, such as harbours, marinas, roads, breakwaters, artificial reefs, seawalls, and more. As a result, these human interventions have disrupted natural balance and increased the vulnerability of coastal areas to degradation and erosion (Prasad and Kumar, 2014; Gomez et al., 2019; Foti et al., 2022a). Compounding this situation are the intensifying effects of climate change, which represent a serious threat by amplifying existing coastal vulnerabilities and criticalities (Bini and Rossi, 2021). Among the most evident consequences are sea level rise (SLR), more frequent and intense storm events, coastal flooding events and accelerated beach erosion (Pang et al., 2023; IPCC, 2023a), factors that potentially compromise the structural and functional integrity of coastal environments. In response to these factors, the development of integrated and sustainable strategies for coastal planning and management is essential to preserve beach resilience and safeguard the integrity of existing ecosystems (Fisichelli et al., 2016; Powell et al., 2019; Cabana et al., 2023).

This thesis aims to improve the understanding of Mediterranean microtidal beaches and to fill specific gaps in the scientific literature by adopting a multidisciplinary approach that incorporates geomorphological, morphometric, hydrodynamic and ecological aspects. In this context, the entire southern coastal stretch of Sardinia Island (Italy) was taken as a reference, as it is characterised by a geomorphological heterogeneity of beaches, ranging from embayed beaches to open ones. Among these beaches, some retain their natural conditions, while others have been strongly affected by human interventions (Biondo et al., 2020; Porta et al., 2021), altering coastal processes and dynamics, as well as the existing ecosystems (Ruju et al., 2022). In addition, the entire study area is characterised by the continuous presence of a wide meadow of *Posidonia oceanica* (L.) Delile (Telesca et al., 2015). Moreover, the frequent occurrence of banquettes deposits along several studied beaches highlights their ecological relevance, offering valuable insight into the interplay between ecological considerations and coastal morphodynamics processes.

Overall, the structure of the thesis is outlined below:

- **Chapter 2** provide a comprehensive review of the scientific literature relevant to the main topics addressed in the thesis.
- **Chapter 3** outlines the main methodologies used to conduct the research in this thesis.
- **Chapter 4** presents a morphometric analysis, and a classification comparison, aimed at estimating the degree of embaymentisation of 79 Mediterranean microtidal beaches. Furthermore, for each beach, the type of hydrodynamic circulation within the surf zone was estimates, as well as the type of embayment (natural or artificial) based on the presence or absence of engineering structures either within the embayment or as artificial headlands.
- **Chapter 5** analyses shoreline movement trends (retreat or accretion) over a period of approximately 70 years (1954 - 2022) for the 79 identified beaches along the southern coast of Sardinia. The analysis highlighted the shoreline trend of the beaches that appear more resilient and stable, as well as those that are more vulnerable and affected by anthropogenic pressure (e.g., construction of artificial structures and coastal defences, damage to the *Posidonia oceanica* meadow, and others).
- **Chapter 6** presents the results of hydrodynamic and wave modelling for an embayed beach (a common beach type observed along the southern coast of Sardinia) under different wave and wind conditions. Particular attention is given to the influence of wind forcing on surf zone hydrodynamics. Specifically, this chapter highlights the key role played by wind forcing in the development, location and spatial extent of rip current systems on embayed beaches.
- **Chapter 7** investigates the role of beach-cast, accumulated, deposited and sedimented on the backshore, by comparing two intense storm events. More precisely, through the use of a coastal video monitoring system, in combination with numerical modelling, the morphodynamic conditions during these storm events were modelled and analysed, highlighting the protective role of beach-cast in limiting backshore flooding. Numerical simulations also showed distinct flow circulation pattens for the two storm events, with both developing longshore and rip currents.
- **Chapter 8** presents a final summary and overall conclusions of the research conducted in this PhD thesis.

Chapter 2: REVIEW OF LITERATURE

2.1 An overview of coast and beach types

Beaches are dynamic coastal systems composed of unconsolidated sediments (sand, gravel or pebbles) and represent the physical and functional interface between terrestrial and marine environments (Short, 1999; Bird, 2008; Davidson-Arnott, 2009). Worldwide, their morphology is continuously reshaped by the action of tides, waves, currents and wind (Bagnold, 1940; Davis and Hayes, 1984; Wright and Short, 1984; Carvalho et al., 2016). Through sediment mobility, beaches maintain a dynamic equilibrium that enables them to absorb and dissipate wave energy, especially during storm events, acting as natural barriers against coastal erosion and flooding events (Dean, 2019; Agulles et al., 2021; Castelle and Masselink, 2023).

Beaches also represent important ecological habitats, hosting and supporting a wide variety of flora and fauna, both in their emerged and submerged zones (McLachlan and Brown, 2006; McLachlan and Defeo, 2013). Furthermore, beaches provide essential ecosystem services to coastal communities, as well as an important contribution to local and regional economies (Orams, 2003; Stronge et al., 2005; Lakshmi, 2021). In fact, coastal areas are among the most densely populated regions on the planet (Small and Nichols, 2003; Bird, 2008; Luijendijk et al., 2018) and have been extensively modified by human activities over time (Lotze et al., 2006). Urban development, coastal infrastructure and land-use changes have profoundly altered the natural dynamics of some beach systems, often intensifying erosion and threatening the ecological integrity of these environments (Cooper, 2022; Zhang et al., 2025).

Several studies in the scientific literature have proposed different classification schemes for coastal and beach systems, aiming to categorise the diverse morphologies observed worldwide (e.g., Inman and Nordstrom, 1971; Wright and Short, 1984; Short, 1999). Over time, these classifications have incorporate a range of key factors, including geological controls, morphodynamic processes and sedimentological characteristics, as well as wave and tide conditions.

A first distinction can be made based on the origin of the coastline, as proposed by Shepard (1963), by classifying them into primary and secondary coasts:

- **Primary coasts** include all those coastal morphologies that developed in non-marine environments as a result of predominantly terrestrial morphogenetic processes (e.g., tectonic uplift, glacial and volcanic activity, etc.).

- **Secondary coasts** are those primarily shaped by marine morphogenetic processes (e.g., waves, tides, currents, etc.).

From a geodynamic perspective, Inman and Nordstrom (1971) proposed a classification scheme based on the location of coastlines relative to tectonic plates at the continental scale. According to this classification, coastlines can be divided into three main categories (Davidson-Arnott, 2009):

- **Collision coasts**, located adjacent to subduction margins.
- **Trailing edge coasts**, located on passive continental margins, distant from active subduction zones.
- **Marginal sea coasts**, located along continental margins that are protected from the open ocean (e.g., Mediterranean Sea).

Beaches can also be categorised based on the degree of geological control that influences their formation, evolution, sediment mobility and hydrodynamic processes (Gallop et al., 2020). Geological control refers to the influence exerted by the physical morphologies of the coastline, such as rocky headlands, cliffs, rocky outcrops, islands and other geological structures (Short, 2006; Short 2010). The degree of beach indentation (or embayment) resulting from geological structures has been estimated through the application of morphometric indices and formulations (e.g., Hsu et al., 1989; Short and Masselink, 1999; Spagnolo et al., 2008; Bowman et al., 2009; Fellowes et al., 2019). It is important to note that in recent decades, urban development along the coasts has led to the construction of artificial structures (e.g., groynes parallel or perpendicular to the shoreline, marinas, ports, etc.), which have disrupted the natural continuity of some beaches, crossing them and acting as artificial headlands (Chew et al., 1986; Bulleri and Chapman, 2010). These natural promontories and rigid artificial structures act as lateral barriers that restrict or direct sediment transport, thereby influencing beach morphologies and hydrodynamic processes (Castelle and Coco, 2012; King et al., 2021). Based on their degree of geological control, beaches can be grouped into two main categories (Gallop et al., 2020) (Fig. 2.1):

- **Embayed beaches**: Beaches are tightly enclosed by rocky headlands on both sides, significantly limiting sediment exchange with adjacent coastal areas. As a result, they tend to exhibit high morphological stability but are particularly sensitive to changes in sediment supply. Being enclosed by headlands, these beaches are less exposed to incoming wave action and therefore more sheltered. Some of these beaches can also be partially constrained when only one headland bounds them. This morphological configuration allows for some degree of alongshore sediment transport, although it remains subject to partial natural restrictions.

- **Open beaches**: Beaches with minimal or no geological constraint, allowing for high sediment mobility. Their morphology is highly dynamic and continually adapts to changing environmental conditions.

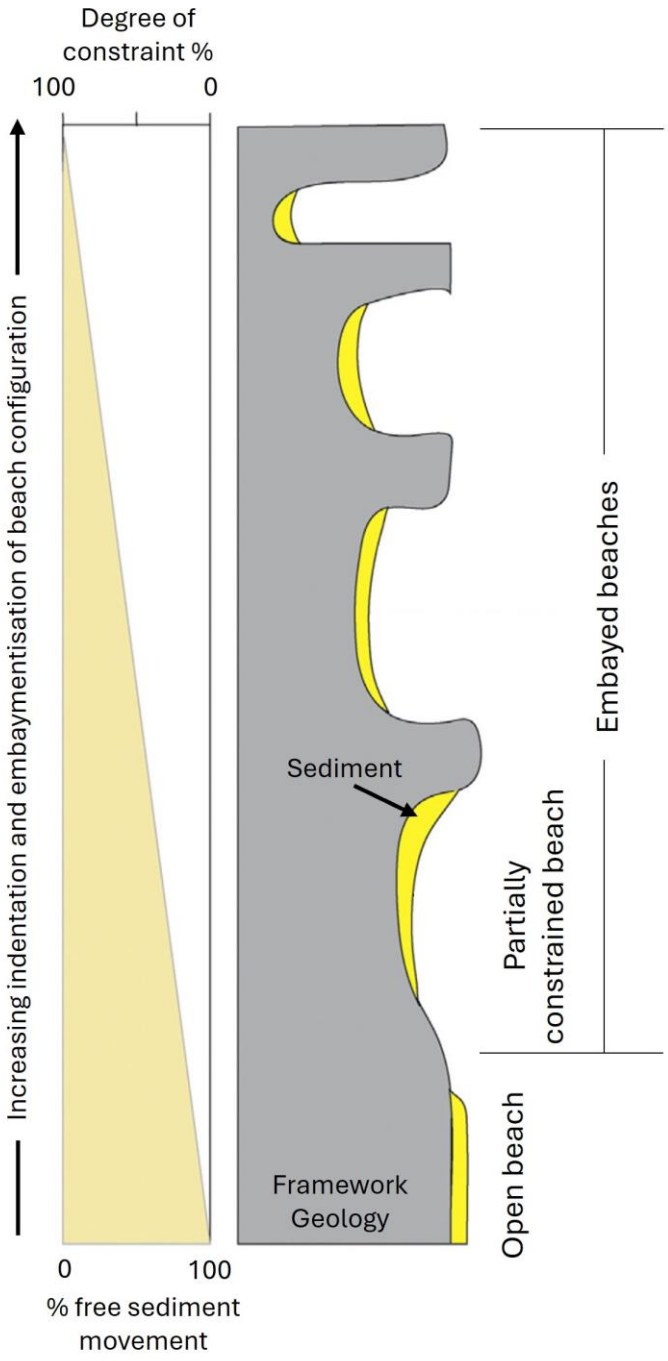

Figure 2.1 - Degree of beach constriction ranging from embayed to open beach. The figure shows the relative variation in sediment mobility associated with the % of beach constraint. The degree of constraint for embayed beaches is based on embayment classes proposed by Fellowes et al., 2019 (modified from Gallop et al., 2020 and adapted here to illustrate this beach subdivision).

While these classifications primarily rely on geological processes, dynamics and morphological characteristics, Davies (1980) proposed an alternative approach that uses tidal range as the principal criteria for distinguishing coastal types. As shown in Figure 2.2, three main types of tidal environments can be identified worldwide:

- **Macrotidal**: tidal range greater than 4 meters.
- **Mesotidal**: tidal range between 2 and 4 meters.
- **Microtidal**: tidal range less than 2 meters.

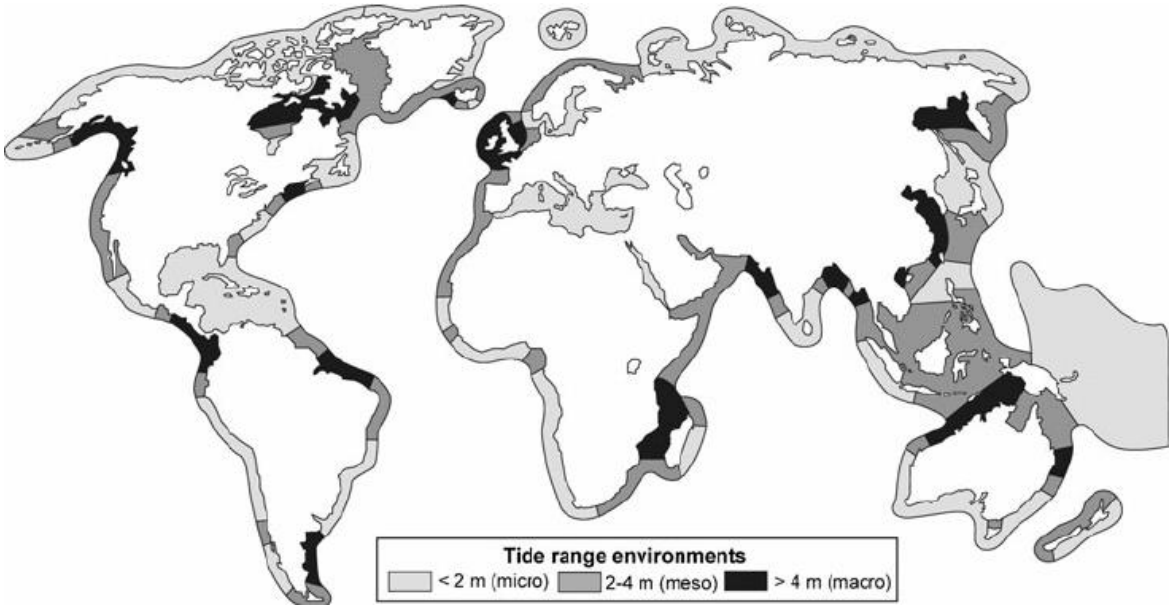

Figure 2.2 - Distribution of tidal environments in the world (Davies, 1980; modified by Masselink and Hughes, 2003).

To further refine the identification of coast types, Hayes (1979), and later Davis and Hayes (1984), introduced a classification scheme that categorises coasts based on the comparison between mean wave height and mean tidal range (Fig. 2.3). By integrating these key parameters, this approach provides a more comprehensive framework for distinguishing coastal environments. As shown in Figure 2.3, three main types of coasts can be identified (Davis and Hayes, 1984):

- **Wave dominated**: Coasts are primarily shaped by wave energy, with relatively low tidal influence. Coastal morphologies are mainly driven by wave action, typically resulting in wide beaches with dune system.
- **Tide dominated**: Coastal areas where tidal processes dominate over wave energy. Coastal morphologies are strongly influenced by tidal range, leading to the formation of extensive estuaries and tidal channels.
- **Mixed energy**: Coasts significantly influenced by both wave and tidal forces, resulting in a combination of coastal morphologies shaped by the interplay of these processes.

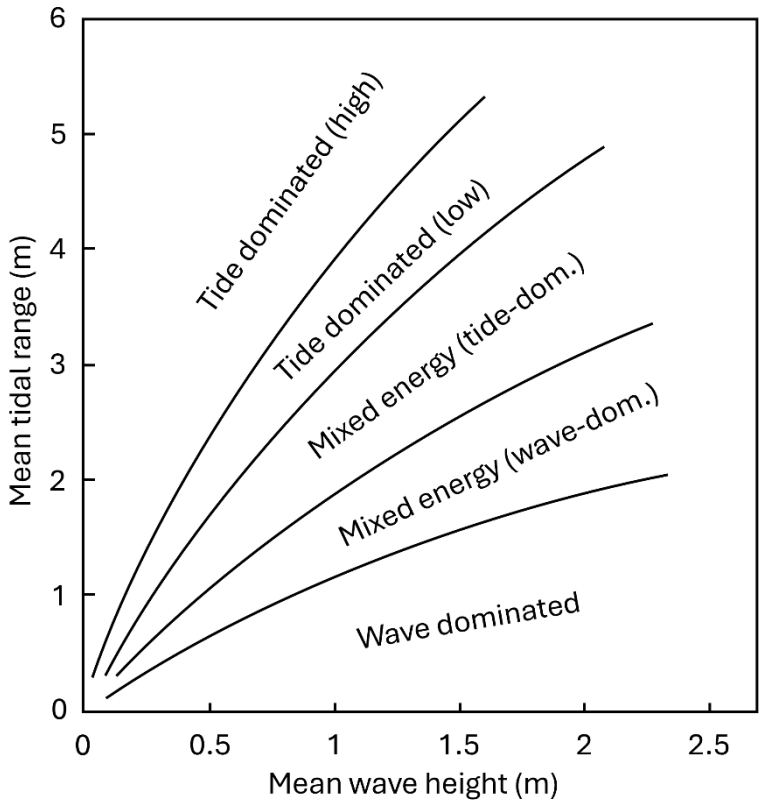

Figure 2.3 - Coast classification based on the relationship between mean wave height and mean tidal range (modified from Davis and Hayes, 1984; Hayes, 1979).

When focusing on the scale of individual wave-dominated beaches with minimal tidal influence, an important further distinction can be based on the "dimensionless fall velocity" parameter (Ω) (Gourlay, 1968; Dean, 1973), which incorporates both wave and sediment characteristics (Equation 2.1).

$$\Omega = \frac{H_b}{W_s T} \tag{2.1}$$

where H_b is the breaker wave height, T is the wave period and W_s is sediment fall velocity.

In this context, Wright and Short (1984) applied the Ω parameter to natural wave-dominated beaches to distinguish three morphodynamic states (Short, 1999):

- **Reflective (Ω < 1)**: These beaches are typically associated with low wave energy, long wave periods, coarse sediments and steep profiles. Wave breaking occurs very close to the shoreline, resulting in limited energy dissipation and a narrow surf zone. Reflective beaches tend to be morphologically stable in shape but more prone to localised erosion.
- **Intermediate (1 < Ω < 6)**: These beaches exhibit a wide range of conditions, with moderate to high wave energy, short to long wave periods and fine to medium sediment sizes. Their profiles are highly dynamic, often showing shallow sandbars

and rip channel systems. This beach type is highly responsive to changing wave conditions, leading to frequent and sometimes rapid transformations in beach morphology.

- **Dissipative (Ω > 6)**: These beaches are shaped by high wave energy, short wave periods and fine sediments. They exhibit gentle slopes and a wide surf zone where waves break progressively across a wide area, allowing much of the wave energy to dissipate before reaching the shoreline.

Finally, following the classification of beach morphodynamic states by Wright and Short (1984), Masselink and Short (1993) introduced the Relative Tide Range (*RTR*) as an additional parameter in the classification to account for tidal influence (Equation 2.2), given that the surf zone, shoaling and swash zones can shift its position over time.

$$RTR = \frac{TR}{H_b} \tag{2.2}$$

where *TR* is the tidal range and H_b is the breaking wave height.

2.1.1 Microtidal Mediterranean beaches

Mediterranean beaches are primarily composed of sandy sediments, often mixed with gravelly or pebbly sediments, or in some cases made up exclusively of the latter (Ortega-Sánchez et al., 2017). These beaches exhibit a wide range of shapes, from small and embayed beaches (commonly known as "pocket beaches"; Bowman et al., 2009) to extensive open beaches (Bird, 2008; Gallop et al., 2020). A key characteristic of Mediterranean beaches is their typically microtidal regime, with tidal ranges generally varying from a few centimeters up to approximately 40 cm (Antonioli et al., 2015). Exceptions include the Gulf of Gabès (Sammari et al., 2006) and some areas of the North Adriatic Sea, where tidal amplitude can reach up to 1.8 m (Antonioli et al., 2015). The tidal cycle in the Mediterranean Sea is generally semi-diurnal, characterised by two high tides and two low tides each day (Lozano and Candela, 1995; Ferrarin et al., 2018). As a result, coastal hydrodynamic circulation in the Mediterranean basin is generally driven by wind action rather than tidal forces (Aspioti and Fourniotis, 2024).

A typical cross-shore beach profile can be divided into several functional zones (*backshore*, *foreshore*, *shoreface*, *offshore*) (Bird, 2008; Davidson-Arnott, 2009; Masselink et al., 2014).

Starting from the inland side, Mediterranean beaches are often characterised by the presence of wetland environments located in the first area behind the *backshore* zone, which may include ponds, lagoons and river mouths or estuarine areas (De Muro and De Falco, 2010) (Fig. 2.4). These features are not present along all Mediterranean beaches, as

their development depends on local geological heritage and geomorphological conditions. Moving seaward, there is a transition from wetlands to coastal dune systems. These are natural accumulations of sediment primarily shaped by the prevailing action of wind and wave (e.g., during storm events) (Nordstrom et al., 1990; D'Alessandro et al., 2020; Husemann et al., 2024). The interaction with river systems is also able to shape and influence the evolution and development of dune systems (Liu and Coulthard, 2015). These coastal dunes play a key role in protecting the inland areas from coastal erosion and contribute significantly to the long-term stability and resilience of the beach system (Stanica and Ungureanu, 2010). Additionally, dune systems are characterised by the presence of psammophilous vegetation, which is essential for stabilising the sediments (Bel and Ashkenazy, 2014; Younsi and Bouziane, 2023). The root systems of dune plants anchor the sand and acts as a natural barrier against wind, thereby reducing erosion and promoting primary dune formation. Mediterranean coastal dunes are recognised under the EU Habitats Directive (*92/43/EEC*) (https://environment.ec.europa.eu/topics/nature-and-biodiversity/habitats-directive_en) and are assigned specific habitat codes within the Natura 2000 network (https://environment.ec.europa.eu/topics/nature-and-biodiversity/natura-2000_en), as they represent important ecosystems with characteristic biodiversity (e.g., Code 2250 - Coastal dune with *Juniperus spp.*).

The *backshore* is the zone of the beach located between the Mean High Water (M.H.W) of the ordinary tide and the dune toe or inland limit, often marked by the presence of psammophilous vegetation (Fig. 2.4). The *backshore* includes the swash zone, which is defined inland by the upper limit of the wave run-up (Holman, 1986; Bird, 2008). Wave motion (swash) in this zone plays a key role in the formation of berm systems (Stanica and Ungureanu, 2010). During intense storm events, the higher areas of the *backshore* may occasionally become inundated, resulting in the formation of berms further inland from the shoreline, a process dependent on energy of incident wave (Stanica and Ungureanu, 2010). Overall, the *backshore* is primarily shaped by both wind and wave action, which promotes the development of various morphological and sedimentary structures such as cusps, ripple marks, etc. (De Muro and De Falco, 2010). Marine plant remains, particularly those from *Posidonia oceanica* meadows, along with other vegetal materials transported by wave motion and deposited in the *backshore* (such as wooden logs, river reeds, etc.), can act as obstacles or barriers to the aeolian transport of sediments, supporting the formation of nuclei for the development of primary dunes. Similarly, large accumulations of beach-cast material deposited in swash zone by wave motion can contributes to the formation of seagrass berms in the *backshore* (Simeone et al., 2013a). When these accumulations are primarily composed by *Posidonia oceanica* remains, they are called "banquettes" (Boudouresque and Meinesz, 1982; Simeone and De Falco, 2013). These vegetal deposits are essential for beach environment and contribute to the eco-geomorphological complexity of the beach system.

Continuing seawards, the next zone is the *foreshore*. This intertidal area is located between the Mean High Water (M.H.W) and the Mean Low Water (M.L.W) of the ordinary tide (McGlashan et al., 2015) (Fig. 2.4). It is the most dynamic part of the beach system, as it is regularly and directly influenced by wave action (McGlashan et al., 2015). The shoreline, boundary between the emerged and submerged part of the beach, can undergo rapid changes due to the combined effects of waves and tides (McGlashan et al., 2015). These changes may involve shoreline accretion and retreat, which are particularly evident with seasonal variations in wave energy (Masselink and Pattiaratchi, 2001; Foti et al., 2022b), such as calm conditions during summer and high-energy storm events in winter season. The morphology of the *foreshore* zone is typically characterised by a gentle slope (Stanica and Ungureanu, 2010) and shows various morphological and sedimentary structures formed by waves and currents, such as intertidal sandbars, troughs, ripple marks, and others (Fig. 2.4). The distribution of sediments can vary along the surf zone, depending on local environmental conditions and the resulting morphodynamic beach state (Wright and Short, 1984). As a dynamic interface between land and sea, the *foreshore* zone plays a crucial role in understanding coastal morphodynamics, sediment transport processes and the interaction between physical and ecological systems.

The *shoreface* is the part of the beach that extends from Mean Low Water (M.L.W) of the ordinary tide to the depth where wave shoaling becomes negligible (Fig. 2.4). This limit is typically referred to as the "depth of closure" (Masselink et al., 2014), often approximated to half of the wave-length (Carobene and Brambati, 1975). In microtidal Mediterranean beaches, the lower limit of the *shoreface* zone often coincides with the upper limit of *Posidonia oceanica* meadow (De Muro and De Falco, 2010). Overall, the *shoreface* zone is continuously influenced by wave motion and currents, which shape its morphology and control sediment dynamics. During storm events, sediments may be eroded from the *backshore* and transported offshore, where they accumulate on the *shoreface* as sandbars. These sedimentary morphologies mark the beginning of the surf zone, where waves generally begin to break under calmer conditions. Sandbar sediments may gradually migrate landward, contributing to the beach's sediment budget and playing a key role in the maintaining the dynamic equilibriums of beach systems. As in the *foreshore* zone, sediments sorting can vary due to the continuous interaction between wave-seabed dynamics, sediment availability, local hydrodynamics and other contributing factors (Broekema et al., 2016).

The last zone, the *offshore*, is the part of the beach system located beyond the *shoreface* zone, extending from the "depth of closure" to the continental shelf (Fig. 2.4). It is typically located at depths where wave motion on the seabed is minimal or absent under normal conditions (Cerkowniak et al., 2015). In contrast to the *shoreface*, this zone is primarily shaped by long-term geological and deep-water processes. In the *offshore* zone,

seabed changes are generally minimal (Cerkowniak et al., 2015), which promotes the deposition of fine-grained sediments.

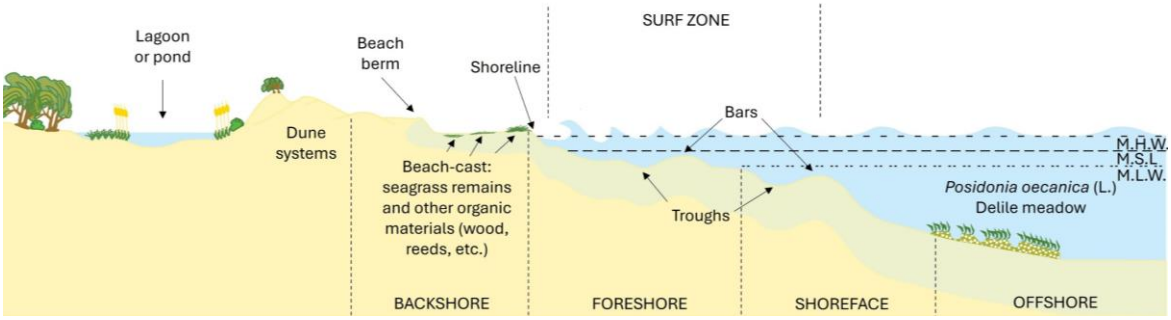

Figure 2.4 - Typical cross-shore profile of a microtidal Mediterranean beach (modified from De Muro and De Falco, 2010).

2.1.2 Global climate changes on coastal areas

In recent decades, coastal areas worldwide have become more vulnerable due to the effects of climate change (Ranasinghe, 2016; Sarkar et al., 2022). The main consequences include sea level rise, increased frequency and intensity of storm events, coastal erosion and the growing risk of coastal flooding (Torresan et al., 2012; Hinkel et al., 2013; Lincke and Hinkel, 2021; Pang et al., 2023). These phenomena are largely driven by global warming, particularly the rise in ocean temperatures, which leads to thermal expansion of seawater and destabilization of ice sheets and glaciers (Shepherd et al., 2012; Cazenave and Cozannet, 2014). Over the past few decades, global mean sea surface temperatures (SST) have increased by approximately 0.13 ± 0.01 °C per decade between 1982 and 2023, with a notable acceleration observed in the most recent years especially in the Northen Hemisphere (IPCC, 2023b; von Schuckmann et al., 2024).

Similarly, as reported by the Intergovernmental Panel on Climate Change (IPCC), the global mean sea level (GMSL) increased faster in the 20th century than in any previous century, with a global mean sea level increase of approximately 0.20 m [0.15 to 0.25] m between 1901 and 2018 (IPCC, 2023b). More precisely, global mean sea level rise has accelerated since the late 1960s, with an average rate of 2.3 [1.6 to 3.1] mm/yr between 1971 and 2018 (IPCC, 2023b). This rate increased to 3.7 [3.2 to 4.2] mm/yr during the period from 2006 to 2018 (IPCC, 2023b) and further accelerated to approximately 4.3 ± 0.3 mm/yr when considering the period from 2013 to 2023 (von Schuckmann et al., 2024). According to future projections, global mean sea level is expected to continue rising by approximately 0.38 [0.28 to 0.55] m by 2100 under the best-case scenario (Shared Socioeconomic Pathways - SSP1-1.9), and potentially by 0.77 [0.63 to 1.01] m in the worst-case scenario (SSP5-8.5) (IPCC, 2023b).

The rise in global sea surface temperatures (SST) has not only contributed to sea level rise but may also significantly increased the frequency and intensity of storm events (Woolf and Wolf, 2013; Goodess, 2013). These changes could potentially affect key wave parameters along global coastlines, including significant wave height, wave period, wave direction and wave energy. Moreover, these changes could affect sediment budget (Simeone et al., 2018), transport processes (Adams et al., 2011) and accelerate coastal erosion rates (Pang et al., 2023), thereby posing growing challengers for coastal managements and the resilience of beach systems.

Since coastal regions are among the most density populated areas in the world (Small et al., 2000; Small and Nicholls, 2003), the impacts of global climate change have also led to substantial social and economic consequences (Klein and Nicholls, 1999; Dolan and Walker, 2006). Rising sea levels, coupled with more frequent storm events and coastal flooding, pose serious threats to the built infrastructures along coastlines (e.g., roads, ports, public building, residential areas, etc.), as well as disrupt key economic sectors upon which coastal communities depend, including tourism, fisheries, aquaculture, local commerce, and others.

Therefore, to effectively address the impacts of climate change on coastal environments, it is essential to implement systematic and long-term monitoring programmes. In fact, data collection is crucial for evaluating both current and future scenarios, as well as to identify the most vulnerable coastal areas (Roukounis et al., 2022). This information provides the scientific basis needed to develop targeted risk mitigation strategies and support coastal management. At the same time, spatial planning plays a strategic role in addressing the impacts of climate change by providing a structured framework through which both mitigation and adaptation measures can be identified, prioritised and implemented along the coastlines.

This is even more relevant in the Mediterranean Sea (Nicholls and Hoozemans, 1996; Marsico et al., 2017), where the sea level has risen with a rate 2.5 ± 0.4 mm/yr (from 1993 to 2017), depending on local factors such as land subsidence and regional wave dynamics (Mohamed et al., 2019; Meli et al., 2023). Since beach systems act as the first natural barrier against wave action, it is equally important to implement effective environmental management practices for these ecosystems. These practices include, for example, prohibiting the passage of heavy vehicles on the beach-dune systems, preserving dune vegetation, limiting “beach cleaning” activities that involve the removal of seagrass banquettes, preventing anchoring on seagrass meadows, etc. (De Muro and De Falco, 2010). These actions are essential to maintain the stability and ecological functionality of coastal environments.

In this scenario, in 2015 the 193 member countries of the United Nations (UN) adopted the 2030 Agenda for Sustainable Development, a global action plan approved by

the United Nations General Assembly and considered a fundamental tool for addressing climate change issues (United Nations, 2015). This plan is based on 17 Sustainable Development Goals (SDGs), divided into a total of 169 specific targets to be achieved by 2030. Since coastal zone represents the dynamic interface between the marine and terrestrial environments, the Goals most closely related to the topics addressed in this thesis have been reported in Table 2.1. More precisely, this thesis contributes to the achievement of SDG 13 (Climate Action) by addressing coastal dynamics in the context of climate change. At the same time, it is also relevant to SDG 14 (Life Below Water) as it supports the importance of *Posidonia oceanica* meadows, and to SDG 15 (Life on Land), as it supports the conservation of dune-beach ecosystems and their associated vegetation.

Table 2.1

Main Sustainable Development Goals (SDGs) and targets of the UN 2030 Agenda (https://www.un.org/sustainabledevelopment/sustainable-development-goals/) related to the topics studied and analysed in this thesis.

SDG 13 (Climate action): "*Take urgent action to combat climate change and its impacts*" (https://www.un.org/sustainabledevelopment/climate-change/)	
Target 13.1	"*Strengthen resilience and adaptive capacity to climate-related hazards and natural disasters in all countries*"
Target 13.3	"*Improve education, awareness-raising and human and institutional capacity on climate change mitigation, adaptation, impact reduction and early warning*"
SDG 14 (Life below water): "*Conserve and sustainably use the oceans, seas and marine resources*" (https://www.un.org/sustainabledevelopment/oceans/)	
Target 14.2	"*By 2020, sustainably manage and protect marine and coastal ecosystems to avoid significant adverse impacts, including by strengthening their resilience, and take action for their restoration in order to achieve healthy and productive oceans*"
SDG 15 (Life on land): "*Sustainably manage forests, combat desertification, halt and reverse land degradation, halt biodiversity loss*" (https://www.un.org/sustainabledevelopment/biodiversity/)	
Target 15.5	"*Take urgent and significant action to reduce the degradation of natural habitats, halt the loss of biodiversity and, by 2020, protect and prevent the extinction of threatened species*"

2.2 *Posidonia oceanica* meadow and seagrass banquettes

Posidonia oceanica meadow represents one of the most important marine ecosystems in the Mediterranean Sea (Duarte, 2002; Telesca et al., 2015) (Fig. 2.5). *P. oceanica* is a marine plant (phanerogam) endemic to the Mediterranean, characterised by roots, rhizomes, leaves, flowers (Hemminga and Duarte, 2000; Pergent-Martini et al., 2006; Díaz-Almela et al., 2007; Larkum et al., 2006). These phanerogams colonize sandy and rocky coastal seabeds, forming extensive and compact underwater meadows (Fornes, et al., 2006; Balestri et al., 2015). Generally, they grow from a few centimeters below the sea surface to depths of about 40 m, depending on water transparency, which affects the amount of sunlight that can penetrate (Pergent et al., 1989; Gobert et al., 2006; Marbà et al., 2014). In fact, in areas with particularly clear waters, *Posidonia oceanica* can grow even at greater depths. The minimum amount of light required to survive is between 0.1 and 2.8 mol photons day^{-1} m^{-2} (Gattuso et al., 2006). Additionally, *Posidonia oceanica* requires well-oxygenated water to survive (Borum et al., 2006) and can tolerate salinity levels ranging from about 33 psu to 39 psu (Fernández-Torquemada and Sánchez-Lizaso, 2005).

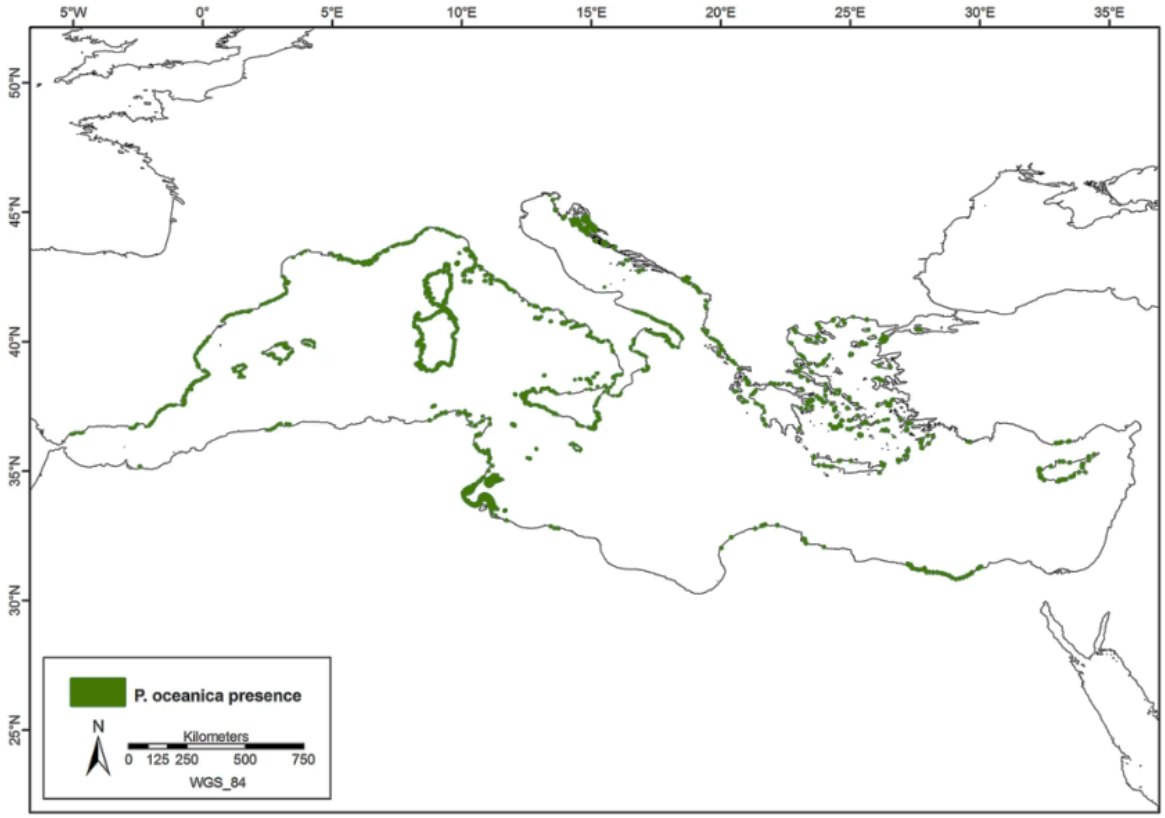

Figure 2.5 - Distribution of the *Posidonia oceanica* meadows along the coast of the Mediterranean Sea (from Telesca et al., 2015).

From an ecological perspective, these meadows play a crucial role in marine biodiversity (Hemminga and Duarte, 2000; Calizza et al., 2013). They provide shelter, food and spawning grounds for numerous species of fish, invertebrates and other marine

organisms (Francour et al., 1999). In particular, the leaves of *P. oceanica* provide ideal surfaces for the colonization of epiphytes (organisms that live attached to the leaves) (Piazzi et al., 2016), many of which produce shells or carbonate structures primarily composed of calcium carbonate ($CaCO_3$) (Perry and Beavington-Penney, 2005). The epiphytic organisms on *P. oceanica* leaves may account for up to about 30% of the total canopy biomass (Mazzella and Ott, 1984; Pardo et al., 2008). When they die, their shells and calcareous fragments settle on the seabed, contributing to the formation of new carbonate sediment (Perry and Beavington-Penney, 2005), which highlights the significant contribute of seagrass meadow in the accumulation and storage of sediment. However, a fraction of siliceous sediment can be also formed within the meadow, mainly from the remains of other marine organisms (Gaglianone et al., 2017).

The seagrass meadows also play an important role in the carbon cycle, as they absorb large amounts of carbon dioxide (CO_2) during photosynthesis and store it within their tissues and sediments, acting as carbon sinks (Duarte et al., 2005; Monnier et al., 2021). The slow decomposition of *P. oceanica* plants allows for long-term carbon storage, thereby contributing to reduce atmospheric CO_2 levels and mitigate the effects of climate change (Pergent-Martini et al., 2021). The plant's vertical growth, combined with horizontal expansion, leads to the formation of dense structures made primarily of rhizomes and sediment, known as "*matte*", which can reach several meters in thickness (Pergent et al., 1989; Boudouresque et al. 2016).

At the same time, *P. oceanica* meadows produce large amounts of oxygen, up to 20 g m^{-2} day^{-1} (Hermand et al., 1998), which is released into both the water column and the atmosphere. This makes their contribution crucial for maintaining marine ecosystem balance and ensuring high water quality. In fact, the health of these meadows serves as an excellent bioindicator of marine environmental conditions, as *Posidonia oceanica* is highly sensitive to environmental pollution (Montefalcone, 2009; Martínez-Crego et al., 2008).

From a morphodynamic perspective, *Posidonia oceanica* meadows play a crucial role in attenuating and dissipating wave energy (Stratigaki et al., 2011; Vacchi et al., 2012; Manca et al., 2012). At the same time, they contribute to the beach sediment budget (De Falco et al., 2017). In fact, an intact upper limit can help retain sediment mobilised by coastal dynamics within the shoreface, reducing its dispersion offshore and stabilize the seabed (De Falco et al., 2000; Gacia and Duarte, 2001). This dual function, attenuating wave energy and containing sediment, enhances coastal protection against erosion and supports the preservation of marine habitats.

Another important aspect concerns the natural cycle of *Posidonia oceanica* meadows, which can reach a leaf production rate from about 300 to 2000 g dry weight m^{-2} $year^{-1}$ (Ott, 1980; Pergent et al., 1994a; Pergent-Martini et al., 1994), mainly due to annual leaf growth. The leaves of *P. oceanica*, especially during autumn, tend to detach and fall on the seabed,

forming layers of leaf litter (Cucco et al., 2020). According to Cocozza et al. (2011), a large stretch of *P*. *oceanica* meadow approximately 1 km long could provide, annually, more than 125 kg (dry material) of leaf litter per meter of coastline. Part of these litters is transported by currents and wave motion to the backshore, where it accumulates as "banquettes" (Boudouresque and Meinesz, 1982) (also known as seagrass berm, seagrass remains, beach-cast or beach wrack). These vegetal structures, mainly composed of dead leaves and rhizomes of *P. oceanica*, typically appear as ridges parallel to the shoreline (Fig. 2.6). These vegetal accumulations, mixed with sediment and other plant and organic remains, settle into deposits that can reach from few centimeters to several meters in thick (Simeone and De Falco, 2012). Especially during storm events, the leaf litter of *P. oceanica* can be mobilised, transported and deposited by wave motion further inland on the backshore, contributing to the formation of storm berms.

The formation of banquettes may be influenced by the availability of seagrass litter along the coast, as well as the morphodynamic characteristics of the beaches, which determine their capacity to retain and accumulate the leaf litter (Simeone and De Falco, 2012). For example, on embayed beaches bordered laterally by rocky headlands, both leaf litter and banquettes can remain for long periods on the seabed and along the backshore. This allows repeated cycles of deposition and erosion of the banquettes (Simeon et al., 2013).

Overall, although banquettes are often removed (De Falco et al., 2008) due to the people perception that they reduce the touristic values of the beach (Mateo et al., 2003), it is important to reemphasize their essential ecological and morphodynamic roles. Banquettes protect the beach from erosion, increase beach permeability, contributes to the vertical accretion of the beach by intertwining with sediments, contributes to the formation of coastal dunes and create microhabitats to various terrestrial organisms.

In the scientific literature, several studies have focused on the role of seagrass banquettes in coastal dynamics, for example in relation to geomorphologic processes (Vacchi et al., 2017; Astudillo-Gutierrez et al., 2022, 2024) and beach flooding (Passarella et al., 2020; Ruju et al. 2022; Trogu et al., 2023). For example, some studies have shown that wave energy during storm events may be dissipated through the destruction of the banquettes (Vacchi et al., 2017), or that these deposits help reduce wave run-up and limit morphological changes to the beach (Passarella et al., 2020). However, the interactions between banquettes, coastal dynamics and sedimentary processes should be further analysed in order to better understand their interconnected effects. These investigations may further contribute to the development of more effective coastal management and conservation strategies, especially considering the decline of these ecosystems due to increasing human activities in the context of climate change scenario (Orth et al., 2006; Marbà et al., 2014; Telesca et al., 2015).

Figure 2.6 - Banquettes of *Posidonia oceanica* deposited on the backshore of Piscinnì beach (Southern Sardinia, Italy), parallel to the shoreline (Photo by A. Usai).

2.2.1 Legislative aspects of *Posidonia oceanica* meadow and seagrass banquettes

Despite playing a crucial role in maintaining the ecological and morphodynamic balance of coastal systems, *Posidonia oceanica* meadow is experiencing significant reduction and degradation due to various human activities (Marbà et al., 2014; Telesca et al., 2015), particularly the growing anthropisation of coastal areas in the Mediterranean Sea. The main causes of this reduction include water pollution, uncontrolled boat anchoring, bottom trawling, coastal infrastructure development and other harmful anthropogenic practices, which also result in increased water turbidity. Additionally, climate change effects continue to exacerbate the degradation of these seagrass meadows, primarily through rising sea surface temperatures and sea levels (Short and Neckles, 1999; Díaz-Almela et al., 2007).

Over the past 50 years, it is observed an overall declining trend of *Posidonia oceanica* meadows in some areas of the Mediterranean Sea, largely due to human impacts (Marbà et al., 2014). Moreover, the growth rate of this species (Ott, 1980) greatly limits its

potential natural recovery after damage. As a result, many habitats associated with these seagrass meadows are at risk of progressive degradation or even complete disappearance over time (Calizza et al., 2013). Given the importance of these marine ecosystems, *Posidonia oceanica* meadows are protected and safeguarded at both national and European levels through a series of specific directives and regulations, which are summarized in Table 2.2.

In Italy, the protection and conservation of *Posidonia oceanica* meadows are regulated by both national and regional legislation, which implement European directives (e.g., Habitat Directive *92/43/EEC*) (https://environment.ec.europa.eu/topics/nature-and-biodiversity/habitats-directive_en). The regulatory framework primarily falls under the jurisdiction of the Italian Ministry, while regional authorities and local entities are responsible for enforcement and adaptation the regulations to local specificities.

Similarly to the seagrass meadows, specific measures and guidelines have been established for the management and protection of *P. oceanica* banquettes. Ministerial Circular no. 8123 of 2006, titled "*Management of beached Posidonia oceanica*" provides operational guidelines for their management, identifying three possible types of intervention:

1. In situ maintenance of banquettes.
2. Temporary removal and subsequent repositioning of banquettes.
3. Removal of banquettes, with subsequent recovery or disposal.

The first intervention represents the primary and preferred management approach from the perspective of environmental conservation. The second intervention consists of the removal of banquettes from the backshore, typically during the summer months, to nearby areas, with the purpose of relocating them during the winter season (e.g., to protect the beach from erosion). This is considered an intermediate measure that balances tourism needs with the environmental conservation of the beach. The third intervention consists of the permanent physical removal of banquettes, with subsequent reuse or disposal at authorised facilities. This is adopted only when the two preceding measures are not practicable.

The management of *Posidonia oceanica* banquettes also refers to the Legislative Decree no. 152 of 2006, known as the "*Environmental Code*". Specifically, the Decree establishes the criteria under which vegetal accumulations present on beaches can be considered as either waste or non-waste.

In addition to these directives, the Regional Council Resolution of Sardinia (the Italian territory where the study area of this thesis is located) no. 40/13 (6 June 2016) provides specific operational guidelines for the management of banquettes, aiming to

ensure environmental protection and the sustainable management of these accumulations along the coastlines of Sardinia.

Within this regulatory framework, some considerations could help and contribute to improving the management of *Posidonia oceanica* banquettes:

- Avoid the removal of *Posidonia oceanica* banquettes during the winter months, when severe storm events are more frequent.
- During removal operations, it is essential to implement measures to minimize the dispersion of sediments mixed with the vegetal materials. In case sediments are removed, they must be restored on the beach.
- Avoid the use of heavy machinery for banquette removal, favoring manual methods or equipment with minimal impact on the beach ecosystem.

Table 2.2

Main national and EU regulations and directives that consider *Posidonia oceanica* meadows.

Habitat Directive (92/43/EEC): Protects natural habitats and wild species by establishing conservation measures and a network of protected areas. https://environment.ec.europa.eu/topics/nature-and-biodiversity/habitats-directive_en. ➢ **Natura 2000**: aims to conserve valuable habitats such as *Posdonia oceanica* meadows (Code 1120: *Posidonion oceanicae*). https://environment.ec.europa.eu/topics/nature-and-biodiversity/natura-2000_en.
Bern Convention (82/72/EEC): Protects wild flora, fauna, and their natural habitats in Europe. https://www.coe.int/en/web/bern-convention.
Barcelona Convention (Italian Law No. 30 of January 25, 1979) in the framework of the **Mediterranean Action Plan of the United Nations Environment Programme (UNEP/MAP)**: Safeguards the marine and coastal environment of the Mediterranean. ➢ Includes the **SPA/BD Protocol**: Specially Protected Areas and Biological Diversity. https://www.unep.org/unepmap/who-we-are/barcelona-convention-and-protocols.
Water Framework Directive - WFD (2000/60/EC): Ensures the ecological quality of inland and coastal waters. https://environment.ec.europa.eu/topics/water/water-framework-directive_en.
Marine Strategy Framework Directive - MSFD (2008/56/EC): Aims to maintain or achieve Good Environmental Status of marine waters. https://research-and-innovation.ec.europa.eu/research-area/environment/oceans-and-seas/eu-marine-strategy-framework-directive_en.
Maritime Spatial Planning Directive (2014/89/EU): Supports sustainable and coordinated use of marine space. https://oceans-and-fisheries.ec.europa.eu/ocean/blue-economy/maritime-spatial-planning_en.
Environmental Impact Assessment Directive - EIA (2014/52/EU): Strengthens environmental checks for projects affecting natural areas. https://environment.ec.europa.eu/law-and-governance/environmental-assessments/environmental-impact-assessment_en.

2.3 Rip currents systems: an overview

Rip currents are narrow, localised flows of water that move underwater from the shore toward the open sea, typically in a direction that is perpendicular or nearly perpendicular to the shoreline (MacMahan et al., 2005, 2006; Short, 2007; Castelle and Masselink, 2023; Castelle and Coco, 2012). They are primarily formed by the action of breaking waves in the surf zone (Dalrymple et al., 2011), especially on sandy beaches with irregular seabeds or morphological variations such as sand bars, channels and depressions (Castelle et al., 2016). These structures can influence the return flow of water pushed toward the shore by the waves, channelling and accelerating it along preferred pathways that direct the currents offshore (Bruneau et al., 2009).

Rip currents are dynamic phenomena whose intensity, location, spacing and persistence can vary over time in response to changes in wave conditions, tide levels and other factors (Short, 1985; Dalrymple et al., 2011). These currents can persist for extended periods, ranging from several hours to days (Castelle et al., 2016), with average velocities (often exceeding 0.5 m/s; Short and Hogan, 1994) enable the offshore transport of large volumes of sediment, especially during storm events (e.g., Loureiro et al., 2012a). The more intense rip currents can also cause localised erosion, resulting in shoreline retreat (e.g., Kim et al., 2013). In some cases, especially on embayed beaches whit high indentation, these systems may reach velocities exceeding 2 m/s (Short, 1999).

The formation and intensity of rip currents are strongly influenced by wave conditions, including wave height, wave period and angle of wave incidence (Yu and Slinn, 2003; MacMahan et al., 2005; Castelle et al., 2016). Waves with greater height (H_0) and relatively short periods (T) can transport large volumes of water toward the shore in rapid succession. This results a significant water accumulation in the surf zone, the area between the shoreline and where the waves begin to break. Since this excess of water cannot remain in the surf zone for long due to the continuous arrival of waves, it is forced to flow seaward through the paths of least resistance (e.g., the channels between sandbars) (Davidson-Arnott, 2009). Moreover, waves with short periods break more frequently, reducing the time interval between successive waves. This determines a constant and pressing flow of water toward the coast, which in turn intensifies the offshore return flow, further strengthening rip current flow.

At the same time, tides can play a significantly role in influencing the behaviour of rip currents (Austin et al., 2010), as variations in sea level directly could affect the morphology of the seabed and the position of the wave breaking zone (surf zone) (Austin et al., 2014; Bruneau et al., 2014; Castelle et al., 2020a). During rising tide phases, the increase in sea level can shift the wave breaking zone landward, thereby altering both the position and intensity of rip currents. In some cases, this can result in a temporary modulation of these currents (Brander, 1999). Conversely, during falling tide phases, the

lowering of sea level could accentuate the interaction between incoming waves and seabed topography. This phase often promotes the formation of more pronounced rip currents (Brander, 1999), which focus the outflow of water accumulated nearshore. In coastal environments with a significant tidal range, sea level fluctuations can activate or deactivate entire rip current systems, depending on the morphological characteristics of the seabed.

Finally, the morphology of the beach and seabed plays a crucial role in the formation, location and intensity of rip current systems, as it determines the preferential channels through which water, pushed shoreward by incoming waves, can return seaward (Short, 1985; Castelle et al. 2012). In particular, beaches with irregular seabeds and significant bathymetric variations are more prone to the development of persistent, well-structured rip currents (Castelle et al. 2016). Conversely, coastal areas characterised by uniform bathymetries and regular seabed profiles tend to develop weaker, more transient and less localised rip currents (Peregrine, 1998; Castelle et al. 2016). Among these morphological controls, beach slope play an important role in rip currents formation (Johnson and Pattiaratchi, 2006). Gently sloping beaches promote a more widespread accumulation of water along the shoreline, resulting in weaker and more diffuse offshore return flows. Conversely, steeper beach slopes can promote the formation of stronger, more concentrate rip currents.

Rip currents are receiving extensive attention in the scientific literature as common and complex coastal phenomena with significant environmental and safety implications. Their formation, evolution and interaction with coastal morphologies have been extensively investigated over time through various multidisciplinary approaches, including field observations (e.g., Bowen and Inman, 1969; Brander, 1999; Austin et al., 2010; etc.), laboratory experiments (e.g., Reniers and Battjes, 1997; Haas and Svendsen, 2002; Kennedy and Thomas, 2004; etc.) and numerical modelling (e.g., Castelle and Coco, 2012; Van Dongeren et al., 2013; Salama et al., 2023; etc.). Overall, these studies have contributed to understanding and identifying the conditions that promote rip current formation and development, as well as the circulation mechanisms that govern them. In recent years, scientific interest has also intensified concerning the risks rip currents pose to swimmers (Castelle et al., 2016), with a growing emphasis on operational forecasting systems and effective strategies for public communication and awareness.

Moreover, several studies have investigated the hydrodynamics processes underlying the formation of rip current systems, successively leading to their classification: Bowen (1969) introduced some fundamental concepts linking wave dynamics to the development of rip currents; Short (1999) proposed a classification based on beach morphology and temporal variability, distinguishing between *Accretionary* (or fixed) *beach rips*, *Erosional* (or migratory) *beach rips*, *Topographic rips*, and *Megarips*; Dalrymple et al. (2011) distinguished rip currents mainly into *offshore morphology-induced* and *structured-*

induced rip currents. Finally, a detailed classification was suggested by Castelle et al. 2016, dividing rip current systems into three main categories: 1) *Hydrodynamically-controlled rip currents*; 2) *Bathymetrically-controlled rip currents*; 3) *Boundary rip currents*.

1) ***Hydrodynamically-controlled rip currents***:

This type of rip current system originates exclusively from hydrodynamic processes related to wave pressure and circulation, independently of the seabed morphology (Castelle et al., 2016) (Fig. 2.7). These currents typically occur along morphologically uniform beaches or in specific planar sections of the beach (e.g., low-tide terraces) where there are no evident topographic discontinuities such as channels or depressions. In this context, rip currents are generated in response to changes in meteo-marine conditions, such as wave motion and wind direction, which lead to the development of concentrated seaward-directed water flows. Their exclusive dependence on hydrodynamic conditions results in highly transient and unstable behaviour, characterised by rapid changes over time. This makes them particularly dynamic and difficult to predict. The most common types are (Castelle et al., 2016):

- ***Flash rips*** (Fig. 2.7a), sudden and temporary currents generated by rapid changes in hydrodynamic conditions.
- ***Shear instability rips*** (Fig. 2.7b), generated by flow instabilities due to velocity differences between adjacent water masses, lending to the formation of vortices and focused offshore currents.

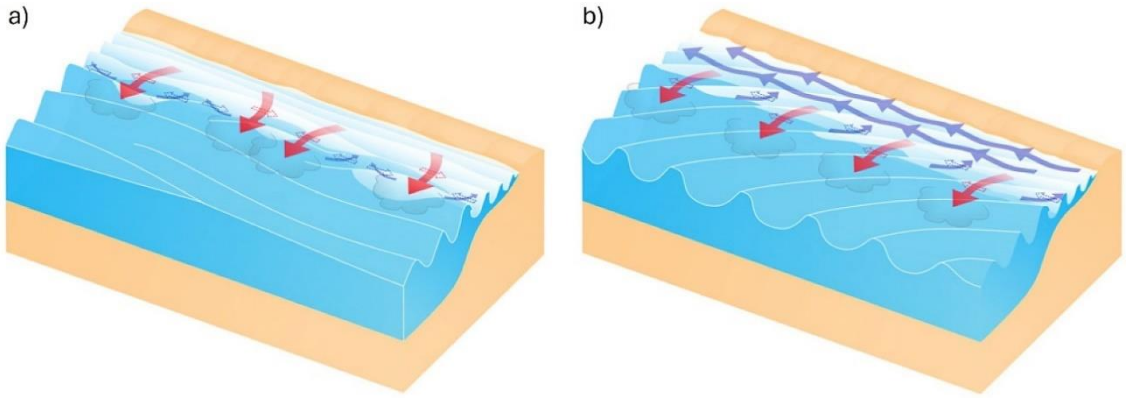

Figure 2.7 - Hydrodynamically-controlled rip currents: **(a)** *Flash rips*; **(b)** *Shear instability rips* (modified from Castelle et al., 2016).

2) Bathymetrically-controlled rip currents:

In this type of rip current system, the depth and the morphology of the seabed play a crucial role (Castelle et al., 2016) (Fig. 2.8). In particular, near morphological changes in the seabed, such as channels or depressions, the water accumulated by the waves tends to concentrate into offshore-directed flows. Contrary to *Hydrodynamically-controlled rip currents*, for a given wave regime and tidal elevation, these currents are generally more persistent and localised. Among the most common types are (Castelle et al., 2016):

- ***Channel Rips*** (Fig. 2.8a) are currents that predominantly form along deep channels located between sandbars within the surf zone, where the seabed's configuration facilitates the outflow of water seaward. These currents are typically associated with an intermediate beach morphodynamic state (Wright and Short, 1984) (see Chapter 2.1 of the thesis) and represent one of the most documented and well-understood types of rip currents, due to their predictability and ease of observation and measurement. The formation of *Channel rips* is driven by variations in the energy dissipation of breaking waves along the coast, which is in turn influenced by the changing seabed depth. This leads to currents that are typically stable and stationary, often maintaining their position for extended periods (days, weeks and, in some cases, months) (Castelle et al., 2016). While most *Channel rips* develop on mobile sandy seabeds, they can also occur in marginal coral reefs, "*Reef Rip Currents*" (De Leon et al., 2008), assuming a nearly permanent position by channelling through natural indentations in the reef.
- ***Focused Rips*** (Fig. 2.8b) are currents generated by variations along the coastline in both wave height and wave breaking angle within the surf zone (Castelle et al., 2016). Their formation is primarily caused by bathymetric anomalies located offshore on the outer part of the surf zone, or on the inner shelf (e.g., in submarine canyons). Similar to *Channel rips*, these currents can appear in relatively fixed positions under specific wave and tide conditions. However, they can also show some variability, shifting along the coast as the wave period and angle of wave incidence change (Castelle et al., 2016).

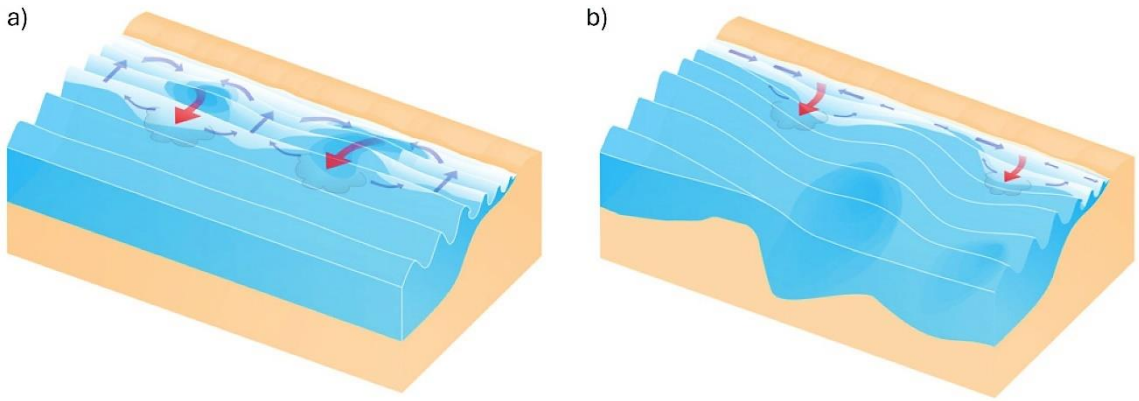

Figure 2.8 - Bathymetrically-controlled rip currents: **(a)** *Channel rips*; **(b)** *Focused rips* (modified from Castelle et al., 2016).

3) Boundary rip currents:

This type of rip current system is typically observed on beaches bordered laterally by physical barriers, either natural (such as rocky headlands) or artificial (e.g., groynes, jetties, harbours, piers, etc.). These barriers influence the beach's hydrodynamics by exerting lateral bathymetric control, thereby affecting the formation and localisation of rip currents, which tend to develop in proximity to the obstacle (Castelle et al., 2016) (Fig. 2.9). As a result, these currents are almost persistent in their location. Thus, both the morphology and lateral extent of the beach's boundaries play a crucial role in the formation and behaviour of this type of currents.

Along geometrically uniform beach exposed to waves approaching at an oblique angle, two main types of rip currents can be distinguished based on the wave orientation relative to the lateral barrier (Castelle et al., 2016):

- ***Shadow rips*** (Fig. 2.9a): which develop on the down-wave side of the physical barrier.
- ***Deflection rips*** (Fig. 2.9b): which form on the up-wave side of the physical barrier.

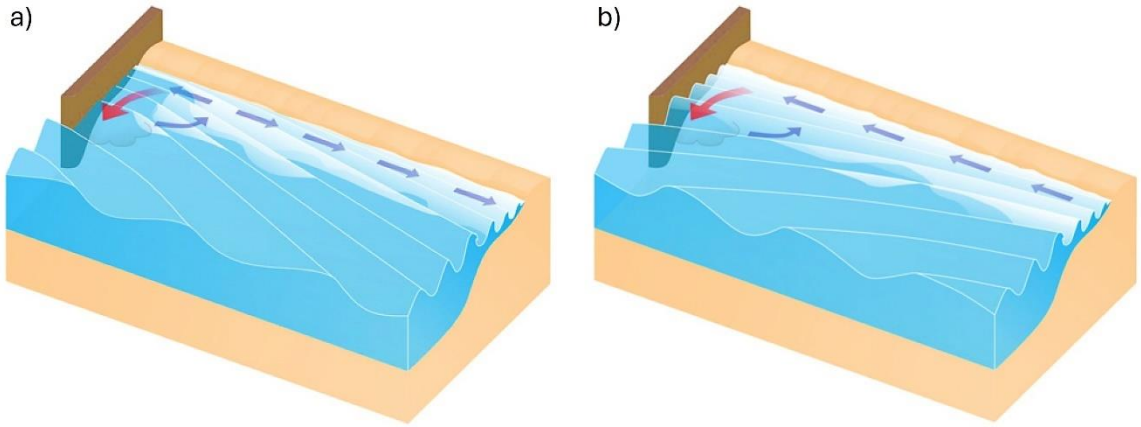

Figure 2.9 - Boundary rip currents: **(a)** *Shadow rips*; **(b)** *Deflection rips* (modified from Castelle et al., 2016).

Another specific type of current circulation that can develop is the *Cellular rip current*, typical of embayed beaches (Castelle et al., 2016) (Fig. 2.10). This occurs when the width of the embayment is reduced compared to the width of the wave breaking zone (surf zone). As a result, the lateral physical boundaries exert a dominant influence on the hydrodynamic circulation within the embayment (Castelle et al., 2016). As suggested in the work of Castelle and Coco (2012), the position of the rip current can vary depending on the beach shape (straight or curved shoreline) and the shape and extent of the headlands that define the embayment. Currents can form at the centre of the embayment (Fig. 2.10a), at one boundary of the headland (Fig. 2.10b), or at both boundaries (Fig. 2.10c). This type of circulation is particularly common and observable on embayed beaches during storm events (Loureiro et al., 2012a) but can also occur under low-moderate energy wave conditions.

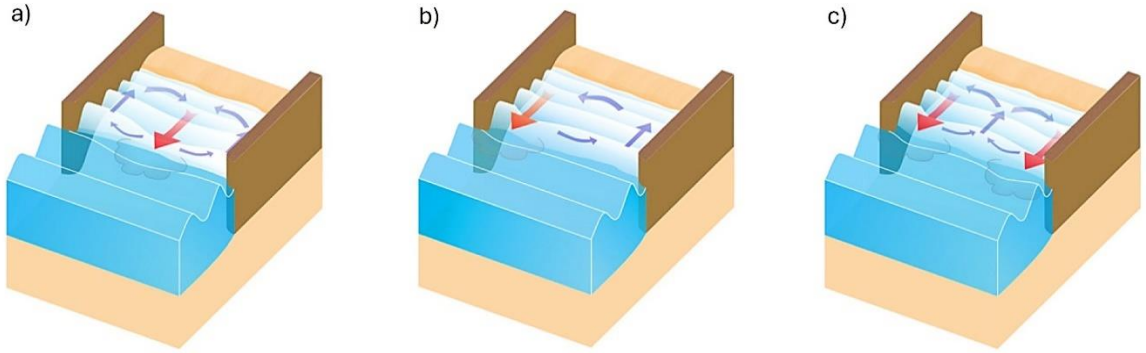

Figure 2.10 - Cellular rip currents on embayed beaches: **(a)** at the centre of the embayment, **(b)** along one boundary of the headland, or **(c)** along both boundaries (modified from Castelle et al., 2016).

2.4 Analysis tools for coastal morphodynamic processes

The study of coastal dynamics and processes is essential for understanding the evolution of coastlines over time, assessing risks related to erosion, planning protection and management interventions, and analysing the impact and effects of human activities and climate change. In this context, to effectively address and understand the complex dynamics of this environment, traditional field surveys and laboratory experiment observations can be complemented using various digital tools and technologies that enable integrated data acquisition, processing and interpretation. Among these are numerical modelling of coastal morphodynamic processes and the analysis of images acquired through coastal video monitoring systems.

2.4.1 Numerical modelling of coastal morphodynamic

The numerical modelling of coastal processes is a powerful computational tool used to simulate the physical phenomena that drive the evolution of coastal environments over time. By integrating hydrodynamic, wave and morphological models, it is possible to perform coupled simulation of various processes, such as wave propagation, current generation, tidal fluctuations and sediment transport (e.g., Haas et al., 2008; Amoudry and Souza, 2011; Ponte et al., 2013; Thomas and Dwarakish, 2015).

From a hydrodynamic perspective, coastal modelling is often based on solving the Navier–Stokes equations, which describe the motion of fluid (e.g., Mayer and Madsen, 2001; Torres-Freyermuth et al., 2007), or on simplified formulations such as the Shallow Water (e.g., Brocchini and Dodd, 2008) or Boussinesq Equations (e.g., Kirby, 2016). In parallel, the morphological component typically focuses on simulating sediment transport, taking into account processes such as erosion, deposition and longshore sediment drift. This transport is generally modelled using empirical or semi-empirical approaches (Amoudry, 2008), which enable the estimation of both the quantities (volumes) and directions of sediment movement along the coastline. The coupling of these numerical models enables an integrated, multi-temporal understanding of coastal morphodynamic evolution, including both short-term changes (e.g., during storm events) and long-term trends.

Moreover, the numerical approach allows for the analysis of scenarios involving human interventions, such as the design and construction of coastal defence structures (e.g., Karambas, 2015). Similarly, it enables the simulation of potential effects and impacts resulting from climate change (e.g., Barnard et al., 2019; Pang et al., 2023), including sea-level rise and changes in the intensity and frequency of severe storm events. This makes modelling a fundamental tool for supporting coastal areas planning and management.

The calibration and validation of numerical models typically rely on data collected both through field surveys and laboratory experiments, such as topographic and bathymetric measurements, flow current and sedimentological data (Williams and Esteves, 2017; Kalligeris et al., 2020). These are essential for achieving a reliable physic representation of the modelled coastal system. Among the most commonly used software and models for coastal numerical modelling are MIKE 21 (developed by DHI), SWAN (Simulating WAves Nearshore; developed by Delft University of Technology), XBeach (developed by Deltares, Delft University of Technology, and the IHE Delft Institute for Water Education), and Delft3D (developed by Deltares).

In the scientific literature, numerous studies have used numerical modelling to analyse coastal processes and dynamics, demonstrating the effectiveness and reliability of these tools in representing and predicting the spatio-temporal evolution of such environments. For example, in the study conducted by Lesser et al. (2004), coastal sediment transport was simulated using the Delft3D software, and the results were subsequently validated with measured data. In another study, Roelvink et al. (2009) modelled the impact of storm events on a beach-dune system using the XBeach software, with validation performed through a combination of laboratory experiments and field analysis. Numerical modelling has also been extensively applied to simulate the development of rip current systems, with the aim of estimating their intensity and location. For example, Castelle and Coco (2012) showed, using coupled wave and flow models in the Delft3D software, how beach morphology, along with the presence of headlands and/or lateral physical barriers of varying shapes and cross-shore extensions, can influence the development and behaviour of rip current systems.

These studies represent only a part of the extensive scientific literature that has used numerical modelling to investigate coastal morphodynamics. However, they clearly demonstrate how such tools provide valuable insights into the complex dynamics governing the evolution of coastal environments, facilitating both the prediction of potential future scenarios and making a significant contribution to the integrated management of coastlines.

2.4.2 Coastal video monitoring system

Coastal video monitoring is a technology that emerged in the late 1980s as a tool for analysing coastal processes, morphologies and their evolution in space and time. The first studies in this field were conducted by the Coastal Imaging Lab (CIL) at Oregon State University (USA), as part of the Argus Project (Holman and Stanley, 2007). One of the initial objectives was to acquire images at regular intervals to study wave run-up and infragravity waves (Holman and Guza, 1984). Over time, researchers discovered that by setting an

exposure time of 10 minutes, the resulting images (known as Time-Exposure or Timex) revealed the morphology of the surf zone, such as submerged sandbars and rip channels (Lippmann and Holman, 1989, 1990). Within this context, the Argus system was developed, designed for the automated and continuous acquisition of coastal images at regular intervals. Since the installation of the first system, the Argus network has gradually expanded, with new operational stations established along coastlines worldwide.

Schematically, an Argus station generally consists of several video cameras mounted on an elevated structure and oriented towards the shoreline to provide continuous coverage of the beach (Holman and Stanley, 2007). These cameras are connected to a local on-site computer, which manages image acquisition and storage. The station communicates externally through conventional network connections.

Overall, the continuous and systematic acquisition of images through video monitoring systems has been a major advancement in the study of coastal evolution (e.g., Armaroli and Ciavola, 2011), allowing for uninterrupted observation of phenomena such as shoreline changes and wave dynamics (e.g., Harley et al., 2014; Valentini et al., 2017a; Andriolo et al., 2020).

In the years following the Argus project, coastal video monitoring systems expanded internationally, driven by significant advancements in digital technologies, data transmission and automated image processing techniques. These innovations have transformed video monitoring systems into essential tools not only for scientific research, but also for coastal managements (Davidson et al., 2006) and operational use by public institutions and competent authorities in environmental management and civil protection, particularly in addressing risks associated with extreme events such as storm events, coastal flooding and phenomena associated with climate change. Moreover, the integration of images acquired from coastal video monitoring stations with Geographic Information Systems (GIS) has greatly improved the analysis and visualization of spatial data, thereby supporting more effective territorial planning and the development of mitigation and adaptation strategies.

Among the main products that can be derived from the images and videos acquired from coastal video monitoring system are (Holman and Stanley, 2007; Ramesh et al., 2020):

- **Snapshot Images**: These are instant images captured at regular intervals set by the video monitoring system, providing a visual representation of the beach at a specific moment in time. While they do not directly provide quantitative data on beach dynamics, they serve as a valuable tool for documenting and monitoring the present morphological condition of the beach.
- **Time-Exposure (Timex) Images**: These are generated by averaging a large number of snapshots taken within a predefined time interval (e.g., 10 minutes). This process

highlights the morphological features present in the surf zone, such as sandbars, troughs, channels and depressions in the seabed, by calculating the arithmetic mean of the RGB light intensity of each pixel across all snapshots. The resulting image (Timex) shows lighter white areas in the surf zone, corresponding to shallow regions where waves break (on the sandbars or near the shoreline), and darker areas that indicate greater depths, where longshore currents and rip currents may develop. These images allow for the observation of sandbar and trough dynamics (e.g., migration during storm events), enabling the estimation of the beach's morphodynamic state, as proposed by the Wright and Short (1984) classification (see Chapter 2.1 of the thesis).

- **Time Variance Images:** In this type of image, for each snapshot acquired during a predefined time interval (similar to Time-exposure images), the variance in light intensity for each pixel is calculated. This statistical processing of the acquired snapshots allows for highlighting temporal changes along the beach, revealing the most dynamic areas of the surf zone (shown in lighter colours), in contrast to the more static areas (shown in darker colours). This representation is particularly useful for identifying the location of the breaking wave line, the shoreline and the wave run-up area.
- **Rectified Images:** These images are obtained through a geometric correction process that removes the perspective distortion in images acquired by fixed cameras. The rectification process transforms the image into a “zenithal” view (top-down), projecting it onto a horizontal plane referenced to real-world spatial coordinate system. To perform this transformation, it is necessary to define control points (Ground Control Points - GCPs) with known coordinates. These images allow for spatial measurements (such as distances and areas) and enable the analysis of the morphological evolution of the beach over time (Valentini et al., 2017b).
- **Timestack Images:** These are spatio-temporal images created by extracting a single pixel line from each snapshot in a continuous temporal sequence. The vertical alignment of these pixel lines over time results in an image where the horizontal axis (x) represents time and the vertical axis (y) corresponds to cross-shore distance along the transect selected as the reference for extracting the pixel line. Timestack images are valuable tools for analysing wave dynamics and the morphodynamic response of the beach, including wave run-up along the shore over time (Aagaard and Holm, 1989).

Southern Sardinia Coastal Video Monitoring System

In line with the methodological approaches used internationally, coastal video monitoring has also been implemented along the southern coast of Sardinia (Italy) through the development of stations for continuous video monitoring and coastal morphodynamic analysis. Specifically, as part of the activities outlined in the PhD programme, the operational management of the coastal video monitoring system of the Coastal and Marine Geomorphology Group - CMGG (Department of Chemical and Geological Sciences, University of Cagliari) was carried out under the technical supervision of the company "SARDEGNA PROGETTA".

Currently, the system consists of five coastal video monitoring stations distributed along the southern coast of Sardinia (Fig. 2.11). To facilitate the description of each station, they have been grouped into three groups, each named according to its geographical location: 1) Piscinnì (blue rectangle in Fig. 2.11); 2) Chia (orange rectangle in Fig. 2.11); 3) Poetto (green rectangle in Fig. 2.11). An overview of the main technical specifications for the five video monitoring stations is provided in Table 2.3.

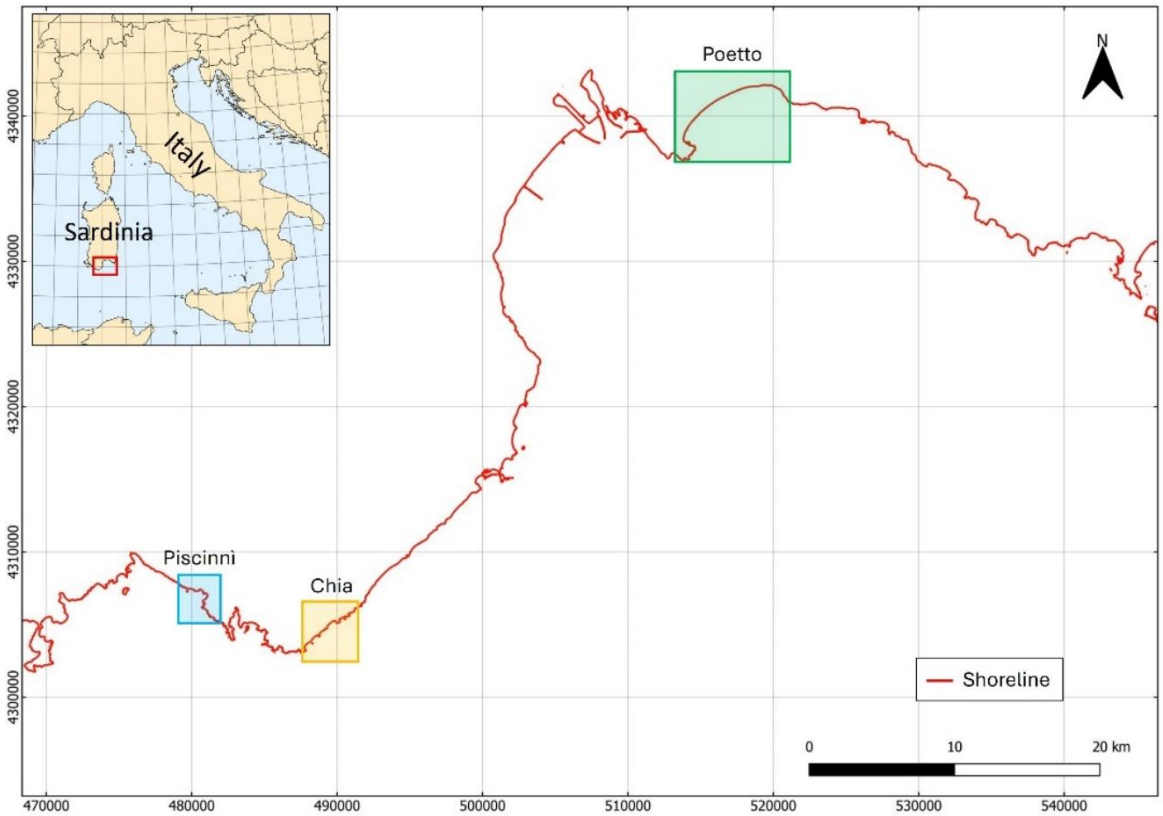

Figure 2.11 - Geographical position of the coastal video monitoring stations. The red line represents the coastline, while the coloured rectangles indicate the groups into which the coastal video monitoring stations are grouped: Piscinnì (blue rectangle); Chia (orange rectangle); Poetto (green rectangle). Coordinate system: UTM 32N; Datum: WGS84.

1) **Piscinnì**: This group consists of a single coastal video monitoring station, located on a promontory southeast of Piscinnì beach, at an altitude of approximately 117 m above the mean sea level (camera coordinates: 38° 54’ 32.40’’ North; 8° 47’ 08.70’’ East) (yellow dot in Fig. 2.12a). The station is installed on a rigid steel frame and equipped with a Dahua Technology 12 Megapixel Ultra HD camera (DH-IPC-HF71242F) with a Dahua DH-PLZ21C0-D lens (focal length: 10.5 - 42 mm). The station acquires images at a frequency of 2 Hz for 10 minutes, 4 times a day at 3 hours intervals (8:00; 11:00; 14:00; 17:00). It is powered by 6 batteries (12 V - 100 Ah / 20 hr) recharged through 4 solar panels installed outside the structure. The acquired images (Fig. 2.12b) are stored locally on an external hard drive connected to a computer at the station, while the data is simultaneously transmitted via internet to a storage server through a router 4G. The entire coastal video monitoring station at Piscinnì beach was developed and integrated as part of a previous project: PROVIDUNE (LIFE07NAT/IT/000519). The station has been operational since 2011 and has progressively undergone upgrades in both its instrumentation and data transmission systems.

Figure 2.12 - **(a)** Location of the coastal video monitoring station (yellow dot) at Piscinnì beach (aerial orthophoto from the WMS of "Regione Autonoma della Sardegna"; Coordinate system: UTM 32N; Datum: WGS84). The dashed lines delimit the camera's field of view. **(b)** Example of snapshot acquired by the Piscinnì station camera.

2) **Chia**: This group consists of two coastal video monitoring stations located along the same coastal stretch (Fig. 2.13a). The first station is oriented towards Sa Colonia beach and is installed on the upper part of an old coastal watchtower, known as "Torre di Chia", which stands on a rocky promontory to the east of the beach at an elevation of approximately 40 m above the mean sea level (camera coordinates: 38° 53' 42.36'' North; 8° 53' 05.58'' East) (yellow dot in Fig. 2.13a). On the other hand, the second station is oriented towards Su Giudeu beach and is installed on a rigid steel structure located on a rocky promontory to the southwest of the beach, at approximately 23 m above the mean sea level (camera coordinates: 38° 52' 47.47'' North; 8° 51' 26.86'' East) (red dot in Fig. 2.13a). Both stations are equipped with a Dahua Technology 12 Megapixel Ultra HD camera (DH-IPC - HF71242F) with a Dahua DH-PLZ21C0-D lens (focal length: 10.5 - 42 mm). Moreover, the stations are configured to acquire images (Fig. 2.13b, c) at a frequency of 2 Hz for 10 minutes, 4 times a day at 3 hours intervals (8:00, 11:00, 14:00, 17:00 for Sa Colonia station; 8:10, 11:10, 14:10, 17:10 for Su Giudeu station).

   Sa Colonia station is powered directly by the *in situ* electrical system (230V AC). The acquired images are stored locally on an external hard drive connected to a computer at the station and are transmitted via internet to a storage server through a router 4G.

   In contrast, the entire system of Su Giudeu station is powered by 6 batteries (12 V - 100 Ah / 20 hr) recharged through 3 solar panels installed outside the structure. The images acquired by the camera are transmitted via a radio link to the nearest station (Sa Colonia). In this way, the images are stored on the external hard drive connected to the computer at the Sa Colonia station and simultaneously transmitted via internet to the dedicated storage server.

   Both coastal video monitoring stations of Sa Colonia and Su Giudeu were developed and integrated as part of a previous project: PROVIDUNE (LIFE07NAT/IT/000519). The system has been operational since 2011 (initially with the Sa Colonia station and subsequently with the Su Giudeu station) and has progressively undergone upgrades in both its instrumentation and data transmission systems.

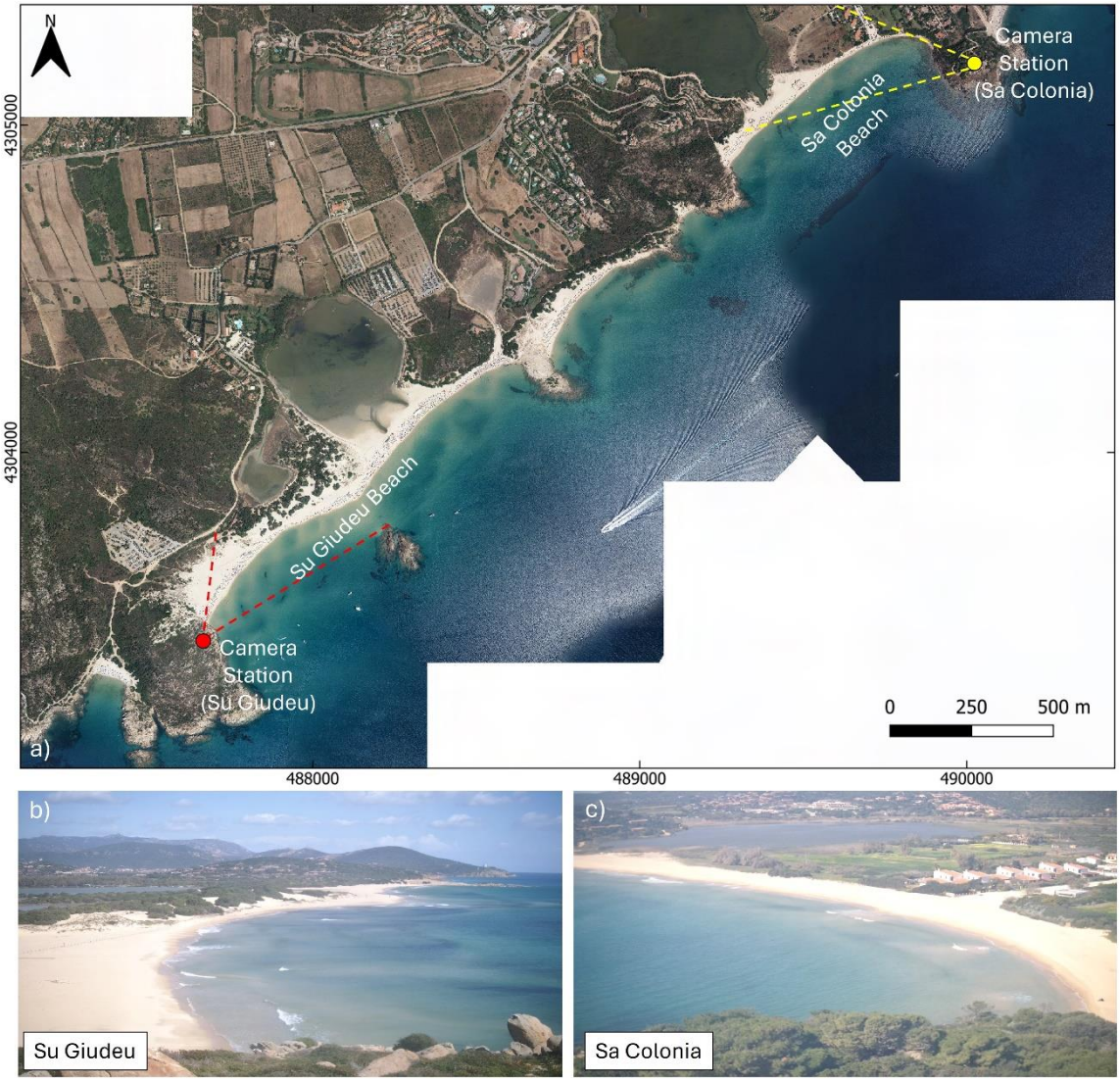

Figure 2.13 - **(a)** Location of the coastal video monitoring stations at Sa Colonia beach (yellow dot) and Su Giudeu beach (red dot) (aerial orthophoto from the WMS of "Regione Autonoma della Sardegna"; Coordinate system: UTM 32N; Datum: WGS84). The dashed lines delimit the cameras' field of view. Panels **(b)** and **(c)** show an example of snapshot acquired by the camera station of **(b)** Su Giudeu beach and **(c)** Sa Colonia beach.

3) **Poetto**: This group consists of two coastal video monitoring stations, both located on Poetto beach.
The first station (Poetto 1) frames a portion of the eastern sector (Poetto 1 - [A]) and the central sector (Poetto 1 - [B]) of the beach (Fig. 2.14a). The station is equipped with two Dahua Technology 12 Megapixel Ultra HD cameras (Poetto 1 [A]: DH-IPC-HF71242F; Poetto 1 [B]: DH-IPC-HF81200E), respectively with Dahua DH-PLZ21C0-D (focal length: 10.5 - 42 mm) and Dahua DH-PLZ20C0-D lenses (focal length: 3.7 - 16

mm) (Table 2.3). The cameras are installed on the roof of a hospital (called "Ospedale Marino"), approximately 25 m above the mean sea level (camera coordinates: 39° 12’ 50.21’’ North; 9° 10’ 27.03’’ East) (yellow and green dots in Fig. 2.14a), and are configured to acquire images (Fig. 2.13b; 2.13c) at a frequency of 4 Hz for 10 minutes, 4 times a day at 3 hours intervals (8:00, 11:00, 14:00, 17:00). The station is powered by the *in situ* electrical system (230V AC). The images acquired by cameras [A] and [B] are stored on the local computer of the Poetto 1 station and simultaneously also transmitted via a radio link directly to the dedicated storage server.

The second station (Poetto 2) is installed on a rigid steel structure and is equipped with a Dahua Technology 12 Megapixel Ultra HD camera (DH-IPC-HF81200F) with a Dahua DH-PLZ21C0-D lens (focal length: 10.5 - 42 mm). The station is located southwest of Poetto beach, on the S. Elia Promontory at an elevation of approximately 125 m above the mean sea level (camera coordinates: 39° 11’ 24.05’’ North; 9° 9’ 29.65’’ East) (red dot in Fig. 2.14a). The image acquisition frequency is the same as that of Poetto 1 station. The entire system is powered by 4 batteries (12 V - 100 Ah / 20 hr) recharged through 2 solar panels installed outside the structure. The transmission of the acquired images (Fig. 2.14d) occurs via a radio link to the nearby Poetto 1 station, which archives the received images on its local computer and then transmits them via a radio link to the dedicated storage server.

The Poetto 1 and Poetto 2 stations were developed as part of previous projects: B.E.A.C.H. (Beach Environment, management and Coastal Hazard) and N.E.P.T.U.N.E. (Natural Erosion Prevision Through Use of Numerical Environment). The station has been operational since 2013 and has progressively undergone upgrades in both its instrumentation and data transmission systems.

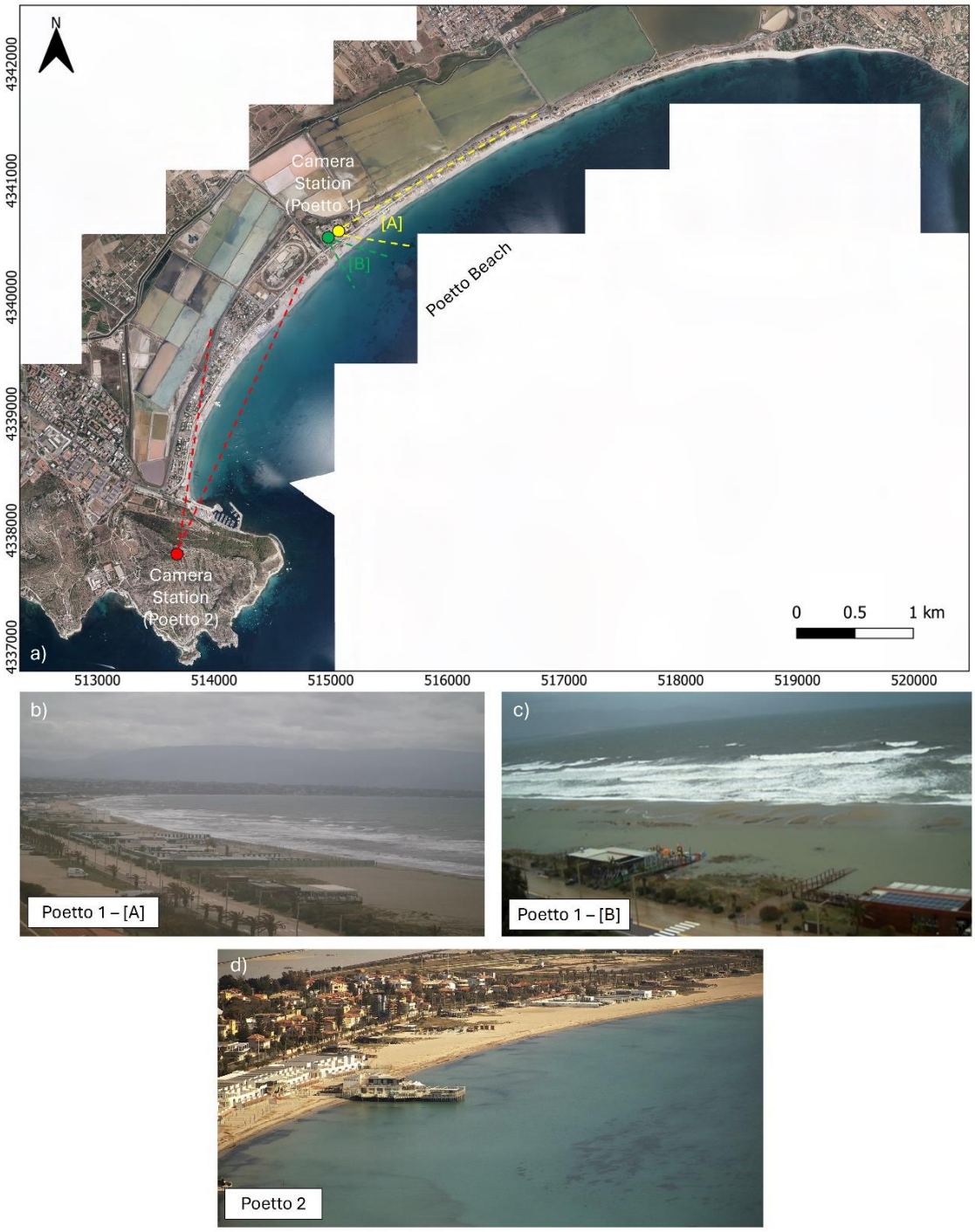

Figure 2.14 - **(a)** Location of the coastal video monitoring stations at Poetto beach. The yellow and green dots indicate the position of camera [A] and [B] at Poetto 1 station, while the red dot indicates the position of camera at Poetto 2 station (aerial orthophoto from the WMS of "Regione Autonoma della Sardegna"; Coordinate system: UTM 32N; Datum: WGS84). The dashed lines delimit the cameras' field of view. Panels **(b)**, **(c)** and **(d)** show an example of snapshot acquired by the cameras station of **(b)** Poetto 1 [A], **(c)** Poetto 1 [B] and **(d)** Poetto 2.

All data transmitted by the coastal video monitoring stations are received and archived on a dedicated storage server managed by the “Direzione per le Reti e i Servizi Informatici” (D.R.S.I.) of the University of Cagliari and located at the Faculty of Engineering (University of Cagliari). To facilitate the management of data acquired by the cameras and enable real-time visualization, a virtual machine (called "Radioserver") has been installed on the storage server.

Following the installation of the five coastal video monitoring stations, the processing and analysis of images acquired over time have allowed scientific studies on the coastal processes and dynamics of Southern Sardinia (e.g., Brambilla et al., 2016; Passarella, 2019; Trogu et al., 2020, 2022, 2023; 2024; Ruju et al., 2022). Furthermore, an experimental early warning system was developed for Poetto beach, aimed at forecasting beach flooding events during severe storm events. The system’s effectiveness was validated using images from the coastal video monitoring station located on the S. Elia Promontory (Poetto 2 station). Further details about the early warning system are provided in the publication listed below:

Chatzipavlis, A., Trogu, D., Ruju, A., Montes, J., Usai, A., Porta, M., Coco, G., De Muro, S., Ciavola, P., **2025**. Development and validation of an early warning system for coastal flooding on a Mediterranean urban beach. *EGUsphere* [preprint]. https://doi.org/10.5194/egusphere-2025-2292.

Table 2.3

Overview of the technical specifications for the five coastal video monitoring stations of Coastal and Marine Geomorphology Group - CMGG (University of Cagliari).

Groups	Stations	Cameras	Resolution	Camera lens	Power supply	Connectivity	Data storage	Acquisition frequency
Piscinnì	Piscinnì	Dahua 12 MP (DH-IPC-HF71242F)	4K - Full HD 1080p	Dahua (DH-PLZ21C0-D) (10.5-42mm)	6 batteries (12 V - 100 Ah / 20 hr) + Solar panels	Router 4G	Local PC with external HD + Remote Server	2 Hz for 10 minutes (4 times a day at 3 hours intervals)
Chia	Sa Colonia				230 V AC	Router 4G	Local PC with external HD + Remote Server	
	Su Giudeu				6 batteries (12 V - 100 Ah / 20 hr) + Solar panels	Radio link with Sa Colonia Station	External HD (Sa Colonia Station) + Remote Server	
Poetto	Poetto 1	Dahua 12 MP (DH-IPC-HF81200E)		Dahua (DH-PLZ20C0-D) (3.7-16 mm)	230 V AC	Radio link with Remote Server	Local PC + Remote Server	4 Hz for 10 minutes (4 times a day at 3 hours intervals)
	Poetto 2			Dahua (DH-PLZ21C0-D) (10.5-42mm)	4 batteries (12 V - 100 Ah / 20 hr) + Solar panels	Radio link with Poetto 1 Station	External HD (Poetto 1 Station) + Remote Server	
	[A]							
	[B]							

Chapter 3: METHODOLOGY

In this thesis, a multidisciplinary methodology was used to carry out an analysis of Mediterranean microtidal beaches along the southern coastal stretch of Sardinia (Italy), covering geomorphological, morphometric, hydrodynamic and ecological aspects. This chapter provides an overview of the main methodologies applied throughout this thesis. However, more detailed descriptions of the specific methods can be found in Chapters 4, 5, 6 and 7 of the thesis.

3.1 Aerial orthophotos processing

The identification and analysis of the beaches along the coastal stretch studied in this thesis were carried out through the use of aerial orthophotos. These are available for consultation online in the Geoportal of Sardegna (www.sardegnageoportale.it). More precisely, the aerial orthophotos were uploaded through GIS software (Geographic Information System) using the WMS (Web Map Service) of "Regione Autonoma della Sardegna" (https://webgis.regione.sardegna.it/geoserverraster/ows?service=WMS&request=GetCapabilities).

Each aerial orthophoto mosaic (Fig. 3.1) covers the entire Sardinia Island over a time period ranging from 1954 to 2022 (for certain coastal areas, aerial orthophotos dating back to 1940s are also available). Given the large amount of available data, the aerial orthophotos covering the analysed coastal stretch were manually extracted and georeferenced (coordinate system: WGS84 - UTM 32N) while maintaining their original pixel resolution. The georeferencing process was carried out using the 2006-2008 aerial orthophotos as a reference.

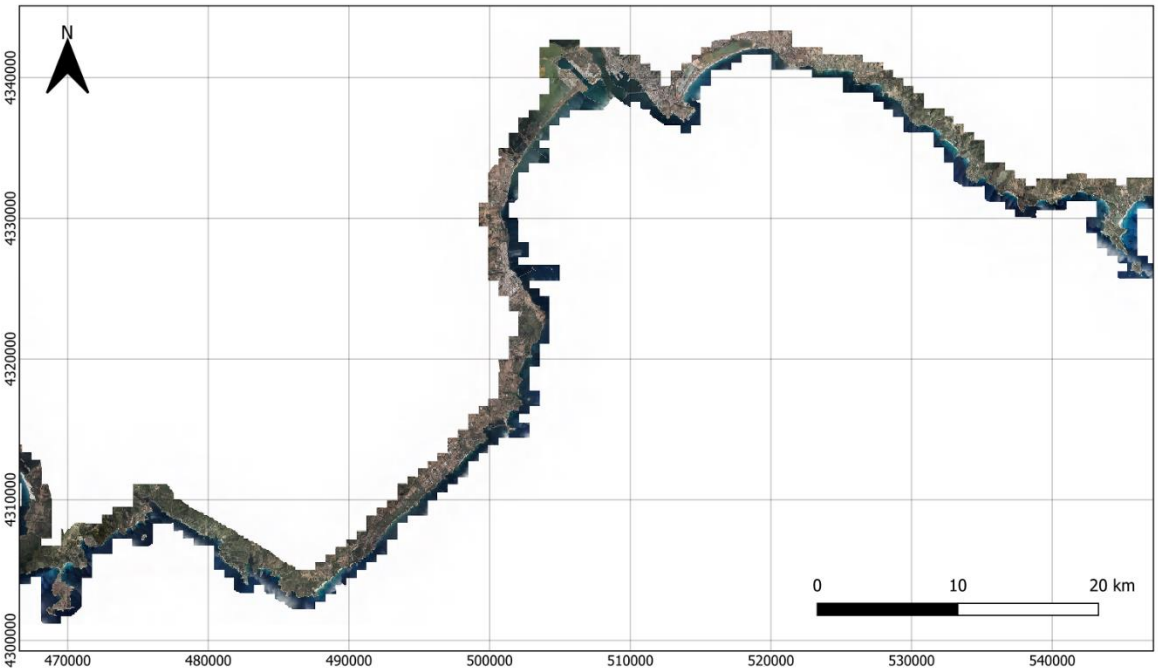

Figure 3.1 - Mosaic of georeferenced aerial orthophotos (time series: 2022) covering the studied coastal stretch and available through the WMS of "Regione Autonoma della Sardegna" (Coordinate system: UTM 32N; Datum: WGS84).

3.2 Digital Shoreline Analysis System (DSAS) data processing

The analysis of shoreline evolution movements (Chapter 5 of the thesis) for the beaches identified along the studied coastline was performed using an application tool called Digital Shoreline Analysis System (DSAS) (Version 5.1) (Himmelstoss et al., 2021), developed by the United States Geological Survey (USGS) as an extension of ESRI ArcGIS software. More precisely, the DSAS tool allows the automated calculation of shoreline change rates (retreat and accretion) through statistical indicators applied to multiple temporal shoreline positions. For each studied beach, DSAS generates a series of equidistant linear transects perpendicular to a baseline defined by the user, which can be located either offshore or onshore relative to the shorelines (both the length of the transects and their spacing can be selected by the user) (Fig. 3.2). By measuring the distance between shoreline positions along each transect (while also accounting for positional uncertainty of each shoreline), DSAS statistically quantifies shoreline rates (accretion and retreat) over a given time period, providing statistical indicators (Genz et al., 2007; Oyedotun, 2014; Himmelstoss et al., 2021):

- **Shoreline Change Envelope** (**SCE**) is the maximum distance of shoreline movement along a given transect, considering all available shoreline positions, regardless of the time interval between them.

- **Net Shoreline Movement** (**NSM**) is the distance between the oldest and most recent shoreline positions measured along a given transect.
- **End Point Rate** (**EPR**) is the rate of shoreline change calculated by dividing the Net Shoreline Movement (NSM) by the time interval between the oldest and most recent shoreline positions.
- **Linear Regression Rate** (**LRR**) is the rate of shoreline change determined by applying a least-squares regression to all shoreline positions over time.
- **Weighted Linear Regression** (**WLR**) is similar to the Linear Regression Rate (LRR), but it assigns weights (based on shoreline uncertainty) to each shoreline position.

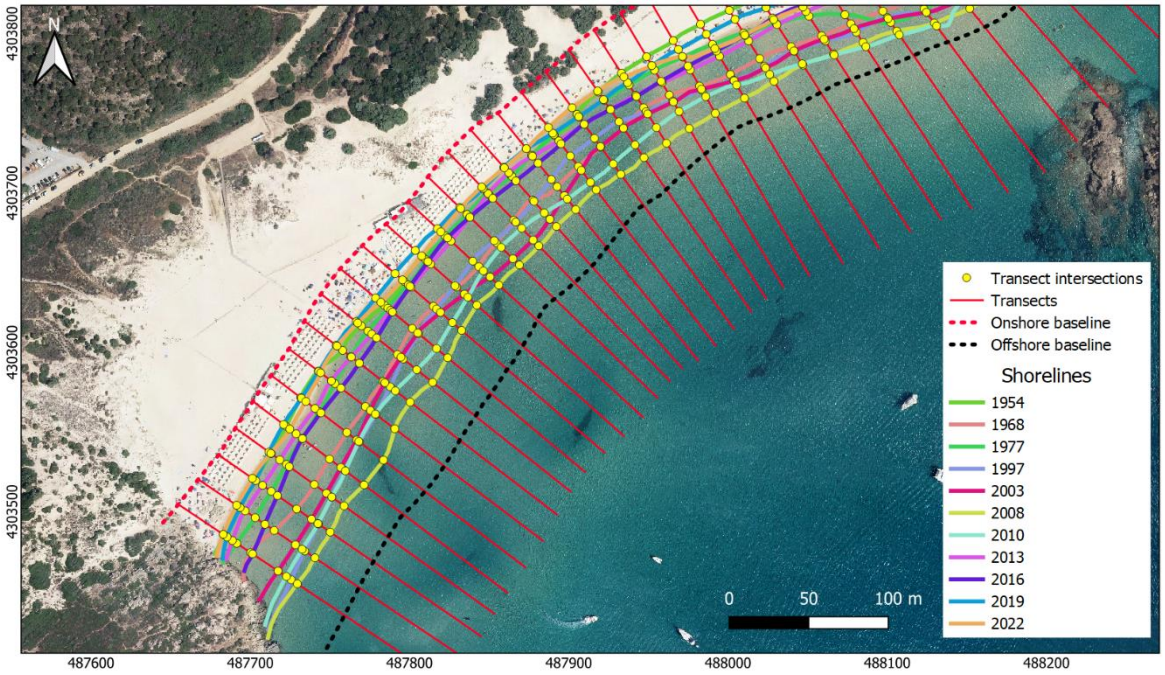

Figure 3.2 - DSAS tool applied to the beaches identified along the studied coastal stretch using the aerial orthophotos available in the WMS of "Regione Autonoma della Sardegna" (Coordinate system: UTM 32N; Datum: WGS84).

3.3 Beach topographic surveys

Topographic surveys on the backshore of Poetto beach were carried out to collect beach elevation data (*xyz* coordinates) for integration into numerical models (Chapter 7 of the thesis). For this purpose, the beach was divided into 21 transects (blue lines in Fig. 3.3), oriented perpendicular to the shoreline and spaced approximately 300 m apart. Each cross-shore transect begins at the landward edge of the dune system, typically marked on Poetto beach by the urban road running parallel to the shoreline, and extends seaward to a depth of approximately 1 m, where the topographic profile connects with the bathymetric profile.

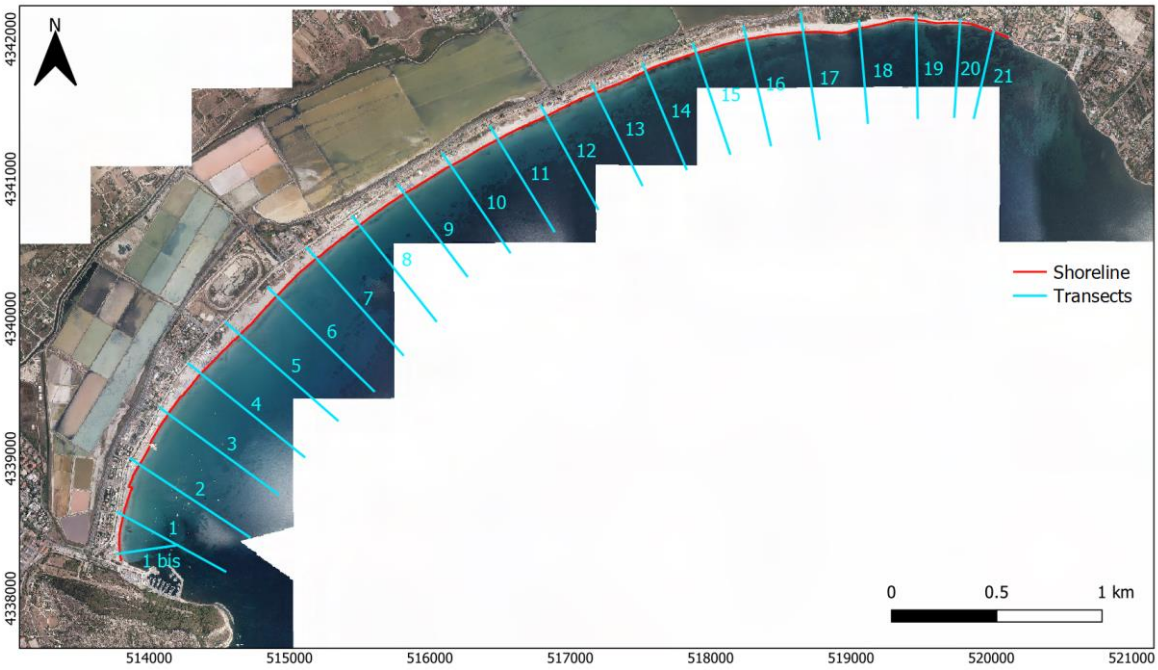

Figure 3.3 - Locations of the transects along Poetto beach where topographic surveys were carried out (aerial orthophoto from the WMS of "Regione Autonoma della Sardegna"; Coordinate system: UTM 32N; Datum: WGS84).

The measurements (*xyz* coordinates) were acquired using a DGPS (Differential Global Positioning System) with a Navcom SF-3040 receiver - GNSS (Global Navigation Satellite System), connected in real time (Real-Time Kinematic - RTK) to a ground correction network (NETGEO Network). The instrument has a horizontal accuracy of 0.01 m + 0.5 ppm and a vertical accuracy of 0.02 m + 1.0 ppm.

To perform the measurements along each transect, the instrument was mounted on a rod at a height of 2 m above ground level. The acquisition of points (*xyz* coordinates) was carried out after properly levelling the instrument (Fig. 3.4). For each point along the transect, 15 *xyz* measurements were collected at an acquisition frequency of 1 Hz and then averaged to obtain a more precise position. On the other hand, to measure the shoreline position and the maximum extent reached by wave swash (which is also useful for further geomorphological observations), the instrument was placed in a special backpack, which its height above ground level varying depending on the operator's height (Fig. 3.5). Overall, topographic measurements were periodically repeated and updated.

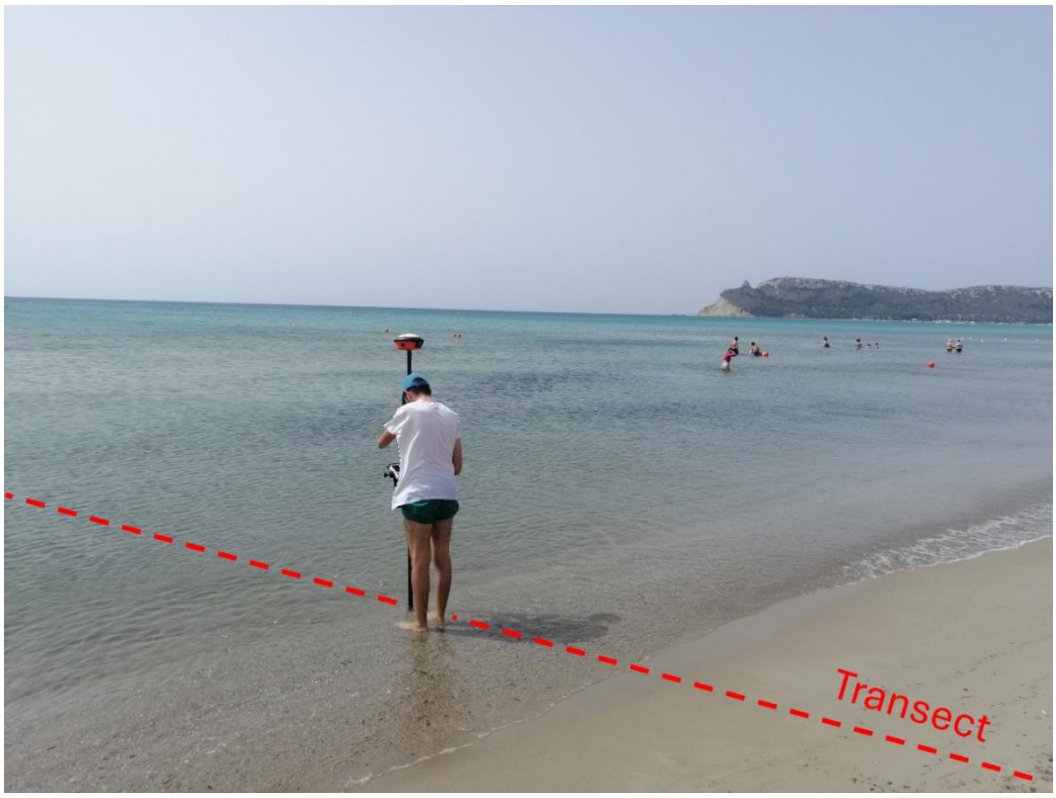

Figure 3.4 - Topographic survey at Poetto beach along a transect.

Figure 3.5 - Topographic survey at Poetto beach: mapping of the shoreline (dashed orange line) and the corresponding maximum limit of the wave swash (dashed red line) along the backshore.

3.4 Beach bathymetric surveys

Bathymetric surveys at Poetto beach were carried out to collect depth elevation data (*xyz* coordinates) for integration into numerical models (Chapter 7 of the thesis). More specifically, bathymetric measurements were carried out along each transect perpendicular to the shoreline (blue lines in Fig. 3.3), in order to ensure continuity with the topographic data collected on the backshore.

The measurements were performed using a RESON - NaviSound 215 Portable Hydrographic Singlebeam Echosounder:

- Emission frequency: 28 kHz - 35 kHz and 190 kHz - 225 kHz (dual frequency).
- Impedance: 100 Ohm.
- Resolution: 0.01 m.
- Accuracy (assuming correct sound velocity and transducer draft): 0.01 m (210 kHz - 1 sigma); 0.07 m (33 kHz - 1 sigma).

The instrument is interfaced with a computer for data recording, which is connected to a DGPS Omnistar 3300HP to record the position of the acquired points. Once the data were acquired, they were corrected for tidal fluctuations and for the vertical draft of the instrument during acquisition. The acquired bathymetric data were subsequently processed by removing outliers and exported in ASCII format (*xyz* coordinates) for interpolation and analysis using GIS software (Fig. 3.6).

Bathymetric surveys at Poetto beach were also performed using a GARMIN EchoMAP Plus 92sv (GPS integrated - update frequency: 5 Hz) whit a Echosounder CHIRP Transducer GT52HW-TM (supported frequency: 50 - 200 kHz).

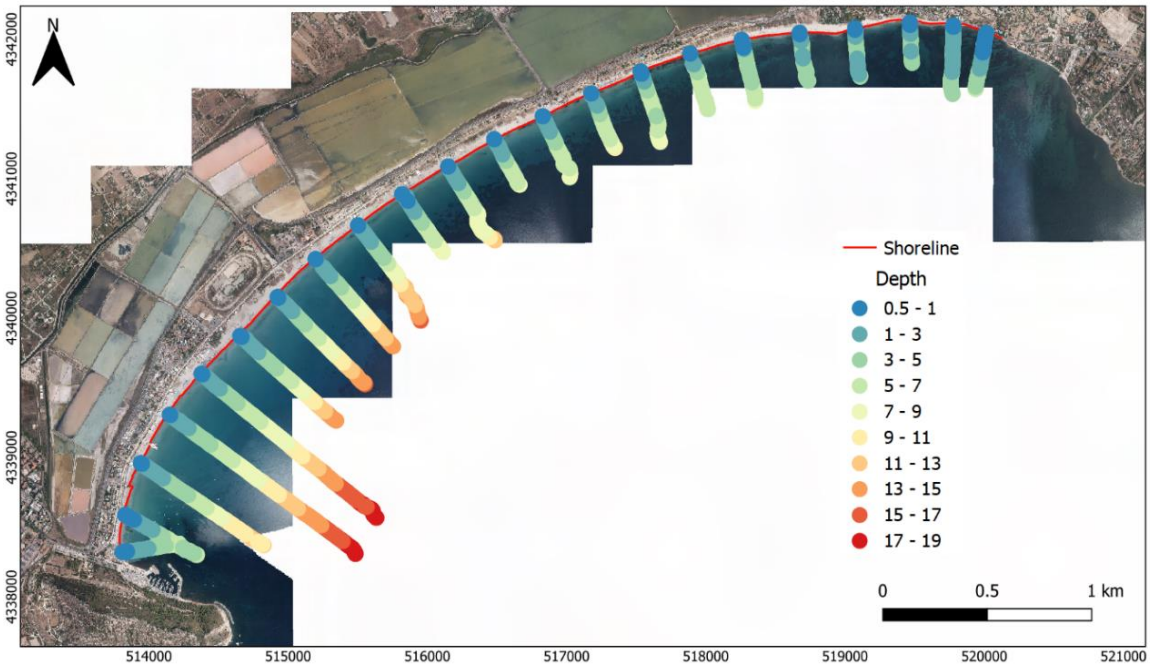

Figure 3.6 - Bathymetric surveys at Poetto beach: depth values along each transect (aerial orthophoto from the WMS of "Regione Autonoma della Sardegna"; Coordinate system: UTM 32N; Datum: WGS84).

3.5 Numerical modelling

The numerical simulations presented in this thesis (Chapter 6 and 7) were performed using the Delft3D software (Deltares). Specifically, this software comprises multiple modules that enable the simulation of various processes and conditions, including waves, currents, coastal and seabed morphology, sediment transport and wind forcing. The Delft3D-WAVE (Booij et al., 1999; Ris et al., 1999) model has been used to simulate wave propagation, which incorporate the spectral model SWAN (Simulating Waves Nearshore) based on the wave action equation. On the other hand, the Delft3D-FLOW (Lesser et al., 2004) model has been used to simulate the hydrodynamic circulation induced by waves, wind, tide and other processes. The FLOW model is based on the Navier-Stokes equations. In each numerical simulation carried out in this thesis, the FLOW model is coupled with the WAVE model to ensure a comprehensive representation of hydrodynamic processes. This coupling allows for the mutual exchange of information between the two models, enabling the simulation of complex interactions between wave dynamics, currents and other forcing mechanisms (e.g., wind forcing).

Overall, different wave and wind conditions were simulated within two distinct contexts: an embayed beach (theoretical study case; see Chapter 6 of the thesis) and at the Poetto beach (real study case; see Chapter 7 of the thesis). Moreover, both wave (CMEMS; Korres et al., 2021) and wind data (ERA5; Hersbach et al., 2023) (offshore significant wave

height - H_s; peak wave period - T_p; wave direction - *Dir*; wind speed at 10 m above the sea surface - U_{10}; wind direction - Dir_w) were used to simulate the different hydrodynamic responses of beaches. The duration of each simulated event varies depending on the wave-wind conditions considered and geometric characteristics of the modelled domain (e.g., grid mesh size): 1 day (time frame: 24 hours) for the theoretical study case of the embayed beach; 3 days (time frame: 72 hours) for the real study case of Poetto beach.

3.6 Coastal video monitoring system for morphodynamic analysis

The study in Chapter 7 of the thesis was realised through the analysis of images (snapshots) acquired from a coastal video monitoring station at Poetto beach. More precisely, the station is located on the S. Elia Promontory (yellow dot in Fig. 3.8), 125 m above SWL (Camera coordinates: 39° 11’ 24.05’’ North; 9° 9’ 29.65’’ East) (Fig. 3.7a). The station comprises a camera (Dahua Technology 12 MP Ultra-HD; Model: DH-IPC-HF81200E) mounted on a steel structure, along with photovoltaic panels system for power supply. The camera frames the western area of Poetto beach and is set to record four times a day at three-hour intervals (from 8:00 to 17:00). Currently, each recording lasts 10 minutes and the images (Fig. 3.7b) are captured at a frequency of 4 Hz with a resolution of 4096x2160 pixels. More information about the entire coastal video monitoring system is provided in the Chapters 2 and 7 of the thesis.

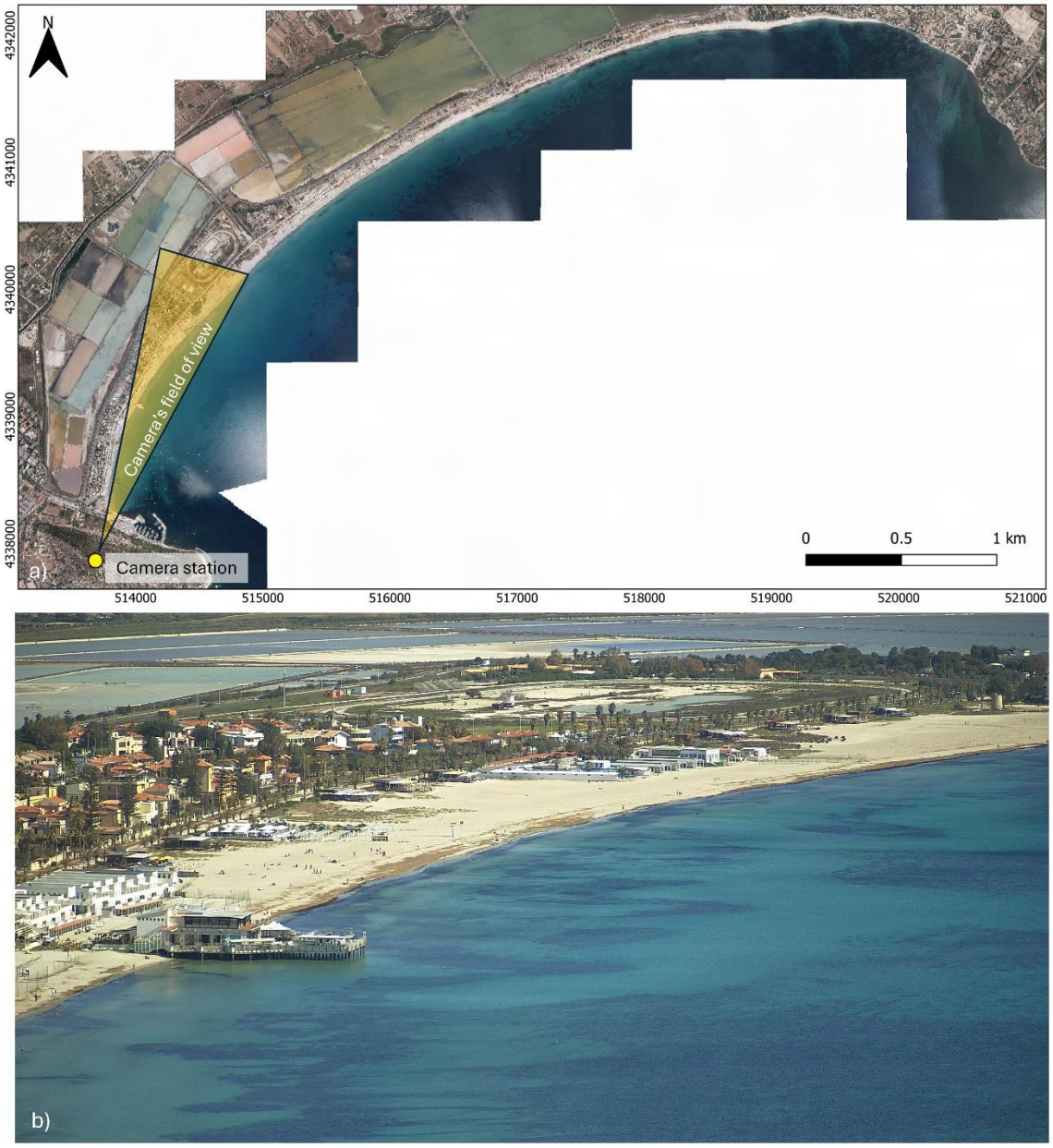

Figure 3.7 - **(a)** Location of the coastal video monitoring system (yellow dot) and the camera's field of view (yellow area) (aerial orthophoto from the WMS of "Regione Autonoma della Sardegna"; Coordinate system: UTM 32N; Datum: WGS84). **(b)** Example of snapshot captured by the camera during recording.

Chapter 4: CLASSIFICATION AND MORPHOMETRIC ANALYSIS OF EMBAYED BEACHES ALONG THE SOUTHERN COAST OF SARDINIA ISLAND (WESTERN MEDITERRANEAN SEA)

This chapter summarises two studies both concerning the morphometric analysis and classification of the embayed beaches along the southern coast of Sardinia (Italy).

1. Usai, A.; Simeone, S.; Trogu, D.; Porta, M.; De Muro, S., **2024**. Morphometric analysis and classification of the embayed beaches on the southern coast of Sardinia Island (Western Mediterranean Sea). In: *Coastlines under change: Proceedings from the International Coastal Symposium (ICS) 2024 (Doha, Qatar)*; Phillips, M.R., Al-Naemi, S., Duarte, C.M., Eds.; *J. Coast. Res.* 113, 748-752. https://doi.org/10.2112/JCR-SI113-147.1.
2. Usai, A.; Simeone, S.; Trogu, D.; Porta, M.; De Muro, S., **2025a**. A morphometric analysis of embayed beaches: southern Sardinia Island. *Geomorphology* 483, 109838. https://doi.org/10.1016/j.geomorph.2025.109838.

In the first article, the embayed beaches identified along the studied coastal stretch were classified using the Embayment Morphometric Parameter (γ_e), an index proposed in literature to estimate the degree of embaymentisation of a beach. In the second article, the values of morphometric parameters and degrees of embaymentisation obtained using the Embayment Morphometric Parameter (γ_e) were compared to those obtained using another classification parameter (Platform Index - I). Overall, a morphometric analysis combined with a classification comparison was performed to better understand the relationship between beach morphometry, the degree of embaymentisation and hydrodynamic circulation.

4.1 Introduction

Embayed beaches are very common along the world's coastlines. They are typically characterised by a curvilinear shape and the presence of lateral physical barriers, either natural (e.g., rocky headlands, rocky outcrops, etc.) and artificial (e.g., harbours, breakwaters, groynes, etc.), at one or both extremities (Short and Masselink, 1999; Gallop et al., 2020). Several terms are used in the scientific literature to refer to embayed beaches: crenulate-shaped bay (Ho, 1971; Wang et al., 2008); pocket beach (Bowman et al., 2009, 2014); headland-bay beach (Phillips, 1985; Klein and Menezes, 2001); static equilibrium bay (Hsu et al., 1989a, 1989b).

The morphometric characteristics of embayments, such as the shape and length of the headlands and cross-shore and longshore extent of the beach, are related to the

geological heritage of the area in which they are located (Short, 2006; Castelle and Coco, 2012). In fact, the degree of constraint given by headlands (also known as "indentation degree" or "degree of embayment") affects beach morphology and hydrodynamic processes and can influence the amount of free sediment available for transport within the system (Gallop et al., 2020). Since most of these embayed beaches are small and nestled along rocky coastlines, the absence of rivers crossing them results in greater geological control over these beaches. As a result, they are often referred to as "geologically controlled beaches" (Gallop et al., 2020).

Given their distribution along coastlines worldwide (Short and Masselink, 1999; Iglesias et al., 2009), the study of embayed beaches is important not only from a scientific perspective, but also from an engineering and beach management point of view. In fact, the construction of artificial structures (e.g., ports, breakwaters, groynes, marinas, etc.) at the edges of beaches can significantly alter their morphodynamic processes, as these structures function as artificial headlands (Ojeda and Guillén, 2008; Ojeda et al., 2011; Castelle et al., 2016).

In recent decades, several studies have focused on identify useful criteria for estimating and defining the degree of embaymentisation of beaches (e.g., Hsu et al., 1989; Spagnolo et al., 2008; Bowman et al., 2009; Fellowes et al., 2019). Estimating the levels of embaymentisation contributes to understand and define the influence of lateral constraints on beach behaviour. In fact, these beaches are often characterised by closely spaced rocky headlands, which can promote the development of rip current systems (Short, 1996). In addition, these beaches may be affected by different wave exposure and breaking conditions (Daly et al., 2011, 2014; Castelle et al., 2020b), which lead to the development of distinct beach morphologies and hydrodynamic processes (Dingler, 1981).

The analysis and geometric calculation of the morphometric parameters is one of the most used methods for estimating the degree of embaymentisation of a beach. Similarly, simulating the morphodynamic processes within embayments through numerical modelling is another valuable approach to estimate the impact of headlands on the hydrodynamic circulation of embayed beaches (Castelle and Coco, 2012).

This study aims to carry out a morphometric analysis and classification of the beaches located along the southern coastal stretch of Sardinia (Western Mediterranean Sea) in order to estimate their degree of embaymentisation. Two classification methods proposed in the scientific literature have been used and compared: the first method (Bowman et al., 2009) is based on the Platform Index (I), which considers the distance between the seaward extremities of the headlands (natural or artificial) that delimit the embayment and the length of the embayment retreat. The second method (Fellowes et al., 2019) is based on the Embayment Morphometric Parameter (γ_e), which takes into account the length of the embayment retreat and its area.

Furthermore, this study also aims to: (I) perform a morphometric analysis using the calculated morphometric parameters for each beach in order to define the geographical distribution of embayed beaches (with their degree of embaymentisation) along the studied coastal stretch; (II) estimate the degree of headlands influence on the beach hydrodynamic circulation using the Non-Dimensional Embayment Scaling Parameter (δ') (Short, 1996; Short and Masselink, 1999); (III) estimate the variations in beach morphometry and degree of embaymentisation in relation to the type of embayment, distinguishing between natural or influenced by artificial structures. Overall, this information represents a valuable resource for coastal management, as understanding and predicting beach behaviour can improve both protection strategies and the sustainable use of coastal environments. This is particularly relevant given the rise in tourism along the Mediterranean coast and the growing demand for new bathing areas, which place additional pressure on these already vulnerable systems.

4.2 Study area

The study focused on the southern coastal stretch of Sardinia (Italy, Western Mediterranean Sea), between Cape Teulada and Cape Carbonara, for a length of approximately 130 km (Fig. 4.1). The studied coastal stretch was previously analysed in the Coastal Plan issued by "Regione Autonoma della Sardegna" (Programma Azione Coste - P.A.C.) (Regione Sardegna, 2013), where 34 beaches were identified and grouped into "Littoral Unit" (Table 4.1).

Beaches along this coastal stretch can be characterised by both sandy and rocky shore. More precisely, most of them are composed of fine sediments, although coarse or pebbly sediments are sometimes present, particularly along the western coastal stretch. This difference in beach sediment grain size is also related to the different wave exposure and breaking conditions that characterise the studied coastal stretch (De Muro et al., 2016; Brambilla et al., 2016; Buosi et al., 2019a; 2019b; Porta et al., 2020; Biondo et al., 2020; Trogu et al., 2020, 2023). Moreover, the entire studied coastline is characterised by a wide *Posidonia oceanica* meadow (Telesca et al., 2015), which can influence both sediment availability and hydrodynamic processes (De Muro et al., 2016).

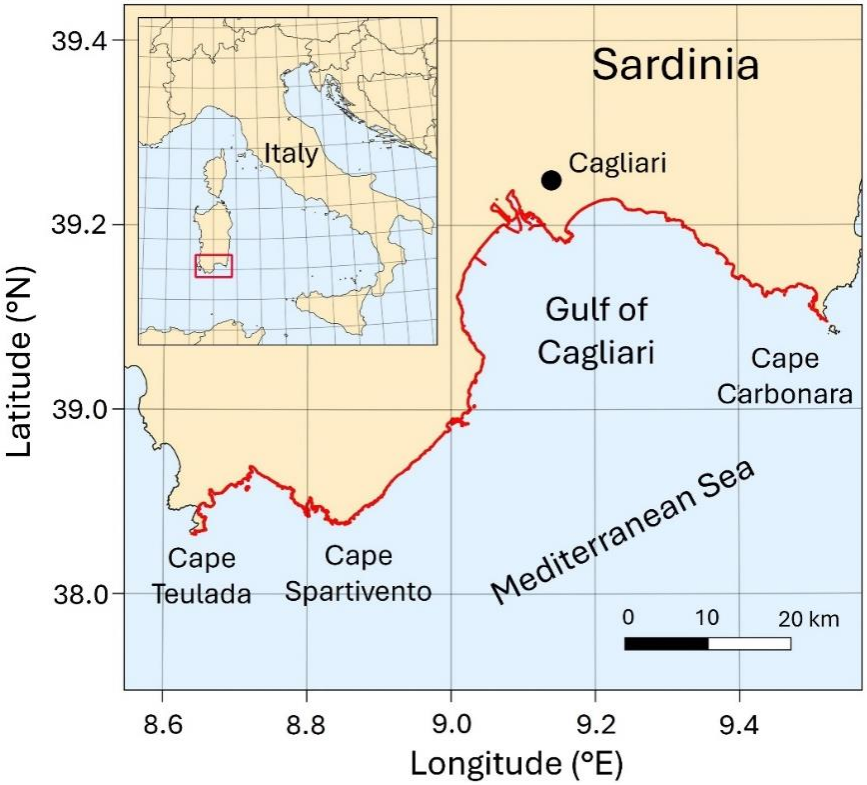

Figure 4.1 - Location of the study area. The red line identifies the coastal stretch investigated between Cape Teulada and Cape Carbonara (modified from Usai et al., 2024)

Table 4.1

Data relating to the beaches of the studied coastal stretch, as reported in the Coastal Plan (P.A.C.) issued by "Regione Autonoma della Sardegna" (from Regione Sardegna, 2013).

Physiographic Unit		Littoral Unit		Beach name	Municipality
8	Capo Teulada - Capo Carbonara	8A	Capo Teulada - Torre di Porto Scudo	Porto Zafferano	-
		8B	Torre di Porto Scudo - Porto Scudo	Porto Scudo	-
		8C	Porto Scudo - Punta Niedda	Porto Tramatzu	-
		8D	Punta Niedda - Torre Budello	-	-
		8E	Torre Budello - Capo di Piscinnì	Piscinnì	Domus de Maria
		8F	Capo di Piscinnì - Capo Malfatano	-	Teulada - Domus de Maria
		8G	Capo Malfatano - Isola Ferraglione	Tuerredda	Teulada
		8H	Isola Ferraglione - Cala Niedda	Cala Cipolla	Domus de Maria
				Campana Pontile - Su Giudeu - S'Acqua Durci	
				Campana	
				Bithia - Sa Colonia	
				Torre Chia - Su Cardolinu	
		8I	Cala Niedda - Capo di Pula	Cala Marina	Pula
				Pinus Village	
				Is Morus	
				Santa Margherita	
				Porto d'Agumu	
		8L	Capo di Pula - Isola S. Macario	Su Guventeddu - Nora	Pula
		8M	Isola S. Macario - Punta Zavorra	Su Stangioni - Foxi Niedda	
				Porto Columbu - Perd'e Sali	Sarroch - Pula
		8N	Punta Zavorra - Porto Canale	Giorgino - La Maddalena - Frutti d'Oro	Cagliari - Capoterra
		8O	Porto Canale - Torre Foxi	Cala Mosca	Cagliari
				Poetto	Cagliari - Quartu S. Elena
		8P	Torre Foxi - Cala Regina	-	Quartu S. Elena

		8Q	Cala Regina - Torre de su Fenugu	Mari Pintau - Cala Regina	
				Geremeas	Maracalagonis - Quartu S. Elena
				Cann'e Sisa	Maracalagonis
		8R	Torre de su Fenugu - Capo Boi	Genn'e Mari	Sinnai - Maracalagonis
				Solanas	Sinnai
		8S	Capo Boi - Capo Carbonara	Porto Sa Ruxi	Villasimius
				Capo Boi	
				Campus	
				Campulongu	
				Spiaggia del Riso e Nuova Spiaggia del Porto	

From a geological perspective, the studied coastal stretch is characterised by different typologies of deposits and rock outcrops (schematically reported in Fig. 4.2).

- The western area (starting from Cape Teulada) is characterised by the presence of Palaeozoic granitic intrusive rocks belonging to the batholith formed during the Hercynian orogeny (Carmignani et al., 2001). Metamorphic rocks with different metamorphic grades are also present in the area of Cape Teulada. Most of this coastal stretch is characterised by rocky headlands that extend seawards, which play a key role in the development of embayed beaches (or "pocket beaches"). These embayments, formed as a result of marine ingression into ancient river valleys ("Rias-type coastline") (Marini and Murru, 1983), extend from Cape Teulada to Cape Spartivento (Fig. 4.2).
- From Cape Spartivento towards the central area of the studied coastal stretch, the Palaeozoic basement is still present. However, this area is also characterised by sedimentary covers, including recent deposits and rocks (Quaternary), which are interrupted by volcanic rocks (Oligocene - Miocene) (Carmignani et al., 2001). Given the lithological heterogeneity, this coastal stretch appears less indented toward the central area, where more straight beaches alternating with smaller embayed beaches can be observed.
- The central area of the studied coastal stretch (representing a portion of the Gulf of Cagliari) (Fig. 4.2) is mainly characterised by sedimentary covers and deposits/rocks dating from the Miocene to the Quaternary (Carmignani et al., 2001). More precisely, this area represents a tectonic graben. In fact, the two extremities of the studied area correspond to the two tectonic horsts (Cape Teulada and Cape Carbonara). Overall, the coastal stretch in this area is mainly characterised by almost straight beaches.

- From the central part of the studied coastal stretch to Cape Carbonara, the Palaeozoic basement outcrops reappear, as in the western area (Cape Teulada) (Carmignani et al., 2001). Proceeding eastward toward Cape Carbonara, smaller beaches reoccur, but with longer shorelines compared to those in the western area.

Overall, part of the studied coastline has been affected by anthropogenic modifications. These impacts are less pronounced at the two capes (Teulada and Carbonara), but more evident in the central area near the urban city of Cagliari, where the coastline morphology has been alternated by the construction of artificial structures such as breakwaters, groynes, marinas, harbours, and other coastal engineering structures.

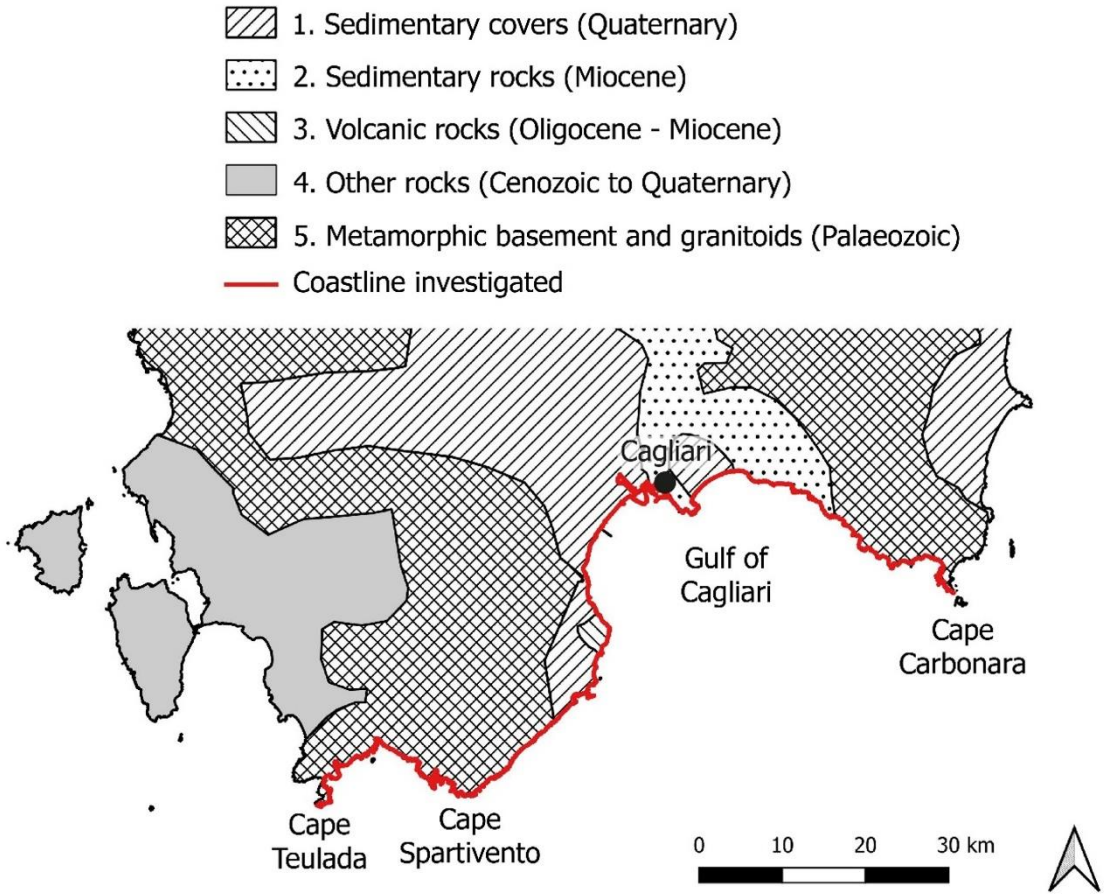

Figure 4.2 - Schematic geological framework of the study area. Main types of deposits and rocks along the studied coastal stretch (red line): 1. Sedimentary covers (Quaternary); 2. Sedimentary rocks (Miocene); 3. Volcanic rocks (Oligocene - Miocene); 4. Other types of rocks outside the study area (Cenozoic to Quaternary); 5. Metamorphic basement and intrusive rocks, mainly granitoids (Palaeozoic) (modified from Usai et al., 2025a).

4.3 Methods

Along the examined coastline, embayed beaches were identified through the analysis of aerial orthophotos available online in the WMS of "Regione Autonoma della Sardegna" (https://webgis.regione.sardegna.it/geoserverraster/ows?service=WMS&request=GetCapabilities). More precisely, this study took into account all those beaches characterised by the presence of lateral physical barriers, whether natural, artificial, or both. Using QGIS software (Version 3.18.2), a set of morphometric parameters were measured for each beach identified, according to the methodologies proposed by Bowman et al. (2009) (Fig. 4.3a) and Fellowes et al. (2019) (Fig. 4.3b). The morphometric parameters considered are:

- $\boldsymbol{R_o}$: Distance between the headlands defining the embayment (length between the two most external seaward points of the headlands).
- $\boldsymbol{a}$: Bay indentation (maximum length of the embayment retreat; the line is perpendicular to the one that defines R_o).
- $\boldsymbol{S_1}$: Total length of the embayment.
- $\boldsymbol{S_2}$: Total length of the emerged beach (backshore).
- $\boldsymbol{S_3}$: Total length of the shaded zone (it is measured using S_2 as a reference).
- $\boldsymbol{B_w}$: Maximum width of the emerged beach (backshore).
- $\boldsymbol{A_e}$: Embayment area.

The length of some morphometric parameters varies depending on the methodology adopted (Fig. 4.3). Morphometric parameters a and S_1 represent the main difference: Bowman et al. (2009) consider the shoreline position as inner limit of the bay indentation a (Fig. 4.3a); Fellowes et al. (2019) consider the beginning of the seaward boundary of the backshore as the inner limit (e.g., the vegetation line or the toe dune) (Fig. 4.3b).

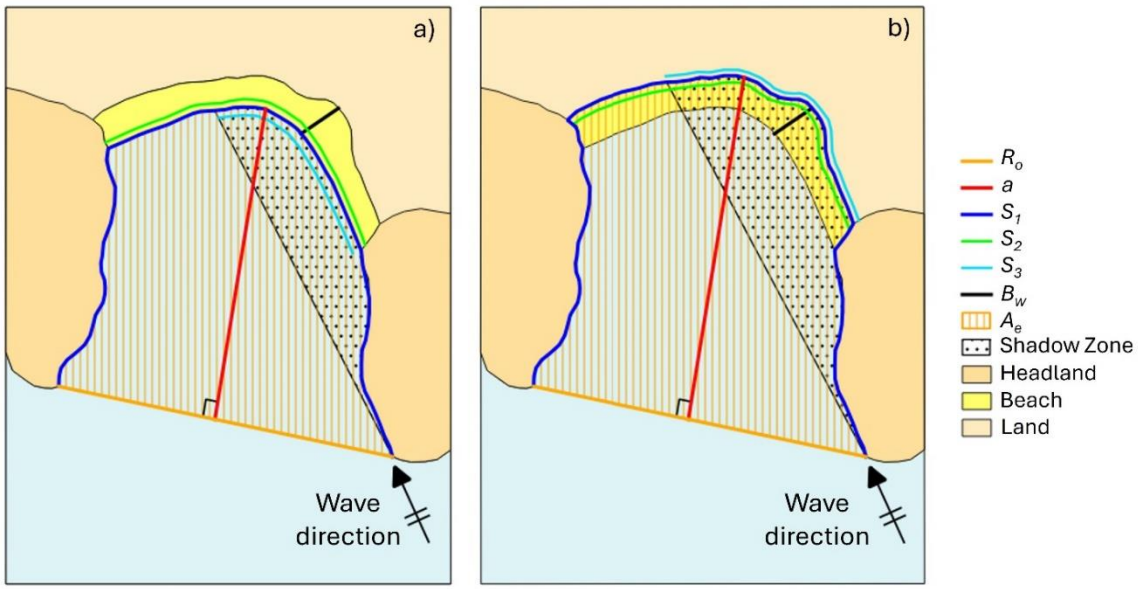

Figure 4.3 - Morphometric parameters measured for each beach identified through aerial orthophotos. The lengths and areas of the morphometric parameters differ according to the methodological approach adopted: **(a)** Bowman et al., 2009; **(b)** Fellowes et al., 2009 (from Usai et al., 2025a).

In this study, two time series of aerial orthophoto mosaics were used:

- **2006-2008 time series** (scale 1: 2000) were used as a working base to identify the beaches along the studied coastline, update the number of beaches reported in the Coastal Plan (P.A.C.) (Regione Sardegna, 2013), and digitize their respective morphometric parameters (except for parameters S_1 and S_2). The shapefile of Sardinia coastline (scale 1:2000), available online in the Geoportal of "Regione Autonoma della Sardegna" (https://www.sardegnageoportale.it/accessoaidati/downloaddati), was taken as a reference to measure the total length of the embayment S_1 and the total length of the emerged beach S_2.
- **2019 time series** (scale 1: 2000) were used to identify and update the changes in the studied coastline compared to the 2006-2008 aerial orthophotos. These changes in the coastline are associated with the construction of new engineering structures (e.g., marinas, jetties, groynes, etc.).

To facilitate the digitization of morphometric parameters and data processing, a regular grid with a mesh size of 4 x 4 km was created in order to extract the aerial orthophoto mosaics of the studied coastline. Subsequently, the overlapping of the extracted aerial orthophotos with the Sardinia coastline enabled the mapping and quantification (lengths and areas) of the morphometric parameters analysed in this study.

To investigate the influence of headlands on embayed beaches and the resulting shadow zones ("degree of protection"), wave data of the study area were analysed. For this purpose, the studied coastal stretch was divided into 10 sectors (Fig. 4.4). Within each sector, a nearshore point (called in this work "virtual buoys"; yellow dots in Fig. 4.4) was selected to extract wave data from the Copernicus Marine Environment Monitoring Service - CMEMS (Korres et al., 2021). The location of the virtual buoys coincides with the nodes of CMEMS grid (Fig. 4.4). For each virtual buoy, the values of offshore significant wave height (H_s), wave period (T) and mean wave direction (Dir) were downloaded over a 10-years period (from 1 January 2011 to 1 January 2021). The main wave directions for each virtual buoy were estimated based on the direction with the highest frequency percentage. For all those beaches located in the same sector, the mean values of the considered wave parameters (H_s, T, Dir) were assumed to be the same.

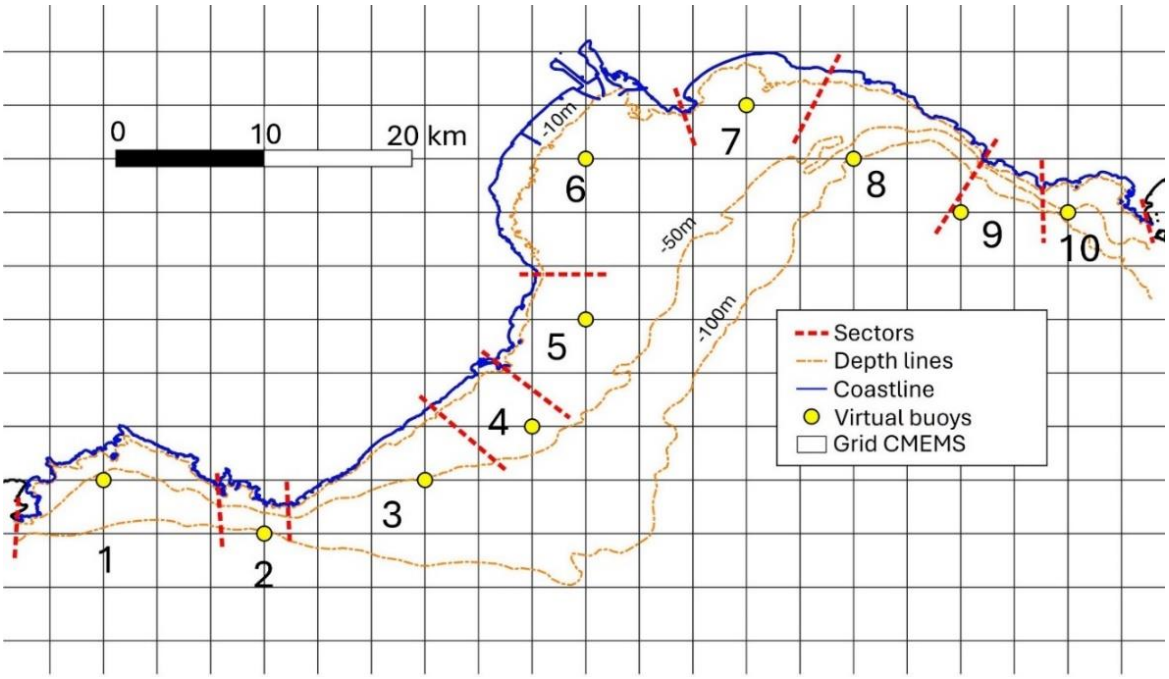

Figure 4.4 - Location of virtual buoys along the studied coastal stretch, which was divided into 10 sectors. The bathymetry is highlighted by the dashed orange lines at -10 m, -50 m and -100 m (from Usai et al., 2025).

Once the morphometric parameters had been measured, a set of indices and parameters was calculated for each beach identified:

- **Platform Index (I)** (Bowman et al., 2009), also known as "Indentation Ratio" (Hsu et al., 1989a, 1989b):

$$I = a/R_o \tag{4.1}$$

where a is the Bay indentation and R_o is the spacing of the headlands.

- **Embayment Morphometric Parameter (γ_e)** (Fellowes et al., 2019):

$$\gamma_e = a/\sqrt{A_e} \tag{4.2}$$

where a is the bay indentation and A_e is the embayment area.

- **Bay filling Index** (Bowman et al., 2009):

$$S_2/S_1 \tag{4.3}$$

where S_1 is the total length of the embayment and S_2 is the total length of the emerged beach (backshore).

In order to estimate the degree of embaymentisation, beaches were grouped into embayment classes following the methodological approach proposed by the authors considered in this study (Bowman et al., 2009 and Fellowes et al., 2019). More precisely, the beaches were grouped based on the calculated values of the Platform Index (I) using a defined classification criterion (Bowman et al., 2009). On the other hand, a K-means cluster analysis was applied to group the beaches according to the calculated values of the Embayment Morphometric Parameter (γ_e) (Fellowes et al., 2019).

Finally, to estimate the degree of headlands impact on the surf zone circulation, the Non-Dimensional Embayment Scaling Parameter (δ') (Short, 1996; Short and Masselink, 1999) were calculated for each beach:

$$\delta' = \frac{{S_1}^2}{R_o 100 H_b} \tag{4.4}$$

where S_1 is the total length of the embayment, R_o is the spacing between the headlands and H_b is the breaking wave height.

The values of H_b were estimated using the equation proposed by Short and Masselink (1999) (Equation 4.5) and Komar and Gaughan (1972) (Equation 4.6):

$$H_b = \sqrt{{H_s}^2 \frac{R_o}{S_1}} \tag{4.5}$$

$$H_b = 0.39\ g\ 0.2\ (H_s)^2\ T\ 0.4 \tag{4.6}$$

where H_s is the offshore significant wave height, R_o is the spacing between the headlands, S_1 is the total length of the embayment, g is the gravitational acceleration and T is the wave period.

Overall, three types of surf zone circulation may occurs based on the δ' values (Short, 1996; Short and Masselink, 1999):

- **δ' < 8**: Cellular beach circulation.
- **δ' = 8 - 19:** Transitional beach circulation.
- **δ' > 19:** Normal beach circulation.

4.4 Results

The analysis of aerial orthophotos resulted in the identification of 79 beaches along the studied coastal stretch (Fig. 4.5). Consequently, the number of beaches reported in the Coastal Plane (P.A.C) (Table 4.1) has been updated (see Appendix A of the thesis).

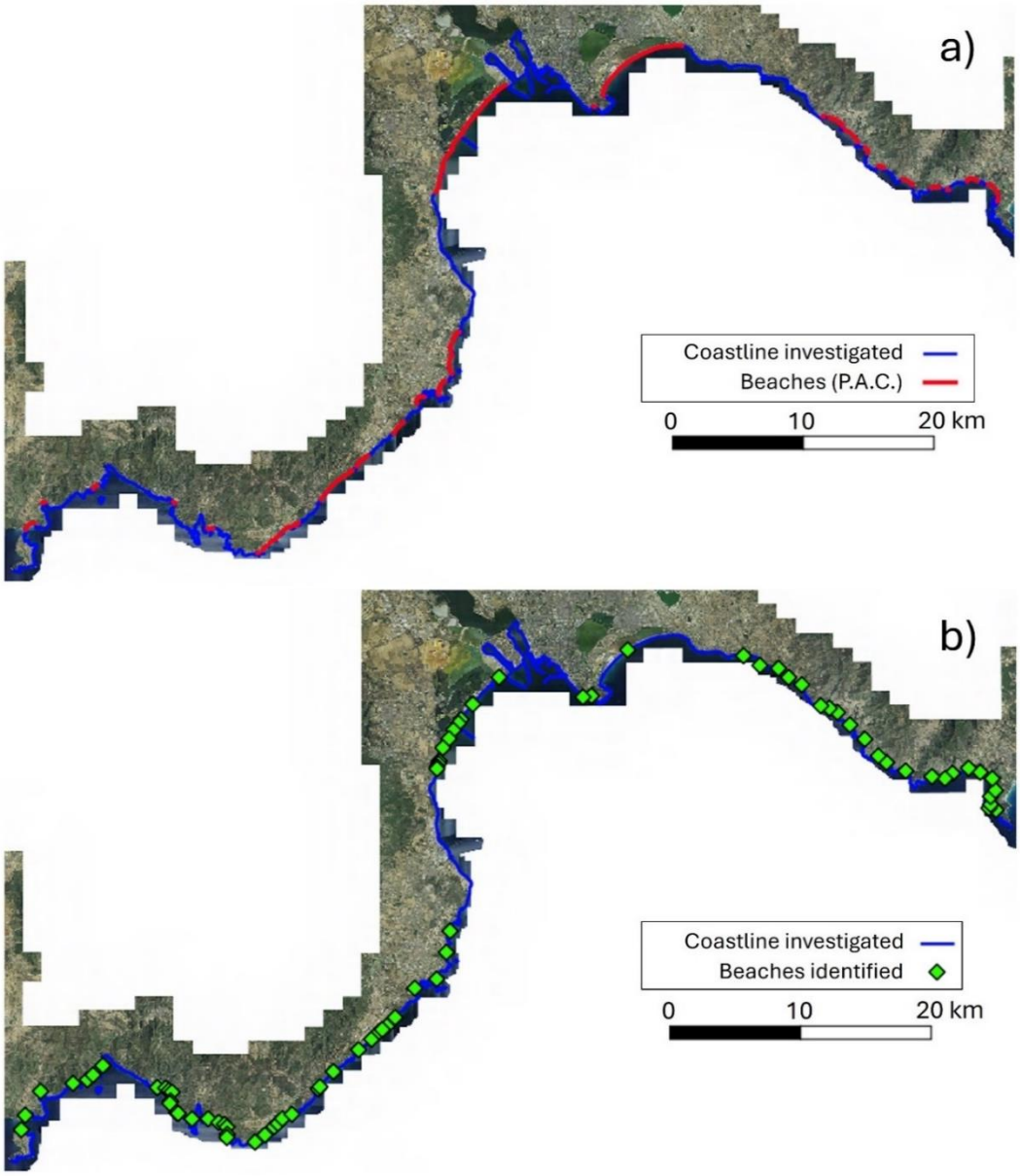

Figure 4.5 - Location of beaches along the studied coastal stretch: **(a)** beaches reported in the Coastal Plane (P.A.C.); **(b)** beaches identified in this study through the analysis of aerial orthophotos from the WMS of "Regione Autonoma della Sardegna" (Coordinate system: UTM 32N; Datum: WGS84) (from Usai et al., 2025a).

Of the 79 beaches identified in this study, two beaches were excluded from the morphometric analysis and classification comparison due to their shoreline length. More precisely, Poetto beach - Cagliari (with an excessively long shoreline; $S_2 > 7$ Km) and Frutti d'Oro beach - Capoterra (with a very short shoreline; $S_2 < 50$ m) were excluded, as their

inclusion resulted in inconsistent grouping of beaches into embayment classes during the K-means cluster analysis of γ_e values. Therefore, the comparison and analysis of morphometric parameters and the degree of embaymentisation were focused exclusively on the remaining 77 beaches.

Once the morphometric parameters for each beach were digitized and calculated, the obtained values of Platform index (I) and Embayment Morphometric Parameter (γ_e) were used to group the beaches into embayment classes according to the methodology proposed by the authors (Bowman et al., 2009; Fellowes et al., 2019). The complete list of morphometric parameter values calculated in this study is provided in Appendix A of the thesis.

The mean wave values obtained for each coastal sector (Table 4.2) were used to define the values and percentages of beach shadow zones, as well as to calculate the *δ'* parameter. The processed wave data revealed that, over a 10-year period (1 January 2011 to 1 January 2021), the studied coastal stretch was characterised by average significant wave heights H_s ranging from 0.8 m to 1.5 m and wave period T ranging from 5.5 s to 6.8 s (Table 4.2). Furthermore, the analysis of average wave direction indicated two predominant directions of incoming waves along the study area: the first (*Dir1*) ranging from 130° and 145° (S-SE); the second (*Dir2*) ranging from 215° and 260° (SW-S) (Fig. 4.6). For Sectors 5, 6 and 7, a single wave direction (*Dir1*) was considered in the calculation of the shaded zones, as the frequency of waves coming from the opposite sector (*Dir2*) was very low (Table 4.2).

Table 4.2

Mean wave values (offshore significant wave height - H_s; wave period - T; mean wave direction - *Dir1* and *Dir2*) associated with each virtual buoy along the studied coastal stretch (from 1 January 2011 to 1 January 2021). The coordinates refer to the WGS84 Coordinate system.

Virtual buoy	H_s (m)	T (s)	*Dir1* (°)	*Dir2* (°)	Latitude (N)	Longitude (E)
1	0.8	5.9	135	235	38° 53’ 45’’	8° 42’ 30’’
2	1.5	6.8	125	260	38° 51' 15"	8° 50' 00"
3	1.2	6.2	130	235	38° 53' 45"	8° 57' 30"
4	1.1	6.0	130	230	38° 56' 15"	9° 02' 30"
5	1.0	5.9	130	-	39° 01' 15"	9° 05' 00"
6	0.8	5.9	135	-	39° 08' 45"	9° 05' 00"
7	0.8	5.5	145	-	39° 11' 15"	9° 12' 30"
8	0.9	5.7	145	215	39° 08' 45"	9° 17' 30"
9	1.1	6.0	135	225	39° 06' 15"	9° 22' 30"
10	1.2	6.0	135	225	39° 06' 15"	9° 27' 30"

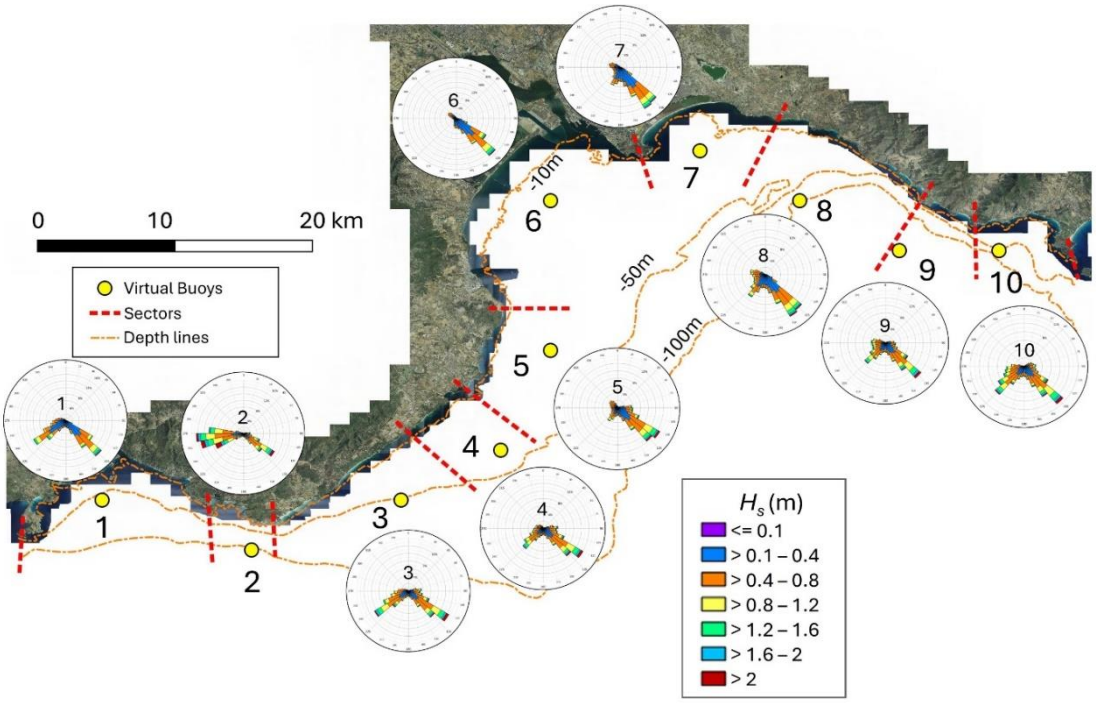

Figure 4.6 - Values of offshore significant wave height H_s and mean wave direction *Dir* for each virtual buoy along the studied coastline (aerial orthophotos from the WMS of "Regione Autonoma della Sardegna"; Coordinate system: UTM 32N; Datum: WGS84) (from Usai et al., 2025a).

4.4.1 Classification of the degree of embaymentisation: Platform Index (*I*)

The degree of embaymentisation, estimated using the Platform Index (I) (Bowman et al., 2009), led to the classification of beaches into five embayment classes. The degree of embaymentisation increases progressively from Class 1 to Class 5. Overall, the values of Platform Index (I) range between 0.05 and 1.94. Each embayment class is defined by a classification criterion based on the values of R_o and a (Table 4.3).

- **Class 1** includes 23 beaches and is defined by I values ranging from 0.05 and 0.25. Beaches in this class show R_o values that are more than 4 times greater than the values of a ($R_o > 4a$). Consequently, beaches in Class 1 are characterised by the highest values of R_o and the lowest values of bay indentation a. The shoreline shapes tend to be almost rectilinear, bordered by headlands with a typically divergent configuration. Furthermore, Class 1 shows the highest values of S_2 and A_e, while the values of S_3 are among the lowest. Overall, Class 1 represents the group of beaches with the lowest degree of embaymentisation.
- **Class 2** includes 15 beaches and is defined by I values ranging from 0.26 and 0.39. Beaches in this class show R_o values ranging from 2.5 and 4 times the values of a ($R_o \approx 2.5a$ - $4a$). Compared to the previous class, the distance between the headlands

R_o begins to decrease, while the bay indentation a increases. Similarly, the values of S_2 and A_e decrease, whereas the lengths of the shaded beach S_3 increase. Beaches in this class begin to acquire more curved shoreline shapes, whit headlands that are not always divergent from each other.

- **Class 3** includes 29 beaches and is defined by I values ranging from 0.40 and 0.70, while **Class 4** includes 5 beaches and is characterised by I values ranging from 0.72 and 0.95. Beaches in Class 3 show R_o values ranging from 1.5 and 2.5 times the values of a ($R_o \approx 1.5a$ - $2.5a$), while beaches in Class 4 show R_o values ranging from 1.5 and 1 times the values of a ($R_o \approx 1.5a$ - $1a$). In both classes, the distances between headlands R_o continue to decrease while the values of bay indentation a continue to increase. At the same time, the values of S_2 and A_e show a continue decreasing, whereas the length of the shaded beach S_3 continues to increase, with average values above 40%. Consequently, beaches in these classes progressively continue to acquire more curved shape. The highest number of beaches identified in this study is found in Class 3.
- **Class 5** includes 5 beaches and is defined by I values ranging from 1.05 and 1.94. Beaches in this class show R_o values lower than a values ($R_o < a$). Compared to the previous class, the distances between headlands R_o continue to decrease, while the values of bay indentation a continue to increase. However, some parameters (S_1, A_e and B_w) show slight variations from the increasing and decreasing values observed in earlier classes (Table 4.3). Class 5 represents the class with the highest degree of embaymentisation, and beaches are characterised by a curved shoreline. Additionally, over 60% of the emerged beach is shaded S_3, due to the very limited shoreline length S_2 in this class.

Considering the increasing and decreasing values obtained for the five embayment classes, the Bay filling Index (S_2/S_1) also shows a decrease in values from Class 1 to Class 5 (Table 4.3).

Table 4.3

Mean values of morphometric parameter and indices calculated for each embayment class identified through the Platform Index (I) (Bowman et al., 2009).

Embayment Class	1	2	3	4	5
Number of beaches	23	15	29	5	5
Platform Index (I)	0.05 - 0.25	0.26 - 0.39	0.40 - 0.70	0.72 - 0.95	1.05 - 1.94
Classification criterion	Ro > 4a	Ro ≈ 2.5-4a	Ro ≈ 1.5-2.5a	Ro ≈ 1-1.5a	Ro < a
R_o (m)	1093	761	481	300	257
a (m)	165	256	251	229	347
S_1 (m)	1358	1279	1026	951	1217
S_2 (m)	972	483	310	281	163
S_3 (*Dir1*) (%)	7	15	43	78	62
S_3 (*Dir2*) (%)	3	10	40	62	75
A_e (m^2 x 10^3)	194	182	139	85	101
B_w (m)	39	36	28	25	38
Bay filling Index (S_2/S_1)	0.65	0.43	0.30	0.21	0.14

4.4.2 Classification of the degree of embaymentisation: Embayment Morphometric Parameter (γ_e)

The degree of embaymentisation, estimated using the Embayment Morphometric Parameter (γ_e) (Fellowes et al., 2019), led to the classification of beaches into four embayment classes. The optimal number of embayment classes and the beach grouping were obtained through the K-means cluster analysis of γ_e values (Fig. 4.7). The degree of embaymentisation increases progressively from Class 1 to Class 4 and the values of Embayment Morphometric Parameter (γ_e) range between 0.34 and 1.63 (Table 4.4). Overall, the increasing and decreasing values of morphometric parameters and indices identified through the previous classification approach (Table 4.3) appear very similar to those obtained following the method proposed by Fellowes et al. (2019) (Table 4.4).

- **Class 1** includes 12 beaches and is defined by γ_e values ranging from 0.34 and 0.56. Beaches in this class show the highest values of R_o and the lowest values of a. Additionally, beaches are characterised by the highest values of A_e, B_w, S_1 and S_2, whereas the values of S_3 are among the lowest within this class. Class 1 includes all those beaches with the lowest degree of embaymentisation.

- **Class 2** includes 31 beaches and is defined by γ_e values ranging from 0.59 and 0.81. Compared to the previous class, the distance between headlands R_o begins to decrease, although the mean value of the bay indentation a remains unchanged. Overall, there is also a decrease in the values of S_1, S_2, A_e and B_w, while an increase in S_3 values is observed. The highest number of identified beaches in this study is found in Class 2.
- **Class 3** includes 25 beaches and is defined by γ_e values ranging from 0.82 and 1.08. Similar to the previous class, a decrease in the mean values of R_o, S_2 and B_w is observed, whereas the mean value of S_3 shows an increase. The mean values of a, S_1 and A_e are slightly higher than in the previous Class 2.
- **Class 4** includes 9 beaches and is defined by γ_e values ranging from 1.12 and 1.63. This class includes all those beaches with the highest degree of embaymentisation. The mean values of R_o, S_1, S_2, A_e and B_w are among the lowest, while the mean values of S_3 is among the highest (considering both wave directions *Dir*). Moreover, the mean value of the bay indentation a is slightly lower than in the previous Class 3.

Overall, the beaches gradually take on a shape from almost rectilinear (Class 1) to very curvilinear (Class 4), accompanied by a decrease in the values of Bay filling Index (S_2/S_1) from Class 1 to Class 4.

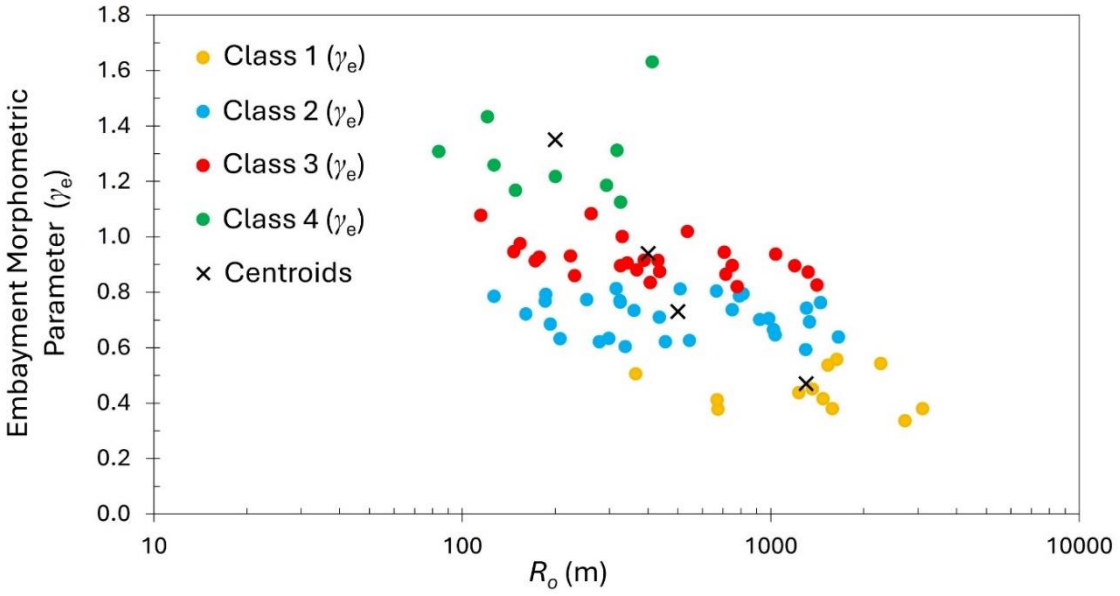

Figure 4.7 - Grouping of the identified beaches into embayment classes using the K-means cluster analysis of the γ_e values. Coloured dots represent individual beaches while black "X" marks indicate the centroid of each cluster (from Usai et al., 2025a).

Table 4.4

Mean values of morphometric parameter and indices calculated for each embayment class identified through the Embayment Morphometric Parameter (γ_e) (Fellowes et al., 2019).

Embayment Class	1	2	3	4
Number of beaches	12	31	25	9
Embayment Morphometric Parameter (γ_e)	0.34 - 0.56	0.59 - 0.81	0.82 - 1.08	1.12 - 1.63
R_o (m)	1557	631	520	226
a (m)	220	220	300	290
S_1 (m)	2034	1144	1231	1036
S_2 (m)	1632	529	412	186
S_3 (*Dir1*) (%)	4	30	34	64
S_3 (*Dir2*) (%)	3	16	41	66
A_e (m^2 x 10^3)	301	144	169	68
B_w (m)	39	36	28	25
Bay filling Index (S_2/S_1)	0.79	0.48	0.29	0.21

4.4.3 Classification comparison: I and γ_e

The comparison between the two classifications (Platform Index and Embayment Morphometric Parameter) highlighted a different grouping of some beaches along the studied coastline (Fig. 4.8; Table 4.5). More precisely, a partial and total overlap of the embayment classes is observed. Beaches in Class 1 identified through the Embayment Morphometric Parameter (γ_e) are entirely contained within Class 1 (I) (Fig. 4.8). On the other hand, beaches in Class 2 (γ_e) are contained in Classes 1, 2 and 3 when classified with the Platform Index (I). Similarly, beaches in Class 3 (γ_e) are contained in Classes 2(I), 3(I) and 4(I), while beaches in Class 4 (γ_e) are contained in Classes 3(I), 4(I) and 5(I). (Fig. 4.8). Despite differences in beach grouping, the comparison between the two classifications revealed a high positive correlation (R = 0.89).

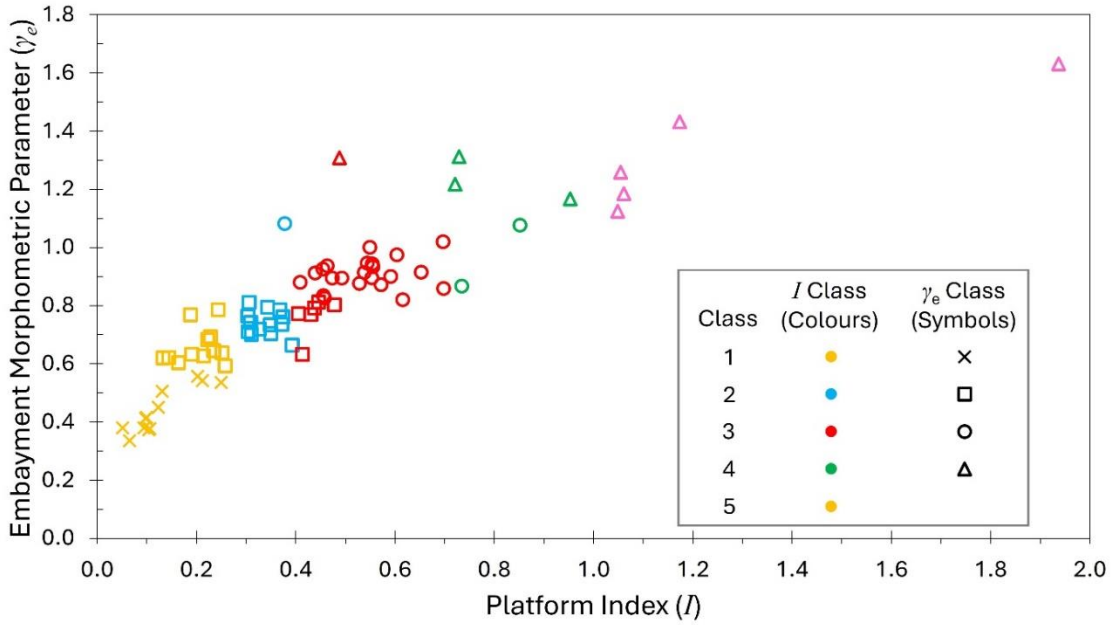

Figure 4.8 - Comparison between the two classifications, Platform Index (classes are marked by colours) and Embayment Morphometric Parameter (classes are marked by symbols), both used to estimate the degree of beach embaymentisation. A high positive correlation (R = 0.89) was observed between the values of I and γ_e (from Usai et al., 2025a).

Table 4.5

Embayment classes resulting from the classification with the Platform Index (I) and the Embayment Morphometric Parameter (γ_e).

ID Code	Embayment Classes		ID Code	Embayment Classes	
	I	γ_e		I	γ_e
1	3	2	**41**	1	1
2	3	3	**42**	1	2
3	5	4	**43**	3	2
4	2	2	**44**	3	2
5	4	4	**45**	-	-
6	3	3	**46**	1	1
7	3	3	**47**	3	2
8	1	2	**48**	1	1
9	3	3	**49**	3	4
10	3	3	**50**	1	1
11	3	3	**51**	1	1
12	5	4	**52**	3	3
13	4	3	**53**	1	2
14	3	3	**54**	3	3
15	3	3	**55**	-	-
16	3	2	**56**	1	1
17	2	2	**57**	3	3
18	3	3	**58**	2	2
19	5	4	**59**	3	3
20	5	4	**60**	2	2
21	4	4	**61**	3	3
22	3	3	**62**	1	1
23	4	4	**63**	2	2
24	1	2	**64**	1	2
25	2	2	**65**	3	3
26	2	3	**66**	3	3
27	2	2	**67**	1	2
28	3	3	**68**	2	2
29	1	2	**69**	2	2
30	1	1	**70**	3	3
31	1	1	**71**	1	2
32	1	1	**72**	2	2
33	1	2	**73**	2	2
34	2	2	**74**	2	2
35	2	2	**75**	5	4
36	1	2	**76**	3	3
37	1	1	**77**	3	2
38	4	3	**78**	1	2
39	3	3	**79**	3	3
40	1	1			

4.4.4 Influence of headlands on surf zone circulation

The calculated values of δ' were used to estimate the degree of headland impact on surf zone circulation within the studied beaches. For this proposal, both classification approaches (Bowman et al., 2009; Fellowes et al., 2019) and both equations for calculating H_b values (Short and Masselink, 1999; Komar and Gaughan, 1972) were applied. The results indicated that the two H_b equations lead to different values of δ' (Table 4.6). The complete list of the surf zone circulation types identified for each beach is provided in Appendix A of the thesis.

- The δ' values obtained using the H_b equation proposed by Short and Masselink (1999) highlighted that most of the identified beaches are characterised by a "normal beach circulation" ($\delta' > 19$). More precisely, 44 beaches (57%) are in this conduction when classified with the Platform Index (I), and 52 beaches (67%) when classified with the Embayment Morphometric Parameter (γ_e). Overall, the values of δ' range from 2.4 to 351.0 (Bowman et al., 2009 method) and from 3.3 to 448.5 (Fellowes et al., 2019 method).
- The δ' values obtained using the H_b equation proposed by Komar and Gaughan (1972) highlighted that most of the identified beaches are characterised by a "cellular beach circulation" ($\delta' < 8$) (45%), when classified with the Platform Index (I), or both "cellular beach circulation" (35%) and "transitional beach circulation" ($8 < \delta' < 19$) (35%), when classified with the Embayment Morphometric Parameter (γ_e). Beaches characterised by "normal beach circulation" ($\delta' > 19$) are less than 30%: 23% when classified with the Platform Index (I) and about 30% when classified with the Embayment Morphometric Parameter (γ_e). Overall, the values of δ' range from 1.2 to 98.2 (Bowman et al., 2009 method) and from 1.7 to 119.5 (Fellowes et al., 2019 method).

Table 4.6

Numbers of beaches within each interval of the Non-Dimensional Embayment Scaling Parameter (δ'), obtained by considering both classification methods (Bowman et al., 2009; Fellowes et al., 2019) and both formulations used for calculation H_b values (Short and Masselink, 1999; Komar and Gaughan, 1972).

Breaking wave height (H_b) equation		Short and Masselink, 1999			Komar and Gaughan, 1972		
Non-Dimensional Embayment Scaling Parameter (δ')		**< 8**	**8 - 19**	**> 19**	**< 8**	**8 - 19**	**> 19**
Platform Index (I)	**Class 1**	8	5	10	12	7	4
	Class 2	3	3	9	7	7	1
	Class 3	3	10	16	14	6	9
	Class 4	0	1	4	1	2	2
	Class 5	0	0	5	1	2	2
Embayment Morphometric Parameter (γ_e)	**Class 1**	0	3	9	1	7	4
	Class 2	6	9	16	15	11	5
	Class 3	0	7	18	9	6	10
	Class 4	0	0	9	2	3	4

4.4.5 Natural and artificial embayments

The identification of beaches along the studied coastal stretch was accompanied by an analysis of the embayment types, distinguishing between natural or artificial embayments. Embayments without the presence of artificial structures within them, or along their lateral boundaries, were considered as "natural". On the other hand, embayments were considered "artificial" if one or both headlands are artificial, or if engineering structures were present within the embayment.

Among the embayments analysed along the studied coastline, 57 (74%) were defined as natural, whereas the remaining 20 (26%) were defined as artificial (Table 4.7). The results highlighted that the mean values of the morphometric parameters R_o, a, S_1, S_2, S_3, A_e and B_w are higher for artificial embayments than for the natural ones. However, the mean values of the morphometric parameters a and B_w do not show wide differences between the two embayment types. In addition, the mean value of Bay filling Index (S_2/S_1) is higher for artificial embayments than for natural ones. Oppositely, natural embayments are more indented than artificial ones, as the mean value of Platform Index and Embayment Morphometric Parameter are higher (Table 4.7).

The analysis of aerial orthophotos revealed that, among the 20 artificial embayments examined, 8 are laterally delimited by a single artificial headland, while 11 are confined by artificial headlands on both boundaries. Furthermore, 4 of the 20 artificial embayments show a harbour or marina as a headland. On the other hand, only one of the identified artificial embayment does not show artificial headland but contain engineering structures within the embayment that influence its hydrodynamic circulation. Overall, 5 of the 20 artificial embayments present engineering structures within their embayment area, such as breakwaters, groynes, or similar structures.

Table 4.7

Morphometric parameter values and main characteristics of natural and artificial embayments identified along the studied coastal stretch.

Morphometric parameters	**Bowman et al., 2009**		**Fellowes et al., 2019**	
	Natural	**Artificial**	**Natural**	**Artificial**
R_o (m)	631	865	631	865
a (m)	229	236	255	256
S_1 (m)	1141	1298	1260	1409
S_2 (m)	448	765	543	850
S_3 (*Dir1*) (%)	26	27	28	28
S_3 (*Dir2*) (%)	31	46	33	47
A_e (m^2 x 10^3)	140	209	150	219
B_w (m)	34	37	34	37
Platform Index (I)	0.46	0.37	-	-
Embayment Morphometric Parameter (γ_e)	-	-	0.832	0.729
Bay filling Index (S_2/S_1)	0.38	0.52	0.40	0.54

Embayment characteristics	**Natural**	**Artificial**
Number of beaches	57	20
One artificial headland	-	8
Both artificial headlands	-	11
Embayment with artificial structures	-	5
Harbour as headland	-	4

4.5 Discussion

Morphometric analysis of the beaches along the studied coastal stretch provided valuable insights into microtidal beaches, particularly in estimating their degree of embaymentisation, understanding their potential hydrodynamic circulation within the surf zone and identifying morphometric characteristics associated with the presence or absence of artificial structures.

4.5.1 Morphometric parameters and classification comparison

The application of the classification methodologies proposed by the authors considered in this study (Bowman et al., 2009; Fellowes et al., 2019) led to an almost appropriate grouping of the beaches along the studied coastal stretch, based on their degree of embaymentisation. Although the comparison of the two classification indices (Platform Index and Embayment Morphometric Parameter) showed a high value of correlation (R = 0.89) (Fig. 4.8), it is appropriate to take into account some differences:

- The methodologies used to attribute the degree of embaymentisation to each beach is different. The Platform Index (I) is based on a ratio between two lengths: the indentation of the embayment (a) and the distance between the headlands (R_o). Beaches are then grouped according to the ranges of I values. In contrast, the Embayment Morphometric Parameter (γ_e) is based on a ratio between a length (bay indentation - a) and an area (embayment area - A_e). In this case, the beaches are grouped using a K-means cluster analysis of the obtained γ_e values. Furthermore, the two methodological approaches adopt different criteria for measuring the morphometric parameters (Fig. 4.3).
- The number of embayment classes considered also differs. The Platform Index (I) grouped the identified beaches into five classes. On the other hand, the Embayment Morphometric Parameter (γ_e) resulted in four embayment classes through a K-mean cluster analysis (Fig. 4.7).

Overall, the observed differences and the relative morphometric analysis indicate that the Embayment Morphometric Parameter (γ_e) appears more suitable than Platform Index (I) for classifying the microtidal embayed beaches under study. Aerial orthophoto analysis of the study area revealed substantial variability in the shape and size of the embayments. In this context, the classification based on the Embayment Morphometric Parameter (γ_e), characterised by a smaller number of embayment classes, proves more effective for grouping beaches according to their embayment area. Conversely, the Platform Index (I), as noted in the scientific literature (Klein and Menezes, 2001; Fellowes et al., 2019), is more appropriate for beaches with curved shorelines and tends to be less effective for those with straighter coastal configurations. Additionally, the length of the emerged

beach S_2 has been identified as a valuable parameter for estimating the degree of embaymentisation of beaches. Beaches with a lower degree of embaymentisation, usually characterised by wider and more open coastal configurations, tend to exhibit longer shoreline lengths. Conversely, beaches with a higher degree of embayment generally show shorter shoreline length.

A more detailed analysis of the morphometric parameters used to classify the degree of embaymentisation highlighted that the length of the bay indentation a show a higher correlation with the area of the embayment A_e (R = 0.81) (Fig. 4.9b) than the headlands spacing R_o (R = 0.47) (Fig. 4.9a). This finding could suggest that the Embayment Morphometric Parameter (γ_e), which is based on A_e, is a more suitable for classifying the degree of embaymentisation of beaches with varying shapes and sizes. In contrast, the Platform Index (I), which is based on the distance of headlands R_o, appears to be less suitable in classifying the morphological beach variability of such coastal configurations.

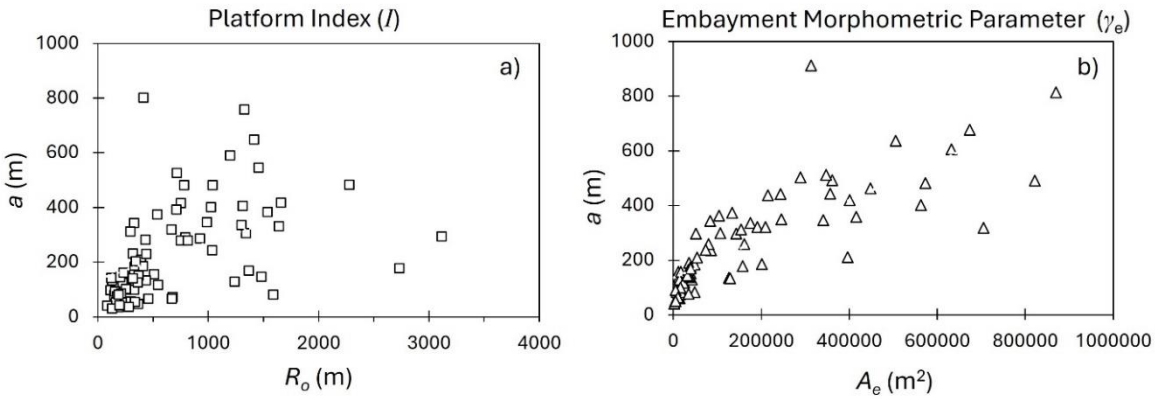

Figure 4.9 - Correlation between morphometric parameters used to classify the embayed beaches: **(a)** bay indentation a and headland spacing R_o (Platform Index; a/R_o) (R = 0.47); **(b)** bay indentation a and embayment area (A_e) (Embayment Morphometric Parameter; $a/\sqrt{A_e}$) (R = 0.81) (from Usai et al., 2025a).

Furthermore, the values of correlation obtained between the morphometric parameters and indices using the two methods (Bowman et al., 2009, Table 4.8; Fellowes et al., 2019, Table 4.9) show a significant high positive correlation between:

- The headlands spacing R_o and the length of the embayment S_1 (R = 0.87 and 0.87), the length of the emerged beach S_2 (R = 0.93 and 0.92) and the area of the embayment A_e (R = 0.80 and 0.82).
- The area of the embayment A_e and the length of the embayment S_1 (R = 0.91 and 0.91) and the length of the emerged beach S_2 (R = 0.76 and 0.76).
- The bay indentation a and the length of the embayment S_1 (R = 0.81 and 0.81).
- The Platform Index (I) and the Embayment Morphometric Parameter (γ_e) (R = 0.89 and 0.89).

Conversely, the correlation values for the maximum width of the emerged beach B_w and length of the shaded zone S_3 (considering both directions *Dir1* and *Dir2*) were not as high as those observed for the other morphometric parameters (Table 4.8; Table 4.9). Although these two parameters (B_w and S_3) vary with the degree of embaymentisation (Table 4.3; Table 4.4), the correlation results suggest that they are not suitable as standalone parameters for defining or classifying the embayment classes of beaches.

Overall, the values of morphometric parameters obtained, and their correlation values, have been essential for estimating the morphometric characteristics of embayments and the "degree of protection" of beaches. In this context, the configuration of headlands plays a crucial role: when headlands are arranged in a convergent configuration and/or are closely spaced, they can contribute to dissipate the energy of incoming waves (Fellowes et al., 2019). In this context, beaches with a high degree of embaymentisation could be better protected than those with a lower degree (Usai et al., 2024). This observation is supported by the obtained values of S_3 considering the main wave directions for each sector, which show that beaches with high degree of embaymentisation typically show shadow zone lengths exceeding 60%, whereas beaches with low degree of embaymentisation show values of S_3 below 10%. Therefore, a higher percentage of shadow zone length could be considered as an indicator of greater beach protection from incoming waves, mainly due to the reduced spacing between headlands.

Table 4.8

Values of correlation (R) for each morphometric parameters and indices, based on the methodological approach suggested by Bowman et al. (2009). Upward arrows (↑) indicate strong correlation ($R^2 > 0.70$), while the bold and underlined values denote statistically significant correlation. Values of correlation were calculated according to the Pearson correlation, considering a significance level of $p < 0.01$.

	I	γ_e	S_2/S_1	***a***	R_o	S_1	S_2	S_3 (*Dir1*)	S_3 (*Dir2*)	A_e	B_w
I	-	**0.89 (↑)**	**-0.61**	**0.36**	**-0.41**	-0.04	**-0.38**	**0.41**	**0.55**	-0.08	0.03
γ_e	**0.89 (↑)**	-	**-0.76**	0.26	**-0.53**	-0.18	**-0.55**	**0.49**	**0.48**	-0.18	-0.11
S_2/S_1	**-0.61**	**0.76**	-	-0.14	**0.51**	0.19	**0.68**	**-0.48**	**-0.35**	0.21	0.19
a	**0.36**	0.26	-0.14	-	**0.47**	**0.81 (↑)**	**0.36**	-0.01	-0.16	**0.82 (↑)**	**0.37**
R_o	**-0.41**	**-0.53**	**0.51**	**0.47**	-	**0.87 (↑)**	**0.93 (↑)**	**-0.37**	**-0.40**	**0.80 (↑)**	0.30
S_1	-0.04	-0.18	0.19	**0.81 (↑)**	**0.87 (↑)**	-	**0.76**	-0.22	-0.23	**0.91 (↑)**	**0.40**
S_2	**-0.38**	**-0.55**	**0.68**	**0.36**	**0.93 (↑)**	**0.76**	-	**-0.36**	**-0.31**	**0.72**	**0.32**
S_3 (*Dir1*)	**0.41**	**0.49**	**-0.48**	-0.01	**-0.37**	-0.22	**-0.36**	-	0.20	-0.20	-0.11
S_3 (*Dir2*)	**0.55**	**0.48**	**-0.35**	-0.16	**-0.40**	-0.23	**-0.31**	0.20	-	**-0.32**	-0.11
A_e	-0.08	-0.18	0.21	**0.82 (↑)**	**0.80 (↑)**	**0.91 (↑)**	**0.72**	-0.20	**-0.32**	-	**0.35**
B_w	0.03	-0.11	0.19	**0.37**	0.30	**0.40**	**0.32**	-0.11	-0.11	**0.35**	-

Table 4.9

Values of correlation (R) for each morphometric parameters and indices, based on the methodological approach suggested by Fellowes et al. (2019). Upward arrows (↑) indicate strong correlation ($R^2 > 0.70$), while the bold and underlined values denote statistically significant correlation. Values of correlation were calculated according to the Pearson correlation, considering a significance level of $p < 0.01$.

	I	γ_e	S_2/S_1	***a***	R_o	S_1	S_2	S_3 (*Dir1*)	S_3 (*Dir2*)	A_e	B_w
I	-	**0.89 (↑)**	**-0.55**	**0.31**	**-0.44**	-0.09	**-0.36**	**0.36**	**0.54**	-0.13	0.10
γ_e	**0.89 (↑)**	-	**-0.71**	0.19	**-0.57**	-0.25	**-0.55**	**0.40**	**0.48**	-0.24	-0.02
S_2/S_1	**-0.55**	**0.71**	-	-0.09	**0.51**	0.25	**0.68**	**-0.50**	**-0.32**	0.26	0.24
a	**0.31**	0.19	-0.09	-	**0.48**	**0.81 (↑)**	**0.41**	-0.01	-0.14	**0.81 (↑)**	**0.47**
R_o	**-0.44**	**-0.57**	**0.51**	**0.48**	-	**0.87 (↑)**	**0.92 (↑)**	**-0.37**	**-0.39**	**0.82 (↑)**	0.30
S_1	-0.09	-0.25	0.25	**0.81 (↑)**	**0.87 (↑)**	-	**0.80 (↑)**	-0.25	-0.22	**0.91 (↑)**	**0.49**
S_2	**-0.36**	**-0.55**	**0.68**	**0.41**	**0.92 (↑)**	**0.80 (↑)**	-	**-0.38**	-0.29	**0.76**	**0.42**
S_3 (*Dir1*)	**0.36**	**0.40**	**-0.50**	-0.01	**-0.37**	-0.25	**-0.38**	-	0.12	-0.21	-0.12
S_3 (*Dir2*)	**0.54**	**0.48**	**-0.32**	-0.14	**-0.39**	-0.22	-0.29	0.12	-	**-0.31**	-0.28
A_e	-0.13	-0.24	0.26	**0.81 (↑)**	**0.82 (↑)**	**0.91 (↑)**	**0.76**	-0.21	**-0.31**	-	**0.40**
B_w	0.10	-0.02	0.24	**0.47**	0.30	**0.49**	**0.42**	-0.12	-0.08	**0.40**	-

4.5.2 Geographical distribution of embayed beaches and their embayment classes

The geographical distribution of the embayment classes along the studied coastline showed that both classification parameters (Platform Index and the Embayment Morphometric Parameter) lead to a consistent distribution of the analysed beaches (Fig. 4.10). However, a more detailed analysis highlighted that the distribution of beaches is more suitable when they are classified with the Embayment Morphometric Parameter (γ_e) (Fig. 4.10b) rather than the Platform Index (I) (Fig. 4.10a). Significant differences were observed in Sectors 1, 2, 10 and the western part of Sector 3, which correspond to the extremities of the studied coastline. The Embayment Morphometric Parameter provided a more consistent grouping of these beaches compared to the Platform Index, despite considering a lower number of embayment classes. The Platform Index appeared more selective, sometimes assigning embayment classes that are higher or lower than those determined using the Embayment Morphometric Parameter.

The geological heritage and geomorphological variability along the studied coastline, combined with the heterogeneity in beach shapes, longshore and cross-shore lengths, strongly influences the geographical distribution of embayment beaches and their corresponding embayment classes. The western and eastern sectors, predominantly characterised by intrusive rocky outcrops (mainly granitoids), feature beaches with a higher degree of embaymentisation, which geometries reflect the geomorphological structures associated with these lithologies. In contrast, the central sectors show a lower degree of embaymentisation, largely due to the presence of flat areas resulting from a tectonic graben structure. As a result, central sectors are dominated by straight beaches with a limited occurrence of rocky headlands.

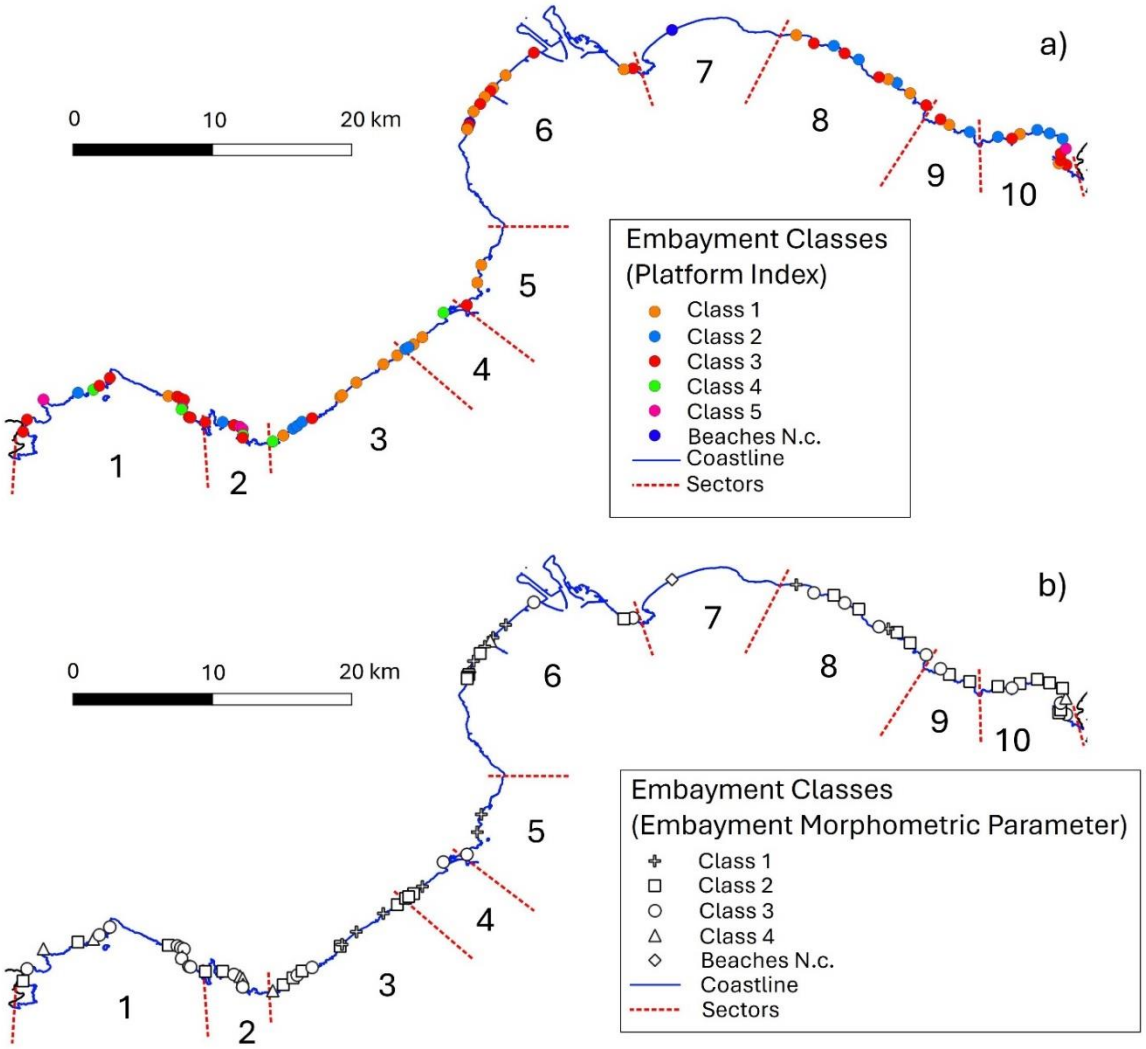

Figure 4.10 - Embayment classes distribution along the investigated coastline, classified using: **(a)** Platform Index (I); **(b)** Embayment Morphometric Parameter (γ_e) (from Usai et al., 2025a).

4.5.3 Types of surf zone circulation on embayed beaches and their geographical distribution

The calculated values of δ' for each beach provided the basis for estimating surf zone circulation types (normal, transitional and cellular) along a coastal stretch featuring different geomorphological characteristics (e.g., shapes and sizes of beach and embayment), wave exposures and breaking wave conditions. The geographical distribution of surf zone circulation types along the studied coastline highlighted a wide variability in values of δ', associated with the H_b equations adopted (Fig. 4.11, 4.12):

- Considering the H_b equation proposed by Short and Masselink (1999), over 50% of the analysed beaches show values of $\delta' > 19$ (Fig. 4.11). These values correspond to a "normal beach circulation", where morphodynamic processes are either not influenced or weakly influenced by the presence of rocky headlands, or are characterised by low significant wave height values (Short, 1996; Short and Masselink, 1999; Castelle and Coco, 2012). Such circulation patterns include rip current systems, as they can develop from other morphodynamic processes (Short, 1996; Castelle et al., 2016). However, it was observed that several beaches with values of $\delta' > 19$ are characterised by the presence of headlands, whose configuration and orientation probably influence their local hydrodynamic processes. As a result, the development of one or more rip current systems within the surf zone may be frequent, particularly where the analysis of aerial orthophotos shows closely spaced headlands and deeply bay indentation. Rip current systems on some beaches analysed along the studied coastal stretch have been reported in earlier studies (De Muro et al., 2016; Buosi et al., 2019a; Porta et al., 2020; Trogu et al., 2020).
- Considering the H_b equation proposed by Komar and Gaughan (1972), approximately less than 30% of the analysed beaches show values of $\delta' > 19$ (Fig. 4.12). In this case, the values of δ' appear more suitable with the identified surf zone circulation types, which show a more uniform distribution along the coastline. However, some beaches still presented values of δ' that outside the ranges defined by Short and Masselink (1999), as also noted in the study of Fellowes et al. (2019). This suggests that the calculated values of δ' tend to either overestimate or underestimate the circulation type within the surf zone and, consequently, the influence of headlands on hydrodynamic processes (particularly in Sectors 1 and 6).

Overall, although the formulation proposed by Short and Masselink (1999) accounts for the effect of embaymentisation, the formulation suggested by Komar and Gaughan (1972), which incorporates a standard correction factor to convert offshore significant wave height H_s into breaking wave height H_b, has proven more effective in estimating surf zone circulation types along the investigated coastline. The integration of real hydrodynamic data (such as velocities and locations of rip current systems), as well as a more detailed analysis of the resulting δ' values, could enhance the understanding of the morphodynamic processes shaping embayed beaches. Additionally, coastal hydrodynamic modelling can be used to estimate whether the predicted circulation types align with those produced by numerical simulations.

These types of analysis are particularly relevant, as the occurrence of rip current systems can lead to significant changes in coastal morphology, including the erosion of dune-systems, beaches and the surf zone, especially during storm events (Loureiro et al.,

2012a; Gallop et al., 2020). In addition, the presence of rip currents may indicate the development of preferential rip channels that facilitate offshore sediment transport. Consequently, classifying surf zone circulation types becomes a valuable tool for identifying all those beaches that are more susceptible to the development of rip currents, information that can be crucial for ensuring the safety of beach users and improving the effectiveness of rescue operations (Castelle et al., 2016).

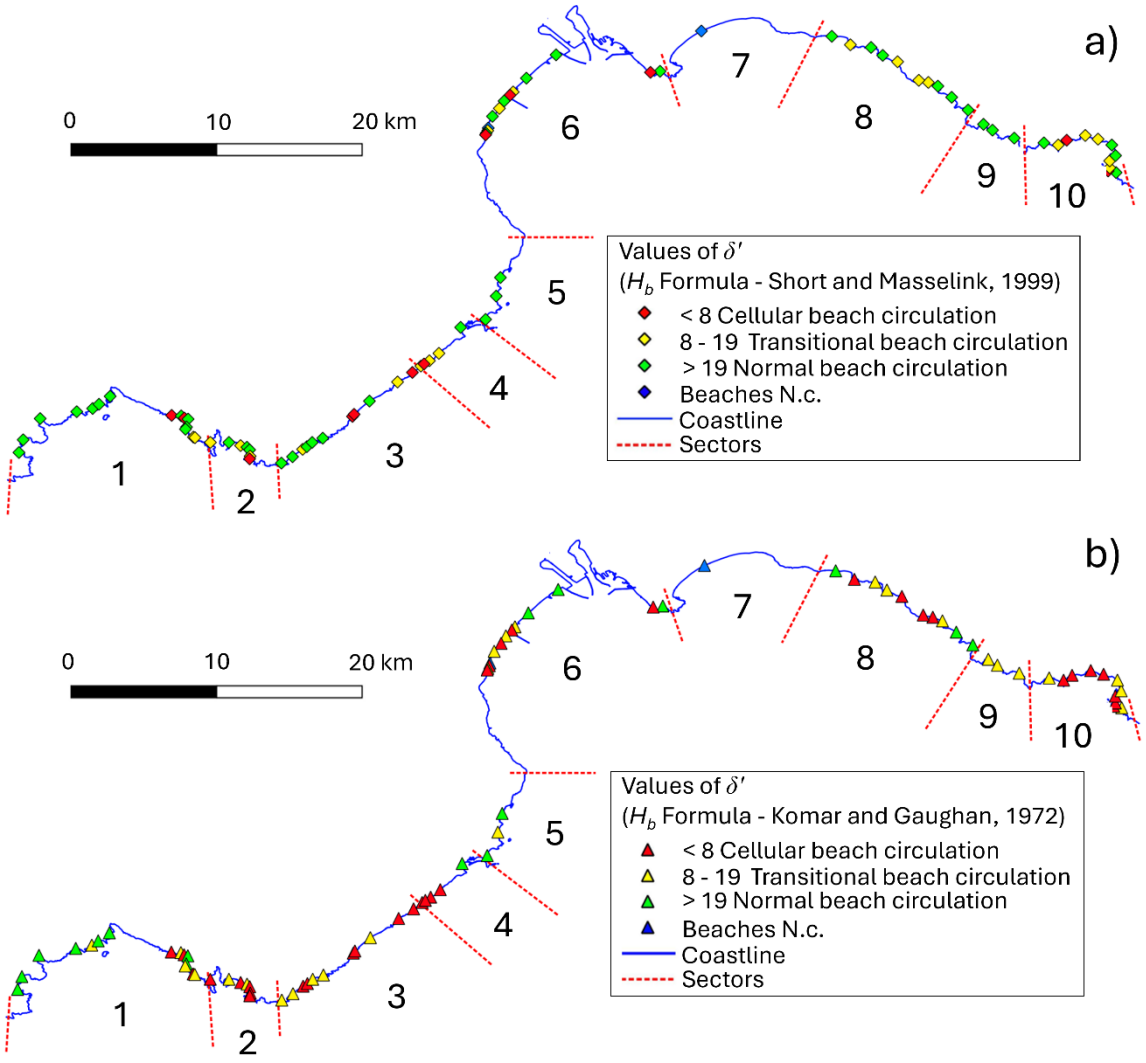

Figure 4.11 - Geographical distribution of surf zone circulation types (range of δ' values) in the studied embayment, classified using the Embayment Morphometric Parameter (Bowman et al., 2009) and the H_b equation suggested by: **(a)** Short and Masselink, 1999 (coloured rhombuses); **(b)** Komar and Gaughan, 1972 (coloured triangles).

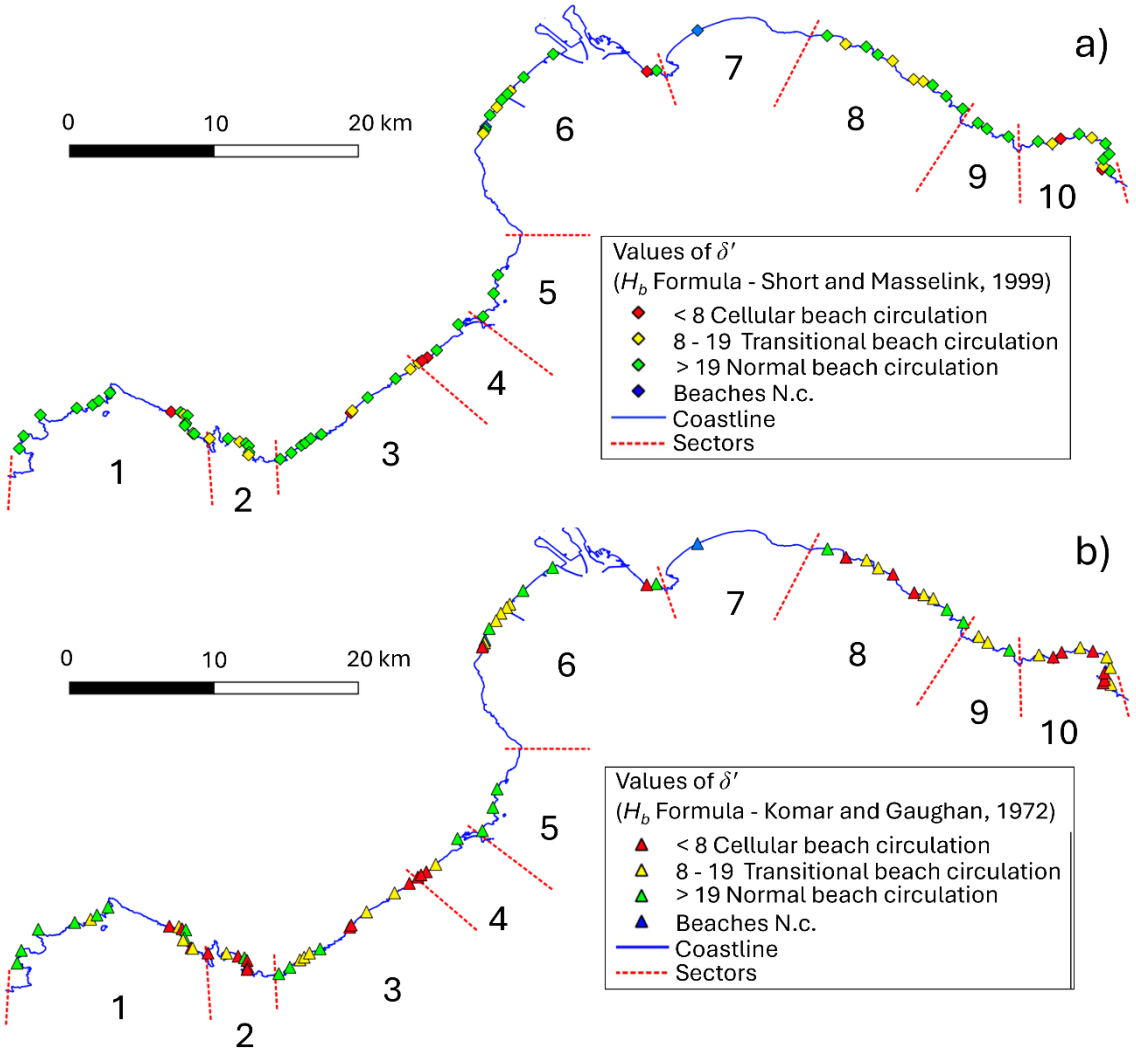

Figure 4.12 - Geographical distribution of surf zone circulation types (range of δ' values) in the studied embayment, classified using the Embayment Morphometric Parameter (Fellowes et al., 2019) and the H_b equation suggested by: **(a)** Short and Masselink, 1999 (coloured rhombuses); **(b)** Komar and Gaughan, 1972 (coloured triangles) (from Usai et al., 2025a).

4.5.4 Types of embayments (Natural and Artificial) and their geographical distribution

The classification of embayments into natural and artificial types highlights the geometric differences based on the calculated morphometric parameters. Figure 4.13 shows the geographical distribution of these embayment types, identifying 20 embayed beaches as “artificial”. These artificial embayments are predominantly located in the central sectors of the study area, which are strongly urbanised due to the proximity of the city of

Cagliari and its hinterland. The flat morphology of these zones has facilitated extensive urban development, resulting in long stretches of predominantly straight beaches.

Analysis of aerial orthophotos reveals that over the past fifty years, the continuity of some of these straight beaches has been significantly altered by the construction of engineering structures (Biondo et al., 2020). As a result, these beaches are segmented by jetties, marinas, and other rigid infrastructures, forming a series of shorter and more embayed beach (e.g., Sector 6). Conversely, where coastal engineering is limited by geomorphological constraints, such as high rocky cliffs, or by distance from urban areas, natural embayments are predominant.

Overall, the morphometric analysis indicates that natural embayments are more common along the studied coast and exhibit a higher degree of embaymentisation than artificial ones. This observation is further supported by the analysis of aerial orthophotos, which show that artificial structures (e.g., breakwaters, harbours, groynes, jetties) are smaller and less massive compared to the natural headlands.

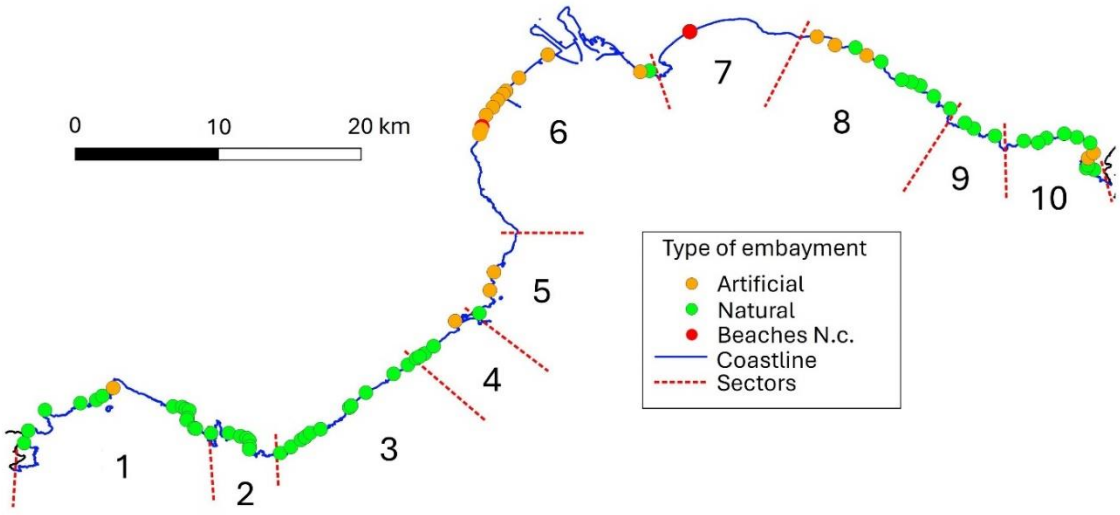

Figure 4.13 - Distribution of embayment types along the studied coastal stretch: natural (green dots); artificial (orange dots) (from Usai et al., 2025a).

4.6 Conclusions

The morphometric analysis and classification comparison carried out in this study led to the geographical distribution of the embaymentisation degrees of a large number of microtidal beaches along the studied coastal stretch, as well as to their main morphometric characteristics. More precisely:

- Detailed geometric analysis of beaches and embayments allowed the association of morphometric parameter values with embayment classes using the two

classification methods considered in this study (Bowman et al., 2009; Fellowes et al., 2019). The Embayment Morphometric Parameter (γ_e) was found to be more suitable for the embayments along the coastal stretch, grouping even those with less curved shapes. Conversely, the Platform Index (I) led to the classification of embayed beaches but sometimes resulted in unexpected class assignments.

- The integration of morphometric parameters and wave data led to the estimation of the "degree of protection" for beaches, facilitating the identification of those less vulnerable to direct wave action and those more exposed. Generally, beaches characterised by a low degree of embaymentisation are typically more exposed to incoming waves, while those with a high degree appear to be better protected (due to the reduced distance of headlands and their influence on coastal hydrodynamics).
- The Non-Dimensional Embayment Scaling Parameter (δ') (Short, 1996; Short and Masselink, 1999), led to an initial estimation of surf zone circulation types influenced by the presence of headlands. However, these estimations did not fully correspond to the embayment characteristics (classes) observed on the analysed beaches. Therefore, further investigation is necessary, integrating field data and numerical modelling. This need is particularly critical in areas where artificial structures have modified the natural hydrodynamic circulation within embayments, as occurred for approximately 25% of the embayments classified as "artificial" in this study.

In conclusion, this study aimed to provide important insights into the behaviour of embayed beaches and their potential responses to artificial and natural pressures (for example, extreme storm events, sea-level rise and climate change). These findings provide a solid scientific basis for improving coastal management and resilience strategies, aiming to protect beach users and preserve beach ecosystems. Increasing human activity on coasts has intensified beach usage and demand for recreational spaces, often leading to the construction of artificial structures that disrupt natural beach continuity. This is especially relevant in Sardinia, located in the central area of Western Mediterranean Sea, where geological features as rocky headlands shape coastal morphology and lead to embayed beach formation. Given the heterogeneity of these coasts, assessing the degree of embaymentisation, as demonstrated in this study, could have wide applications for coastal planning worldwide.

Chapter 5: ANALYSIS OF SHORELINE CHANGES OF 79 MEDITERRANEAN MICROTIDAL BEACHES IN SOUTHERN SARDINIA (ITALY): ACCRETION AND RETREAT TRENDS OVER 70 YEARS

This chapter provides the main findings presented in:

Usai, A.; Trogu, D.; Porta, M.; Demuro, S.; Simeone, S., **2025b**. 70 years of shoreline changes in southern Sardinia (Italy): Retreat and accretion on 79 Mediterranean microtidal beaches. *Water* 17 (17), 2517. https://doi.org/10.3390/w17172517.

5.1 Introduction

Coastal areas represent some of the most dynamic and evolving environments in the world, constantly reshaped by the interplay between natural forces and human activities. These interactions drive and govern key coastal processes such as erosion and sediment accumulation and redistribution (Green et al., 2003). In particular, coastal erosion has become a widespread phenomenon that is expected to accelerate in the coming decades due to a convergence of factors: sea level rise and modification in wave regimes due to climate change, reduced sediment input from rivers and the increasing pressures due to coastal urbanization (Hemer et al., 2013; Luijendijk et al., 2018; Vousdoukas et al., 2020).

Although the Mediterranean Sea is a semi-enclosed basin, it appears highly susceptible to the effects of global climate change (Schroeder et al., 2017). In fact, recent studies have highlighted significant environmental changes in the Mediterranean basin associated with increasing sea temperatures, sea level rise and changes in storm dynamics (e.g., Chefaoui et al., 2018). Nevertheless, due to coastal heterogeneity and limited spatio-temporal data availability, projecting future trends in storm activities, both in terms of frequency and intensity, remains particularly complex in the Mediterranean context (Lionello et al, 2006; Nissen et al., 2010; Casa-Prat and Sierra, 2013; Knutson et al., 2020; Lira-Loarca and Besio, 2020). Since the early 21st century, measurements made using satellite altimetry and tide-gauge networks have revealed a rate of sea level rise in the Mediterranean Sea ranging from approximately 2.5 to 3.6 mm/yr, whit notable variation on a regional scale due to geological factors such as, for example, subsidence processes (Dieng et al., 2021; Sarkar et al, 2022; Pérez Gómez et al., 2022; Meli et al., 2023). The impacts of sea level rise are already evident, particularly in semi-enclosed sub-basins such as the Aegean and Adriatic Sea, as well as along the Tunisian coast, where both the intensity and occurrence of storm events are intensifying (Pérez Gómez et al., 2022). As a result, coastal

flooding in these regions may become more frequent, driven by the combined interaction of wave dynamic, tidal fluctuations and weather conditions.

From an ecological perspective, the Mediterranean Sea is characterised by an important ecosystem composed of extensive meadows of *Posidonia oceanica*, a seagrass species of this region. These meadows support high levels of marine biodiversity by serving as essential nursery areas for numerous species. In addition to their ecological significance, *Posidonia oceanica* meadows contribute to coastal protection by stabilising seabed sediments and dissipating wave energy, as well as improve water quality through oxygen production (Duarte, 1991; Gobert et al, 2006).

Mediterranean beaches, typically characterised by microtidal regimes, are particularly sensitive to slight changes in hydrodynamic conditions or sediment availability, which can result in significant alterations in shoreline position (Armenio et al., 2019; Feyssat et al., 2024). Similarly, embayed beaches (commonly referred to as “pocket beaches”; Bowman et al., 2009) are particularly susceptible to these changes due to their limited sediment exchange with adjacent sandy beaches and minimal sedimentary input from rivers or longshore currents. Embayed beaches are geometrically enclosed by rocky headlands (Short and Masselink, 1999; Gallop et al., 2020) and rely on a delicate interplay between wave dynamics, sediment supply and local topographic features to maintain their morphodynamic equilibrium (Ruessink et al., 2015). In addition, their limited beach cross-shore extension, combined with intense tourism pressures, makes them particularly prone to erosion and loss of coastal habitats.

Research on coastal vulnerability indicate that approximately half of the Mediterranean coastlines, particularly sandy and low-lying beaches, face significant threats from coastal erosion, beach flooding and saltwater intrusion (Le Cozannet et al., 2015; Sarkar et al., 2022; Celata and Gioia, 2024). These physical risks are further intensified by growing socio-economic pressures, such as urban expansion, tourism and infrastructure development. Addressing these complex challenges require adaptive, local-specific coastal management approaches grounded in robust objective data. Evidence-based strategies are essential not only to mitigate the impact of sea level rise but also to enhance the resilience of Mediterranean coastal systems.

The Mediterranean coastline has been extensively reshaped by human activities (Marriner et al., 2010; Ginesu et al., 2012), particularly through the development of tourist facilities, harbours, coastal defences and urban areas. These interventions have significantly altered natural sediment transport along the beaches, contributing to accelerate erosion process on many coastal areas (Porta et al., 2021; Foti et al; 2023). Among recent anthropogenic practices along the studied coastline, a common practice is the extensive removal of *Posidonia oceanica* banquettes using heavy mechanical vehicles (De Falco et al., 2008). These vegetal accumulations (composed mainly of *Posidonia oceanica* leaves, roots,

rhizomes and sand) naturally deposits along the backshore (De Falco et al., 2008). Despite their ecological importance, banquettes are often removed for aesthetics reasons, a practice that further compromising beach stability. In fact, removing banquettes reduces the beach's natural capacity to absorb wave energy, which in turn decreases its resilience, increasing vulnerability to storm impacts and potentially promoting shoreline retreat (Boudouresque et al., 2017; Astier et al., 2020; Simeone et al., 2021; Trogu et al., 2024; Dentamare et al., 2025). Similarly, beach nourishments are often employed as a mitigation strategy (Bitan et al., 2020; Costa et al., 2023), but such intervention can sometimes disrupt the natural dynamics of coastal systems, unintentionally accelerating erosion (Pranzini, 2008). Effective coastal management, therefore, requires an integrated approach that includes long-term shoreline monitoring, spatio-temporal assessments and strategic planning to preserve both the ecological integrity and socio-economic value of Mediterranean beaches.

The combined use of remote sensing tools, GIS-based shoreline analysis and coastal vulnerability indices, has significantly improved the ability to assess coastal hazards and implement region-specific monitoring frameworks, as well as facilitate long-term monitoring (Cenci et al., 2017; Kumar et al., 2019; Chawalit et al., 2025). In fact, central to these methodologies is the detailed reconstruction of historical shoreline movements (accretion and retreat), essential for understanding how coastal morphodynamics evolve (Castedo et al., 2015; Sytnik et al., 2018; Franco-Ochoa et al., 2020; Islam and Crawford, 2022; Fernández-Hernández et al., 2023). Globally, the Digital Shoreline Analysis System (DSAS) (Himmelstoss et al., 2021) stands out as one of the most widely adopted tools for measuring shoreline change, proving effective at different spatio-temporal scales and in a wide range of coastal settings (Kuleli et al., 2011; Kaddour et al., 2020; Pepe et al., 2023; Laksono et al., 2023). While technological advancements have significantly improved the availability of analytical and geospatial tools, many sectors of the Mediterranean coastline remain poorly investigated, leaving scientific gaps in local coastal processes and dynamics.

This study examines shoreline changes along 79 Mediterranean microtidal beaches on the southern coast of Sardinia (Italy) by applying the DSAS tool. Through the analysis of aerial orthophotos ranging from 1954 to 2022, this study quantifies long-term rates of shoreline movement (accretion and retreat), while assessing the role of wave-climatic influences and human intervention in shaping these trends. The findings contribute a detailed database to support informed beach management and conservation strategies, addressing the challenges posed by ongoing environmental changes linked climate change.

5.1.1 Study area

The study area is located in Southern Sardinia (Italy, western Mediterranean Sea), encompassing approximately 130 km of coastline between Cape Teulada and Cape Carbonara (Fig. 5.1). This coastal stretch is characterised by a heterogeneous coastal morphology, comprising both rocky and sandy shores. Overall, 79 microtidal beaches were analysing in this study, showing considerable variability in both longshore and cross-shore length. Some of these beaches can be classified as embayed, showing a curved shape and a high degree of embayment (Usai et al., 2024), while others appear more linear in shape and extend for several kilometres with minimal bay indentation (Usai et al., 2025a). The beaches are predominantly composed of sandy sediments, with grain sizes ranging from fine to coarse. Pebble sediments are also present in some coastal areas, particularly along the western sectors, which contribute to the structural diversity of these beaches.

One of the most distinctive features along the entire coastline is the extensive presence of *Posidonia oceanica* meadows. The upper limit of these meadows varies between beaches, occurring at varying distances from the shore (Vacchi et al., 2017) (Fig. 5.1). This spatial variability results from a combination of factors, including water turbidity, hydrodynamic conditions and seabed morphologies. These seagrass meadows not only support marine life but also contribute significantly to coastal stability by dissipating wave energy and trapping sediment offshore, which enhances the system's resilience to extreme storm events (Vacchi et al., 2017).

Lastly, the study area is characterised by spatial heterogeneity in coastal exposure and wave conditions (Porta et al., 2021; Usai et al., 2024, 2025a; Trogu et al., 2020, 2023), further contributing to the variety of beach morphology and sedimentary processes along the studied coastal stretch.

Along the study area, human activities modified the coastline and its river basins in various ways, largely depending on their distance from main urban centres. The analysed coastal stretch includes several artificial basin (n= 26) and dams (n= 15) (Geoportal of "Regione Autonoma della Sardegna"; https://www.sardegnageoportale.it/accessoaidati/downloaddati), which may influence sediment supply to coastal zone. In addition, along coastal cliff, stabilisation interventions, particularly those using anchored mesh systems, may limit the natural contribution of sediment from rock erosion, thereby altering the sediment to adjacent beaches and their natural balance (Porta et al., 2021). Another widespread anthropogenic impact on coastal systems is the urban development in coastal dune environments. Roads, buildings and infrastructure built on dunes interfered with their natural dynamics, reducing their resilience and ability to recover from human disturbances and increasing the risk of shoreline retreat. Furthermore, the health of *Posidonia oceanica* meadows, especially their upper limits, is also critical to sediment dynamics. In fact, these underwater meadows function as a natural barrier, limiting the offshore transport of

sediment and contributing to coastal stability (De Falco et al., 2000). Significantly degradation or fragmentation of this upper limit, often driven by human activities, compromises the system's ability to maintain morphological balance and buffer high-energy wave conditions, thereby increasing its vulnerability to coastal erosion. Overall, these factors, in combination, could significantly alter sediment dynamics and morphodynamic processes, influencing shoreline configuration and persistence.

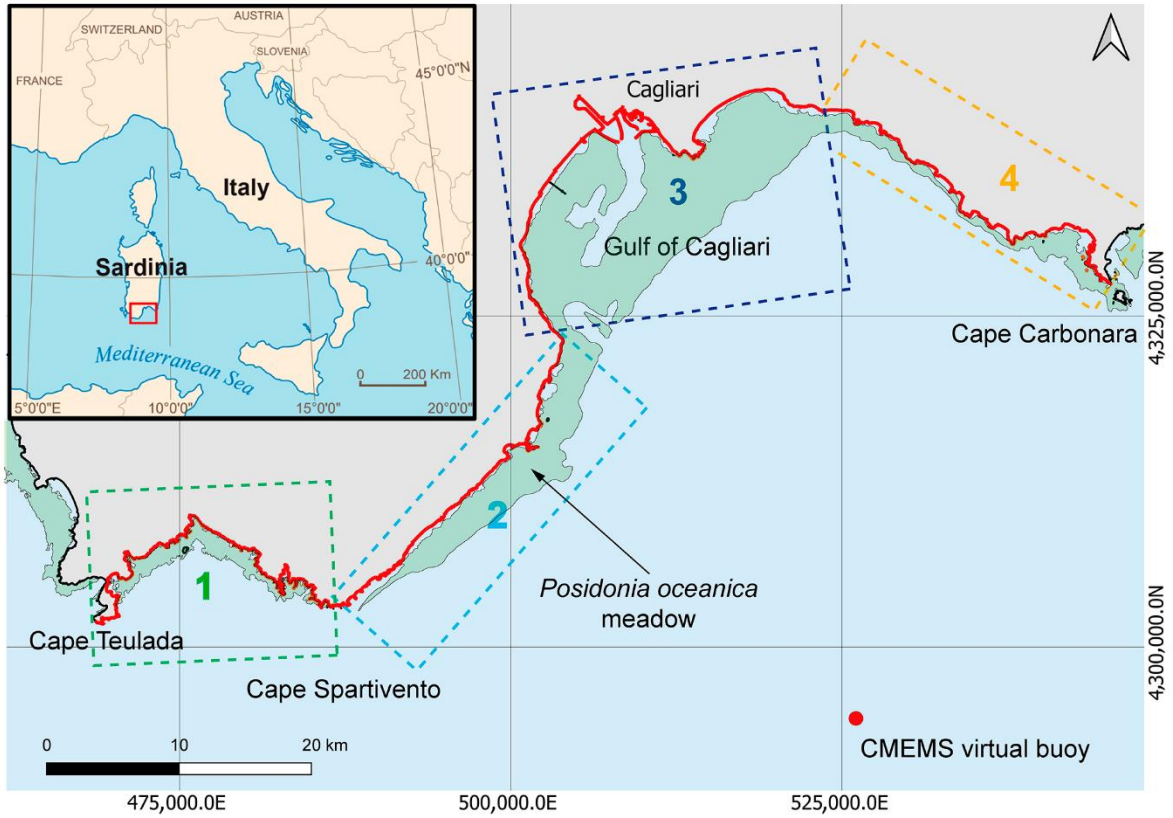

Figure 5.1 - Location of the study area. The red line marks the coastal stretch under investigation (Southern Sardinia - Italy). The *Posidonia oceanica* meadows, shown in green, highlights its distribution and proximity to the coastline. The dashed boxes represent the four sectors into which the coastline was divided for shoreline analysis. The red dot indicates the location of the buoy CMEMS (Copernicus Marine Environment Monitoring Service) used for wave data extraction. (Coordinate system: UTM 32N; Datum: WGS84) (from Usai et al., 2025b).

To support the analysis and interpretation of the obtained data, the studied coastal area was divided into four sectors (Fig. 5.1):

- **Sector 1** covers the coastline between Cape Teulada and Cape Spartivento (green dashed box in Fig. 5.1).
- **Sector 2** continues from Cape Spartivento to the western part of the Gulf of Cagliari (blue dashed box in Fig. 5.1).

- **Sector 3** includes the central area of the Gulf of Cagliari (dark blue dashed box in Fig. 5.1).
- **Sector 4** extends eastward to Cape Carbonara (orange dashed box in Fig. 5.1).

In Sector 1, the coastline is primarily characterised by the presence of embayed beaches. These typically develop within deep rias inlets, which were formed by marine ingression into ancient river valleys (Marini and Murru, 1983). Human intervention along this coastal stretch is limited and mainly concerns a small marina located near a beach to the east of Cape Teulada.

Moving into Sector 2, the shoreline becomes less indented compared to Sector 1. Here, broader beaches alternate with smaller, more sheltered ones. This sector shows greater signs of human impact, evidenced by the presence of coastal engineering structures, such as breakwaters, groynes and jetties, constructed both parallel and perpendicular to the shore.

Sector 3 presents a relatively uniform coastal morphology, primarily composed of long, continuous beaches that are occasionally interrupted by artificial structures. This sector encompasses the urban area of Cagliari, the largest city in Sardinia, and its expanding hinterland, which has experienced significant urban growth over time. Human activities here have significantly altered the landscape through the development of marinas, commercial and recreational ports, piers, breakwaters, and other permanent coastal defence systems. Additionally, beach nourishment projects have further reshaped some parts of the coastline. The presence of transversal groynes and similar coastal engineering structures, aimed at regulating sediment transport and stabilising the coastline, highlights the considerable anthropogenic influence that characterises this central area of the studied coastline (Biondo et al., 2020; Usai et al., 2025a).

Sector 4, similarly to Sector 1, shows small beaches enclosed by rocky headlands, these occasionally alternate with extended stretches of sandy coastline. Significant morphological alterations have also occurred in this sector, largely driven by intense human activities along parts of the shore.

The overall coastal morphology along the study area is largely governed by the local geology. Both Sectors 1 and 4 are predominantly underlain by Palaeozoic intrusive rocks, mainly granites, associated with the Hercynian Basement of Sardinia (Carmignani et al., 2001). Sector 1 also includes metamorphic rock formations (Funedda and Oggiano, 2009). In Sector 2, intrusive rocks continue to dominate, but there is a progressive transition towards Quaternary sedimentary deposits (interrupted by Oligocene-Miocene volcanic rocks) (Carmignani et al., 2001). Finally, the Sector 3 is primarily composed of a more recent post-Hercynian sedimentary cover (Quaternary) (Carmignani et al., 2001).

5.2 Methods

5.2.1 Analysis of shoreline changes

Shoreline evolution, encompassing both retreat and accretion trends, was conducted using the Digital Shoreline Analysis System (DSAS) (Himmelstoss et al., 2021), an add-in of Esri ArcGIS Desktop software (Version 4.10). For each of the 79 microtidal beaches examined in this study, shoreline positions were manually digitalised considering a time series of aerial orthophotos (from 1954 to 2022) available online in the WMS of "Regione Autonoma della Sardegna" (https://webgis.regione.sardegna.it/geoserverraster/ows?service=WMS&request=GetCapabilities).

In line with the methodology adopted by Usai et al. (2024, 2025a), aerial orthophotos were extracted using a spatial grid composed of cells measuring 4 x 4 km, preserving the original pixel resolution of each image. This process resulted in the creation of 11 orthophoto mosaics in GeoTIFF format, each corresponding to a specific year within the study period (1954, 1968, 1977, 1997, 2003, 2008, 2010, 2013, 2016, 2019 and 2022). To enhance the accuracy of shoreline position estimates, all orthophotos underwent manual georeferencing within a GIS environment. The aerial orthophotos of 2008, characterised by the highest resolution and accuracy, was selected as the base reference images. The polynomial transformation method was used during the georeferencing process to reduce spatial discrepancies.

For each year examined in this study, the shoreline positions were manually digitised using QGIS software (Version 3.4.10) at a fixed digitisation scale of 1: 800. The instantaneous waterline was adopted as the shoreline proxy (Boak and Turner, 2005; Thieler et al., 2009) as it was deemed the most appropriate reference given the variable quality and temporal inconsistencies present in some of the earlier orthophoto mosaics (Thieler et al., 2009). It is important to note that shoreline positions are inherently subject to positional uncertainties. These arise from both natural factors, such as wind, wave motion and tidal conditions, and methodological factors, including digitisation errors and inaccuracies related to the georeferencing of the orthophotos (Thieler et al., 2009).

To enhance the precision of the analysis of shoreline changes, the uncertainty associated with each orthophoto mosaic was systematically estimated (Table 5.1). The total positional uncertainty, referred as σ_T, is quantified by the Equation 5.1 (Virdis et al., 2012; Manca et al., 2013; Manno et al., 2017):

$$\sigma_T = \sqrt{\sigma_d^2 + \sigma_p^2 + \sigma_r^2 + \sigma_{co}^2 + \sigma_{wr}^2 + \sigma_{td}^2} \quad (5.1)$$

where:

- σ_d **(Digitisation Error)** calculated as the standard deviation of the residual shoreline position obtained by repeatedly digitising the same shoreline (30 times) within a single aerial orthophotos. This reflects operator-induced shoreline variability during manual digitisation.
- σ_p **(Pixel Error)** corresponds to the spatial resolution of the image (the size of a single pixel), which defines the minimum measurable unit.
- σ_r **(Orthorectification Error)** derived from the root mean square error (RMSE) between image coordinates and corresponding Ground Control Points (GCPs) used during the orthorectification process.
- σ_{co} **(Co-registration Error)** represents the RMSE associated with the alignment of pixels across the multi-temporal image dataset, accounting for residual pixel misalignments.
- σ_{td} **(Tidal Error)** reflects shoreline fluctuation due to natural sea level variations. This component was calculated using the Equation 5.2 (Allan et al., 2003):

$$\sigma_{td} = \frac{VC}{S} \tag{5.2}$$

where *VC* is the vertical change in water level and *S* is the beach slope.

Tidal range data used in this study were obtained from the tide gauge station located at the Port of Cagliari and are available online on the website of "Rete Ondametrica Nazionale - ISPRA" (https://www.mareografico.it/it/stazioni.html). A representative tidal range of 0.35 m was adopted for the entire study area. To estimate the swash zone slope for each beach, high-resolution Digital Terrain Models (DTMs) derived from LiDAR data were analysed. These DTMs are available online in the Geoportal of "Regione Autonoma della Sardegna" (https://www.sardegnageoportale.it/webgis2/sardegnamappe/?map=download_raster) and were originated from LiDAR surveys conducted by the Italian Ministry for the Environment (MATTM) between 2008 and 2009, covering the entire Sardinia coastline. These datasets have a vertical accuracy of 15 cm and a horizontal accuracy of 30 cm. From these DTMs, the slope of each beach profile was calculated, allowing for the estimation of the tidal uncertainty component σ_{td}. For each year of aerial orthophotos considered, the final values of σ_{td} were determined by averaging the individual values obtained for each beach.

- σ_{wr} **(Wave run-up Error)** represents the positional variability of the shoreline caused by the fluctuating wet/dry boundary within the swash zone. This boundary was adopted as a proxy for shoreline position in the multi-temporal analysis. According

to Stockdon et al. (2006), the run-up elevation ($R_{2\%}$) can be estimated empirically by considering the significant deep-water wave height (H_0), the wave period (T) and the beach slope (S). Using offshore wave data from the Copernicus Marine Environment Monitoring Service (CMEMS) (Korres et al., 2021), representative values of H_0 = 0.5 m and T = 1 s were adopted for the study area. Based on the previously derived beach slopes (S) from the DTMs, the values of $R_{2\%}$ was calculated for each beach. This analysis resulted in an average value of $R_{2\%}$ = 0.2 m, which correspond into a mean shoreline positional uncertainty of approximately 1.93 m attributable to wave run-up processes.

Table 5.1

Values of shoreline uncertainties (unit in meters) associated with year of aerial orthophotos considered in this study (from 1954 to 2022).

Year	σ_d	σ_p	σ_r	σ_{co}	σ_{wr}	σ_{td}	σ_T
1954	2.86	0.95	3.23	1.64	1.93	1.35	5.27
1968	1.87	0.50	2.13	1.37	1.93	1.35	3.97
1977	1.37	0.52	2.02	1.32	1.93	1.35	3.67
1997	2.19	0.25	1.72	0.99	1.93	1.35	3.79
2003	1.47	1.00	1.03	1.22	1.93	1.35	3.36
2008	0.45	0.10	0.00	0.00	1.93	1.35	2.40
2010	0.89	0.50	1.39	0.51	1.93	1.35	2.96
2013	0.71	0.50	1.07	0.78	1.93	1.35	2.84
2016	0.48	0.20	1.30	0.50	1.93	1.35	2.79
2019	0.57	0.20	0.92	0.59	1.93	1.35	2.67
2022	0.38	0.20	0.79	0.19	1.93	1.35	2.53

The digitalised shorelines, along with their associated uncertainties, were subsequently analysed using the DSAS tool to estimate values and rates of shoreline retreat and accretion for each studied beach. Specifically, a series of equidistant transects, each 200 m in length and spaced 20 m apart, were generated perpendicular to a user-defined baseline for every beach. For each transect, various statistical indicators were calculated to evaluate shoreline dynamics:

- **Shoreline Change Envelope (SCE)** quantifies the overall extent of shoreline movement by capturing the maximum distance between all recorded shoreline positions throughout the observation period (Manca et al., 2013; Nerves et al., 2024). This indicator provides a non-directional measure of shoreline variability.

- **Net Shoreline Movement (NSM)** indicates the total displacement of the shoreline between the earliest and most recent shoreline positions (Shafique et al., 2024).
- **End Point Rate (EPR)** calculates the rate of shoreline movement by dividing the Net Shoreline Movement (NSM) by the time elapsed between the first and last shoreline records (Akköprü and Taş, 2023; Gharnate et al., 2024).
- **Weighted Linear Regression (WLR)** assigns variable weights to shoreline positions based on both their temporal spacing and associated positional uncertainties (Theieler et al., 2005; Dutta et al., 2022). In the DSAS tool, these weights are typically determined as the inverse of the squared positional error, thereby giving more influence to measurements with higher accuracy. This method enhances the reliability of trend estimation, especially in datasets characterised by variable data quality or inconsistent temporal coverage.
- **Linear Regression Rate (LRR)** derived by fitting a least-squares linear regression line through all shoreline positions, providing an estimate of long-term shoreline movement trends (Baig et al., 2020; Crawford et al., 2020). However, LRR values were deliberately excluded from the result figures to avoid redundancy with WLR results, both being linear regression values.

Additionally, the maximum cross-shore width of each beach was digitised from the 2022 aerial orthophotos. This step aimed to facilitate correlation analyses with the statistical indicators mentioned above.

5.2.2 Analysis of wave storm events

An evaluation of the potential morphodynamic responses of the beach to wave storm impact was conducted through the analysis of wave data from the Copernicus Marine Environment Monitoring Service (CMEMS) (Korres et al., 2021). Specifically, wave data were extracted from a virtual buoy located within an offshore computational grid (red dot in Fig. 5.1). The extracted data cover the period from 1 January 1985 to 31 December 2022 and include wave parameters such as significant wave height (H_s) and wave direction (θ). Wave storm events were detected using the Peak Over Threshold (POT) approach (Mathiesen et al., 1994), which identifies all sea states in which the significant wave height (H_s) exceeds a predefined threshold (1 m) for a minimum continuous duration (6 hours). To avoid counting multiple peaks from the same storm as separate events, peaks occurring within 48 hours of each other were merged into a single event. For each identified storm event, the following parameters were calculated:

- **Maximum significant wave height** (H_{smax}; in meters).
- **Duration of the storm event** (D; in hours).

- **Mean wave direction** (θ; in degrees) calculated using the circular mean equation ($\bar{\theta}$, in degrees) (Equation 5.3) to accurately represent the direction of wave data:

$$\bar{\theta} = \text{atan2}\left(\sum_{i=1}^{n} \sin(\theta_i), \sum_{i=1}^{n} \cos(\theta_i)\right) \tag{5.3}$$

where θ represents the wave direction of each record (in radians). The resulting mean direction was then converted back to degrees and normalised within the interval [0°, 360°].

Finally, the Storm Power Index *Ps* (m²h) (Equation 5.4) (Dolan and Davis, 1994; Karunarathna et al., 2014) was calculated for each storm event identified through Peak Over Threshold (POT) analysis. This index serves as an effective parameter to quantify the storm's strength and depends on the maximum significant wave height (H_s) and the storm duration (D). In this study, the Storm Power Index *Ps* was used as a proxy to estimate the potential erosive power of each event.

$$P_s = H_{smax}^2 D \tag{5.4}$$

where H_{smax} is the maximum significant wave height for each storm event and D is the storm event duration.

5.3 Results and Discussion

Of the coastal stretch examined in this study, approximately 52 km of coastline encompasses the 79 beaches analysed. Based on the DSAS processing, 2573 transects were used for calculating the Shoreline Change Envelope (SCE), Net Shoreline Movement (NSM) and End Point Rate (EPR). However, due to incomplete overlap among the historical shoreline datasets, only 2568 transects were used for the Linear Regression Rate (LRR) and Weighted Linear Regression (WLR) analyses. The statistical results are shown in Tables B.1, B.2, B.3 and B.4 (see Appendix B of the thesis), while the comparison between the values of the SCE and NSM statistical indicators is illustrated in Figure 5.2.

- The SCE analysis indicated an average shoreline variability of 24.1 m along the entire studied coastline, with the highest value observed in Sector 3 (135.4 m; Beach ID 47; Table B.3 - Appendix B) and the lowest in Sector 4 (0.7 m; Beach ID 58; Table B.4 - Appendix B).
- The NSM analysis reveals an average shoreline retreat of -1.47 m along the study area. In total, 1631 transects (representing 63.4% of all transects) exhibit negative displacement values, indicating a net landward movement of the shoreline, while

942 transects (representing 36.6% of all transects) show positive values, corresponding to a shoreline accretion. The most significant retreat was identified in Sector 3 (Beach ID 47; Table B.3 - Appendix B), where the shoreline retreated by -132.2 m. Conversely, the highest accretion occurred in Sector 4 (Beach ID 58; Table B.4 - Appendix B), with a maximum positive displacement of 108.1 m.

- According to the EPR analysis, the shoreline along the study area shows a general condition of stability, with an average rate of -0.02 m/yr. A total of 1631 transects (representing 63.4% of all transects) show a shoreline retreat trend and, within this group, 34.7 % present statistically significant retreat rates (reaching up to -1.9 m/yr in Sector 3; Beach ID 47; Table B.3 - Appendix B). On the other hand, 942 transects (representing 36.6% of all transects) indicate shoreline accretion trends, with 20.5% showing statistically significant positive trends. The highest accretion rate was recorded in Sector 4 (Beach ID 58; Table B.4 - Appendix B), reached 1.59 m/yr.
- The WLR analysis indicates a general condition of stability across the studied coastline, with a mean shoreline change rate of -0.02 m/yr. Despite this overall trend, 67 beaches (84.4%) exhibit negative rates indicative of shoreline retreat, while 12 beaches (15.2%) show positive trends associated with shoreline accretion. Overall, 1708 transects (representing 66.5% of all transects) display a retreating trend, with 23.8% of them showing statistically significant retreat rates. The highest retreat rate was recorded in Sector 3 (Beach ID 47; Table B.3 - Appendix B), reaching -1.59 m/yr. Conversely, 860 transects (33.5%) exhibit accretional trend, and 12% show statistically significant accretion, with the maximum positive rate measured in Sector 4 (1.94 m/yr; Beach ID 58; Table B.4 - Appendix B). When separating natural beaches from those influenced by anthropogenic structures, distinct patterns can be observed: natural beaches present a mean shoreline accretion rate of 0.05 m/yr and a mean retreat rate of -0.07 m/yr. In contrast, anthropised beaches show a mean shoreline accretion rate of 0.22 m/yr and a mean retreat rate of -0.33 m/yr.
- The LRR analysis across the studied coastline reveals an average shoreline change rate of -0.01 m/yr. A total of 1615 transects (representing 62.9% of all transects) exhibit a retreating trend, with 29.1% showing statistically significant rates of retreat. The most pronounced retreat was observed in Sector 3 (Beach ID 47; Table B.3 - Appendix B), with a maximum rate of -1.76 m/yr. Conversely, 953 transects (37.1%) display a trend of shoreline accretion, among which 14.2% demonstrate statistically significant positive rates. The highest accretion rate was identified in Sector 4 (Beach ID 58; Table B.4 - Appendix B), reaching 1.58 m/yr.

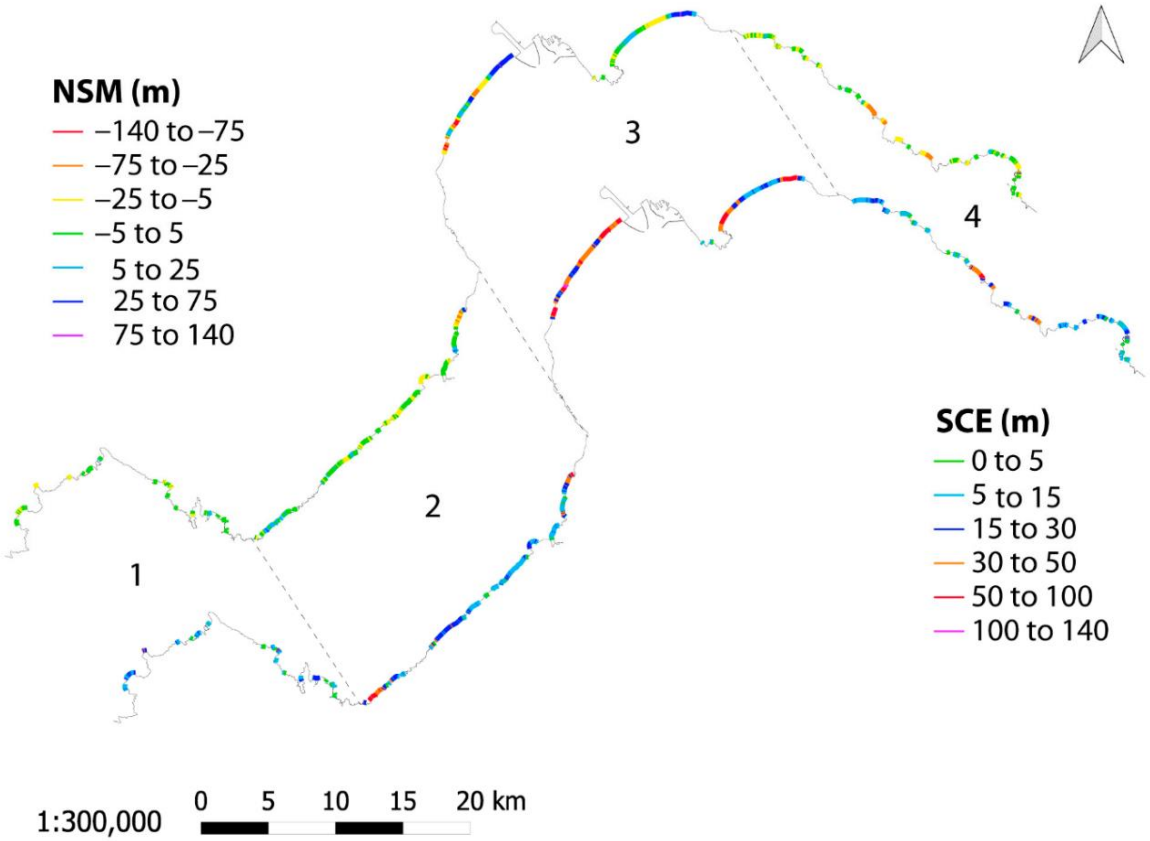

Figure 5.2 - Geographic comparison along the studied coastal stretch between the values of SCE (Shoreline Change Envelope) and NSM (Net Shoreline Movement) (from Usai et al., 2025b).

A comparison between the maximum beach width, extracted from 2022 aerial orthophotos, and the values of Shoreline Change Envelope (SCE) across the studied coastline reveals notable differences between natural and anthropised beaches (represented as green and red dots in Figure 5.3). Beaches affected by artificial structures, such as groynes, harbours and marinas, generally exhibit narrower widths, typically falling within the range of 10 m to 50 m, with only one beach extending to approximately 120 m (Fig. 5.3). In contrast, natural beaches tend to be broader, spanning from approximately 10 m to 70 m, with only two beaches surpassing 100 m in width.

Natural beaches also show lower SCE values, suggesting greater natural resilience and adaptation over time. For natural beaches, a moderate correlation between maximum beach width and SCE values was observed (R^2 = 0.49) (Fig. 5.3). On the other hand, anthropised beaches exhibit greater variability in SCE values and more persistent shoreline changes. No correlation between maximum beach width and SCE values was observed (R^2 = 0.001) (Fig. 5.3). This pattern may be largely due to the influence of artificial coastal structures, which inhibit the natural ability of shoreline to return to its original position. In this study, where SCE values exceeded 60 m, significant shoreline accretions or retreats

were associated with the construction of groynes and harbours, often resulting in long-term alteration to the shoreline's position.

Overall, the results emphasise the necessity of considering human factors when studying shoreline changes, since localised deviations from general shoreline pattern often result from complex interactions that large-scale analysis alone cannot fully explained.

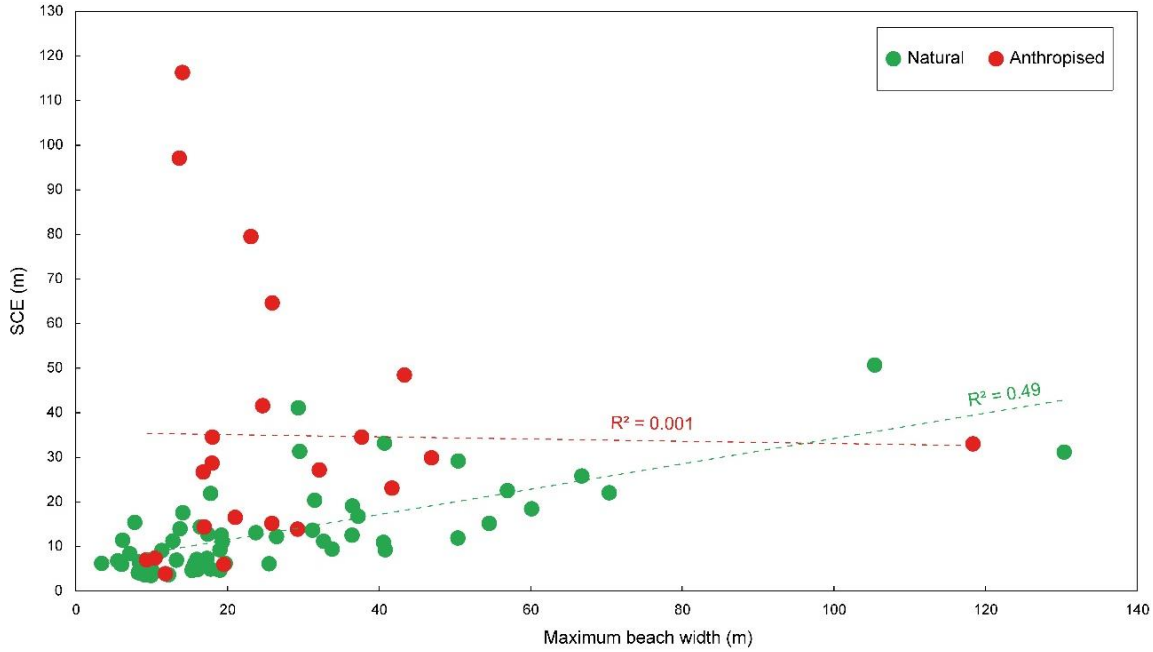

Figure 5.3 - Comparison between Shoreline Change Envelope (SCE) values and maximum beach width values for the 79 analysed microtidal beaches. The graph shows a moderate corelation between natural beaches (green dots) (R^2 = 0.49) and no correlation for anthropised beaches (red dots) (R^2 = 0.001) (from Usai et al., 2025b).

5.3.1 Shoreline changes: Sector 1

Among all the sectors analysed, Sector 1 displays the least anthropogenic changes along the studied coastline, which also correspond with the relativity stability of its beach shorelines. Within this sector, Beaches ID 3, 11 and 17 exhibited the highest SCE values. Figures 5.4 and 5.5 illustrate the values and trends (shoreline accretion and retreat) linked to the SCE, NSM, EPR and WLR statistical indicators.

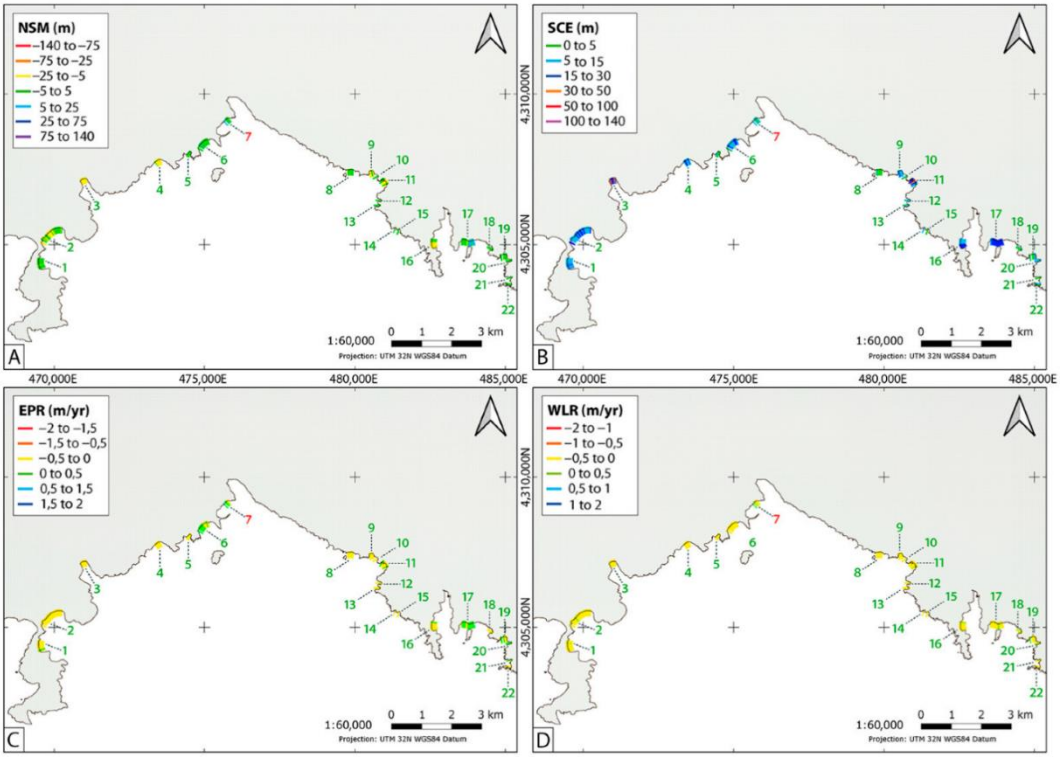

Figure 5.4 - Sector 1: Geographical distribution and values of **(A)** NSM, **(B)** SCE, **(C)** EPR and **(D)** WLR for each transect across the beaches in this sector. The colours of the Beach ID indicate whether the beach is natural (green number) or anthropised (red number). All panels are based on the UTM 32N coordinate system (Datum: WGS84) (from Usai et al., 2025b).

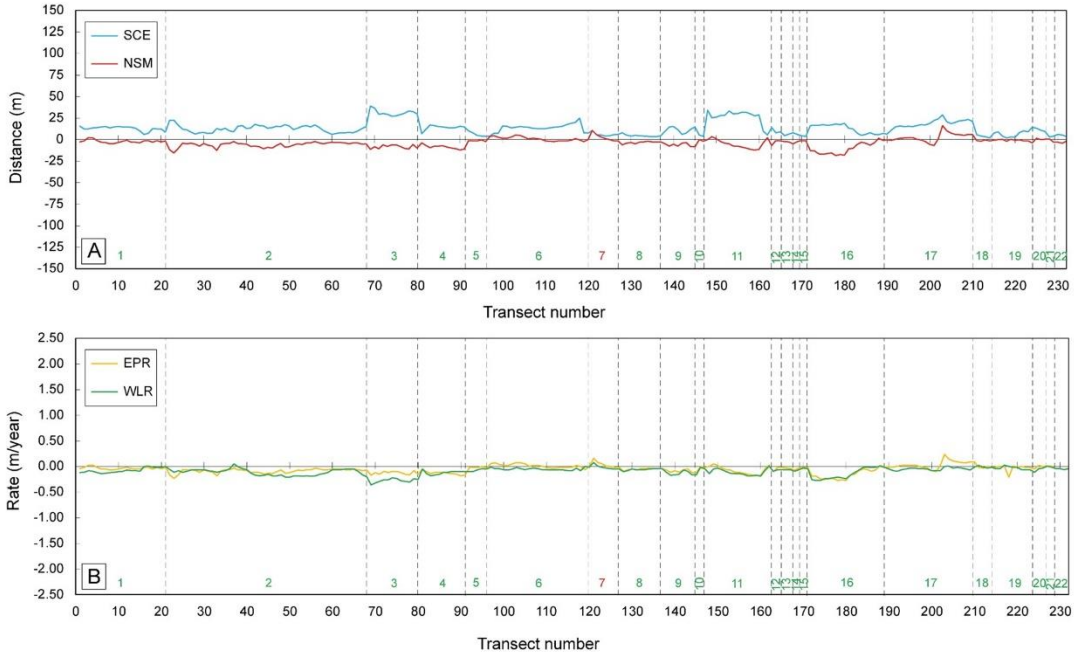

Figure 5.5 - Sector 1: **(A)** SCE and NSM and **(B)** EPR and WLR values for each transect across the beaches in this sector. Beach ID colours indicate the beach type: green for natural and red for anthropised (from Usai et al., 2025b).

At Beach ID 3 (Porto Scudo beach), the shoreline change analysis revealed a high SCE value, along with the most pronounced retreat rate (-0.36 m/yr; WLR) in this sector. This specific retreat pattern appears to be driven by human disturbance, as the beach lies within the military training area of Cape Teulada, active since 1956. The site is periodically used for military exercises with heavy vehicles and amphibious operations, which exert significant pressure on the beach environment (Fig. 5.6A, 5.6B). The analysis of aerial orthophotos highlights the extent of these impacts, showing clear alterations such as the flattening of natural beach's natural forms and the fragmentation of the foredune structure (Fig. 5.6B). These physical changes compromise the beach's geomorphological integrity, limiting its resilience and natural capacity to buffer storm events. The loss of micro-topographic features and dune fragmentation compromise sediment accumulation, making the system increasingly prone to episodic retreat. These interacting factors help clarify the observed rate of shoreline retreat and emphasize the need to account for human influence when assessing coastal stability, particularly in areas that appear largely natural.

In contrast, at Beach ID 11 (Piscinnì beach) the high values of SCE (maximum value 34.1 m) are primarily attributed to the natural dynamics. A key driver of this variability is the cyclical accumulation and erosion of *Posidonia oceanica* remains, or banquettes (Boudouresque et al., 2017; Vacchi et al., 2017), which deposit in large quantities along the shoreline. Historical data from a coastal video monitoring system, operatives since 2011 (see Chapter 2 of the thesis), reveal that, following high-energy storm events capable of reaching the foredune, these banquettes contribute significantly to shoreline position recovery. In fact, some extreme storm events have been followed by shoreline accretion of up to 30 m (Trogu et al., 2020). While this natural mechanism offers protective benefits by reinforcing sections of the foreshore against wave action during storm events, its irregular distribution can leave areas more exposed, shifting wave energy toward unprotected zones and triggering localised erosion. This dynamic may explain the occurrence of positive NSM values at the beach margins, contrasted by slight retreat trends in the central areas.

Ultimately, the significant shoreline changes observed along the Beach ID 17 (Tuerredda beach), which includes both retreating and accretion trend sections, can be linked to its cusped shape. This morphology makes the beach more susceptible to long-term shoreline reorientation, reflected in an average WLR value of -0.04 m/yr.

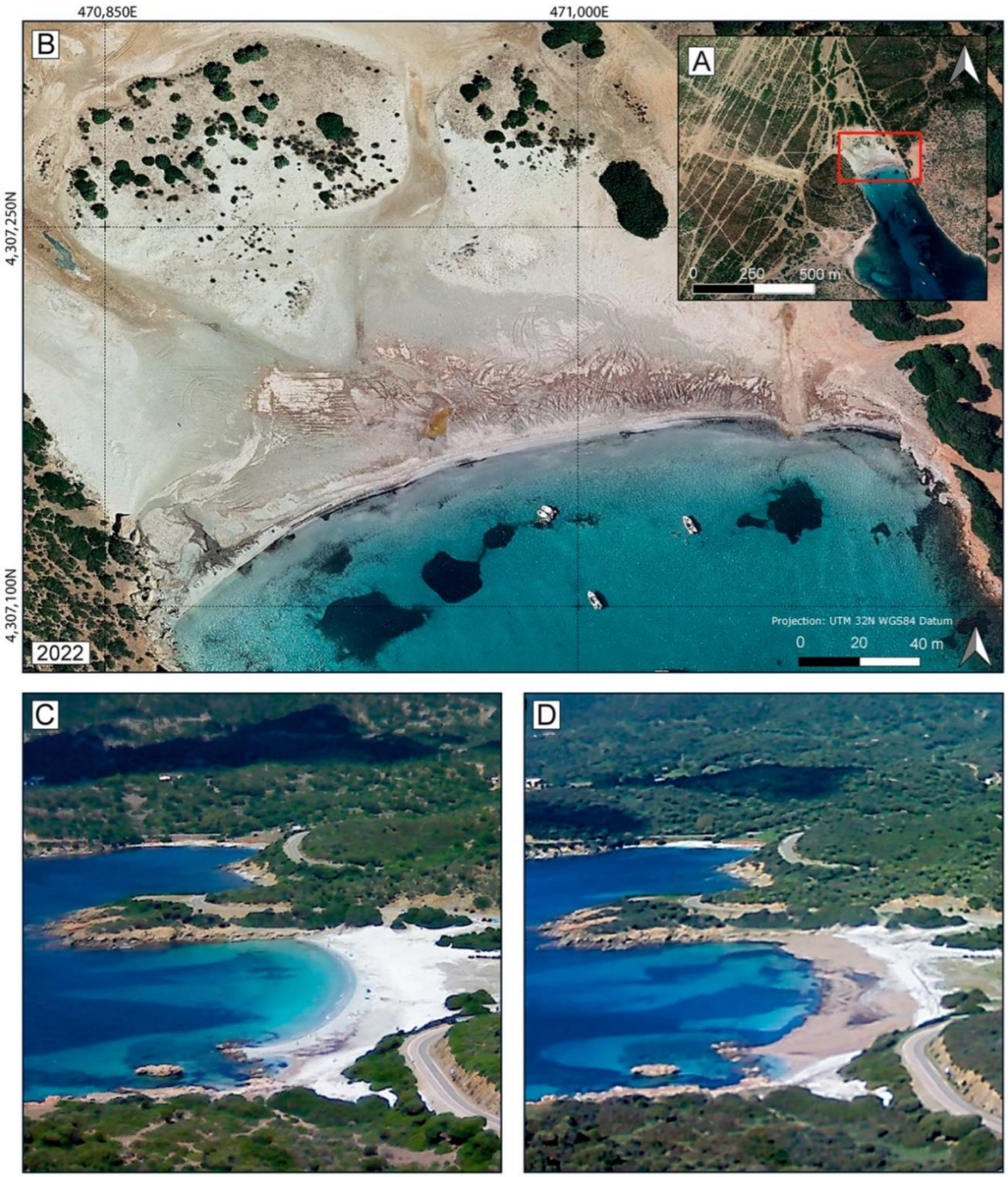

Figure 5.6 - Panels **(A)** and **(B)** show Beach ID 3 (Porto Scudo beach), localised within the military training area of Cape Teulada. The impact of frequent heavy vehicle transit is clearly visible across the dune system. Similarly, the natural features of the beach are entirely flattened when amphibious vehicles land directly on the shore. These panels are based on the aerial orthophotos from the WMS of "Regione Autonoma della Sardegna" (Coordinate system: UTM 32N; Datum: WGS84) (Datum: WGS84). Panels **(C)** and **(D)** show Beach ID 11 (Piscinnì beach) from the coastal video monitoring system and reveal how the accumulation of large *Posidonia oceanica* banquettes contributes to significant shoreline variability along this beach (from Usai et al., 2025b).

5.3.2 Shoreline changes: Sector 2

Sector 2 presents a coastline behaviour similar to that observed in Sector 1, characterised by a general condition of shoreline stability. Figures 5.7 and 5.8 show the corresponding values and trends of shoreline retreat and accretion based on the SCE, NSM, EPR and WLR indicators. Beaches ID 24 and 41 recorded the highest SCE values.

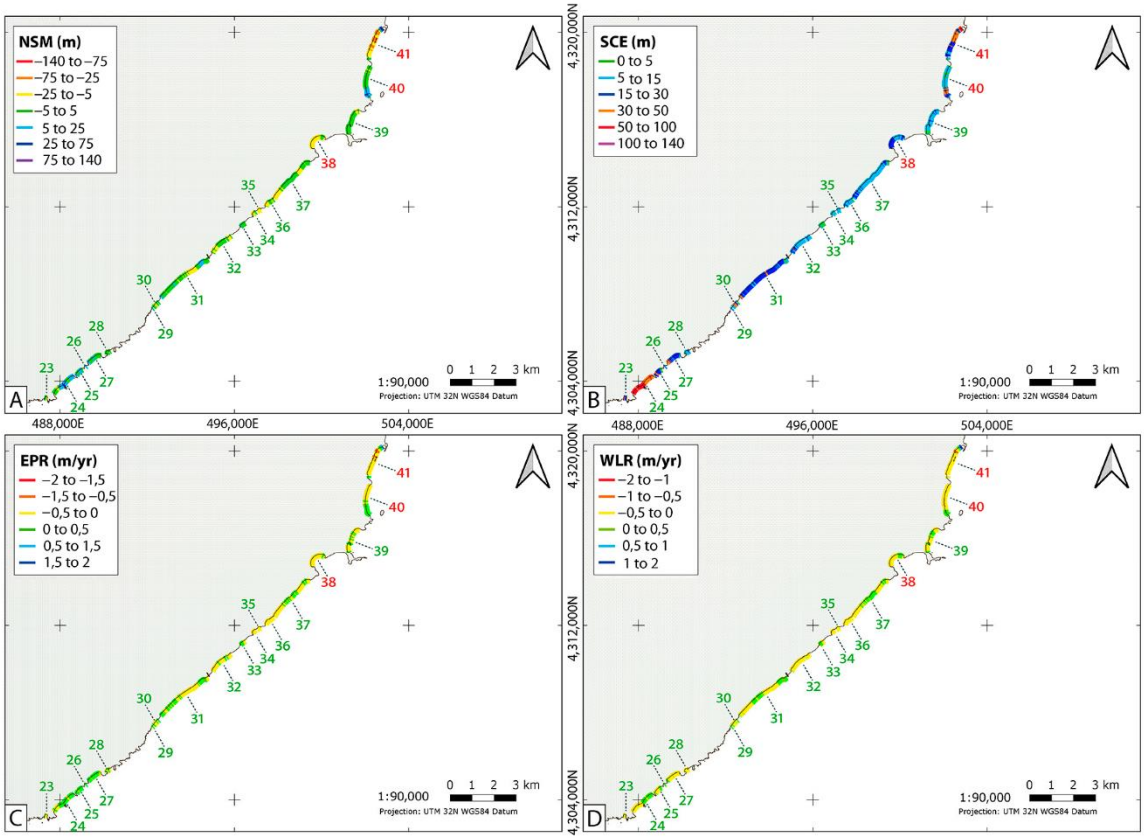

Figure 5.7 - Sector 2: Geographical distribution and values of **A)** NSM, **B)** SCE, **C)** EPR and **(D)** WLR for each transect across the beaches in this sector. The colours of the Beach ID indicate whether the beach is natural (green number) or anthropised (red number). All panels are based on the UTM 32N coordinate system (Datum: WGS84) (from Usai et al., 2025b).

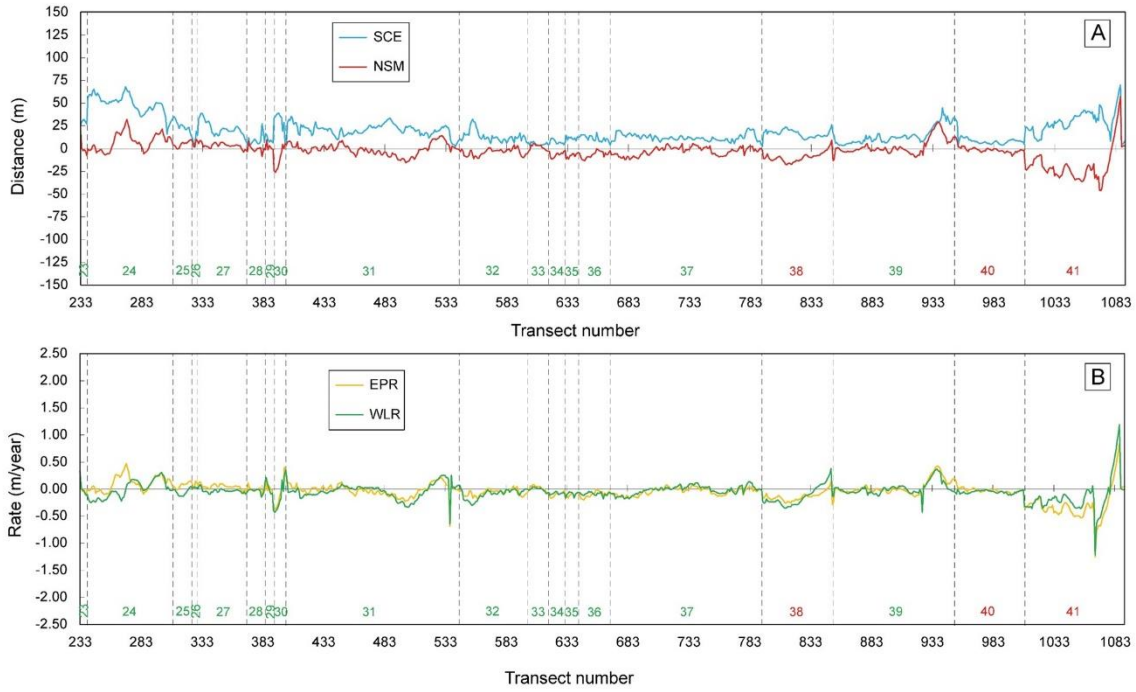

Figure 5.8 - Sector 2: **(A)** SCE and NSM values and **(B)** EPR and WLR values for each transect across the beaches in this sector. Beach ID colours indicate the beach type: green for natural and red for anthropised (from Usai et al., 2025b).

Among the natural beaches in this sector, Beach ID 24 (Su Giudeu beach) shows the highest values of shoreline change: SCE whit a maximum value of 68.0 m, NSM whit a maximum value of 32.0 m and WLR whit a maximum trend of 0.31 m/yr. This high level of shoreline variability could be mainly influenced by three factors: the large volume of sediment stored in the backshore dunes, which acts as a buffer and source for natural sediment redistribution; the beach's distinctive cuspate shape, which makes it more sensitive to changes in wave direction and energy; the intermittent flow from a nearby pond, which varies with rainfall changing the sediment processes and beach hydrodynamics (Fig. 5.9A, 5.9B). As a result, extreme storm events can cause short-term shoreline retreat, also capable of eroding the foredune, as observed in the comparison between the 2008 and 2022 aerial orthophotos (Fig. 5.9A, 5.9B). However, the shoreline has shown a general trend of accretion over the longer period from 1954 to 2022. Despite occasional shoreline retreat, the beach continues to recover over time due to ongoing sediment exchanges and the contribution of foredune systems. This reinforces the value of preserving natural buffers and maintaining the connection between dune systems and the shore in coastal management strategies.

In comparison, Beach ID 41 (Perd'e Sali beach) shows evident transformations resulting from human activity (Fig. 5.9C, 5.9D): 85.5% of transects present negative NSM values, and 48.2% show a statistically significant shoreline retreat based on the WLR statistical indicator. The retreat reaches a maximum NSM value of -46.2 m and a maximum

WLR rate of -1.22 m/yr (Fig. 5.7, 5.8). On the other hand, the eastern extremity of the beach reveals positive trends and values, with shoreline accretion indicated by a maximum NSM value of 57.4 m and a maximum WLR rate of 1.2 m/yr, with 9.6% of transects in statistically significant accretion. This retreat and accretion shoreline patterns is most likely linked to the establishment of a marina and the construction of coastal defence structures, such as groynes aligned parallel to the shore, installed in this sector between 1977 and 1997 (Fig. 5.9D). These artificial structures appear to have interfered with the natural longshore sediment transport processes, potentially leading to sediment trapping and flow disruption. Consequently, areas located downdrift of the structures, deprived of sediment supply, are likely undergoing intensified erosion, whereas zones situated just updrift are experiencing increased sediment accumulation. Moreover, the high level of anthropogenic influence and urban development may be diminishing the beach's natural resilience and recover to high-energy wave events, impeding sediment redistribution and limiting dune system formation. This could contribute to a continued retreating trend, underlining the importance of adopting integrated coastal management strategies that promote sediment connectivity and enhance the system's resilience capacity.

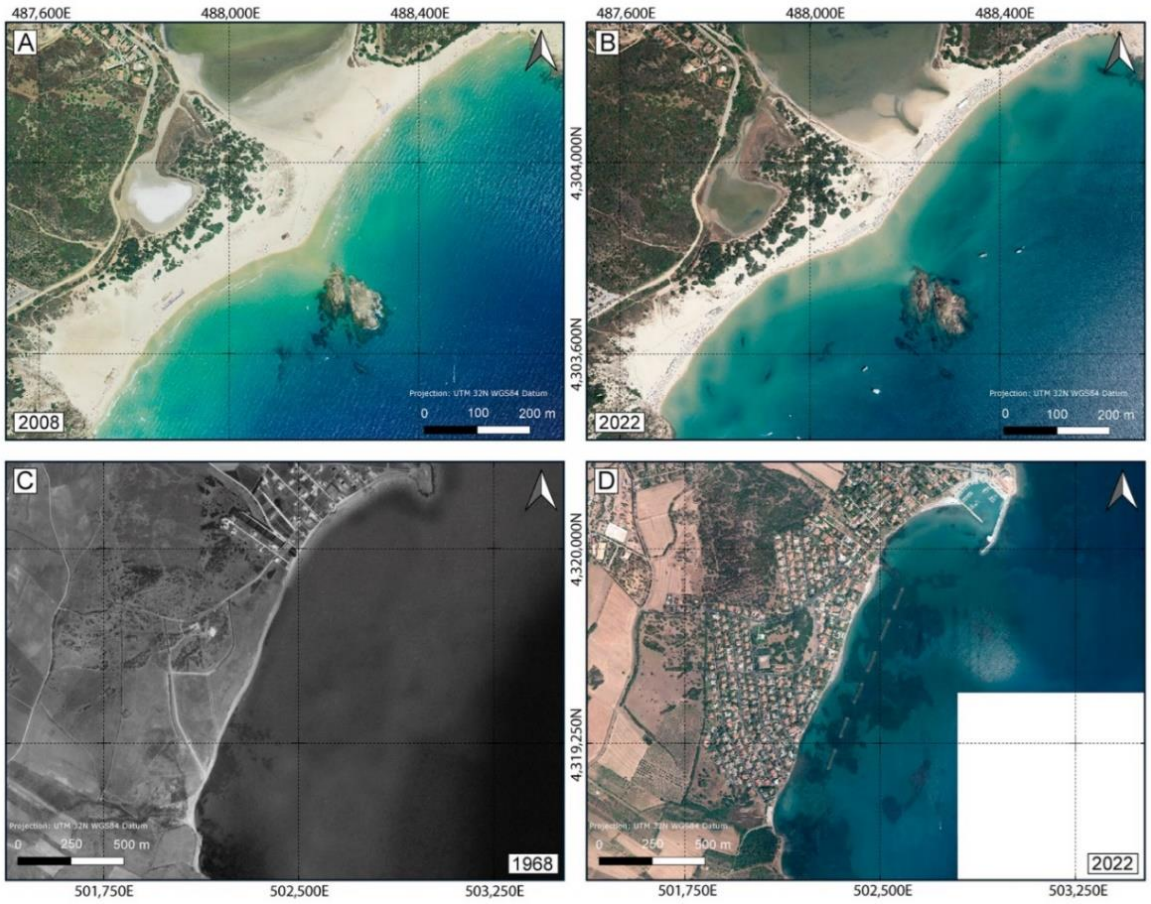

Figure 5.9 - Panels **(A)** and **(B)** show Beach ID 24 (Su Giudeu beach). The beach's cuspate morphology, combined with the substantial sediment stored within its dune system and the presence of a nearby pond, likely contribute to the notable shoreline variability observed here, with some areas showing shoreline accretion and others undergoing retreat. Panels **(C)** and **(D)** show Beach ID 41 (Perd'e Sali beach), where the development of a marina and the placement of groynes aligned parallel to the coast have disrupted local hydrodynamics, resulting in zones of pronounced retreat alongside areas experiencing moderate accretion. All panels are based on the aerial orthophotos from the WMS of "Regione Autonoma della Sardegna" (Coordinate system: UTM 32N; Datum: WGS84) (Datum: WGS84) (from Usai et al., 2025b).

5.3.3 Shoreline changes: Sector 3

Sector 3 presents a coastline behaviour strongly influenced by anthropogenic modifications, the highest compared to the other sectors. It encompasses the metropolitan area of Cagliari (Fig. 5.1), which includes several urban beaches, widespread hard engineering coastal defences and a significant port infrastructure. Figures 5.10 and 5.11 illustrate the values and trends of shoreline accretion and retreat, based on the statistical indicators SCE, NSM, EPR and WLR.

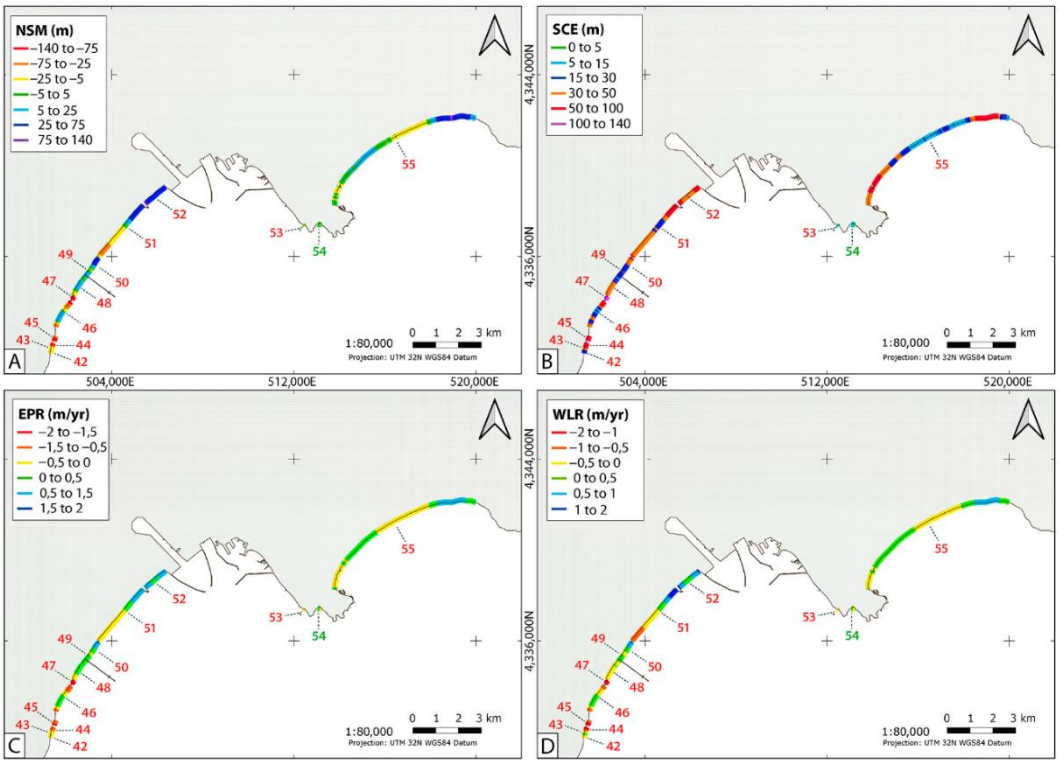

Figure 5.10 - Sector 3: Geographical distribution and values of **(A)** NSM, **(B)** SCE, **(C)** EPR and **(D)** WLR for each transect across the beaches in this sector. The colours of the Beach ID indicate whether the beach is natural (green number) or anthropised (red number). All panels are based on the UTM 32N coordinate system (Datum: WGS84) (from Usai et al., 2025b).

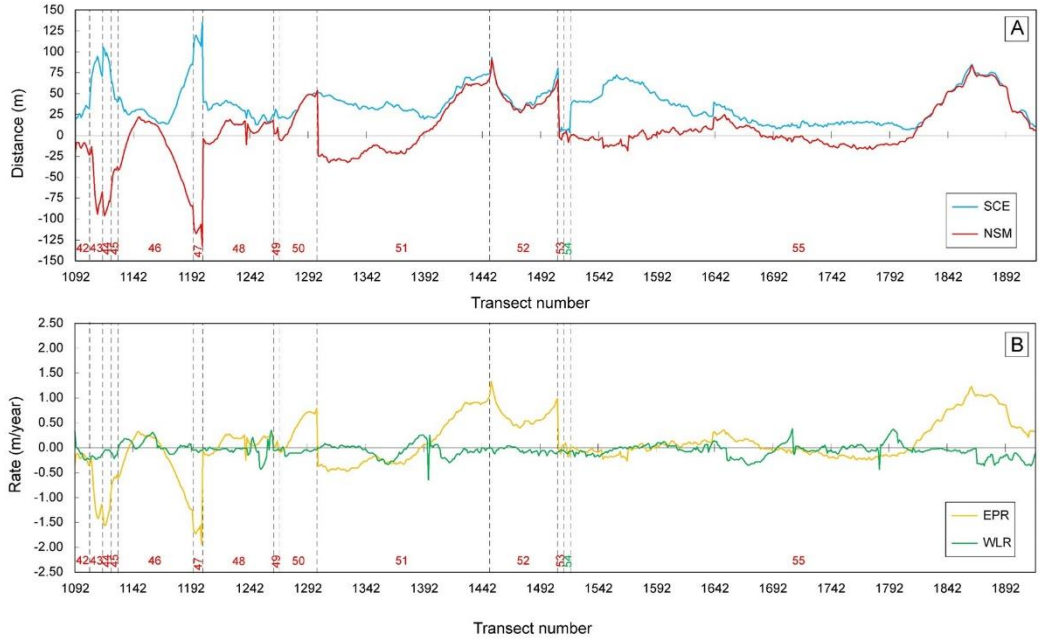

Figure 5.11 - Sector 3: **(A)** SCE and NSM values and **(B)** EPR and WLR values for each transect across the beaches in this sector. Beach ID colours indicate the beach type: green for natural and red for anthropised (from Usai et al., 2025b).

This sector shows the highest SCE values across the entire studied coastline, reaching at Beach ID 47 (La Maddalena beach) with a values of 135.4 m. In this beach, the shoreline changes are further characterised by a minimum NSM of -132.2 m and the lowest WLR rate of -1.6 m/yr (Fig. 5.10, 5.11).

A similar pattern was identified at Beaches ID 43 and 44 (both known as Frutti d'Oro beach), both of which are confined by groynes set oblique to the shoreline. These coastal engineering defences were intended to shield infrastructure and buildings from direct wave action and induced erosion. However, they may have markedly influenced the sediment transport dynamics of this area, potentially disrupting the predominant south to north longshore current (De Muro et al., 2018). Moreover, these groynes may have induced the formation of localised circulation cells, which trap and redirect sediment flows. This disruption has contributed to the gradual degradation of the beach areas enclosed by these structures, leading to a steady loss of sediment and a notable retreat of the shoreline (Fig. 5.12A, 5.12B). In fact, Beaches ID 43 and 44 recorded maximum SCE values of 94.8 m and 105.1 m, respectively, along with minimum NSM values of -94.1 m and -96.1 m, highlighting a pronounced net shoreline retreat. The WLR trends further support these observations, with average retreat rates of -0.78 m/yr for Beach ID 43 and -1.32 m/yr for Beach ID 44.

Another case study of recent shoreline alteration resulting from the construction of rigid coastal infrastructure is shown in Figure 5.12C. This is evident at the boundary between Beaches ID 50 and ID 51, both beaches known as Giorgino beach, where two jetties have been constructed perpendicular to the shoreline to accommodate a channel that links the sea with the adjacent lagoon. These structures disrupt the natural flow of longshore sediment transport, leading to sediment accumulation on the updrift side. This zone displays significant accretion, as demonstrated by the maximum SCE value of 54 m and the corresponding maximum positive NSM value of 54 m at Beach ID 50. In contrast, the downdrift side experiences a notable sediment deficit. As a result, Beach ID 51 records the most pronounced shoreline retreat, with maximum negative NSM values of -32.8 m and SCE values reaching 75.7 m. In response to this ongoing retreat, a seawall was constructed to safeguard the coastal road located between the beach and the lagoon (Biondo et al., 2020; Porta et al., 2021) (Fig. 5.12C). Moreover, the beach in this area lacks the capacity to recover naturally following intense storm events, causing a progressive shoreline retreat. This retreat may be aggravated by the degradation of the *Posidonia oceanica* meadows (stretching from Beach ID 42 to Beach ID 52), whose presence is essential in buffering and mitigating wave energy and reducing sediment loss toward deeper waters.

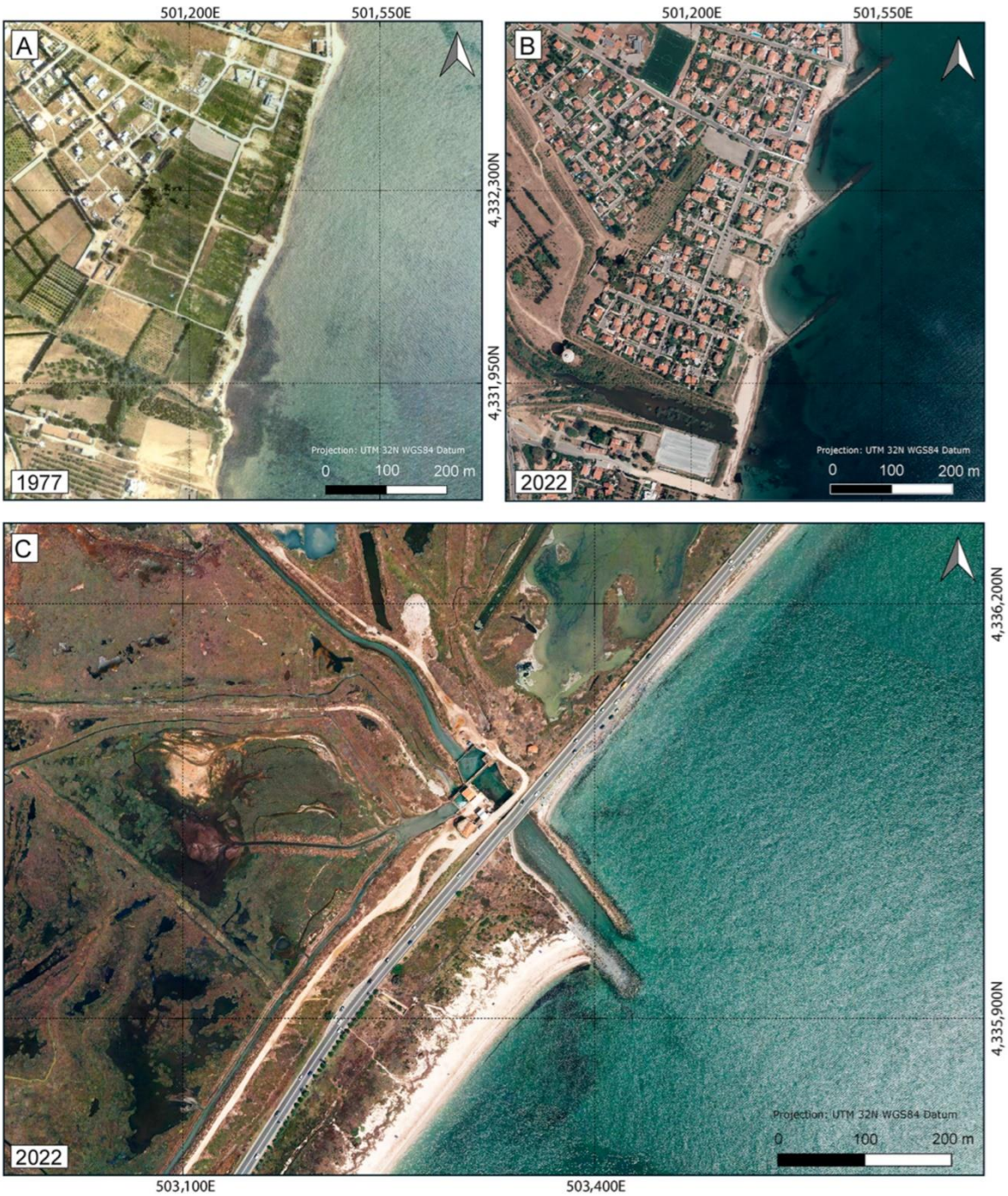

Figure 5.12 - Panels **(A)** and (**B)** show Beach ID 43 and 44 (Frutti d'Oro beach), where the presence of oblique groynes has led to substantial shoreline retreat. Panel **(C)** illustrates the effects of two jetties constructed across Beaches ID 50 and 51 (Giorgino beach), which have disrupted the natural longshore sediment flow. This intervention has resulted in marked shoreline accretion on the updrift side and pronounced retreat on the downdrift side. All panels are based on the aerial orthophotos from the WMS of "Regione Autonoma della Sardegna" (Coordinate system: UTM 32N; Datum: WGS84) (from Usai et al., 2025b).

Finally, within this sector, Beach ID 55 (Poetto beach) has been subject to several artificial modifications (Porta et al., 2021), including a beach nourishment project carried out in the early 2000s. This intervention focused on the south-western area of the beach, particularly near transect no. 1555 (Fig. 5.13), and resulted in a maximum SCE value of 72.4 m and a minimum NSM of -15.4 m within the nourished area (Fig. 5.10, 5.11). Although historical analysis of shoreline positions between 1954 and 1997 (Fig. 5.13D) showed no significant retreat, a beach nourishment was implemented in 2002. Approximately 300,000 m^3 of sand, different in both grain size and composition from the native beach sediment (Ferrara and Palmerini, 1974; Brambilla, 2015), were deposited. The beach nourishment significantly reshaped the beach profile and morphodynamic of the beach (Brambilla, 2015). This artificial sedimentary input caused a rapid and substantial shoreline accretion, exceeding 60 m, clearly visible in aerial orthophotos of 2003. However, this shoreline modification resulted in rapid erosion of the introduced sediment. In just seven years (2010), the beach had retreated by around 50 m from its 2003 extent at transect no. 1555 (Fig. 5.13C, 5.13D). Long-term observations reveal that, approximately twenty years after the intervention, the shoreline had effectively returned to its pre-nourishment position (Fig. 5.13C, 5.13D). The shoreline position of transect no. 1760, positioned centrally along Poetto beach, supports this observation: the shoreline in this area has shown long-term stability, with little to no accretion resulting from the longshore movement of the nourished sediments (Fig. 5.13D). In contrast, transect no. 1880, located in the north-eastern portion of the beach (Fig. 5.13A), exhibited a consistent accretion pattern between 1954 and 1997, after which the shoreline position remained relatively constant (Fig. 5.13D). Nonetheless, to fully understand the mechanisms behind this localised shoreline accretion, further investigations would be necessary.

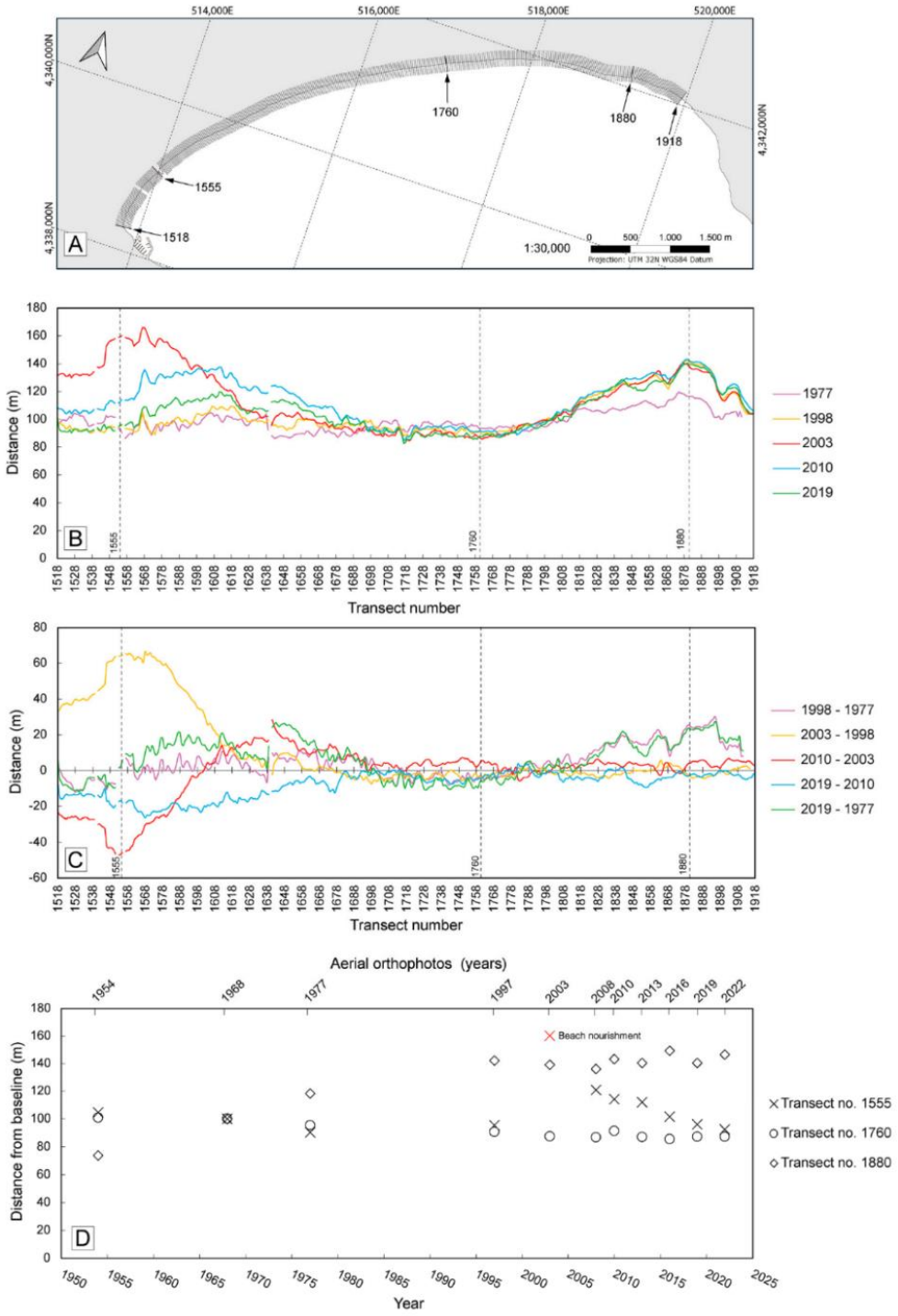

Figure 5.13 - Panel **(A)** illustrates the positions of the transects at Beach ID 55 (Poetto beach) used for calculating DSAS statistical indicators. This panel is based on the UTM 32N coordinate system (Datum: WGS84). Panel **(B)** presents the shoreline's displacement from the baseline across the aerial orthophotos time series analysed in this study, while Panel **(C)** shows shoreline changes over distinct temporal intervals. Panel **(D)** focuses on the temporal variation in shoreline distance from the baseline for 3 selected transects: 1555 (marked with crosses), 1760 (marked with circles), and 1880 (marked with squares) (from Usai et al., 2025b).

5.3.4 Shoreline changes: Sector 4

In Sector 4, anthropic alterations to the coastline are less pronounced compared to those observed in Sector 3. Figures 5.14 and 5.15 show the corresponding values and trends of the statistical indicators (SCE, NSM, EPR and WLR) used to assess shoreline evolution in this sector.

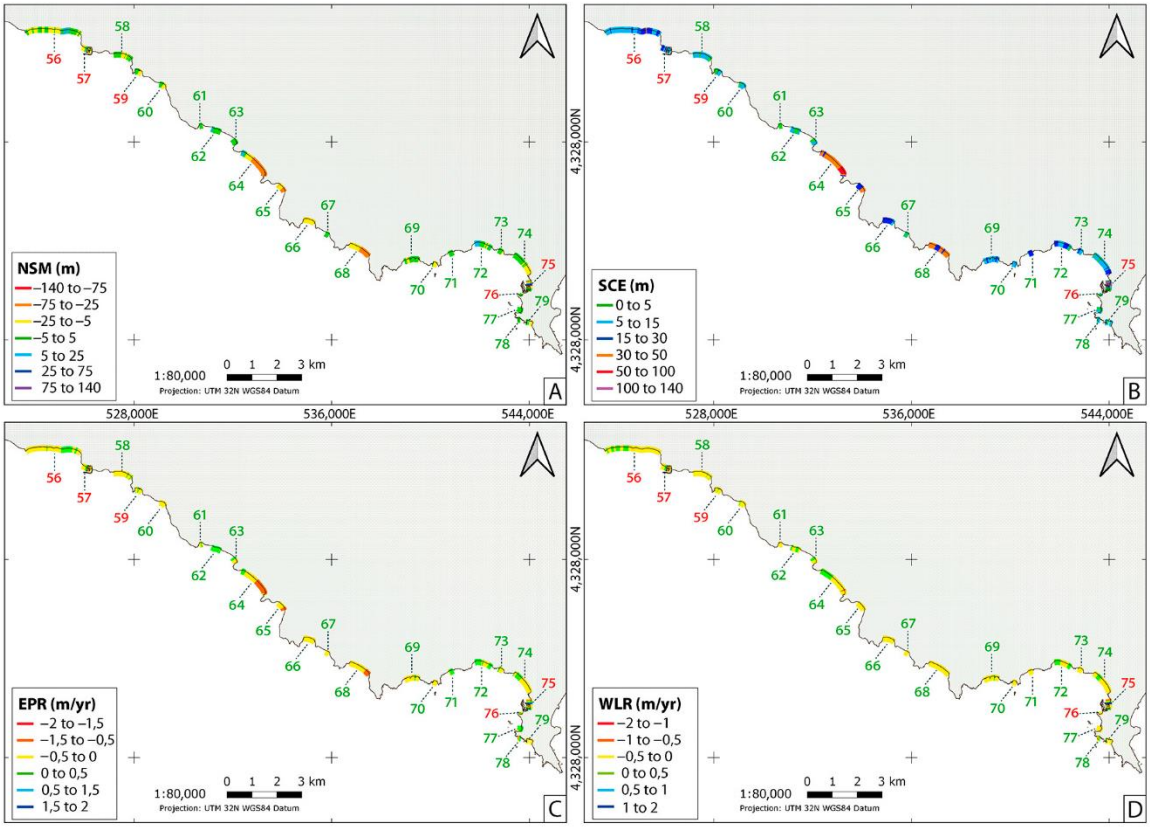

Figure 5.14 - Sector 4: Geographical distribution and values of **(A)** NSM, **(B)** SCE, **(C)** EPR and **(D)** WLR for each transect across the beaches in this sector. The colours of the Beach ID indicate whether the beach is natural (green number) or anthropised (red number). All panels are based on the UTM 32N coordinate system (Datum: WGS84) (from Usai et al., 2025b).

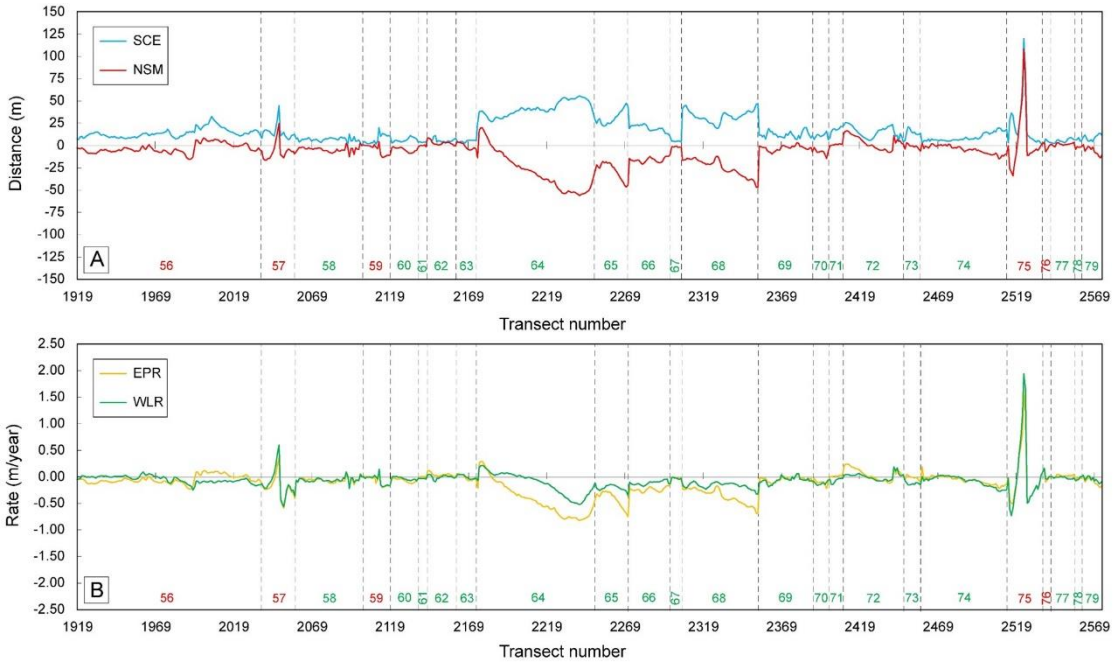

Figure 5.15 - Sector 4: **(A)** SCE and NSM values and **(B)** EPR and WLR values for each transect across the beaches in this sector. Beach ID colours indicate the beach type: green for natural and red for anthropised (from Usai et al., 2025b).

At Beach ID 57 (Capitana beach) and Beach ID 75 (Spiaggia del Riso beach), where coastal alterations are present, maximum SCE values of 44.6 m and 119.9 m, respectively, have been recorded (Fig. 5.14, 5.15). At both beaches, the development or expansion of small marinas has significantly impacted local hydrodynamics, disrupting the natural pathways of sediment transport. These modifications have caused notable alterations in the nearby beach systems: some areas have undergone significant retreat, while others show evidence of localised accretion. This variability highlights how even relatively modest coastal infrastructure can profoundly influence sediment dynamics, especially in coastal areas highly sensitive to changes.

The shoreline evolution observed at Beaches ID 64 (Kal'e Moru beach), 65 (Cann'e Sisa beach), 68 (Solanas beach) and 74 (Campulongu beach) appears to be governed by a different set of controlling processes. These beaches share a comparable shoreline orientation, ranging between 120° N and 135° N, which results in similar exposure to prevailing wave directions (Fig. 5.14). This common wave exposure, however, translates into considerable morphological differences and spatial variability in shoreline evolution. Notably, the south-eastern areas of these beaches display pronounced retreat, with maximum negative NSM values of -55.9 m (in Beach ID 64), - 46.6 m (in Beach ID 65), -47.0 m (in Beach ID 68) and -15.0 m (in Beach ID 74) (Fig. 5.14, 5.15). In contrast, the north-western areas show greater stability, with some locations experiencing only minor retreat or even slight accretion. The NSM values in these areas are of 19.9 m in Beach ID 64, -20.2

m in Beach ID 65, -13.4 m in Beach ID 68 and 2.6 m in Beach ID 74 (Fig. 5.14, 5.15). These divergent trends suggest a complex interaction between wave action and local geological controls, such as the headland configuration that affect the beach dynamics along this coastal stretch.

To better interpret the observed spatial patterns, a Peaks Over Threshold (POT) analysis was performed, focusing on significant storm events. The dataset was derived from a CMEMS virtual buoy, covering the period from 1 January 1985 to 31 December 2022. The Peaks Over Threshold (POT) analysis identified a total of 1161 storm events that exceeded the defined thresholds, corresponding to an average of approximately 31 events per year. The year 1987 emerged as the most intense period, registering 27 storm events with an average Storm Power Index (*Ps*) of 2520 m^2h and a predominant storm direction of 221° N. In contrast, the least intense year was 1994, during which only 36 events were recorded, with a mean *Ps* value of 514 m^2h and an average direction of 248° N.

Storm events predominantly originated from wave directions ranging between 250° N and 290° N, as revealed by the analysis of mean wave directions (Fig. 5.16). These directional sectors not only accounted for the majority of occurrences (447 events, or 38.5% of the total) but were also linked to the most energetic storms, with an average Storm Power Index (*Ps*) of 1279.8 m^2h. The most extreme event in the dataset occurred in January 1987, when the *Ps* value reached 46248 m^2h. This storm was characterised by a mean wave direction of 273° N, a maximum significant wave height (H_s) of 7.3 m and a duration of 861 hours.

In contrast, 158 storm events, accounting for 13.6% of the total, approached from angles ranging between 120° N and 150° N. These events exhibited a lower average Storm Power Index (*Ps*) of 606.2 m^2h. The most intense storm within this directional range occurred between March and April 2022, reaching a *Ps* value of 14,265 m^2h. This event was characterised by a mean wave direction of 139° N, a mean significant wave height (*Hs*) of 3.6 m and a total duration of 1079 hours.

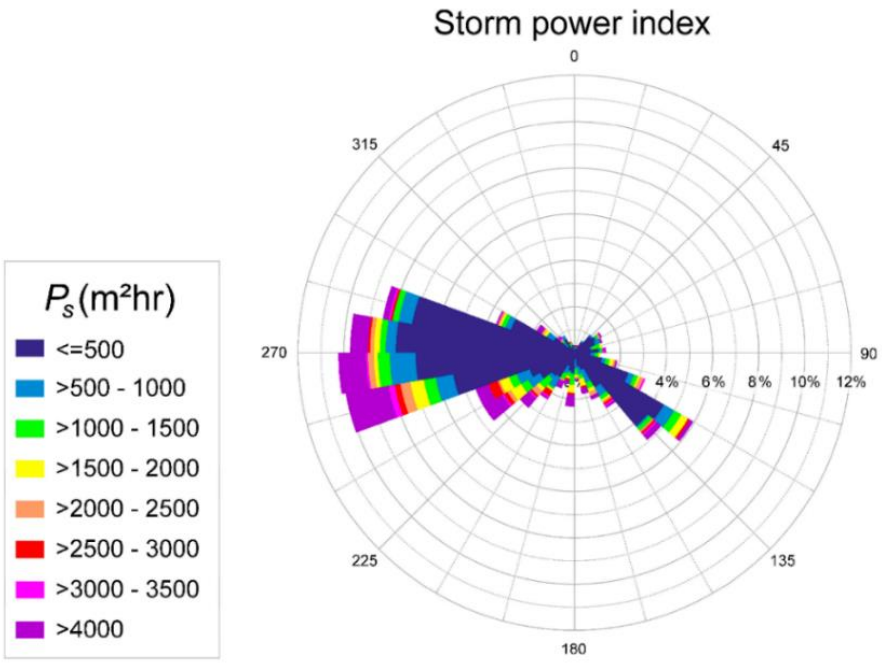

Figure 5.16 - Values of Storm Power Index (*Ps*) and mean wave direction calculated using the Peaks Over Threshold (POT) method for the 1161 storm events identified in the period between 1985 and 2022 (from Usai et al., 2025b).

Coastal morphology, particularly the orientation of headlands, plays a significant role in modulating sediment transport under these wave conditions. Wave-exposed shores tend to undergo retreat, while sheltered areas near the headlands often promote shoreline accretion. This spatial variability in shoreline response is largely governed by the interplay between wave energy, the shape of embayments and local geomorphology. Such interactions enhance longshore current activity, accelerating coastal retreat in high-energy zones, whereas in sheltered areas, wave attenuation promotes shoreline stability (Fig. 5.17).

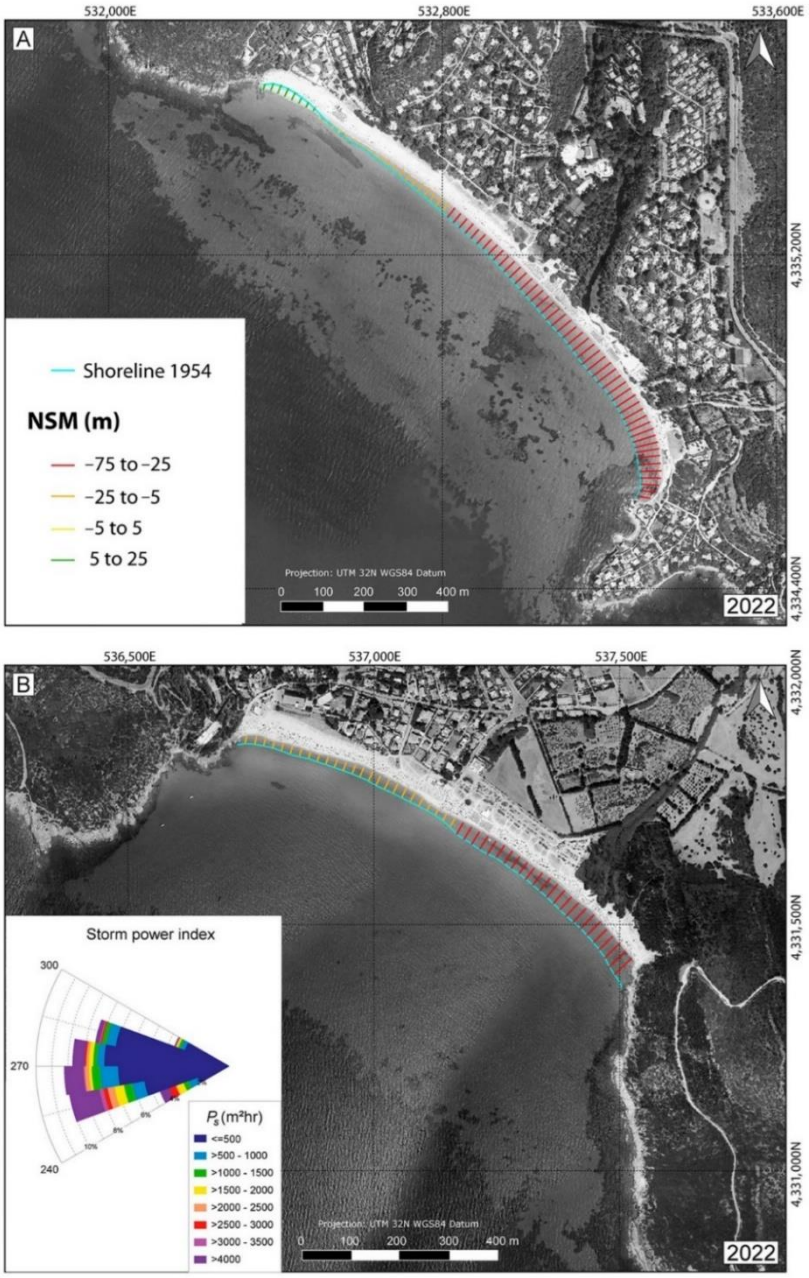

Figure 5.17 - Panels **(A)** and **(B)** illustrate Beach ID 64 (Kal'e Moru beach) and 68 (Solanas beach), respectively. The prevailing wave regime, as indicated by the Storm Power Index (*Ps*), combined with the partial sheltering effect of nearby headlands, contributes to a spatially variable pattern of shoreline change. In both cases, the south-eastern sectors are more exposed to wave energy and consequently exhibit more pronounced shoreline retreat. In contrast, the north-western sectors are more sheltered and generally remain more stable, with limited or negligible retreat. These spatial trends are clearly reflected in the NSM values, visualised by the coloured transects in Panels **(A)** and **(B)**. The blue line represents the shoreline position derived from 1954 aerial orthophotos. All panels are based on the aerial orthophotos from the WMS of "Regione Autonoma della Sardegna" (Coordinate system: UTM 32N; Datum: WGS84) (from Usai et al., 2025b).

Overall, shoreline evolution within the studied coastal area can be influenced by different factors, among which human activities play a significant role. In particular, the expansion of settlements and tourist infrastructure has led to substantial alterations of several dune systems located landward of the beaches (Table B.5 - see Appendix B of the thesis). For example, this is especially evident in the coastal stretch between Beach ID 65 (Cann'e Sisa) and 66 (Genn'e Mari), where a continuous dune field has been entirely replaced by residential buildings. This type of urban expansion likely disrupted sediment connectivity between adjacent dune-beach systems, potentially impacting the long-term dynamics of shoreline evolution. Moreover, the results indicate that the sectors with the greatest shoreline variability correspond to areas with high levels of anthropogenic pressure, primarily from urban and industrial development rather than coastal defence structures. Infrastructure such as roads, piers and ports appear to interfere with natural coastal processes, accelerating and contributing to shoreline retreat.

In addition, several beaches within Sector 3 shows signs of degradation in the *Posidonia oceanica* meadow (Table B.5 - Appendix B). The health and seaward extent of these meadows play a crucial role in modulating coastal hydrodynamics and sediment retention, thereby exerting a strong influence on shoreline stability. In regions where large-scale anthropogenic infrastructure, such as ports and coastal engineering structures, compromises the health of *Posidonia oceanica* meadows, disruptions to coastal processes can be expected, with probable shoreline retreat as a consequence. Consequently, preserving the ecological integrity of *Posidonia oceanica* meadows is important in the context of future coastal developments or interventions. Particular attention should be taken to avoiding infrastructure that may disrupt the natural dynamics and resilience of the coastal system. This is especially critical in areas where the seagrass meadow is well-developed and extend close to the shoreline.

5.4 Conclusions

This study analysed trends in long-term shoreline changes of 79 Mediterranean microtidal beaches along the southern coast of Sardinia, using the Digital Shoreline Analysis System (DSAS) applied to a time series of aerial orthophotos ranging from 1954 to 2022. The analysis reveals significant spatial variability in shoreline dynamics across this coastal stretch, reflecting the interplay of natural factors, local geomorphology, wave conditions and human interventions.

A major insight from the study is the contrast between predominantly natural beaches and those impacted by urbanisation and engineered coastal structures. Beaches with minimal anthropogenic disturbance generally exhibit greater resilience to natural shoreline fluctuations. This resilience is largely attributed to the balance between natural

coastal processes and protective morphology features such as dunes and rocky headlands, which collectively buffer the impacts of intense storm events and pressure driven by climate change.

Conversely, shoreline segments adjacent to urban areas, ports, or protected by rigid structures such as groynes and breakwaters, experience the highest rates of retreat within the study area. While these structures aim to safeguard specific infrastructures or assets, they often disrupt natural longshore sediment transport, resulting in downdrift erosion hotspots and unintended shoreline retreat. The case of nourishment at Poetto beach further illustrates how artificial sediment addition can temporarily alter beach morphology but frequently lacks long-term effectiveness.

Overall, the findings highlight the paramount importance of conserving and enhancing the natural resilience of coastal systems. Key strategies for reducing shoreline retreat risk and adapting to future climate scenarios include protecting natural sediment sources, maintaining healthy dune systems, preserving the ecological integrity of *Posidonia oceanica* meadows and accounting for local wave exposure and sediment transport processes. Where coastal modifications are unavoidable, management approaches must rely on robust, site-specific data and a comprehensive understanding of coastal dynamics.

This study demonstrates how integrating detailed historical shoreline analyses with local morphodynamic insights can provide a strong foundation for developing adaptive and sustainable coastal management strategies. These findings are not only applicable to Sardinia Island but also extend to other microtidal Mediterranean coastlines facing comparable environmental and anthropogenic challenges.

Chapter 6: EFFECTS OF WIND ON THE HYDRODYNAMICS OF RIP CURRENT SYSTEMS IN EMBAYED BEACHES: A THEORETICAL CASE STUDY

This chapter of the thesis presents the main results obtained through hydrodynamic numerical modelling of wave and wind conditions on embayed beaches. These results are also intended for future publication.

6.1 Introduction

Embayed beaches are generally characterised by a curved shape and are laterally bordered by headlands, rocky outcrops or engineering structures (Short and Masselink, 1999; Ojeda et al., 2008). Generally, the morphology of embayed beaches is strongly influenced by the geometry of the headlands (length, width and orientation) (Short, 1996), and therefore by the geological heritage of the coastal stretch (Short, 2010; Gama et al., 2011; Loureiro et al., 2012a; Gallop et al., 2020). In fact, embayed beaches are also defined in the scientific literature as "geologically controlled beaches" (Gallop et al., 2020). Embayed beaches can be affected by different wave exposures and breaking wave conditions (Dingler, 1981; Usai et al., 2024, 2025a), sediment exchange (Simeone et al., 2012) and by the presence of longshore and rip currents (Loureiro et al., 2012a, 2012b; Castelle and Coco, 2012; Fellowes et al., 2019).

Rip currents are narrow channels of water flows generated in the surf zone and directed seawards outside the wave breaking zone (Castelle et al., 2016; MacMahan, 2005; MacMahan et al., 2006). Usually, these flows have a direction normal to shoreline and are controlled by the propagation of incoming waves that subsequently break on the beach (Bowen, 1969; Yu and Slinn, 2003; Castelle et al., 2016). The main forcing factors that lead to the generation of rip currents are the variation in wave conditions and bathymetry along the coastline, which result in different wave breaking patterns (MacMahan, 2005). Rip current velocities increase as the water depth decreases and the wave height increases (Dronen et al., 2002; Haller et al., 2002). Once generated, rip currents can last for sufficiently long periods (hours and/or days) and even reach average velocities of about 0.5-1.0 m/s (MacMahan, 2005; Castelle et al., 2016; Yuan et al., 2023). "Mega rips" have also been measured in embayed beaches with flow velocities of 2 m/s (Short, 1985, 1996). The study of rip current systems, especially in embayed beaches, is critical to improve the safety of beach users, as these currents can pose a fatal hazard to swimmers with hundreds of drownings recorded worldwide (Li and Zhu, 2018; Brewster et al., 2019; Yuan et al., 2023; Rashid et al., 2023; Venkateswarlu et al., 2023; Diez-Fernández et al., 2023).

Laboratory experiments have been conducted to understand the characteristics of rip currents associated with beach morphologies and wave conditions (e.g., Bowen and Inman, 1969; Haller et al., 2002; Dronen et al., 2002; Castelle et al., 2010, Choi and Roh, 2021; Xu et al., 2024). Similarly, a number of studies have used numerical models to simulate and predict the development of rip currents and associated morphology in the surf zone (e.g., Falqués et al., 2000; Caballeria et al., 2002; Castelle and Coco, 2013; Reniers et al., 2009; Castelle et al., 2013; Marchesiello et al., 2015; McCarroll et al., 2015).

Relevant to this study, Castelle and Coco (2012) used a non-linear morphodynamic model to simulate the development and evolution of rip channels in embayed beaches. Their results showed that the characteristics of rip currents depend on the wave conditions, the curvature and long-shore extension of the embayed beach and the shape and cross-shore extension of the headlands bordering the embayment, as also highlighted by Short and Masselink (1999). The numerical model was able to simulate difference types of flow circulation including the case of cellular circulation, when either headland rips or a single rip at the centre of the embayment are present. Their numerical simulations did not take into account the wind effect on sea surface, which we here hypothesize can influence the velocity and direction of rip currents. Also relevant to this study is the work of Kumar et al. (2015), where SWAN and ROMS were coupled and used to simulate coastal dynamics from the mid-shelf to the surf zone. Their results highlight that wind forcing accounts for approximately 50% of the variability observed in the inner-shelf alongshore currents within the modelled domain.

In light of the above results, we focus on simulating cellular circulation patterns within embayed beaches under normally incident wave conditions, comparing scenarios in which wind direction is either onshore or offshore-directed relative to the incoming waves. More precisely, we used a coupled hydrodynamic-wave model (Delft3D) to estimate variations in rip current velocities and circulation patterns within the surf zone. Overall, this study aims to improve the understanding and predictability of rip current system on embayed beaches, as these finding also have important implications for coastal management and the safety of beach users.

6.2 Methods

6.2.1 Hydrodynamic and wave numerical modelling

To investigate how rip current systems develop within embayed beaches, the Delft3D-FLOW (Lesser et al., 2004) and Delft3D-WAVE (Booij et al., 1999; Ris et al., 1999) models were used to simulate the hydrodynamics characteristics of such systems under different wind and wave conditions.

Wave motion in Delft3D-WAVE is described by the SWAN model (Simulating Waves Nearshore) (Booij et al., 1999; Ris et al., 1999), which considers the two-dimensional wave action density spectrum *N* (Equation 6.1), accounting for spatial and directional energy distribution (Booij et al., 1999):

$$\boldsymbol{N(\sigma,\theta) = \frac{E(\sigma,\theta)}{\sigma}} \tag{6.1}$$

where *E* is the wave energy density spectrum; σ is the relative frequency and θ is the wave direction.

More precisely, the evolution of the wave spectrum in the SWAN model is governed by the spectral action balance equation (Booij et al., 1999), which is formulated here in Cartesian coordinates (Equation 6.2) (Hasselmann et al., 1973):

$$\boldsymbol{\frac{\partial}{\partial t}N + \frac{\partial}{\partial x}c_x N + \frac{\partial}{\partial y}c_y N + \frac{\partial}{\partial \sigma}c_\sigma N + \frac{\partial}{\partial \theta}c_\theta N = \frac{S}{\sigma}} \tag{6.2}$$

where *t* is time; *c* is the propagation velocity; *x* and *y* represent the two-dimensional space; σ is the relative frequency; θ is the wave direction and *S* [= $S(\sigma, \theta)$] is the source term.

According to Hasselmann et al. (1973), the source term in the spectral action balance equation is described as follows:

$$\boldsymbol{S = S_{in} + S_{nl} + S_{ds}} \tag{6.3}$$

where S_{in} is the energy input from the atmosphere, specifically the wind contribution (Snyder et al., 1981); S_{nl} is the non-linear transfer due to wave-wave interactions (Hasselmann and Hasselmann, 1985) and S_{ds} is the dissipation term of wave energy (Komen et al., 1984).

In the SWAN model, the wave energy dissipation S_{ds} is described as the summation of three different contributions: whitecapping $S_{ds,w}(\sigma, \theta)$, bottom friction $S_{ds,b}(\sigma, \theta)$ and depth-induced breaking $S_{ds,br}(\sigma, \theta)$ (Deltares, 2024a):

$$\boldsymbol{S_{ds} = S_{ds,w}(\sigma,\theta) + S_{ds,b}(\sigma,\theta) + S_{ds,br}(\sigma,\theta)} \tag{6.4}$$

On the other hand, in the SWAN model the waves growth due to wind occurs through a series of processes (Phillips, 1957; Miles, 1957) summarised in Equation 6.5 (Booij et al., 1999):

$$\boldsymbol{S_{in}(\sigma,\theta) = A + BE(\sigma,\theta)} \tag{6.5}$$

where the coefficients *A* (Cavaleri and Rizzoli, 1981) and *B* (Komen et al., 1984; 1994; WAMDI Group, 1988) are functions of wave direction and frequency, as well as the wind direction and speed.

The coefficient *A* describes the linear growth of the waves, whereas the term *BE* describes the exponential growth of the waves (Deltares, 2024a). The equations used to calculate *A* (Equation 6.6) and *B* (Equation 6.7) are shown below:

$$\boldsymbol{A = \frac{80\,\rho_a^2\,\sigma}{\rho_\omega\,g^2\,k^2}\,C_D^2\,U^4} \tag{6.6}$$

where ρ_a is the air density; ρ_ω is the water density; g is the gravitational acceleration; σ is the relative frequency; k is the wave number vector; C_D is the drag coefficient and U is the wind speed component.

$$\boldsymbol{B = max\left(0, 0.25\,\frac{\rho_a}{\rho_\omega}\left(28\,\frac{U_*}{c_{ph}}cos(\theta-\theta_\omega)-1\right)\right)\sigma} \tag{6.7}$$

where $(\theta - \theta_\omega)$ is the angle between the wind and wave propagation directions; U_* is the friction velocity and c_{ph} is the phase speed of waves. Values of the friction velocity U_* can be calculated using Equation 6.8 (Cavaleri and Rizzoli, 1981; Komen et al., 1984; Deltares, 2024a):

$$\boldsymbol{U_*^2 = C_D U_{10}^2} \tag{6.8}$$

where U_{10} is the wind speed at 10 m elevation above the mean sea surface and C_D is the drag coefficient (e.g. as suggested by Wu, 1982).

In the Delft3D-FLOW model, the depth-averaged hydrodynamic flows are described through the non-linear shallow water equations (Deltares, 2024b). More specifically, the continuity equation is described as:

$$\boldsymbol{\frac{\partial \eta}{\partial t} + \frac{\partial Q_i}{\partial x_i} = 0} \tag{6.9}$$

where η is the mean free surface elevation of the water; t is time and $Q_i=hU_i$ is the volume of water flux (h is the average water depth and U_i the velocity of the mass-flux driven by waves, as suggested by Mei, 1989). The subscript i corresponds to the horizontal coordinate directions: x (alongshore) and y (cross-shore) axis.

On the other hand, the momentum balance equation is described as:

$$\frac{\partial Q_i}{\partial t} + \frac{\partial}{\partial x_j}\left(\frac{Q_i Q_j}{h}\right) + gh\frac{\partial \eta}{\partial x_i} + \frac{1}{\rho_\omega}\frac{\partial S_{ij}}{\partial x_j} - \frac{1}{\rho_\omega}\frac{\partial T_{ij}}{\partial x_j} + \frac{\tau_i^b}{\rho_\omega} + \frac{\tau_i^w}{\rho_\omega} = 0 \quad (6.10)$$

where S_{ij} is the radiation stress tensor (Philipps, 1977); T_{ij} is the lateral mixing term (Battjes, 1975); τ_i^b is the bed shear stress; τ_i^w is the wind shear stress at the sea surface; g is the acceleration due to gravity and ρ_ω is the density of water.

Finally, the wave-induced force was calculated to estimate the variations in wave energy nearshore. In the Delft3D-FLOW model, the wave-induced force F_i is described through the spatial gradient in radiation stress as (Deltares, 2024b):

$$F_i = \frac{\partial S_{ij}}{\partial x_j} \quad (6.11)$$

where S_{ij} is the radiation-stress tensor and x_j is the spatial direction expressed in Cartesian coordinates.

6.2.2 Model configuration

Hydrodynamics processes under different wind and wave conditions were investigated by analysing a simplified embayed beach with a curved shoreline with length L of 500 m (Fig. 6.1). The beach is laterally bordered by non-erodible physical barriers that simulate the presence of headlands, extending 440 m offshore. The adopted bathymetry is very similar to that of Castelle and Coco (2012), consisting of a gently sloping plane (1:30) with depths ranging between 2.5 m and -15 m (Fig. 6.1a). A longshore sandbar is located 60 m from the shoreline, with its crest located 0.8 m below the mean sea level (Fig. 6.1b). Unlike the setup presented in the study by Castelle and Coco (2012), the bathymetric profile is kept fixed in order to exclusively examine the influence of wind forcing on the development and behaviour of rip currents.

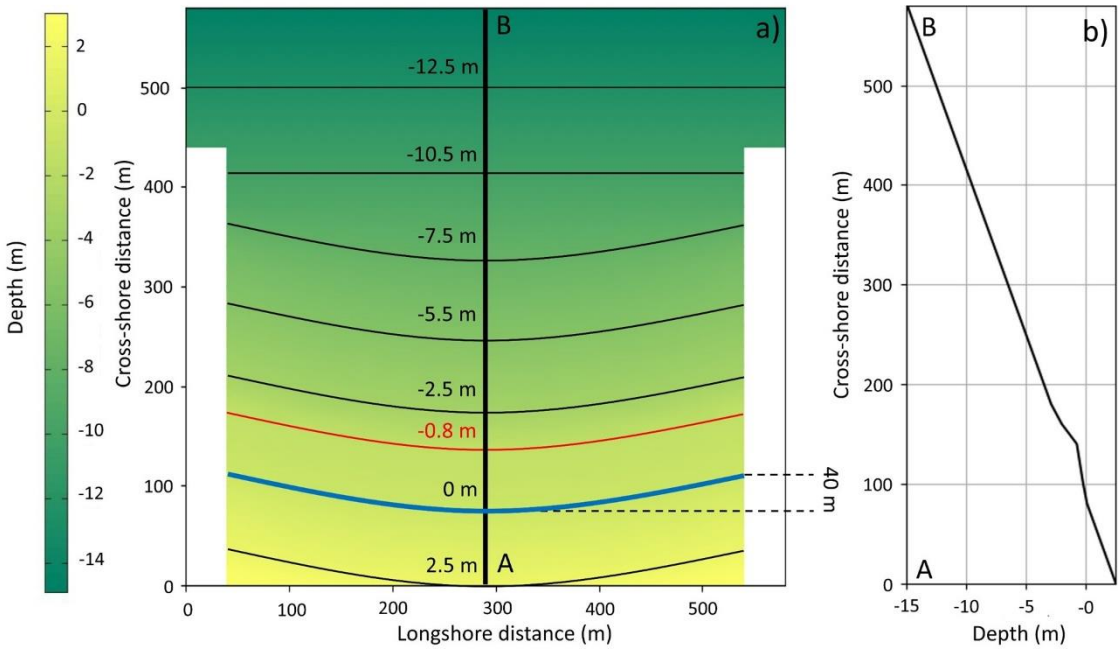

Figure 6.1 - **(a)** Embayed beach domain selected for the case study. The sandbar crest is marked by the red line, while the shoreline is indicated by the blue line. Bathymetric depths range from 2.5 m above sea level to -15 m below. **(b)** Bathymetric cross-profile along the central area of the embayment, corresponding to transect A-B (black line).

The computational domain is characterised by a uniform grid (cell size: 20 x 20 m) with a longshore and cross-shore extension of 580 m (including the headlands). For each numerical simulation, wave forcing was applied along the offshore boundaries using different values of significant wave height H_s and a peak wave period T_p (Table 6.1). The wave directional spreading, which describes how wave energy is distributed across different propagation directions, was set to 4 (expressed as meaning cosine power). The direction of waves θ coming from the offshore boundaries was maintained perpendicular to the shoreline, with an angle of 0° (north). Throughout each simulation, wave conditions (H_s, T_p, θ), wind forcing (direction θ_W and speed U_{10}) and the computational grid remain unchanged (Table 6.1). Numerical simulations were run for a duration of 1 day (morphological time steps: 1440), until stable conditions were reached.

Table 6.1

Values of wave parameters (significant wave height - H_s; wave direction - θ; peak wave period - T_p) and wind parameters (wind speed - U_{10}; wind direction - θ_W) used to simulate surf zone circulation patterns within the modelled domain.

Wave parameters			Wind parameters	
H_s (m)	θ (°)	T_p (s)	U_{10} (m/s)	θ_W (°)
1	0	10	-	-
1	0	10	5	0
1	0	10	5	180
1	0	10	10	0
1	0	10	10	180
1	0	10	15	0
1	0	10	15	180
1	0	10	20	0
1	0	10	20	180
1	0	10	25	0
1	0	10	25	180
1	0	10	30	0
1	0	10	30	180
0.5	0	10	-	-
0.5	0	10	15	0
0.5	0	10	15	180
1.5	0	10	-	-
1.5	0	10	15	0
1.5	0	10	15	180
2	0	10	-	-
2	0	10	15	0
2	0	10	15	180
2.5	0	10	-	-
2.5	0	10	15	0
2.5	0	10	15	180

6.3 Results

Results showed that under wave conditions of H_s = 1 m, T_p = 10 s, θ = 0° and in the absence of wind forcing, two distinct rip cells develop within the embayment (Fig. 6.2a). Within the surf zone, the flows converge toward the central area of the embayment, where an offshore-directed rip current is generated. Along the shoreline (blue line in Fig. 6.2), a cellular circulation pattern develops with flows directed either toward the central area of the embayment or toward the headlands. Given the symmetry of the circulation cells developed, the remaining analyses focus solely on one of the headlands. In the central area of the embayment, wave propagation appears homogeneous until the waves encounter the submerged sandbar. Beyond this point, the values of significant wave height (H_s) gradually

decrease as the wave approach the shoreline (Fig. 6.2b). In contrast, values of significant wave height H_s near the headlands are slightly lower compared to those in the central area of the embayment, and the wave direction is slightly modified due to the interference with the headlands (Fig. 6.2b).

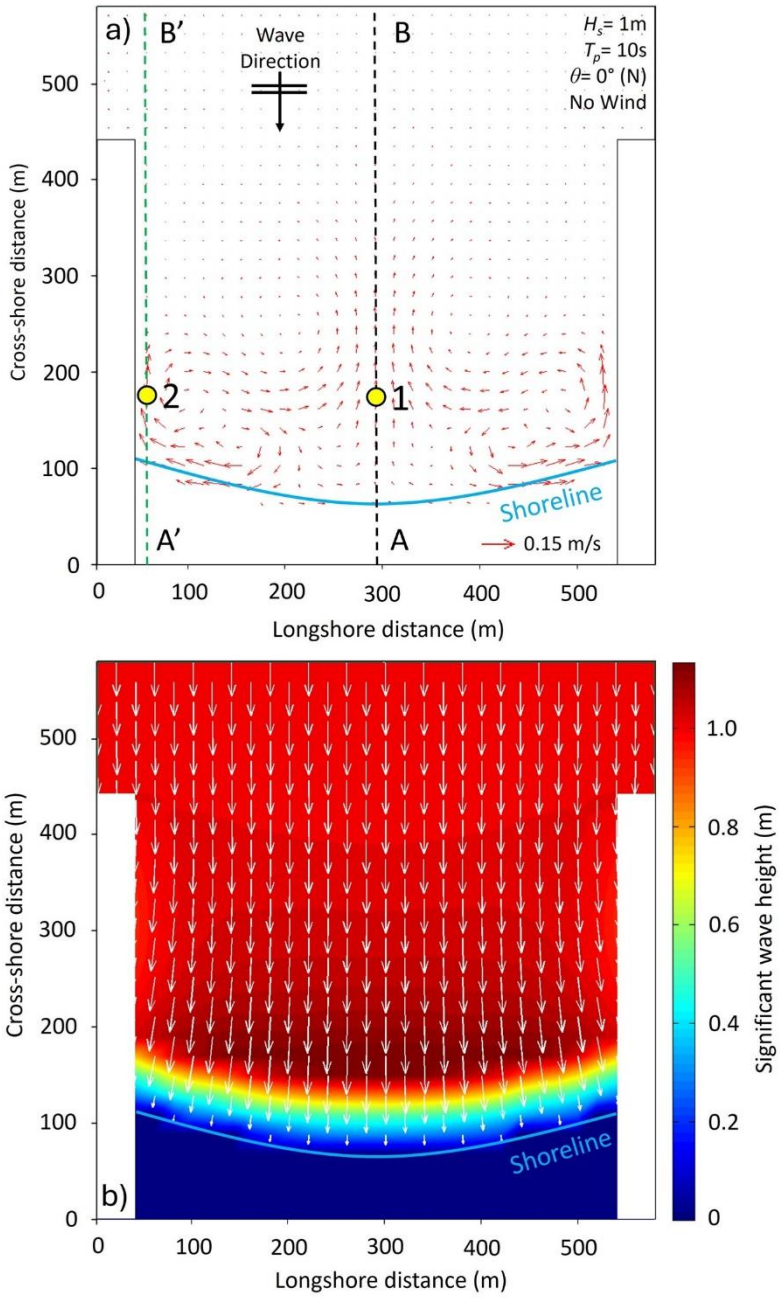

Figure 6.2 - **(a)** Flow circulation pattern within the embayment under wave conditions (H_s = 1 m, T_p = 10 s, θ = 0°) without wind forcing. Flow intensity is represented by red vectors indicating depth-averaged velocities. Dashed lines (black and green) show the locations of longitudinal transects (A-B and A'-B'), while yellow dots represent the location of monitoring points used in the data analysis. Panel **(b)** shows the distribution of significant wave height (H_s) values within the embayment.

The values of depth-averaged velocities obtained along the cross-shore transects (represented by the dashed black and green lines in Fig. 6.2a) were analysed to show how wind forcing influences the overall flow circulation pattern. Rip currents velocities show significant variations depending on both wind speed and direction (onshore or offshore) (Fig. 6.3). In the absence of wind forcing (continuous black and green lines in Fig. 6.3), the maximum depth-averaged velocities reached approximately 0.09 m/s in the central area of the embayment and approximately 0.18 m/s near the headland.

By introducing wind forcing into the numerical simulation, the role of wind speed and wind direction becomes more evident in the circulation patterns (Fig. 6.3). As wind speed U_{10} increases in the onshore direction, an increase in depth-averaged velocities is observed in the central area of the embayment, while a decrease occurs near the headlands (Fig. 6.3). The opposite trend emerges under offshore winds: depth-averaged velocities increase near the headlands, while decreasing in the central area of the embayment (Fig. 6.3).

At a wind speed U_{10} of 30 m/s, the maximum depth-averaged velocities in the central area of the embayment range from approximately 0.17 m/s (under onshore winds) to less than 0.01 m/s (under offshore winds) (Fig. 6.3f). In contrast, near the headland, the maximum depth-averaged velocities range from approximately 0.07 m/s, with onshore winds, to about 0.32 m/s under offshore winds (Fig. 6.3f).

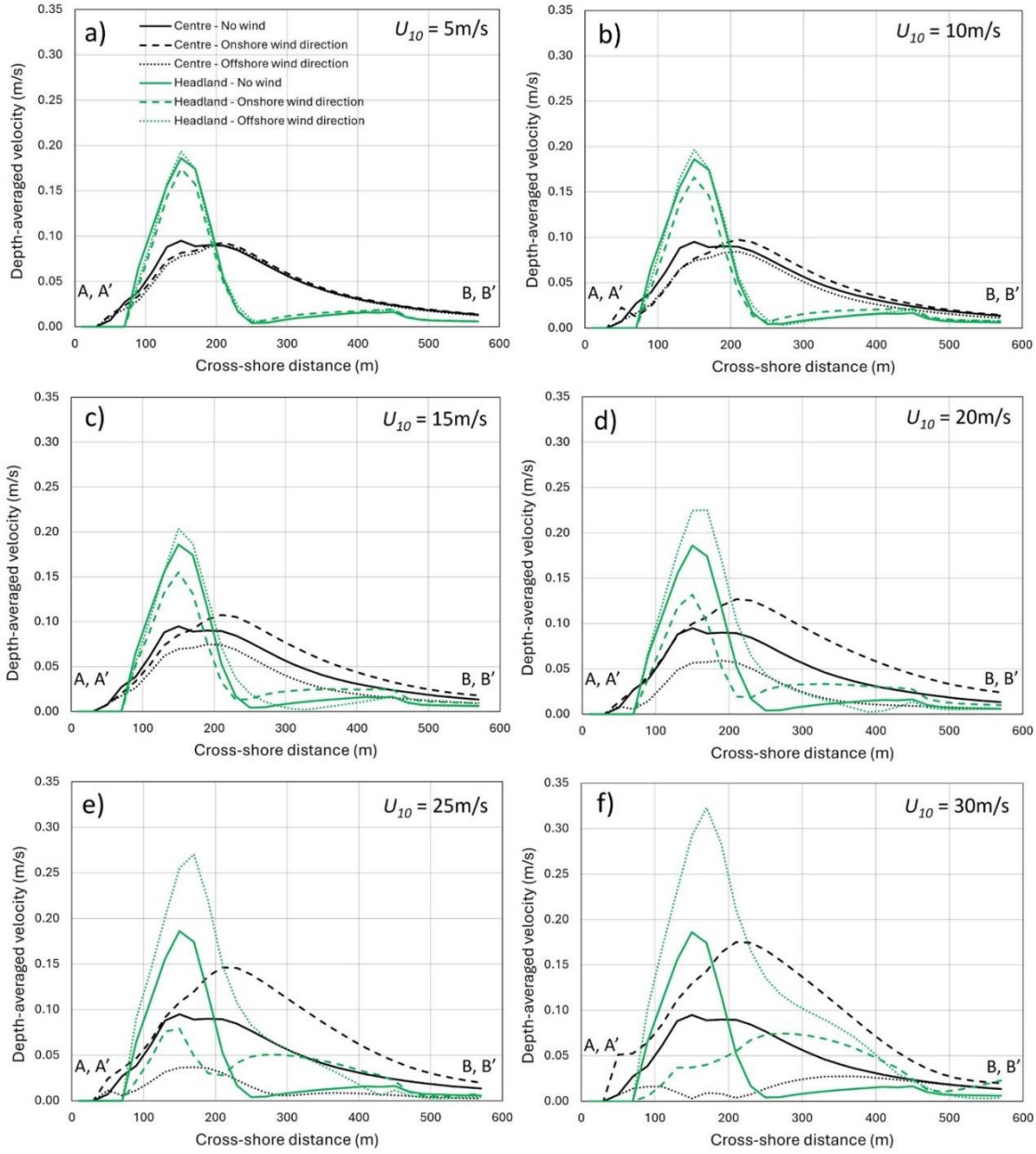

Figure 6.3 - Values of depth-averaged velocity along the cross-shore transects A-B and A'-B' (see Fig. 6.2), under different wind conditions. Continuous black and green lines represent scenarios without wind forcing. Dashed black and green lines are referent to onshore wind forcing, while dotted black and green line correspond to offshore wind forcing. Simulations were performed using wind speed U_{10} of: **(a)** 5 m/s, **(b)** 10 m/s, **(c)** 15 m/s, **(d)** 20 m/s, **(e)** 25 m/s and **(f)** 30 m/s.

An increase in wind speed also led to changes in depth-flow circulation patterns within the embayment (Fig. 6.4). More specifically, when an onshore wind speed U_{10} = 10 m/s is considered (Fig. 6.4.a), the circulation pattern remains similar to that shown in Figure 6.4b (offshore wind direction), but the rip currents at the headlands are weaker. When the

wind speed increased to 30 m/s and maintains an onshore wind direction (Fig. 6.4c), the flow along the headlands shows a prevalent onshore direction, while a single offshore-directed rip current dominates the central area of the embayment.

By changing the wind direction to offshore (Fig. 6.4d), the flow pattern appears totally different compared to that in Figure 6.4c. An offshore-directed rip current develops along the headland, while there are no rip currents in the central area of the embayment (Fig. 6.4d). Overall, strong onshore winds tend to induce onshore-directed currents along the headlands (Fig. 6.4c), which could reduce the wave-induced rip currents. Conversely, strong offshore winds tend to induce an offshore-directed current along the headlands (Fig. 6.4d), thereby enhancing the development and intensity of wave-induced rip currents.

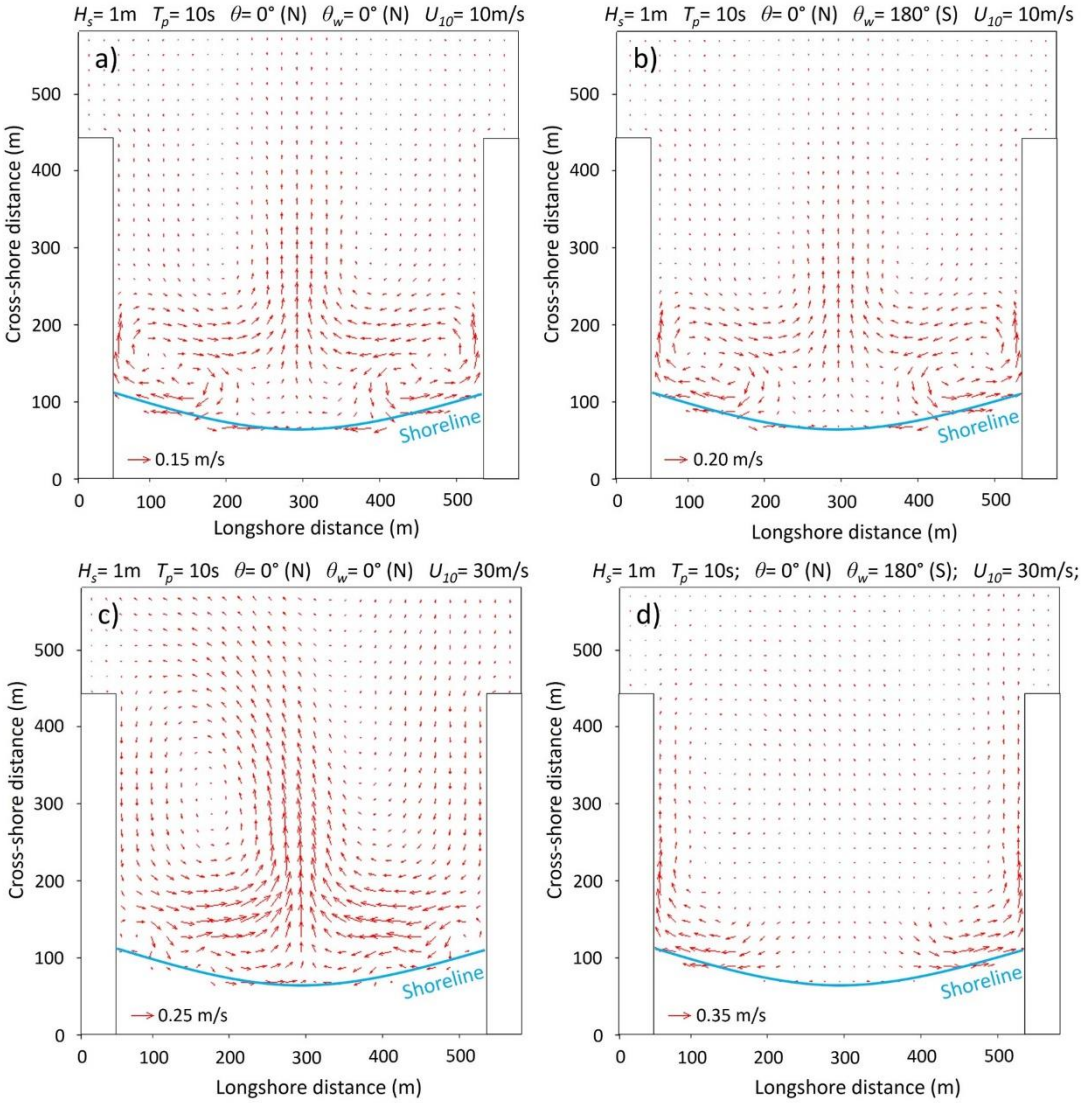

Figure 6.4 - Flow circulation patterns within the embayment under different wind conditions. Panels **(a)** and **(c)** correspond onshore wind forcing, while Panels **(b)** and **(d)** correspond offshore wind forcing. Wind speed U_{10} is set to 10 m/s in Panels **(a)** and **(b)**, while to 30 m/s in Panels **(c)** and **(d)**.

To better understand the characteristics of the flow patterns, the values of depth-averaged velocity from the monitoring points (yellow dots in Fig. 6.2a) were examined. The analysis highlights how flow intensity (increasing and decreasing values) responds to changes in wind forcing (speed and direction), as well as variations in significant wave height (Fig. 6.5).

The flow velocities in the central area of the embayment increase when onshore winds are considered, while they decrease when considering winds from offshore (Fig. 5a). Specifically, with a wind speed U_{10} of 30 m/s, the depth-averaged velocities in the central area of the embayment range from approximately 0.20 m/s (under onshore winds) to approximately 0.02 m/s (under offshore winds) (Fig. 6.5a). On the other hand, the flow velocities at the headland increase when offshore winds are considered, while they decrease when considering winds from onshore (Fig. 6.5b). For wind speed U_{10} of 30 m/s, the depth-averaged velocities at the headland reach from of approximately 0.33 m/s (under offshore winds) to approximately 0.04 m/s (under onshore winds) (Fig. 6.5b).

Moreover, the analysis of the cross-shore components of the depth-averaged velocity showed that, under intensified wind forcing, wind direction significantly influences both the magnitude and circulation patterns of the flow currents. For example, with a wind speed U_{10} = 20 m/s, onshore winds enhance rip current intensity in the central area of the embayment, whereas offshore winds lead to stronger flow currents near the headlands (Fig. 6.5c, d).

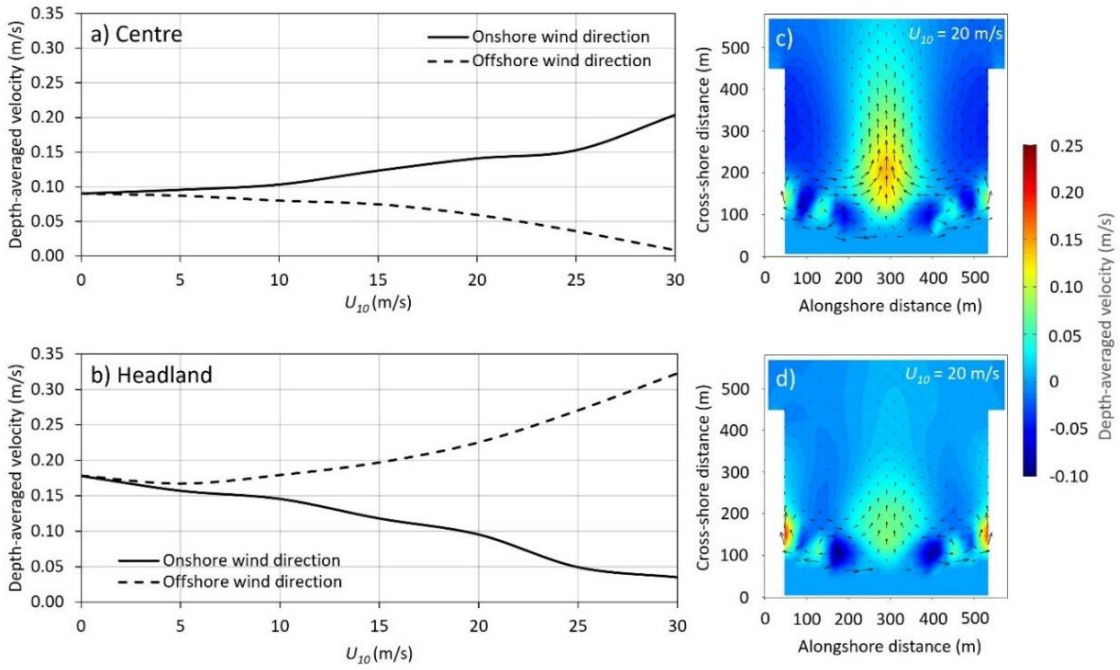

Figure 6.5 - Values of depth-averaged velocity and wind speed recorded at the monitoring points: **(a)** within the central area of the embayment and **(b)** at the headland (both indicated by yellow dots in Fig. 6.2). Continuous black lines represent onshore wind conditions, while dashed black line correspond to offshore wind conditions. Panels **(c)** and **(d)** show the corresponding cross-shore component of the depth-averaged velocity for a wind speed U_{10} of 20 m/s, under **(c)** onshore and **(d)** offshore wind direction, respectively.

Numerical simulations were also performed by increasing the values of significant wave height H_s, maintaining a fixed wind speed U_{10} of 15 m/s. The results showed an overall increase in the values of depth-averaged velocity both in the central area of the embayment and near the headland (Fig. 6.6). This increase follows an approximately linear trend for H_s values between 0.5 m and 2.5 m (Fig. 6.6), both in absence and in presence of wind forcing. When wind forcing is considered (U_{10} = 15 m/s), the values of depth-averaged velocity at the centre of the embayment (Fig. 6.6a) are always higher (under onshore winds) or lower (under offshore winds) compared to the no wind scenario (continuous black line in Fig. 6.6). For values of H_s = 2.5 m, the values of depth-averaged velocity are greater than 0.20 m/s both considering the absence or presence of wind forcing. An increase in the values of depth-averaged velocity is also observed near the headland (Fig. 6.6b). With an offshore wind, the flow velocities are always higher compared to the no wind scenario, or lower when an offshore wind is considered (Fig. 6.6b). For H_s = 2.5 m, the values of depth-averaged velocity are greater than 0.30 m/s both considering the absence and presence of wind.

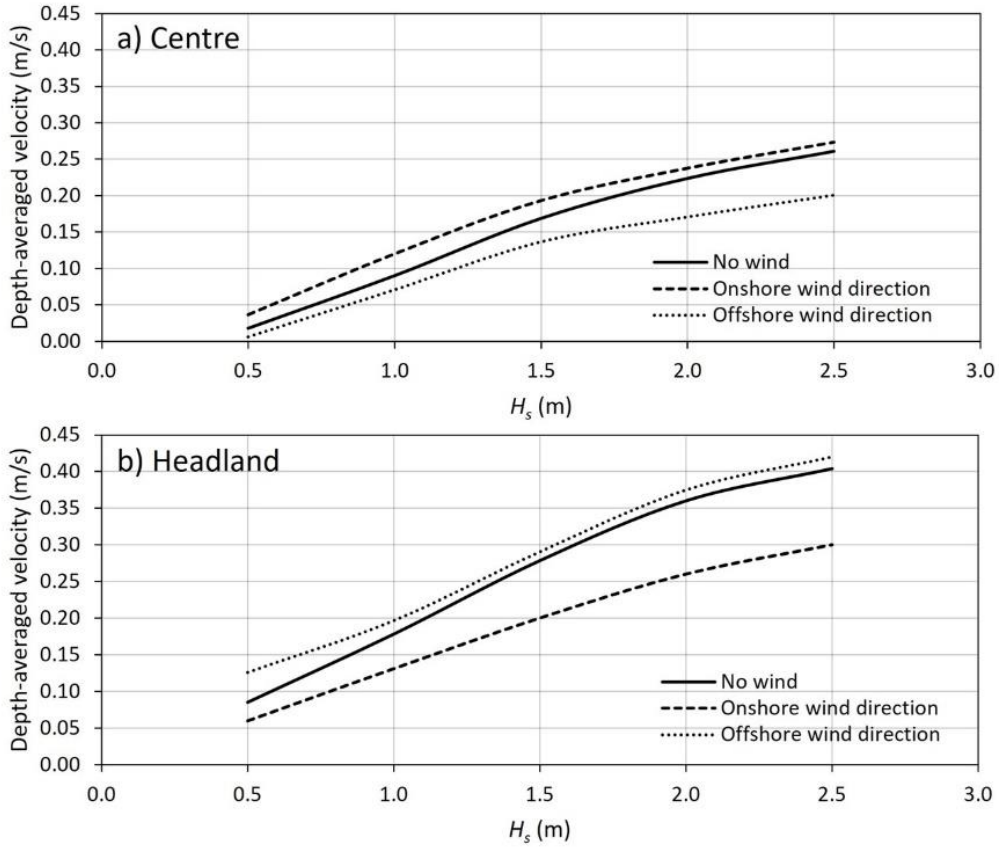

Figure 6.6 - Values of depth-averaged velocity and significant wave height H_s at the monitoring points: **(a)** central area of the embayment and **(b)** at the headland (both indicated by yellow dots in Fig. 6.2). The analysis includes scenarios with and without wind forcing, under both onshore and offshore wind conditions, assuming a constant wind speed U_{10} of 15 m/s.

Different cross-shore extensions of rip currents are observed from the numerical simulations (Fig. 6.7). Rip currents that develop at the centre of the embayment generally have a greater cross-shore extension seaward than those that develop along headlands (Fig. 6.7). In both scenarios, the numerical simulations highlighted that the seaward cross-shore extension of rip current increases in response to rising wind speed and significant wave height. However, it is important to consider that the geometry of the beach system is highly idealised. In the bathymetry considered, the depth at the heads of the headlands is the same as the central area of the embayment (depth > 10 m). It is likely that the seaward cross-shore extension of the rip currents would be greater if the depth along the headlands and at their heads was shallower.

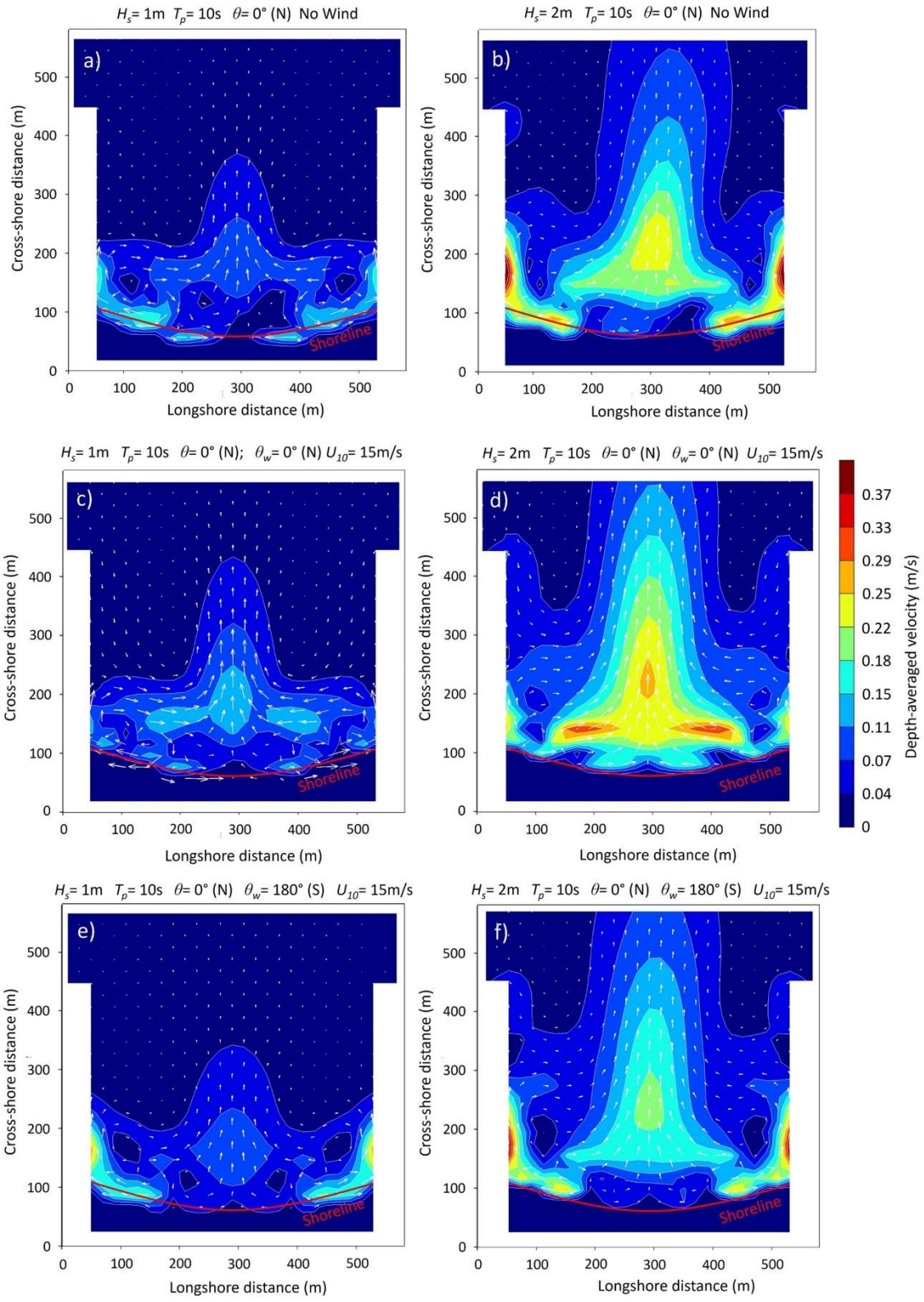

Figure 6.7 - Values of depth-averaged velocity and associated flow circulation patterns within the embayment, for significant wave height H_s values of **(a, c, e)** 1 m and **(b, d, f)** 2 m. The panels show variations under different wind conditions: **(a, b)** no wind forcing; **(c, d)** onshore wind with a speed U_{10} of 15 m/s; **(e, f)** offshore wind with a speed U_{10} of 15 m/s.

Moreover, the numerical simulations highlighted how wind forcing can influence wave-induced forcing and wave dissipation processes. Figure 6.8 shows the values of wave-induced force (Fig. 6.8a, c) and wave dissipation (Fig. 6.8b, d) along the breaking area of the embayment. In particular, Figure 6.8c shows how an increase in wind speed results in an increase or decrease in wave-induced force under the presence of onshore or offshore winds. This increase or decrease in wave-induced force values is further supported by the wave dissipation values at the sandbar, which are slightly higher or lower at the sandbar depending on the wind direction (Fig. 6.8b, d).

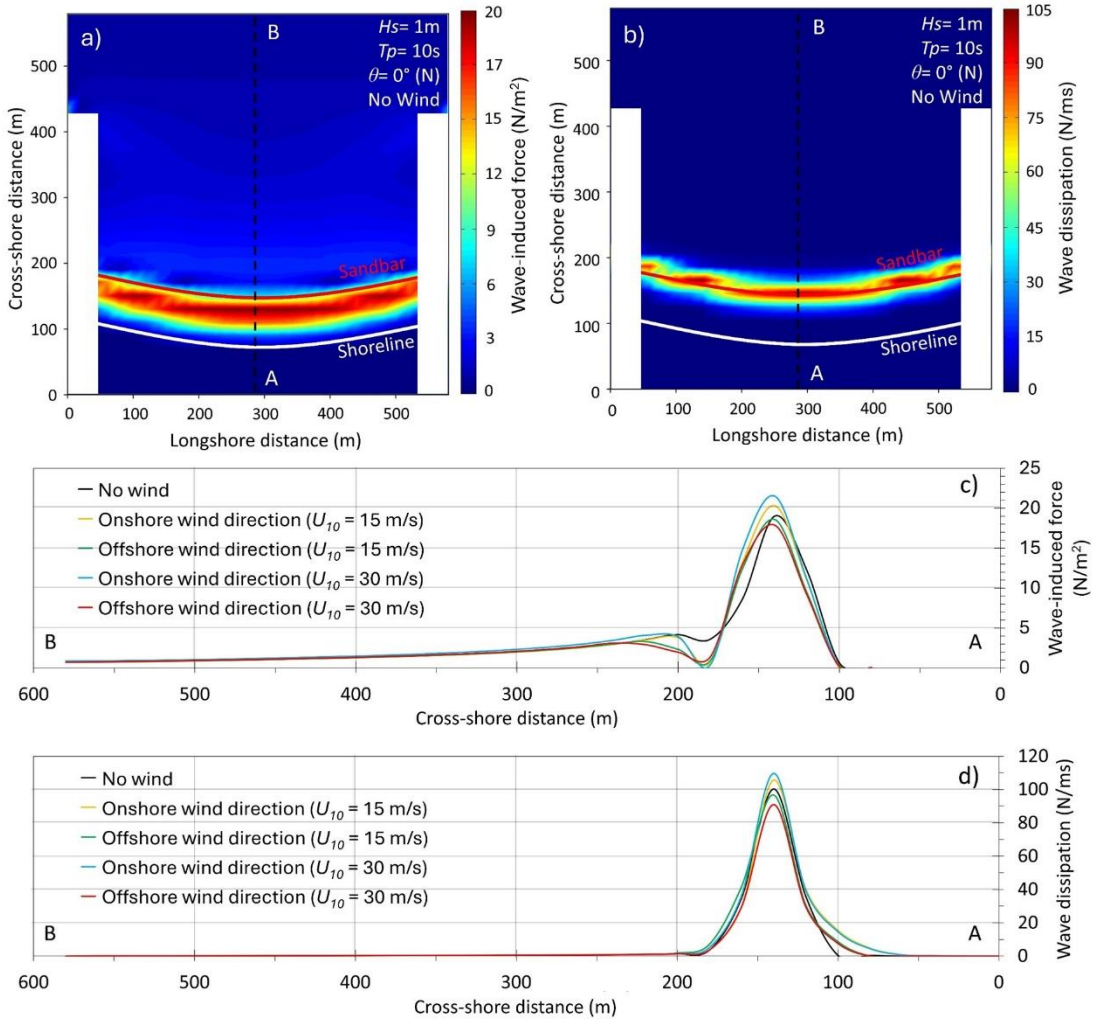

Figure 6.8 - Values of **(a)** wave-induced force and **(b)** wave dissipation across the model domain. Panels **(c)** and **(d)** show the corresponding values along the cross-shore transect A-B (dashed black line in Panels **(a)** and **(b)**), under wind speeds U_{10} of 15 m/s and 30 m/s, for both onshore and offshore wind directions.

Finally, the analysis of wave set-up values (Fig. 6.9) showed that they begin to increase after the sandbar (red line in Fig. 6.10a), whose crest is located at 0.8 m below the mean sea level. In the absence of wind forcing and with wave conditions of H_s = 1 m and T_p = 10 s, wave set-up values along the central transect (A-B; dashed black line in Fig. 6.9a) and along the headland transect (A'-B'; dashed green line in Fig. 6.9a) showed a decrease of approximately -0.01 m (set-down) at the sandbar and then an increase up to approximately 0.13 m at the shoreline (blue line in Fig. 6.9a).

When an onshore wind is considered with different wind speed (U_{10} = 5 m/s, 15 m/s and 30 m/s), the values of wave set-up are higher compared to the no wind scenario (Fig. 6.9b, c, d). Oppositely, when an offshore wind is considered, the wave set-up values are lower compared to the no wind scenario (Fig. 6.9b, c, d). Within the surf zone (e.g., cross-shore distance = 150 m), wave set-up is always higher at the headland compared to the central area of the beach, which could support a flow from the headland towards the centre of the beach. At the same time, due to the shape of the beach, wave set-up near the shoreline at the centre of the beach (cross-shore distance = 100 m) could induce flows towards the headlands.

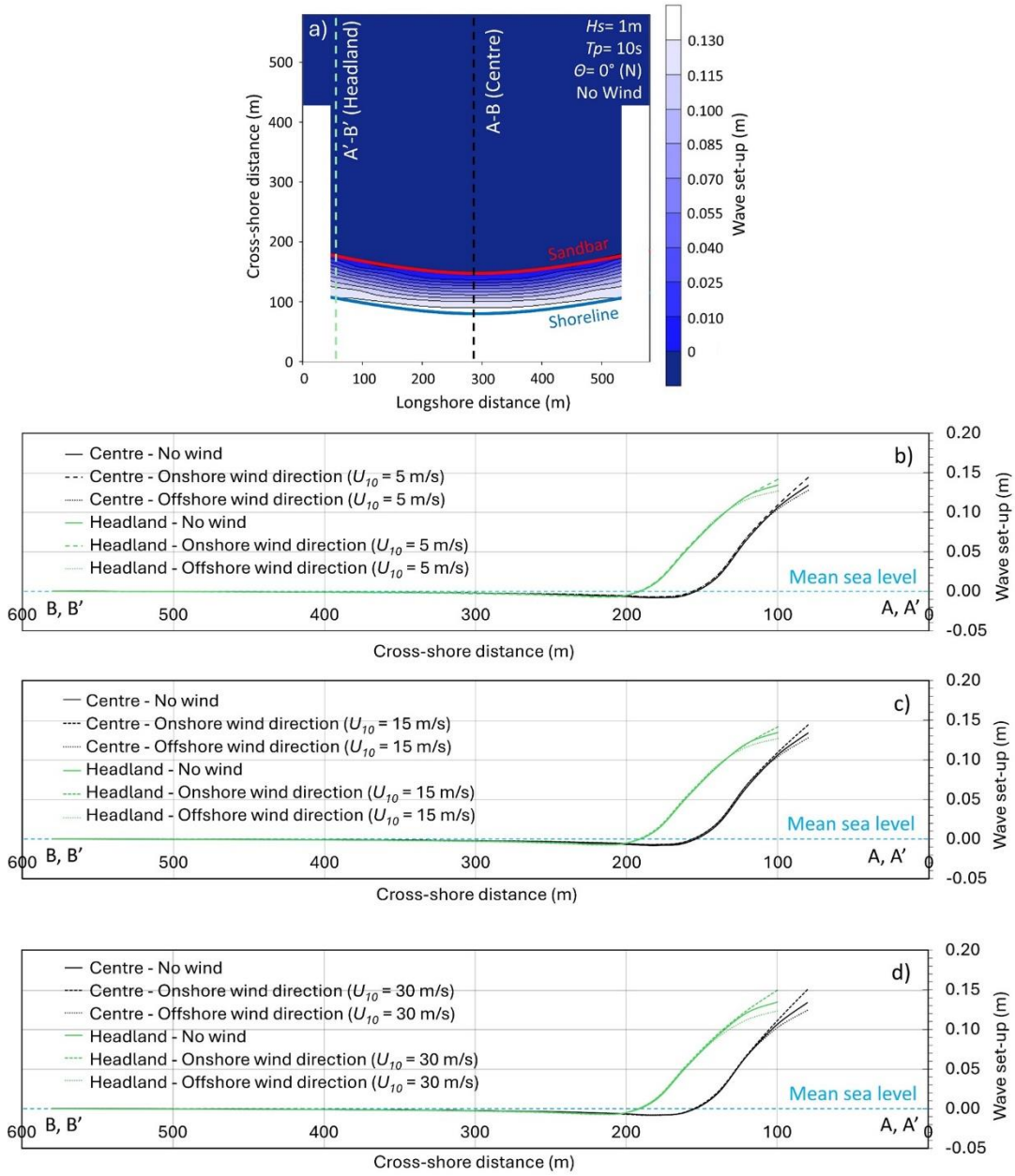

Figure 6.9 - Values of **(a)** wave set-up within the modelled domain (H_s = 1 m, Tp = 10 s, θ = 0°). The dashed black and green lines indicate the cross-shore transects: "Centre" (A-B) and "Headland" (A'-B'). Panels **(b, c, d)** show wave set-up values along these transects under different wind conditions, including no wind and wind forcing at speeds U_{10} of 5 m/s, 15 m/s and 30 m/s, for both onshore and offshore directions.

6.4 Discussion

We used a hydrodynamics model, coupled with a wave model, to simulate the development of rip current systems on a simplified embayed beach under different wind and wave conditions. Using a similar geometry to Castelle and Coco (2012), we considered an embayed beach (L = 500 m) bounded laterally by two physical barriers with wave conditions of H_s = 1 m, T_p = 10 s and θ = 0°. The results showed how the increase in wind speed led to variation of depth-averaged velocities, and such variations were particularly clear in the central area of the embayment and at the headlands, where rip currents develop. The velocity of rip currents can increase or decrease (sometimes even causing the current to disappear) depending on wind speed and direction (relative to wave direction).

Variations in rip current velocities are linked to the formulations assumed in numerical modelling of hydrodynamic processes. Wave growth strongly depends on the wind velocity components (Equation 6.6, 6.7), which are related to the wind friction velocity and the drag coefficient. In the work of Lin and Sheng (2020), the authors point out how the drag coefficient, combined with the roughness of the sea surface, is fundamental to compute the wind stress. Therefore, variations of these parameters at the air-sea interface led to a change in wave characteristics and, consequently, to a different seabed-wave interaction (Deltares, 2024a). Also, in terms of formulation adopted, we focused on depth-averaged modelling of hydrodynamics processes and leave for future studies the analysis of 3D effects induced by wind. Despite the limitations, rip current velocities appear consistent with those measured in case studies of embayed beaches (e.g., Huntley et al., 1988; MacMahan et al., 2006; McCarroll et al., 2015; Yuan et al., 2023).

The simulated rip current patterns find similarities with the numerical models illustrated in the work of Castel and Coco (2012), where the development of a cellular circulation with a central rip channel can be favoured by a large beach curvature and a short beach length. On the other hand, the development of a cellular circulation with two rip currents at the headlands can be favourited by both a small beach curvature and short beach length. Our simulations showed that, with unchanged morphological and wave conditions, both types of cellular circulation (central rip channel and headlands rips) can occur within the same embayment when an offshore or onshore wind is considered (Fig. 6.7).

Overall, the location of rip currents into the embayment is primarily influenced by both the beach's shape and the presence of lateral physical barriers, which affect the hydrodynamic processes in the model domain. When waves physically interact with a rigid boundary, they can lose energy and slow down due to friction (Deltares, 2024b). In this context, as shown in the work of Castelle and Coco (2012), wave directional spreading plays a fundamental role in this type of beach configuration, potentially causing headland-

induced shadowing to dominate over other processes, such as wave refraction and diffraction.

Numerical simulations, including and excluding wave refraction and diffraction, have shown that wave refraction can influence the resulting flow velocity field. In particular, higher velocities are observed near the headlands when wave refraction is considered (Fig. 6.10a), whereas these velocities almost disappear when wave refraction is excluded (Fig. 6.10c). As expected, due to the geometry of the domain and the use of normally incident waves with directional spreading of 4, wave diffraction has a negligible effect on the hydrodynamic circulation (Fig. 6.10b). Although the refraction processes related to the presence of headlands influence the flow circulation within the embayment (Fig. 6.10c), the wave field (white arrows in Fig. 6.10d) still shows a deflection toward the headlands, even when wave refraction is excluded from the model (Fig. 6.10d). This deflection is more pronounced when wave refraction is included, as shows in Figure 6.2b, although the values of significant wave height remain very similar. Furthermore, these results highlight how the shading effect induced by the headlands significantly influence the characteristics of emerging currents.

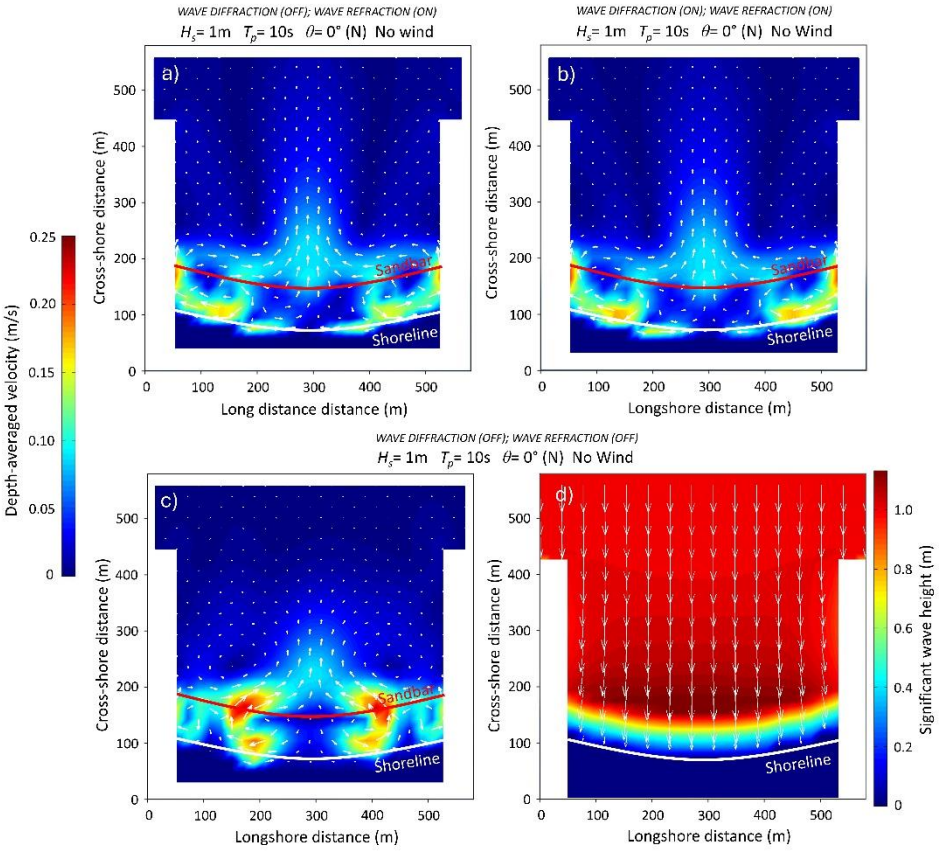

Figure 6.10 - **(a, b, c)** Comparison of depth-averaged velocity values within the modelled domain, with and without wave diffraction and refraction. **(d)** Values of significant wave height H_s obtained from the numerical simulations when wave diffraction and refraction are excluded.

The circulation patterns observed within the surf zone are primarily controlled by two key physical drivers: the wave breaking field, which generates spatial gradients in wave radiation stress that drive flow currents, and the wind stress, which exerts a direct forcing on the sea surface. Understanding both the individual and combined effects of these forcing mechanisms is essential for characterising rip current dynamics, particularly on embayed beaches where headlands significantly influence the hydrodynamic characteristic of the surf zone.

The effects of these forcing mechanisms are summarised in Figure 6.11, which shows the results of four different simulation scenarios. In the scenario with only wave propagation (H_s = 1 m, T_p = 10 s and θ = 0°) and without wind forcing (Fig. 6.11a), the surf zone circulation exhibits a symmetric cellular pattern. Here, longshore currents converge toward the headlands along the shoreline and then return offshore through a pronounced rip current located at the centre of the embayment (Fig. 6.11a). This flow pattern highlights the influence of wave breaking in generating cellular circulation patterns even in the absence of wind. Moreover, this scenario is consistent with those previously modelled on embayed beaches (Castelle and Coco, 2012).

When wind forcing is incorporated into the numerical model (Fig. 6.11b), specifically under onshore wind conditions with U_{10} = 20 m/s, the central rip current intensifies, exhibiting higher velocities and greater cross-shore extension, while flow velocities near the headlands decrease. This suggests that onshore wind reinforces the offshore-directed rip current at the centre of the embayment, likely due to a combination of increased surface wind stress and modifications in the wave-breaking pattern.

Panels c and d in Figure 6.11 isolate the contribution of wind forcing by completely removing the contribution of wave propagation. In the onshore wind scenario (Fig. 6.11c), a central offshore-directed rip current still develops, indicating that wind-driven circulation alone can induce flow cellular patterns, although with different spatial characteristics compared to the wave-driven scenario (Fig. 6.11a). In contrast, the offshore wind scenario (Fig. 6.11d) shifts the location of flows toward the headlands, effectively inverting the current pattern observed under wave-driven forcing (Fig. 6.11a). Although highly idealised, these simulations further highlight the sensitivity of surf zone circulation to wind forcing in embayed beaches (Fig. 6.11c, d).

Collectively, these results highlight the complex interplay between wave and wind forcing in shaping surf zone hydrodynamics. The amplification or attenuation of specific circulation patterns, such as the central rip current or the rip cells near headland, depends not only on the presence of individual forcings, but also on their relative intensity and spatial distribution. Consequently, these findings emphasize the importance of considering multi-forcing scenarios when studying rip current behaviour.

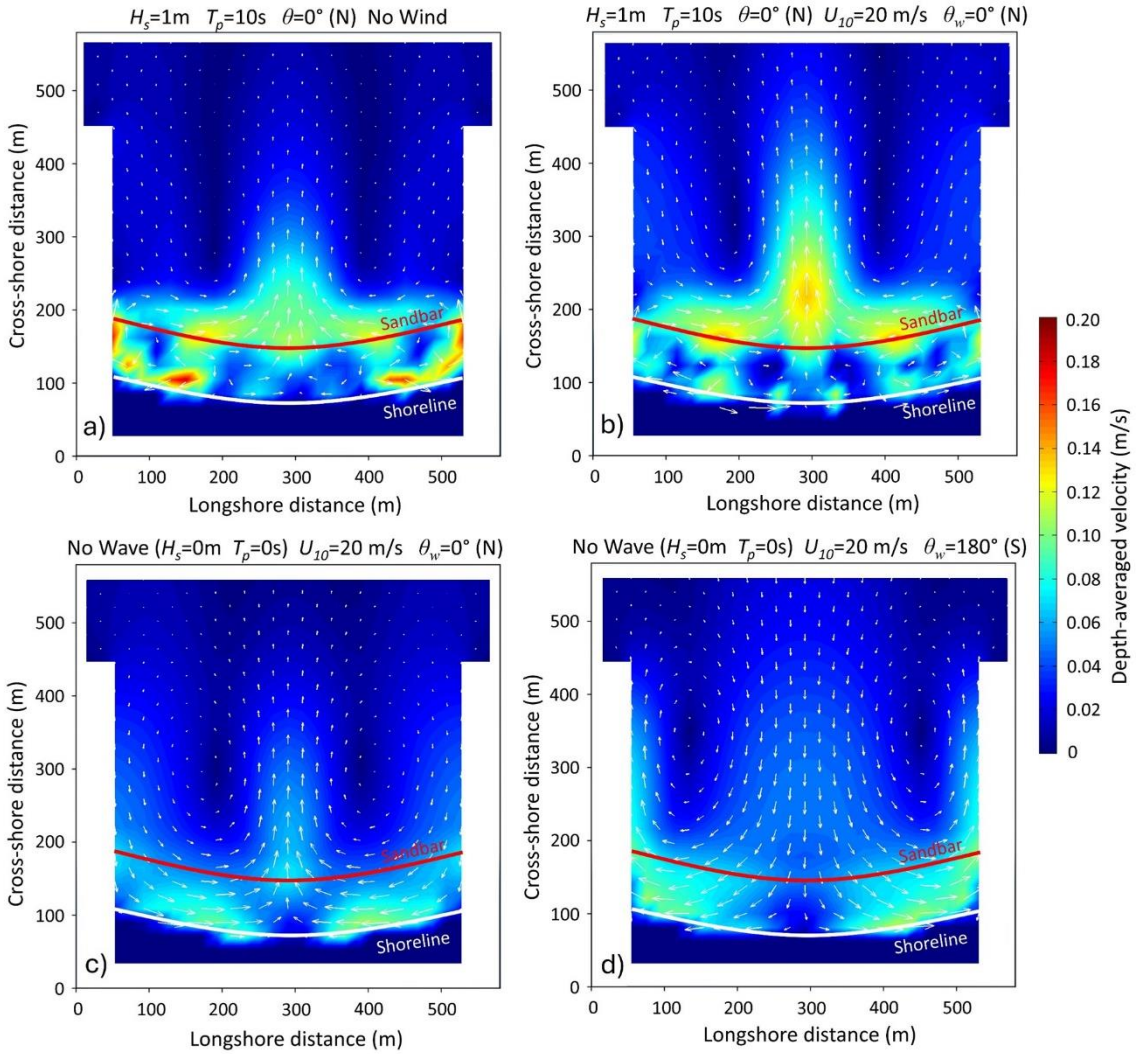

Figure 6.11 - Values of depth-averaged velocity from numerical simulation under different scenarios: **(a)** wave forcing only (H_s = 1 m, T_p = 10 s, θ = 0°) without wind forcing; **(b)** combined wave forcing and onshore wind at 20 m/s; **(c)** onshore wind only at 20 m/s; **(d)** offshore wind only at 20 m/s. Both Panels **(a)** and **(b)** are set with wave conditions of H_s = 0 m and T_p = 0 s.

6.5 Conclusions

Numerical modelling was implemented to analyse the effects of wind on an embayed beach with idealised bathymetry. The results show that the cellular circulation patterns within the embayment can change depending on wind speed and direction. When strong winds blow in the same direction as the waves, a rip current can develop at the centre of the embayment, significantly influencing the overall flow circulation. On the other hand, strong winds blowing in the opposite direction of the waves tend to generate headland rips, which can modify the established circulation pattern. In addition, the results

highlighted how wind conditions can influence the offshore extent of rip currents, particularly under onshore wind scenarios.

Given the influence of wind forcing on surf zone flow circulation, the results highlighted the importance of incorporating wind parameters into hydrodynamic models. However, the numerical simulations also showed that flow circulation patterns are primarily driven by a combination of factors related to wave conditions and morphological features of the embayment. Further investigations and field observations, especially using real wave-wind data, are needed to fully establish the role of wind in the development of rip current systems within embayed beaches. However, these findings are relevant not only from a physical coastal hydrodynamic perspective, but also for informing beach management strategies and improving safety planning. In fact, hazardous rip current systems can develop, posing a serious risk to both swimmers and coastal infrastructures (especially during strong wind events or when recreational beach use continues under adverse weather conditions).

Chapter 7: THE ROLE OF BEACH-CAST IN COASTAL FLOODING EVENTS ON MICROTIDAL BEACHES (WESTERN MEDITERRANEAN SEA)

This chapter contains the main findings published in the following paper, with the numerical modelling component integrated.

Trogu, D.; Simeone, S.; Usai, A.; Porta, M.; De Muro, S., **2024**. On the role of wood and seagrass rests in coastal flooding events in Mediterranean microtidal beaches. In: *Coastlines under change: Proceedings from the International Coastal Symposium (ICS) 2024 (Doha, Qatar)*; Phillips, M.R., Al-Naemi, S., Duarte, C.M., Eds.; *J. Coast. Res.* 113, 115–119. https://doi.org/10.2112/JCR-SI113-023.1.

7.1 Introduction

Beach-cast, typically deposited and sedimented along the backshore, can be often observed along the world's coastlines (Tomasello et al., 2022). Their origin can be linked to both terrestrial ecosystems (e.g., vegetal material transported by rivers that flow into the sea) and marine ecosystems (e.g., debris from seagrass meadows located on the submerged beach). Along the Mediterranean coasts, temporary seagrass remains (commonly referred as "banquettes") are primarily composed of dead leaves from *Posidonia oceanica* (L.) Delile meadows (Mateo et al., 2003). In fact, these meadows cover approximately 1-2 % of the seabed on the inner continental shelf of the Mediterranean Sea (estimated area between 25.000 km^2 and 50.000 km^2) (Gobert et al., 2006; Pasqualini et al., 1998), with their distribution extending to depths of around 40-45 m (Telesca et al., 2015; Rotini et al., 2020). Moreover, *Posidonia oceanica* meadows are considered among the most valuable and productive marine ecosystems in the Mediterranean Sea. They play a fundamental role in oxygen production, support marine biodiversity and provide natural protection for coastlines by dissipating wave energy, especially during storm events (Duarte, 2002; Rotini et al., 2020). In addition, they act as significant carbon sinks, thus contributing to climate change mitigation (Tomasello et al., 2022).

Similar to the seagrass meadows, *Posidonia oceanica* banquettes are crucial in controlling the morphological and hydrodynamic processes of beach environments (Ruju et al., 2022; Trogu et al., 2023). In fact, these accumulations can reach thicknesses of up to 2.5 m (Rotini et al., 2020; Boudouresque et al., 2017), effectively acting as a buffer against waves action (Kennedy and Woods, 2012). Therefore, their presence can determine an increase in the beach permeability, facilitating the drainage of water volumes during wave overtopping events across the berm (Ruju et al., 2022). In addition to *Posidonia oceanica* remains, these deposits may be also characterised by other types of vegetal materials, such

as woody debris, dead trees, river reeds and large logs. Similarly to seagrass wracks, these vegetal remains can play a crucial role in the natural dynamism and evolution of beach systems, mitigating wave energy by reducing coastal erosion and promoting sediment retention (Trogu et al., 2020; Simeone et al., 2013a; Grilliot et al., 2019).

In this context, numerical modelling represents a valuable tool for improve the understanding of the hydrodynamic behaviour of coastal systems influenced by the presence of beach-cast (Cucco et al., 2020). By integrating field observations with morphodynamic models, the interactions between wave dynamics and these natural accumulations can be simulated under various wave and wind conditions (Ruju et al., 2022). Therefore, numerical models can help to assess the protective role of beach-cast in mitigating coastal erosion and wave overtopping, as well as in the prediction of long-term beach morphological changes. These insights are particularly useful in supporting coastal management and strategies, and for supporting conservation and protection of ecosystems.

This study aims to investigate the role of beach-cast (such as seagrass remains and river reeds), deposited along the backshore, by comparing two storm events characterised by similar wave conditions. More precisely, an urban microtidal beach (Poetto beach - Sardinia, Italy) was selected as a case study and its response to the two storm events was analysed.

During the first event, which occurred in October 2018, the beach area analysed in this study was completely flooded by waves that overtopped the berm. No seagrass wracks were observed on the backshore during this event. On the other hand, during the second event, which occurred in January 2020, the emerged beach (backshore) was not flooded. In this case, a berm composed of beach-cast material acted as a natural barrier, limiting wave overtopping. However, wave action caused an inland displacement of beach-cast during this latter storm. To further understand these dynamics, both images from a coastal video monitoring system and numerical modelling were used to analyses these two events.

Overall, the findings highlight that a more accurate management of beach-cast, deposited and sedimented along the backshore, can provide important benefits to the beach system. In particular, it can enhance the beach's resilience especially during storm events. However, along most of the Sardinia's coastlines, it is common practice to remove seagrass wracks during the summer months as part of "beach cleaning" operations. Driven by the growth of coastal tourism, these practices are often carried out to meet aesthetic expectations, as beaches without banquettes are perceived by beach users as cleaner and more usable. However, such operations can lead to important geomorphological changes (e.g., reduced beach slope and permeability) and have negative impacts on the entire coastal ecosystem (Manfra et al., 2024).

7.2 Event analysis

At the end of October 2018, Poetto beach was impacted by a severe storm event that caused the flooding of large part of the backshore. In the days leading up to the event, the beach was still being frequented by beach users, and "beach cleaning" operations to remove deposited banquettes were actively underway along the backshore. The beach flooding caused significant damage both to local structures and nearby economic activities. Following the storm event, several sections of the backshore remained flooded for days until the water drained away naturally.

Nearly a year later, on 18 December 2019, another intense storm event occurred. The entire area of Southern Sardinia was affected by heavy rainfall, with pick reaching 20 mm/h between 18:00 and 24:00, as recorded by the meteorological station located in Cagliari (Ruju et al., 2020). As a result, the flow rates of the rivers flowing into the Gulf of Cagliari increased, mobilizing and transporting vegetal materials from their riverbeds towards the sea. The transported material was primarily composed of vegetal remains and river reeds, mostly attributed to the species *Arundo donax*. Subsequently, these vegetal materials were transported and deposited on Poetto beach by sea currents and intense waves (from the south-eastern sector with a maximum offshore wave height of 1.5 m).

After this event, the entire area of Southern Sardinia was affected by another severe storm event, with waves primarily coming from the south-western sector (offshore significant wave height in the Western Mediterranean Sea reaching 6 m). The increased wave intensity and shift in wave direction, compared to the previous event occurred on 18 December 2019, led to a further redistribution, deposition and sedimentation of beach-cast material along the backshore of Poetto beach (Ruju et al., 2020). It is estimated that over 85 tonnes of beach-cast were deposited this storm event. Due to the subsequent lockdown caused by the Covid-19 pandemic, the deposited vegetal materials remained undisturbed on backshore for an extended period. This absence of human interference allowed for further interaction between vegetal material and natural beach processes and dynamics.

7.3 Study area

The study area is located on Poetto beach, in the southern coast of Sardinia Island (Western Mediterranean Sea) (Fig. 7.1). More precisely, Poetto beach is located within the Gulf of Cagliari and is characterised by a longshore extension of approximately 8 km and a cross-shore width that varies along its length, reaching a maximum of about 100 m. The S. Elia Promontory, where the coastal video monitoring system is located (blue dot in Fig. 7.1), geomorphologically divides the beach systems of the Gulf of Cagliari into two areas: to the west is Giorgino beach, a wide-open beach interrupted by artificial structures, while to the east is Poetto beach.

Poetto beach is a microtidal, wave dominated sandy beach with a geographic fetch mainly oriented to the south-east (Trogu et al., 2023). The beach is not crossed by rivers, resulting in the absence of direct fluvial sediment input. The main sedimentary supply consists of authigenic bioclastic sediments produced by the *Posidonia oceanica* meadow located in front of the beach, as well as the erosion of the carbonate and siliciclastic rocks of the S. Elia Promontory (Porta et al., 2020). However, several river systems discharge into the Gulf of Cagliari. The main ones, located in the "Campidano" and "Cixerri" plains, flow into the Santa Gilla Lagoon without directly affecting the sediment dynamics of Poetto beach (Barca et al., 2005). Further details regarding the geomorphological characteristics and wave conditions of this area can be found in Chapter 4 of the thesis.

Due to the development of the city of Cagliari and its urban hinterland behind the Poetto beach, the entire beach is subject to significant anthropogenic pressure from residential development and increased commercial activity, resulting in a substantial alteration of its original morphology. In fact, during the summer season, Poetto beach is one of the most popular and visited beaches in Sardinia (Porta et al., 2020). This combination of morphological changes driven by anthropogenic pressure significantly reduced the beach's resilience, especially during storm events, often leading to events of beach flooding and coastal erosion (Brambilla et al., 2016; Biondo et al., 2020).

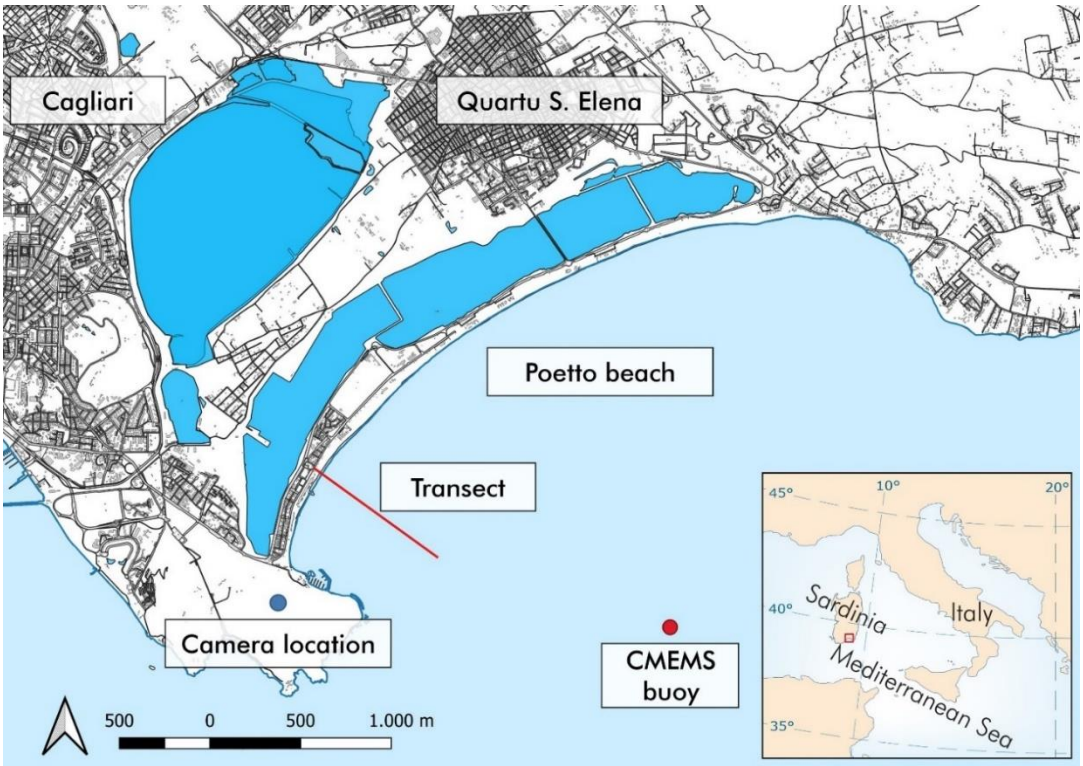

Figure 7.1 - Location of the Poetto beach: the blue dot identifies the location of the coastal video monitoring station located on the S. Elia Promontory; the red dot identified the location of the virtual buoy Copernicus (CMEMS); the red line highlights the transect used to generate the time-stack images (modified from Trogu et al., 2024).

7.4 Methods

7.4.1 Coastal video monitoring system: Image Processing

The storm events were analysed through a series of images (snapshots) acquired by the coastal video monitoring system of the Coastal and Marine Geomorphology Group (CMGG - University of Cagliari). The station is located 125 m above SWL on the S. Elia Promontory (blue dot in Fig. 7.1) and frames the western part of the Poetto beach (Camera coordinates: 39° 11' 24.05'' North; 9° 9' 29.65'' East). More precisely, the station consists of a digital camera (Dahua Technology 12 MP Ultra-HD - Model: DH-IPC-HF81200E) placed on a steel structure and powered by photovoltaic panels. The digital camera was set to record 30 minutes, 4 times a day every 3 hours (from 8:00 to 17:00) for a recording interval of 3 hours (acquisition frequency: 4 Hz). The dimensions of the acquired images are x = 4096 px and y = 2160 px. Further details regarding the coastal video monitoring system can be found in Chapter 2 and 3 of the thesis.

Due to the distortion induced by the camera lens, the acquired images were corrected by setting calibration parameters (e.g., principal point position, radial and tangential distortion coefficients, focal length). The calibration process was preformed using an open-source toolbox called "Camera Calibration Toolbox for MATLAB" (Bouguet, 2022), widely adopted in scientific literature for similar coastal studied (e.g., Vousdoukas et al., 2011; Taborda and Silva, 2012; Passarella, 2019; Trogu et al., 2023). The complete calibration procedure referred to this coastal video monitoring station is described in the work of Passarella (2019).

Once the lens-induced distortion was corrected, the acquired images were rectified and georeferenced using 12 GCPs (Ground Control Points) and the aerial orthophotos available online in the WMS of "Regione Autonoma della Sardegna" (https://webgis.regione.sardegna.it/geoserverraster/ows?service=WMS&request=GetCapabilities). GCPs refer to points that are clearly visible in both images considered (snapshots and aerial orthophotos). In this way, the pixels of the acquired images (snapshots) can be associated with precise real-word coordinates (WGS 84 - UTM 32N) (Fig. 7.2). The complete snapshot georeferencing procedure was performed following the work of Trogu et al. (2023).

For each storm event analysed, the most representative time interval was selected to generate time-stack images, which were used to compare the main features of the wave-swash processes. More precisely, a sequence of snapshots (Fig. 7.3) taken at 30-minute intervals was considered to create the time-stack image for the storm event that occurred on 29 October 2018. On the other hand, for the storm event on 21 January 2020, another sequence of snapshots (Fig. 7.4) taken at 10-minute intervals was considered. Each time-stack image is characterised by a horizontal (x) and a vertical (y) axis, representing time and

space, respectively. The time-stack images were created along a linear transect across the submerged-emerged beach transition zone (cross-shore distance: 55 m) (red line in Fig. 7.1).

Overall, these two storm events were selected for analysis due to their similar wave conditions. Wave data (significant wave height - H_s; peak wave period - T_p; mean wave period - T_m; wave direction - *Dir*) were downloaded from the Copernicus Marine Environment Monitoring Service (CMEMS) (Korres et al., 2021) at a virtual buoy located offshore of the Poetto beach (Ruju et al., 2022). The virtual buoy corresponds to a specific CMEMS grid node (coordinates: 39° 11' 15'' Noth; 9° 12' 30'' East) (red dot in Fig. 7.1). Similarly, wind data (wind speed at 10 m above the ground level - U_{10}; wind direction - Dir_w) were download from the ERA5 reanalysis dataset (Hersbach et al., 2023), produced by the European Centre for Medium-Range Weather Forecast (ECMWF), at a virtual buoy located further offshore than the one used for wave data virtual buoy (coordinates: 39° 00' 00'' Noth; 9° 12' 30'' East). Both wave and wind data cover the period from 27 to 29 October 2018 and from 19 to 21 January 2020, encompassing both the pre-storm and storm event. These datasets were considered representative of the environmental conditions during the two storm events (a complete list of wave and wind data used in this study is provided in Appendix C of the thesis).

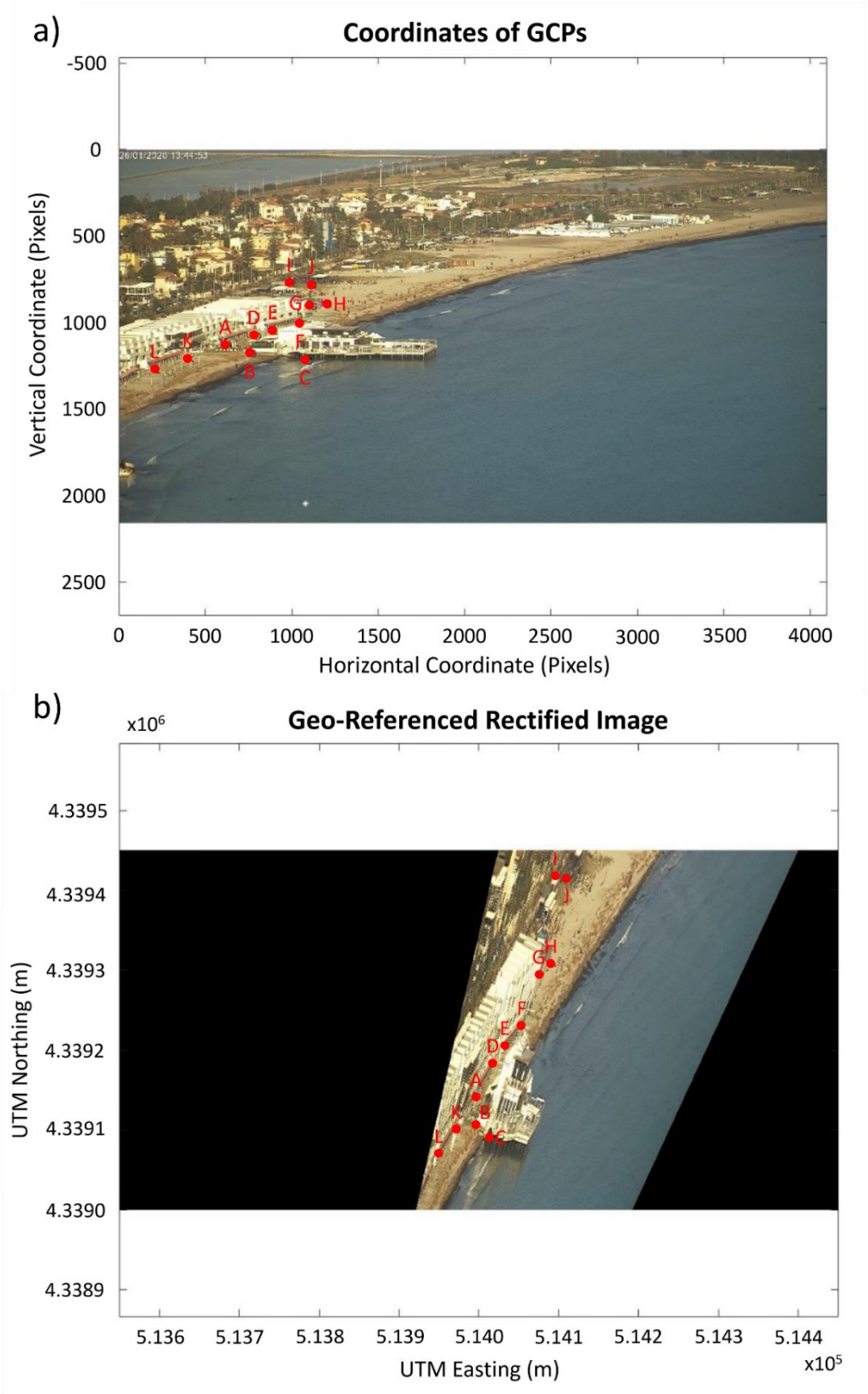

Figure 7.2 - Location of the GCPs (Ground Control Points) on the western Poetto beach used to rectify and georeference the images (snapshots) acquired by the digital camera of the coastal video monitoring system.

Figure 7.3 - Snapshot acquired by the coastal video monitoring system during the storm event that occurred on 29 October 2018.

Figure 7.4 - Snapshot acquired by the coastal video monitoring system during the storm event that occurred on 21 January 2020.

7.4.2 Hydrodynamic circulation: Model Set-up

Models Delft3D-WAVE (Booij et al., 1999; Ris et al., 1999) and Delft3D-FLOW (Lesser et al., 2004) were used to simulate the hydrodynamic circulation at the Poetto beach during the two storm events. Further details regarding the formulations adopted by the two models (hydrodynamic coupled to wave) can be found in Chapter 6.2 of the thesis.

Two computational grids were used to represent the two storm events (Fig. 7.5). The first grid A (green grid in Fig. 7.5a) is characterised by a large mesh with an average cell size of approximately 150 x 125 m. Computational grid A was designed with curvatures to align with the coastal morphology of the study area (red line in Fig. 7.5). The offshore boundary of the grid A was defined by considering the typical wave conditions of the study area, in particular the length of waves. Computational grid A, coupled with Computational grid B, was used to simulate wave and wind conditions from the offshore boundaries of the modelled domain. The second grid B (blue grid in Fig. 7.5a) is characterised by a more refined mesh with an average cell size of approximately 30 x 30 m. Computational grid B was designed as a structured mesh with uniform spacing, with curvature introduced only along the landward axis to conform to the shoreline morphology. More precisely, Computational grid B were used to estimate the hydrodynamic circulation patterns in Poetto beach.

In each simulation, wave (H_s, T_p and Dir) and wind (U_{10} and Dir_w) conditions were applied at the offshore boundaries of the modelled domain for a duration of 3 days (72 hours), in order to simulate the conditions before and during the storm event (from 27 to 29 October 2018; from 19 to 21 January 2020). The bathymetry adopted in the two grids, constant in each simulation, ranges from 1 m to approximately -70 m in Grid A, and from 2.5 m to -25 m in Grid B (Fig. 7.5). The bathymetric data derive both from bathymetric surveys carried out near the coastline (see Chapter 3.4 of the thesis) and from the European Marine Observation and Data Network - EMODnet (https://emodnet.ec.europa.eu/geoviewer). Similarly, the shoreline position of Poetto beach was acquired from topographic surveys using a DGPS (Differential Global Position System) connected in real time (Real Time Kinematic - RTK) to a correction network (NETGEO network) (see Chapter 3.3 of the thesis). The portions of the coastline not covered by topographic surveys were integrated using the shapefile of the coastline of Sardinia Island provided by the Geoportal of “Regione Autonoma della Sardegna” (https://www.sardegnageoportale.it/accessoaidati/downloaddati).

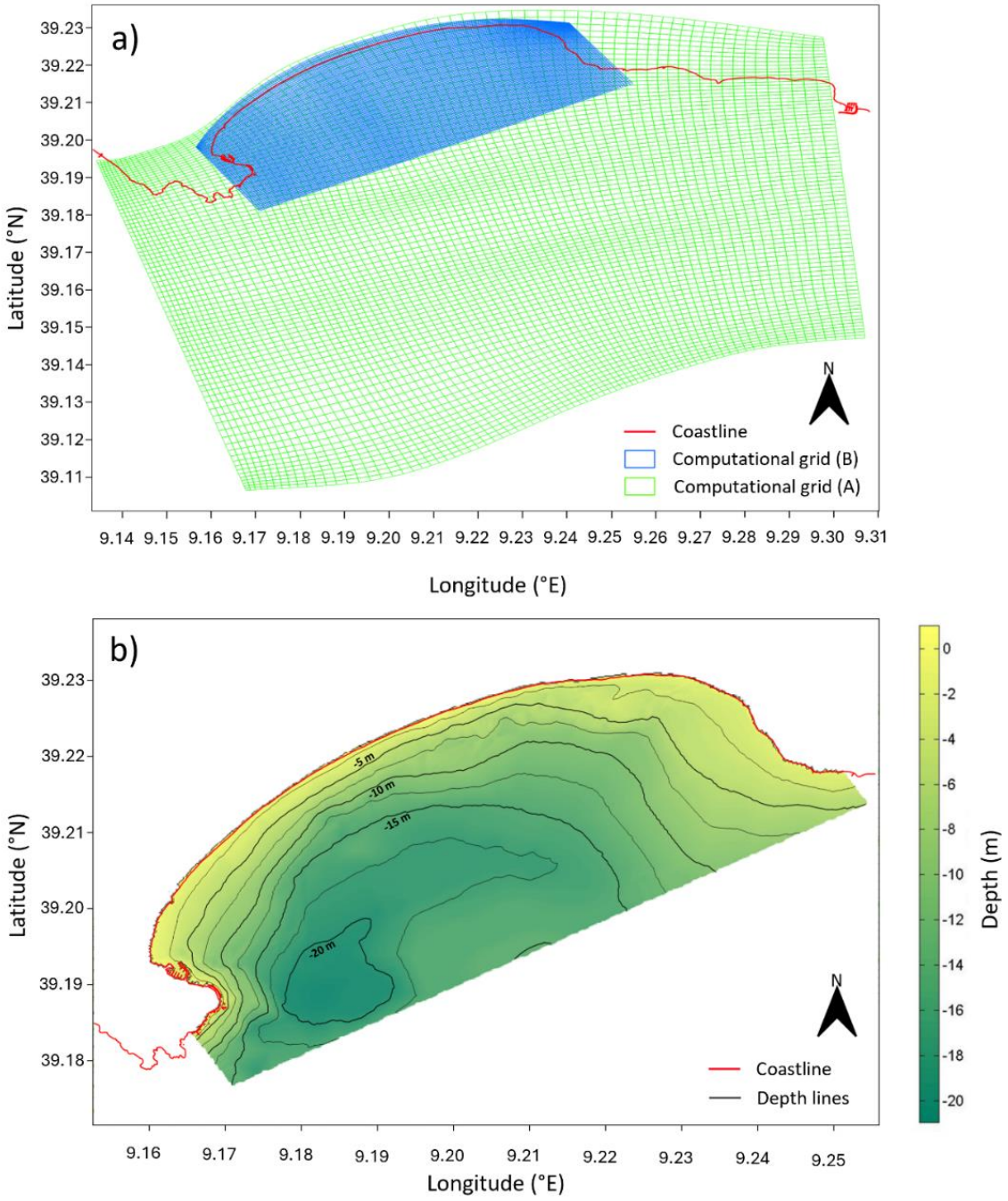

Figure 7.5 - **(a)** Computational grids A (green) and B (blue) used for the hydrodynamic model, coupled to wave model, at the Poetto Beach. **(b)** Bathymetry used for Computational grid B to estimate hydrodynamic circulation in Poetto beach.

7.5 Results

7.5.1 Image analysis

Time-stack images and georeferenced-rectified snapshots enabled to the identification and analysis of wave-swash processes during the two storm events (29 October 2018 and 21 January 2020). Although the wave conditions were similar, the two events resulted in different effects on the backshore.

The comparison of georeferenced-rectified snapshots (Fig. 7.6) showed that, during the storm event of 29 October 2018, the berm was completely overtopped, resulting in the flooding of the backshore (Fig 7.6a). On the other hand, no berm overtopping occurred during the storm event of 21 January 2020, and the backshore remained unflooded (Fig 7.6b). More precisely, during the first storm event, no seagrass wracks were observed along the emerged beach. Conversely, the second storm event was characterised by huge accumulations of beach-cast (mainly remains of *Arundo donax* and *Posidonia oceanica*), deposited in ridges parallel to the shoreline.

The analysis of the processed time-stack images (Fig. 7.7), referred to the cross-shore transect (red line in Fig. 7.6), highlighted that during the first storm event (29 October 2018) incoming waves continued to supply volumes of water to the already flooded backshore through successive wave uprush over the berm (Fig. 7.7a). On the other hand, during the second storm event (21 January 2020), the incoming waves nearly reached the top of the berm but did not cause flooding of the backshore. This was likely due to the presence of beach-cast accumulation along the backshore, which acted as a barrier limiting wave overtopping (Fig. 7.7b).

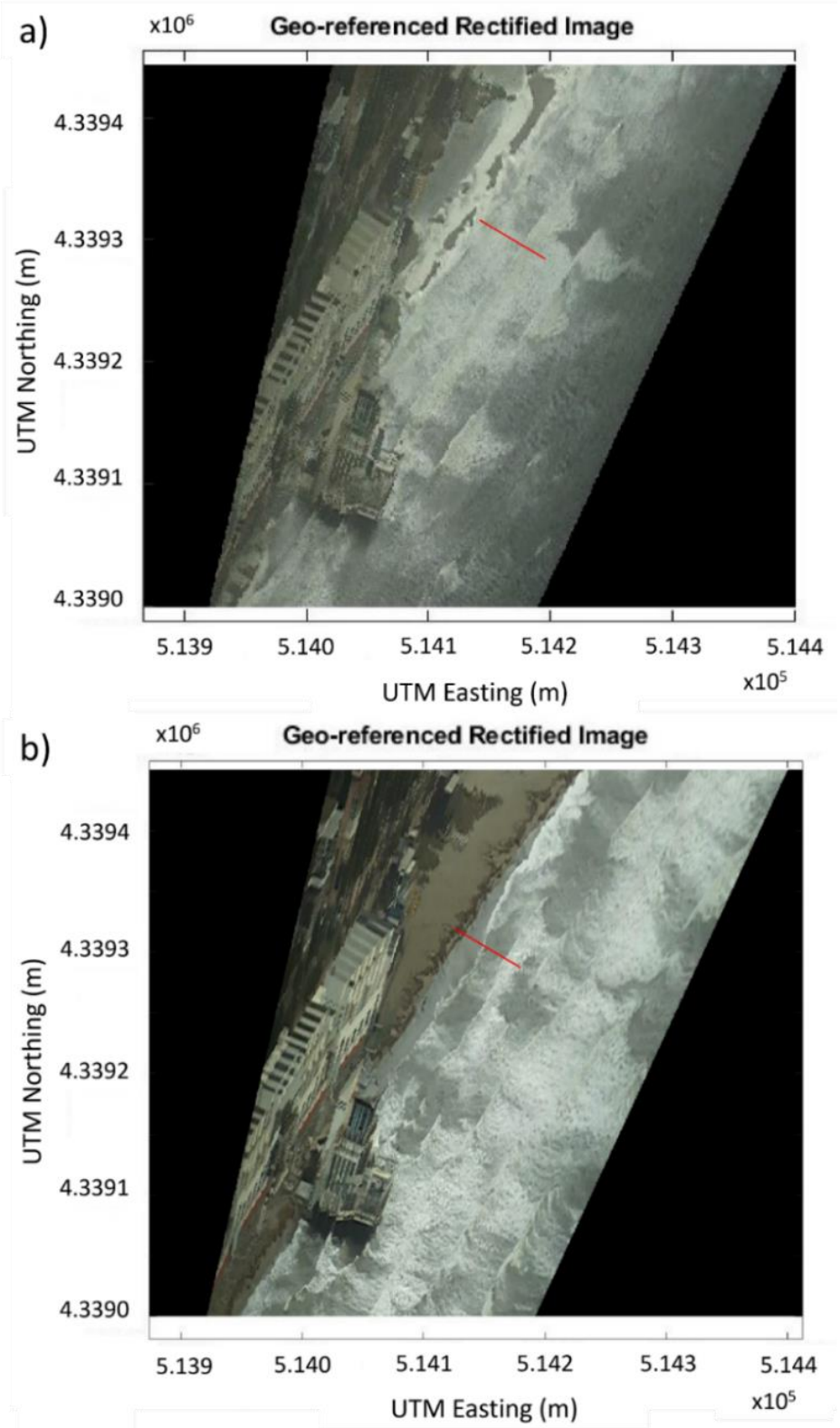

Figure 7.6 - Georeferenced-rectified snapshots acquired by the coastal video monitoring system during the two storm events: **(a)** 29 October 2018; **(b)** 21 January 2020. The red line shows the linear transect used for processing the time-stacks images at each time interval (modified from Trogu et al., 2024).

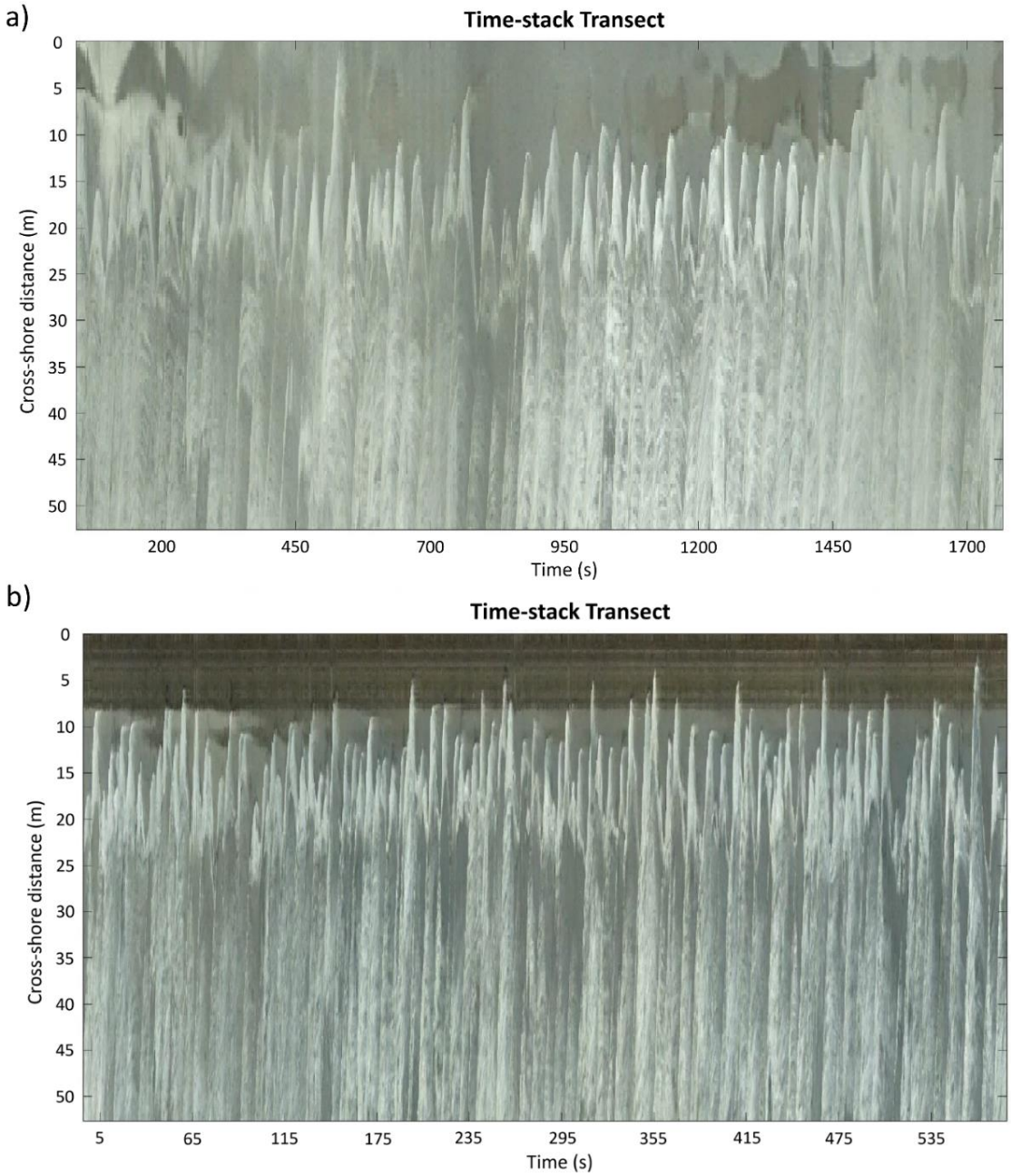

Figure 7.7 - Time-stack images processed along the linear transect corresponding to the two storm events: **(a)** 29 October 2018; **(b)** 21 January 2020 (modified from Trogu et al., 2024).

As mentioned above, both storm events are characterised by similar wave conditions (Table 7.1; Fig. 7.8). Table 7.1 shows the wave data (H_s, T_p, T_m and *Dir*) referred to daily average values, daily peak values and values corresponding to the time interval recorded by the camera. The daily average value of significant wave height (H_s) is similar for the 2018 (H_s = 2.2 m) and 2020 (H_s = 2.7 m) storm event. Likewise, the daily average value of the peak and mean wave period (T_p and T_m) appears similar: T_p = 8.9 s and T_m = 5.3 s for the 2018 storm event; T_p = 8.5 s and T_m = 6.0 s for the 2020 storm event (Table 7.1).

In addition, both storm events are characterised by a mean wave direction from the south-eastern sector (Table 7.1; Fig. 7.8). During the 2018 storm event, the daily average value of *Dir* was 167°, whereas it was 184° during the specific time interval recorded by the camera. On the other hand, during the 2020 storm event, the daily average value of *Dir* was 137°, whereas it was 138° during the camera recording time interval. Therefore, these values indicate that the mean wave direction during the 2020 storm event showed less lateral wave dispersion compared to that of the 2018 storm event (Fig. 7.8d).

Table 7.1

Wave data (significant wave height - H_s; peak wave period - T_p; mean wave period - T_m; wave direction - *Dir*) referred to the two storm events (29 October 2018; 21 January 2020): daily average values, daily peak values and values associated to the time interval recording by camera.

	29 October 2018			21 January 2020		
Wave parameter	**Daily average value**	**Daily peak value**	**Recorded value (camera time interval)**	**Daily average value**	**Daily peak value**	**Recorded value (camera time interval)**
***H_s* (m)**	2.2	2.9	2.5	2.7	2.9	2.8
***T_p* (s)**	8.9	9.2	9.2	8.5	9.2	8.4
***T_m* (s)**	5.3	6.4	5.0	6.0	6.2	6.1
***Dir* (°)**	167	147	184	137	138	138

The comparison of the significant wave height (H_s) values during the two storm events highlighted that the H_s values were consistently lower during the 2018 event compared to the 2020 event (Fig. 7.8a). A similar pattern is observed for the values of mean wave period (T_m) (Fig. 7.8c). More precisely, during the 2018 storm event, the peak of wave intensity was reached with values of H_s = 2.9 m and T_m = 6.4 s. After the peak, wave intensity gradually decreased, reaching values of H_s = 2.5 m and T_m = 5.0 s at the camera recording point (yellow dots in Fig. 7.8). Similarly, during the 2020 storm event, the peak of wave intensity was reached with values of H_s = 2.9 m and T_m = 6.2 s. At the camera recording point (yellow dots in Fig. 7.8), values of H_s = 2.8 m and T_m = 6.1 s were observed. Likewise, the values of the peak wave period reached during both storm events also appear comparable at the values referred to camera recording point (T_p = 9.2 s for the 2018 event and T_p = 8.4 s for the 2020 event) and remain nearly constant throughout the day of each event (Fig. 7.8b). Overall, the temporal evolution of wave parameter during the 2020 storm event appears more consistent and regular than during the 2018 storm event (Fig. 7.8).

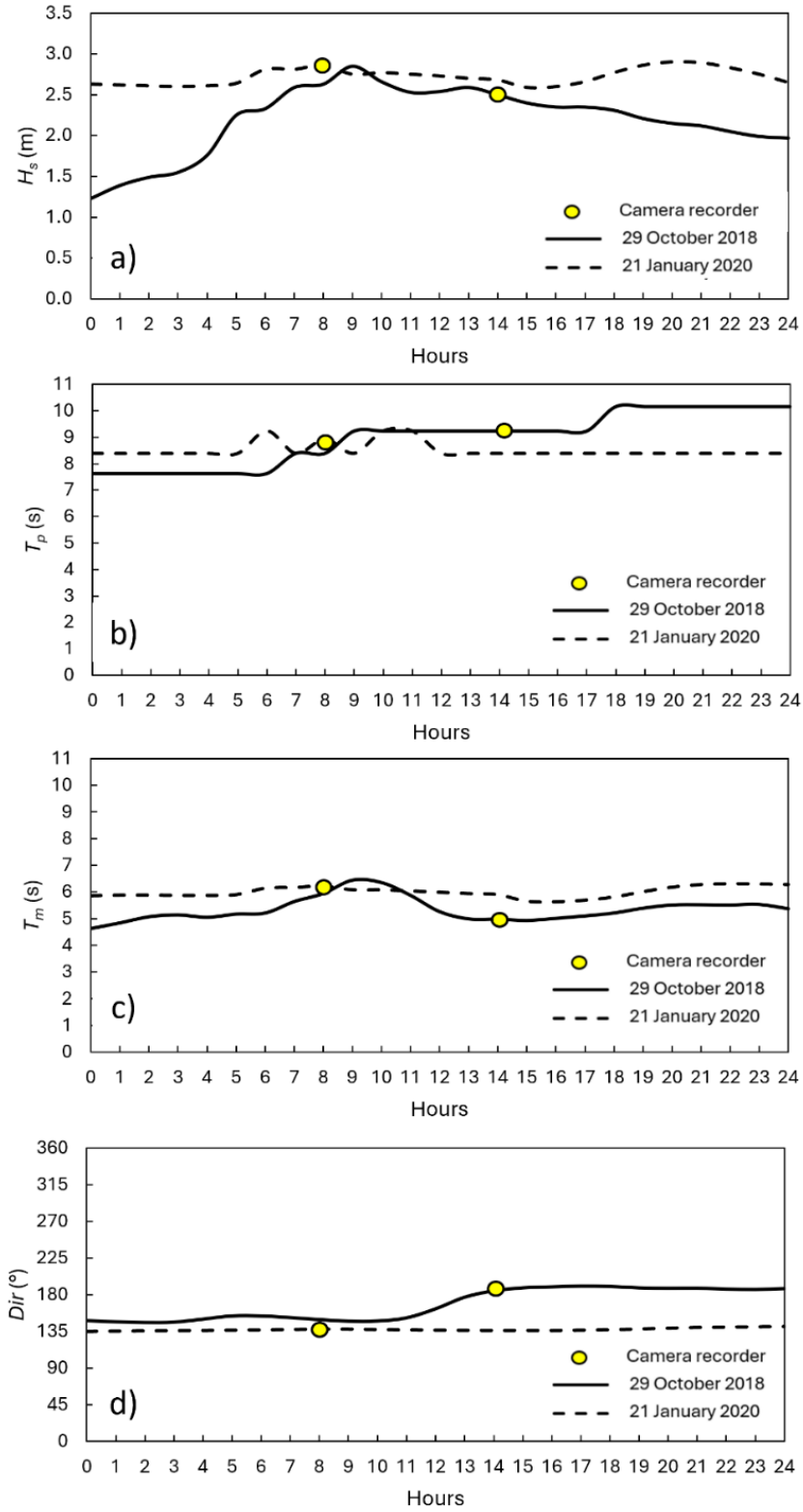

Figure 7.8 - Values of **(a)** significant wave height (H_s), **(b)** peak wave period (T_p), **(c)** mean wave period (T_m) and **(d)** wave direction (*Dir*) of the two storm events considered (29 October 2018; 21 January 2020). The yellow dot represents the wave data associated with the time interval recorder by camera.

The comparison of the wind speed (U_{10}) values during the two storm events highlighted that the U_{10} values were higher during the 2018 event compared to the 2020 event (Table 7.2; Fig. 7.9a). More precisely, during the 2018 storm event, the peak of wind speed was reached at U_{10} = 15.2 m/s prior to the camera recording point, where it reached U_{10} = 13.2 m/s. On the other hand, during the 2020 storm event, the peak of wind speed (U_{10} = 6.6 m/s) was reached after the camera recording point (U_{10} = 6.0 m/s) (Table 7.2).

On the other hand, the values of wind direction (Dir_w) appeared more consistent during the 2020 event than the 2018 event (Table 7.2; Fig. 7.9b). During the 2018 storm event, the daily average value was 209°, while the Dir_w value during the time interval recorded by the camera value was 240°. On the other hand, during the 2020 storm event, the daily average value Dir_w was 277°, and 259° during the camera recording time interval. Therefore, the wind direction during the 2018 storm event was predominately from the southern and south-western sectors, whereas during the 2020 event it was mainly from the western and south-western sectors (Fig. 7.10b).

Table 7.2

Wind data (wind speed - U_{10}; wind direction - U_{10}) referred to the two storm events (29 October 2018; 21 January 2020): daily average values, daily peak values and values associated to the time interval recording by camera.

	29 October 2018			21 January 2020		
Wind parameter	**Daily average value**	**Daily peak value**	**Recorded value (camera time interval)**	**Daily average value**	**Daily peak value**	**Recorded value (camera time interval)**
U_{10} (m/s)	12.0	15.2	13.2	5.2	6.6	6.0
Dir_w (°)	209	245	240	277	296	259

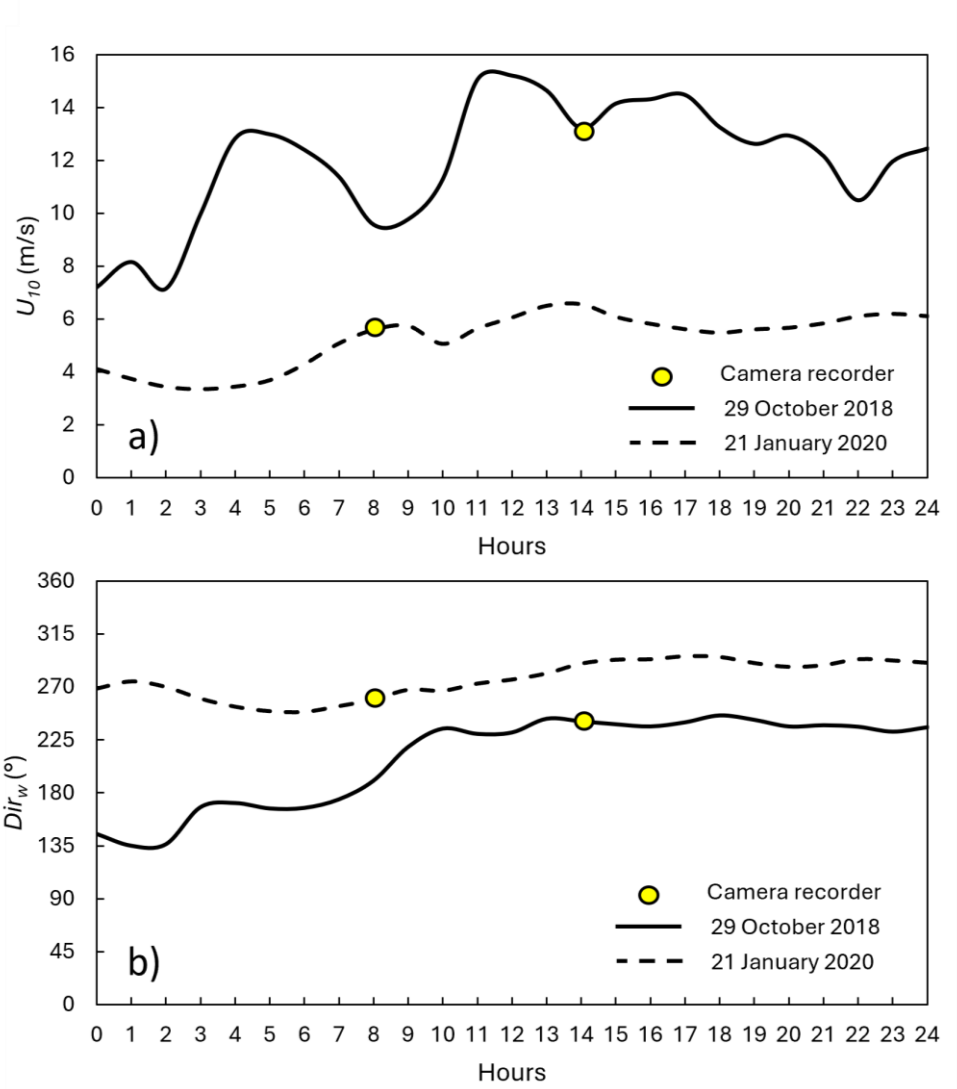

Figure 7.9 - Values of **(a)** wind speed (U_{10}) and **(b)** wind direction (Dir_w) of the two storm events considered (29 October 2018; 21 January 2020). The yellow dot represents the wind data associated with the time interval recorder by camera.

7.5.2 Hydrodynamic circulation on Poetto beach

The analysis of wave and wind data from the Copernicus Marine Environment Monitoring Service (CMEMS) (Korres et al., 2021) and ERA5 reanalysis dataset (Hersbach et al., 2023) enabled the estimation of hydrodynamic circulation at Poetto beach during the two storm events. Table 7.3 schematically shows the values of H_s, T_p, Dir, U_{10} and Dir_w at the beginning of the simulated event, during the camera recording time interval and at the end of the numerical simulation. A complete list of wave and wind data used for the numerical modelling is provided in Appendix C of the thesis.

Table 7.3
Wave and wind parameters used for numerical modelling at Poetto Beach during the two storm events (29 October 2018; 21 January 2020). The table highlights the values at the beginning of the simulated event, during the camera recording time interval and at the end of the simulated event.

Date of simulated events		**27 to 29 October 2018**	**19 to 21 January 2020**
Simulation duration (hours)		72	72
H_s (m)	Start of the simulated event	0.3	0.2
H_s (m)	Camera recording point	2.5	2.9
H_s (m)	End of the simulated event	2.0	2.7
T_p (s)	Start of the simulated event	5.2	4.7
T_p (s)	Camera recording point	9.2	8.4
T_p (s)	End of the simulated event	10.2	8.4
Dir (°)	Start of the simulated event	150	209
Dir (°)	Camera recording point	184	138
Dir (°)	End of the simulated event	187	141
U_{10} (m/s)	Start of the simulated event	1.4	3.2
U_{10} (m/s)	Camera recording point	13.2	6.0
U_{10} (m/s)	End of the simulated event	12.4	6.1
Dir_w (°)	Start of the simulated event	178	275
Dir_w (°)	Camera recording point	240	259
Dir_w (°)	End of the simulated event	236	291

During the camera recording time interval of the 2018 storm event, waves predominantly approached from the southern sector of the modelled domain (white arrows in Fig. 7.10a), with values of significant wave height of approximately 2.5 m (Table 7.3). The values of H_s gradually decrease as the waves propagated toward the eastern and western coastal areas of Poetto beach (the area monitored by the coastal video monitoring system). However, this decrease was not observed in the central area of the modelled domain, where waves reached the shoreline with higher values of significantly wave height H_s. Numerical simulation showed the development of longshore currents flowing from west to east along the western and central sector of Poetto beach. These currents were interrupted by rip current systems offshore-oriented (white arrows in Fig. 7.10b). A similar

flow pattern was observed in the eastern sector of Poetto beach, although the directions of the longshore currents were opposite to that of the western and central sectors. Overall, during this storm event, the nearshore hydrodynamic circulation showed a prevalent east-west flow direction (Fig. 7.10b).

During the camera recording time interval of the 2020 storm event, waves primarily approached from the south-eastern sector of the modelled domain (white arrows in Fig. 7.11a), with values of significant wave height of about 2.8 m (Table 7.3). As with the 2018 storm event, the values of H_s gradually decrease toward the eastern and western sectors of Poetto beach, while this attenuation was not observed in the central area of the modelled domain. The numerical simulation showed a hydrodynamic circulation pattern similar to that of the 2018 storm event (white arrows in Fig. 7.11b). However, the western and central sectors of Poetto beach during this event were characterised by the presence of multiple offshore-oriented rip current systems.

The 2018 storm event was associated with stronger longshore and rip current systems compared to those estimated during the 2020 storm event (Fig. 7.10b; 7.11b). Overall, the values of depth averaged velocity for both simulated events ranged approximately from 0.2 m/s to 0.7 m/s. However, in both cases, the maximum values of depth averaged velocity were reached at the extremities of the beach, due to both the variation in bathymetry and the morphological characteristics of the coastline (particularly the presence of a rocky headland at the western part of the modelled domain).

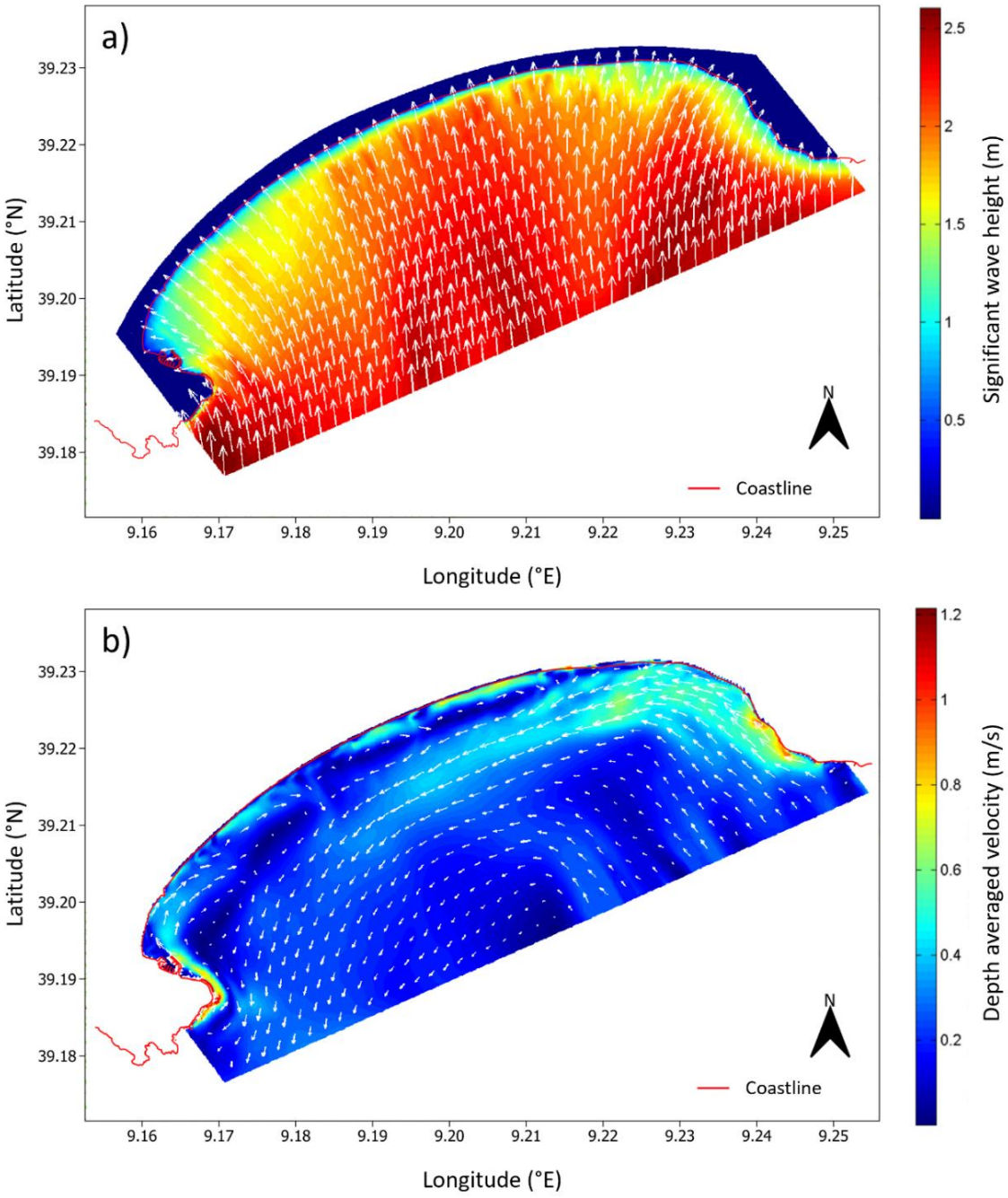

Figure 7.10 - Numerical simulation of wave and wind conditions during the storm event of 29 October 2018. The hydrodynamic characteristics shown in both Panels **(a)** and **(b)** represent the conditions at the exact time of the camera recording.

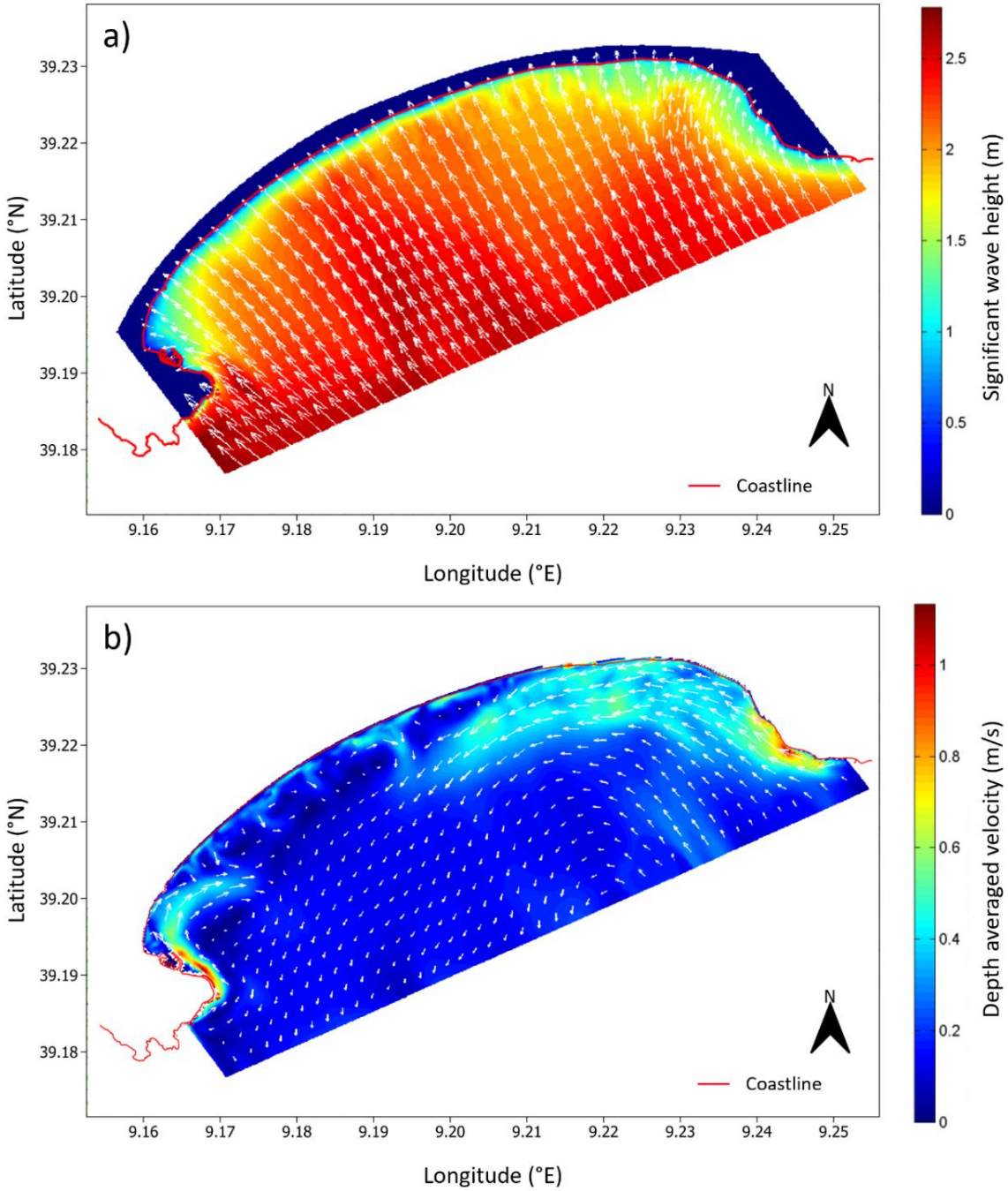

Figure 7.11 - Numerical simulation of wave and wind conditions during the storm event of 21 January 2020. The hydrodynamic characteristics shown in both Panels **(a)** and **(b)** represent the conditions at the exact time of the camera recording.

7.6 Discussion

The analysis of snapshot acquired by the coastal video monitoring system led to a further investigation into the role of beach-cast in coastal flooding events. Wave data downloaded from CMEMS showed that both storm events (2018 and 2020) were characterised by similar wave conditions (Table 7.1). However, the processed images (snapshots and time-stack images) revealed that the two events produced different effects along the backshore. The first storm event (2018) caused widespread flooding due to wave overtopping of the berm. On the other hand, the second storm event (2020) did not result in flooding, likely due to the abundant accumulations of seagrass remains and river reeds aligned parallel to the shoreline. Therefore, the presence of sedimented banquettes and woody debris deposited along the backshore contributed to mitigate wave overtopping processes.

The absence or presence of beach-cast denotes their influence on wave processes acting on the beach. In fact, this vegetal material can change the morphological characteristics of beaches, such as beach slope and permeability (Trogu et al., 2023). In the study of Ruju et al. (2022), conducted on Poetto beach, the authors demonstrated that sedimented banquettes on the backshore contribute the drainage of water volumes supplied by waves overtopping the berm. Infiltrometric measurements carried out in the absence and presence of banquettes confirmed that seagrass wracks have a higher permeability coefficient than the underlying sediment (Ruju et al., 2022), thus reducing beach flooding events.

Nevertheless, the sedimentary structures formed on the backshore did not always prevent the wave overtopping processes over the berm. Field observations carried out before (Fig. 7.12) and after the storm event (Fig. 7.13) occurred on 21 January 2020, revealed that the deposits of river reeds and seagrass remains, originally arranged parallel to the shoreline, were redistributed along the backshore by the wave motion following the storm. This redistribution led to the formation of cusps mainly composed of coarse material, which further sedimented and intertwined the river reeds and seagrass remains (Fig. 7.13).

Numerical modelling of the two storm events, particularly the one that occurred in 2020, highlighted how the presence of longshore currents and offshore-oriented rip current systems likely played a significant role in transporting, redistributing and depositing beach-cast (mainly seagrass remains and river reeds) along the shoreline (Fig. 7.14). Therefore, incorporating the influence of longshore and rip current on the role of beach-cast deposition may be crucial for understanding the processes governing the deposition of this vegetal material along the shore, as well as for assessing the short and long-term impacts of storm events on coastal environments.

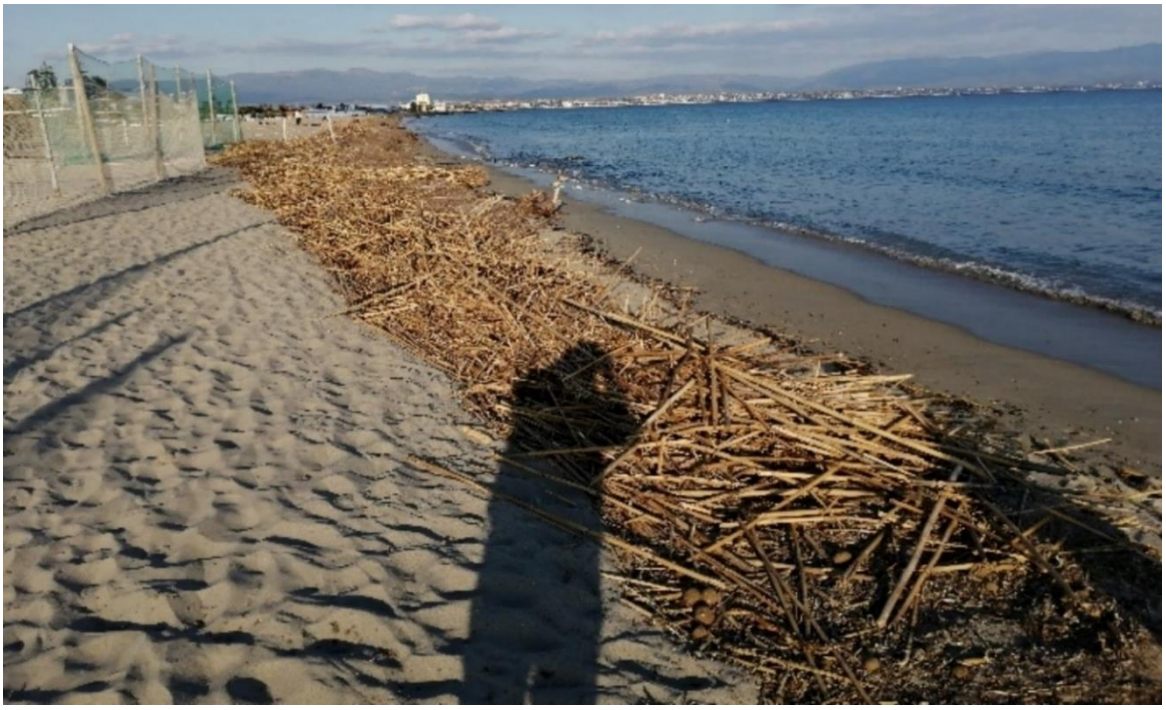

Figure 7.12 - Accumulations of beach-cast (seagrass remains and river reeds) along the backshore in Poetto beach before the storm event that occurred on 21 January 2020 (from Trogu et al., 2024).

Figure 7.13 - Sedimentary structures along the backshore of Poetto beach after the storm event on 21 January 2020. The red dotted line highlights the shape of the cusps formed by incoming waves. These cusps are mainly composed of coarse sediments and beach-cast, which were laterally redistributed along the backshore (modified from Trogu et al., 2024).

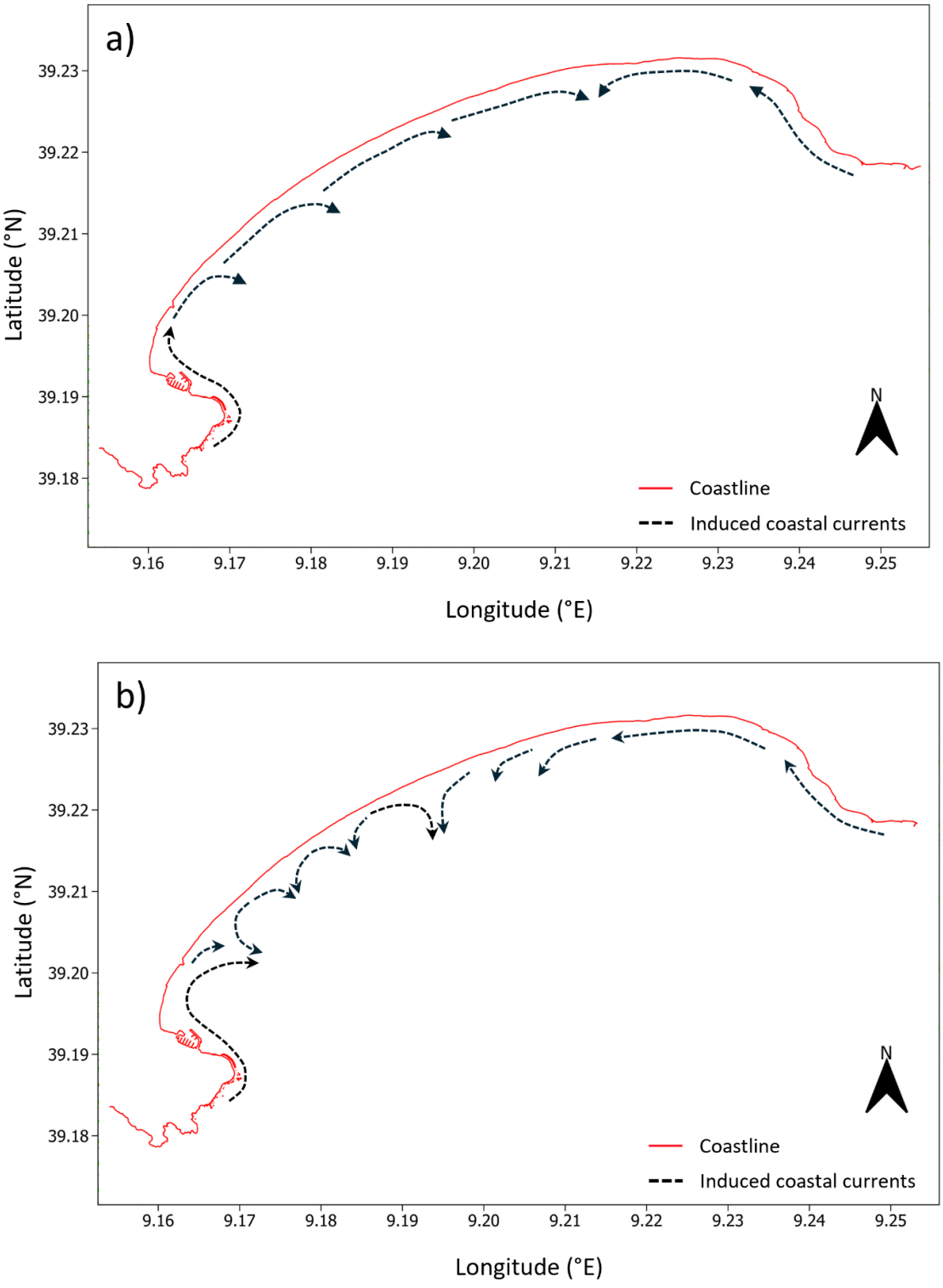

Figure 7.14 - Schematic representation of the hydrodynamic circulation (main induced-coastal currents) at the Poetto beach during the two storm events: **(a)** 29 October 2018; **(b)** 21 January 2020. The representations refer to the exact time of the camera recording.

7.7 Conclusions

Overall, this study on the seagrass remains and woody debris observed along Poetto beach has provided valuable insights and recommendations for the management, protection and conservation of beach ecosystems. The comparison between the two storm events serves as an excellent example of a nature-based solution: the presence of abundant accumulations of vegetal material (mainly *Arundo donax* reeds and *Posidonia oceanica* remains) contributed significantly to mitigating beach flooding and beach erosion.

The growing tourism along the Mediterranean coastlines has led local authorities responsible for beach management to implement regular beach cleaning operations in response to beach users' preferences. However, considering the effectiveness of seagrass berms in mitigating flooding events, their removal should be more carefully managed, particularly in highly urbanised areas such as Poetto beach, since such operations can significantly compromise the beach's resilience to extreme events. Therefore, this study showed that preserving seagrass wracks and river reeds on the backshore can serve as an effective coastal management strategy to enhance beach resilience and protect both beach users and nearby artificial structures.

These considerations are particularly relevant in the context of ongoing sea level rise, which increases the vulnerability of coastal areas to erosion and flooding events. Rather than using solely artificial interventions, incorporating natural strategies (e.g., maintaining banquettes) into coastal planning not only mitigates the immediate impacts of storm events but also contributes long-term adaptation by promoting sediment retention, shoreline stability and ecological continuity.

Chapter 8: CONCLUSIONS

This study highlighted the main morphometric and hydrodynamic characteristics of microtidal Mediterranean beaches along a wide coastal stretch. It also highlighted the fundamental role of *Posidonia oceanica* accumulations (banquettes) deposited and sedimented on the emerged beach (backshore), in mitigating beach flooding during storm events and in limiting coastal erosion. The research was carried out using a multidisciplinary scientific approach that integrates coastal geomorphology, hydrodynamics, sedimentological processes and their connection with the ecological context. The study area analysed in this thesis is characterised by the presence of an extensive *Posidonia oceanica* meadow and a wide variety of beaches, which differ in their geomorphological and sedimentological characteristics, as well as coastal dynamics. All this makes Southern Sardinia an ideal area for the application of this methodological approach, which includes field observations, topographic and bathymetric surveys, spatio-temporal analysis of aerial orthophotos and images acquired from coastal video monitoring systems, as well as numerical modelling of hydrodynamic and wave processes.

Chapter 4 aimed to create the basis for a multidisciplinary study of the microtidal beaches along this coastal stretch, which covers the entire southern area of Sardinia (from Cape Teulada to Cape Carbonara). The main intent was to address specific gaps in scientific knowledge regarding these types of beaches. For this propose, a detailed morphometric analysis and classification comparison of 79 microtidal beaches was performed to estimate their degree of embaymentisation, a parameter that reflects their degree of natural protection from wave action. This analysis also enabled the identification of the main types of hydrodynamic circulation within the surf zone, highlighting which beaches are most prone to the development of cellular rip current systems. Additionally, anthropogenic alteration was assessed for all the beaches analysed, differentiating between natural and anthropised embayments, where artificial structures or coastal defences (breakwaters, groynes, ports, harbours, marinas, etc.) have altered the beach geometry.

In this context, Chapter 5 aimed to calculate the rates of shoreline movement (accretion and retreat) of the previously identified 79 beaches. By applying the Digital Shoreline Analysis System (DSAS), the obtained statistical parameters highlight a general stability of the shorelines along southern coast of Sardinia, with limited rates of both retreat and accretion. However, some beaches diverge from this general trend, showing greater shoreline variability due to a combination of anthropogenic and natural factors.

Since part of the study area is characterised by embayed beaches bordered by rocky headlands (or artificial structures), Chapter 6 analysed the influence of wind forcing on the

formation and development of rip current systems in these environments using numerical modelling. Hydrodynamic and wave simulations revealed that both the intensity and direction of winds can significantly influence the hydrodynamic characteristics of the rip currents generated, which makes this analysis particularly important from the perspective of coastal management and beach user safety.

Finally, Chapter 7 presents a detailed analysis of the role of vegetal accumulations (beach-cast) on a Mediterranean microtidal urban beach (Poetto beach), through the analysis of images from a coastal video monitoring system and the simulation of wave and wind conditions using numerical modelling. Two storm events with similar wave conditions were compared, differing only in the presence or absence of beach-cast on the backshore (mainly composed of *Arundo donax* reeds and *Posidonia oceanica* remains). The results showed that the presence of these vegetal accumulations greatly limited the flooding of the emerged beach (backshore) during intense storm event, whereas beach flooding occurred in the event without banquettes. Numerical modelling also highlighted distinct circulation flow patterns, developing coastal longshore currents and rip current systems during the two storm events, which may explain the subsequent transport and movement of these vegetal materials along the shore observed during the 2020 storm event.

In conclusion, this thesis provides valuable insights that enhance the scientific understanding of coastal processes and offer practical tools for public institutions and authorities responsible for coastal management and civil protection. Moreover, the research also aims to contribute to the achievement of some Sustainable Development Goals outlined in the UN 2030 Agenda. In fact, coastal areas worldwide, particularly in the Mediterranean Sea, have been increasingly experiencing the intensified effects of climate change over recent decades. These impacts include sea level rise and a greater frequency and intensity of extreme storm events, often occurring during unexpected periods. For these reasons, the implementation of integrated coastal management strategies is essential to mitigate and reduce these risks such as coastal erosion and flooding, ecosystem degradation and loss, as well as damage to artificial infrastructure along or near the coast.

Bibliography

Aagaard, T.; Holm, J., **1989**. Digitization of wave run-up using video records. *J. Coast. Res.* 5, 547–551.

Adams, P. N.; Inman, D. L.; Lovering, J. L., **2011**. Effects of climate change and wave direction on longshore sediment transport patterns in Southern California. *Climatic Change* 109 (Suppl. 1), 211–228. https://doi.org/10.1007/s10584-011-0317-0.

Akköprü, E.; Taş, M., **2023**. Coastal geomorphology and coastal erosion of Phaselis Ancient City and its surroundings. *Phaselis* 9, 51–63. https://doi.org/10.5281/zenodo.10407367.

Allan, J.C.; Komar, P.D.; Priest, G.R., **2003**. Shoreline variability on the high-energy Oregon Coast and its usefulness in erosion-hazard assessments. *J. Coast. Res.* 38, 83–105.

Amoudry, L., **2008**. A review on coastal sediment transport modelling. Liverpool, Proudman Oceanographic Laboratory (POL Internal Report No. 189).

Amoudry, L.O.; Souza, A.J., **2011**. Deterministic coastal morphological and sediment transport modeling: A review and discussion. *Rev. Geophys.* 49, RG2002. https://doi.org/10.1029/2010RG000341.

Andriolo, U.; Mendes, D.; Taborda, R., **2020**. Breaking wave height estimation from Timex images: Two methods for coastal video monitoring systems. *Remote Sens.* 12 (2), 204. https://doi.org/10.3390/rs12020204.

Antonioli, F.; Lo Presti, V.; Rovere, A.; Ferranti, L.; Anzidei, M.; Furlani, S.; Mastronuzzi, G.; Orru, P.E.; Scicchitano, G.; Sannino, G.; Spampinato, C.R.; Pagliarulo, R.; Deiana, G.; de Sabata, E.; Sansò, P.; Vacchi, M.; Vecchio, A., **2015**. Tidal notches in Mediterranean Sea: A comprehensive analysis. *Quaternary Sci. Rev.* 119, 66–84. https://doi.org/10.1016/j.quascirev.2015.03.016.

Armaroli, C.; Ciavola, P., **2011**. Dynamics of a nearshore bar system in the northern Adriatic: a video-based morphological classification. *Geomorphology* 126, 201–216, https://doi.org/10.1016/j.geomorph.2010.11.004.

Armenio, E.; De Serio, F.; Mossa, M.; Petrillo, A.F., **2019**. Coastline evolution based on statistical analysis and modeling. *Nat. Hazards Earth Syst. Sci.* 19, 1937–1953. https://doi.org/10.5194/nhess-19-1937-2019.

Aspioti, A.G.; Fourniotis, N.T., **2024**. A brief review of hydrodynamic circulation in the Mediterranean gulfs. *Dynamics* 4 (4), 873–888. https://doi.org/10.3390/dynamics4040045.

Astier, J.M.; Boudouresque, C.; Pergent, G.; Pergent-Martini, C., **2020**. Non-removal of the *Posidonia oceanica* "banquette" on a beach very popular with tourists: Lessons from Tunisia. *Sci. Rep. Port-Cros Natl. Park* 34, 15–21.

Austin, M.; Scott, T.; Brown, J.; Brown, J.; MacMahan, J.; Masselink, G.; Russell, P., **2010**. Temporal observations of rip current circulation on a macro-tidal beach. *Cont. Shelf Res.* 30 (9), 1149–1165. https://doi.org/10.1016/j.csr.2010.03.005.

Austin, M.J.; Masselink, G.; Scott, T.M.; Russell, P.E., **2014**. Water-level controls on macro-tidal rip currents. *Cont. Shelf Res.* 75, 28–40. https://doi.org/10.1016/j.csr.2013.12.004.

Astudillo-Gutierrez, C.; Gracia, V.; Cáceres, I.; Sierra, J.P.; Sánchez-Arcilla, A., **2022**. Beach profile changes induced by surrogate Posidonia Oceanica: Laboratory experiments. *Coast. Eng.* 175, 104144. https://doi.org/10.1016/j.coastaleng.2022.104144.

Astudillo-Gutierrez, C.; Rabionet, I.C.; Garcia, V.G.; Pedrico, J.P.S.; Conejo, A.S.-A., **2024**. Study of velocity changes induced by *Posidonia oceanica* surrogate and sediment transport implications. *J. Mar. Sci. Eng.* 12 (4), 569. https://doi.org/10.3390/jmse12040569.

Bagnold, R.A., **1940**. Beach formation by waves: Some model experiments in a wave tank. *J. Inst. Civ. Eng.* 15 (1), 27–75. https://doi.org/10.1680/ijoti.1940.14279.

Baig, M.R.I.; Ahmad, I.A.; Shahfahad; Tayyab, M.; Rahman, A., **2020**. Analysis of shoreline changes in Vishakhapatnam coastal tract of Andhra Pradesh, India: An application of digital shoreline analysis system (DSAS). *Ann. GIS* 26 (4), 361–376. https://doi.org/10.1080/19475683.2020.1815839.

Balestri, E.; De Battisti, D.; Vallerini, F.; Lardicci, C., **2015**. First evidence of root morphological and architectural variations in young *Posidonia oceanica* plants colonizing different substrate typologies. *Estuar. Coast. Shelf Sci.* 154, 205–213. https://doi.org/10.1016/j.ecss.2015.01.002.

Barnard, P.L.; Erikson, L.H.; Foxgrover, A.C.; Hart, J.A.F.; Limber, P.; O'Neill, A.C.; van Ormondt, M.; Vitousek, S.; Wood, N.;Hayden. M.K.; Jones, J.M., **2019**. Dynamic flood modeling essential to assess the coastal impacts of climate change. *Sci. Rep.* 9, 4309. https://doi.org/10.1038/s41598-019-40742-z.

Battjes, J.A., **1975**. Modelling of turbulence in the surf zone. In: *Proceedings of Symposium on Modelling Techniques, ASCE*. 1050–1061.

Bel, G.; Ashkenazy, Y., **2014**. The effects of psammophilous plants on sand dune dynamics. *J. Geophys. Res. Earth Surf.* 119 (7), 1636–1650. https://doi.org/10.1002/2014JF003170.

Benavente, J.; Ruiz de Alegría-Arzaburu, A.; Plomaritis, T.A.; Sedrati, M.; Ariffin, E.H., **2023**. Editorial: Coastal environment in a changing world. *Front. Mar. Sci.* 10, 1213689. https://doi.org/10.3389/fmars.2023.1213689.

Bini, M.; Rossi, V., **2021**. Climate change and anthropogenic impact on coastal environments. *Water* 13 (9), 1182. https://doi.org/10.3390/w13091182.

Biondo, M.; Buosi, C.; Trogu, D.; Mansfield, H.; Vacchi, M.; Ibba, A.; Porta, M.; Ruju, A.; De Muro, S., **2020**. Natural vs. anthropic influence on the multidecadal shoreline changes of Mediterranean urban beaches: Lessons from the Gulf of Cagliari (Sardinia). *Water* 12 (12), 3578. https://doi.org/10.3390/w12123578.

Bird, E.C.F., **2008**. *Coastal Geomorphology: An Introduction*. 2nd ed.; John Wiley & Sons, Ltd.: Chichester, UK.

Bitan, M.; Galili, E.; Spanier, E.; Zviely, D., **2020**. Beach nourishment alternatives for mitigating erosion of ancient coastal sites on the Mediterranean Coast of Israel. *J. Mar. Sci. Eng.* 8 (7), 509. https://doi.org/10.3390/jmse8070509.

Boak, E.H.; Turner, I.L., **2005**. Shoreline definition and detection: A review. *Coast. Eng.* 214, 688–703. https://doi.org/10.2112/03-0071.1.

Booij, N.; Ris, R.C.; Holthuijsen, L.H., **1999**. A third-generation wave model for coastal regions: 1. Model description and validation. *J. Geophys. Res. Oceans* 104 (C4), 7649–7666. https://doi.org/10.1029/98JC02622.

Borum, J.; Sand-Jensen, K.; Binzer, T.; Pedersen, O.; Greve, T.M., **2006**. Oxygen movement in seagrasses. In: *Seagrasses: Biology, Ecology and Conservation*; Larkum, A.W.D., Orth, R.J., Duarte, C.M., Eds.; Springer: Dordrecht, The Netherlands; pp. 255–270. https://doi.org/10.1007/978-1-4020-2983-7_10.

Boudouresque, C.F.; Meinesz, A., **1982**. Découverte de l'herbier de Posidonie. *Cah. Parc Nation. Port-Cros*, Fr., 4, 1–79.

Boudouresque, C.F.; Pergent, G.; Pergent-Martini, C.; Ruitton, S.; Thibaut, T.; Verlaque, M., **2016**. The necromass of the *Posidonia oceanica* seagrass meadow: fate, role, ecosystem services and vulnerability. *Hydrobiologia* 781, 25–42. https://doi.org/10.1007/s10750-015-2333-y.

Boudouresque, C.F.; Ponel, P.; Astruch, P.; Barcelo, A.; Blanfuné, A.; Geoffroy, D.; Thibaut, T., **2017**. The high heritage value of the Mediterranean sandy beaches, with a particular focus on the Posidonia oceanica "banquettes": A review. *Sci. Rep. Port-Cros Natl. Park* 31, 23–70.

Bouguet, J.Y., **2022**. Camera Calibration Toolbox for Matlab (1.0). Caltech DATA. https://doi.org/10.22002/D1.20164.

Bowen, A.J., **1969**. Rip currents: 1. Theoretical investigations. *J. Geophys. Res.* 74 (23), 5467–5478. https://doi.org/10.1029/JC074i023p05467.

Bowen, A.J.; Inman, D.L., **1969**. Rip currents: 2. Laboratory and field observations. *J. Geophys. Res.* 74 (23), 5479–5490. https://doi.org/10.1029/JC074i023p05479.

Bowman, D.; Guillén, J.; López, L.; Pellegrino, V., **2009**. Planview geometry and morphological characteristics of pocket beaches on the Catalan coast (Spain). *Geomorphology* 108, 191–199. https://doi.org/10.1016/j.geomorph.2009.01.005.

Bowman, D.; Rosas, V.; Pranzini, E., **2014**. Pocket beaches of Elba Island (Italy) - Planview geometry, depth of closure and sediment dispersal. *Estuar. Coast. Shelf Sci.* 138, 37–46. https://doi.org/10.1016/j.ecss.2013.12.005.

Brambilla, W., **2015**. Caratterizzazione morfodinamica della Spiaggia del Poetto. *PhD Thesis*, University of Cagliari, Cagliari, Italy.

Brambilla, W.; Van Rooijen, A.; Simeone, S.; Ibba, A.; De Muro, S., **2016**. Field observations, video monitoring and numerical modeling at Poetto Beach, Italy. *J. Coast. Res.* 75, 825–829. https://doi.org/10.2112/SI75-166.1.

Brander, R.W., **1999**. Field observations on the morphodynamic evolution of a low-energy rip current system. *Mar. Geol.* 157 (3–4), 199–217. https://doi.org/10.1016/S0025-3227(98)00152-2.

Brewster, B.C.; Gould, R.E.; Brander, R.W., **2019**. Estimations of rip current rescues and drowning in the United States. *Nat. Hazards Earth Syst. Sci.* 19, 389-397. https://doi.org/10.5194/nhess-19-389-2019.

Brocchini, M.; Dodd, N., **2008**. Nonlinear shallow water equation modeling for coastal engineering. *J. Waterw. Port Coast. Ocean Eng.* 134 (2), 104–120. https://doi.org/10.1061/(ASCE)0733-950X(2008)134:2(104).

Broekema, Y.B.; Giardino, A.; van der Werf, J.J.; van Rooijen, A.A.; Vousdoukas, M.I.; van Prooijen, B.C., **2016**. Observations and modelling of nearshore sediment sorting processes along a barred beach profile. *Coast. Eng.* 118, 50–62. https://doi.org/10.1016/j.coastaleng.2016.08.009.

Bruneau, N.; Bertin, X.; Castelle, B.; Bonneton, P., **2014**. Tide-induced flow signature in rip currents on a meso-macrotidal beach. *Ocean Model.* 74, 53–59. https://doi.org/10.1016/j.ocemod.2013.12.002.

Bruneau, N.; Castelle, B.; Bonneton, P.; Pedreros, R.; Almar, R.; Bonneton, N.; Sénéchal, N., **2009**. Field observations of an evolving rip current on a meso-macrotidal well-developed inner bar and rip morphology. *Cont. Shelf Res.* 29 (14), 1650–1662. https://doi.org/10.1016/j.csr.2009.05.005.

Bulleri, F.; Chapman, M.G., **2010**. The introduction of coastal infrastructure as a driver of change in marine environments. *J. Appl. Ecol.* 47 (1), 26–35. https://doi.org/10.1111/j.1365-2664.2009.01751.x.

Buosi, C.; Ibba, A.; Passarella, M.; Porta, M.; Ruju, A.; Trogu, D.; De Muro, S., **2019a**. Geomorphology, beach classification and seasonal morphodynamic transition of a Mediterranean gravel beach (Sardinia, Gulf of Cagliari). *J. Maps* 15 (2), 165–176. https://doi.org/10.1080/17445647.2019.1567402.

Buosi, C.; Porta., M.; Trogu., D.; Casti, M.; Ferraro, F.; De Muro, S.; Ibba, A., **2019b**. Data on coastal dunes vulnerability of eleven microtidal wave-dominated beaches of Sardinia (Italy, western Mediterranean). *Data Br.* 24, 103897. https://doi.org/10.1016/j.dib.2019.103897.

Caballeria, M.; Coco, G.; Falqués, A.; Huntley, D.A., **2002**. Self-organization mechanisms for the formation of nearshore crescentic sand bars. *J. Fluid Mech.* 465, 379-410. https://doi.org/10.1017/S002211200200112X.

Cabana, D.; Rölfer, L.; Evadzi, P.; Celliers, L., **2023**. Enabling climate change adaptation in coastal systems: A systematic literature review. *Earth's Future* 11 (8), e2023EF003713. https://doi.org/10.1029/2023EF003713.

Calizza, E.; Costantini, M.L.; Carlino, P.; Bentivoglio, F.; Orlandi, L.; Rossi, L., **2013**. *Posidonia oceanica* habitat loss and changes in litter-associated biodiversity organization: A stable isotope-based preliminary study. *Estuar. Coast. Shelf Sci.* 135, 137–145. https://doi.org/10.1016/j.ecss.2013.07.019.

Carlini, D., **2024**. Valutazione preliminare delle applicazioni operative in tema di rimozione delle biomasse sui sistemi di spiaggia della Sardegna: Analisi dei Dati R.A.S. per le annualità 2018–2022. *Bachelor's Thesis*, University of Cagliari, Cagliari, Italy.

Carmignani, L.; Oggiano, G.; Barca, S.; Conti, P.; Salvadori, I.; Eltrudis, A.; Funedda, A.; Pasci, S., **2001**. Geologia della Sardegna: Note illustrative della Carta geologica della Sardegna a scala 1:200.000. *Memorie Descrittive della Carta Geologica d'Italia* (Vol. 60). Servizio Geologico d'Italia, Roma, pp. 283.

Carobene, L.; Brambati, A., **1975**. Metodo per l'analisi morfologica quantitativa delle spiagge. *Boll. Soc. Geol. It.* 94, 479–493.

Carvalho, A.M.; Ellis, J.T.; Lamothe, M.; Maia, L.P., **2016**. Using wind direction and shoreline morphology to model sand dune mobilization. *J. Coast. Res.* 32 (5), 1005–1015. https://doi.org/10.2112/JCOASTRES-D-14-00258.1.

Casas-Prat, M.; Sierra, J.P., **2013**. Projected future wave climate in the NW Mediterranean Sea. *J. Geophys. Res. Oceans* 118 (7), 3548–3568. https://doi.org/10.1002/jgrc.20233.

Castedo, R.; de la Vega-Panizo, R.; Fernández-Hernández, M.; Paredes, C., **2015**. Measurement of historical cliff-top changes and estimation of future trends using GIS data between Bridlington and Hornsea–Holderness Coast (UK). *Geomorphology* 230, 146–160. https://doi.org/10.1016/j.geomorph.2014.11.013.

Castelle, B.; Michallet, H.; Marieu, V.; Leckler, F.; Dubardier, B.; Lambert, A.; Berni, C.; Bonneton, P.; Barthélemy, E.; Bouchette, F., **2010**. Laboratory experiment on rip current circulations over a moveable bed: Drifter measurements. *J. Geophys. Res.* 115 (C12). https://doi.org/10.1029/2010JC006343.

Castelle, B.; Coco, G., **2012**. The morphodynamics of rip channels on embayed beaches. *Cont. Shelf Res.* 43, 10–23. https://doi.org/10.1016/j.csr.2012.04.010.

Castelle, B.; Coco, G., **2013**. Surf zone flushing on embayed beaches. *Geophys. Res. Lett.* 40, 1–5. https://doi.org/10.1002/grl.50485.

Castelle, B.; Reniers, A.; MacMahan, J., **2013**. Numerical modelling of surfzone retention in rip current systems: on the impact of the surfzone sandbar morphology. In: *Proceedings of 7th International Conference on Coastal Dynamics*. 295–304.

Castelle, B.; Masselink, G., **2023**. Morphodynamics of wave-dominated beaches. *Cambridge Prisms: Coastal Futures* 1 (e1), 1–13. https://doi.org/10.1017/cft.2022.2.

Castelle, B.; Scott, T.; Brander, R.; McCarroll, R.J.; Tellier, E.; de Korte, E.; Tackuy, L.; Robinet, A.; Simonnet, B.; Salmi, L.R., **2020a**. Wave and tide controls on rip current activity and drowning incidents in Southwest France. *J. Coast. Res.* 95, 769–774. https://doi.org/10.2112/SI95-150.1.

Castelle, B.; Robinet, A.; Idier, D.; D'Anna, M., **2020b**. Modelling of embayed beach equilibrium planform and rotation signal. *Geomorphology* 369, 107367. https://doi.org/10.1016/j.geomorph.2020.107367.

Castelle, B.; Scott, T.; Brander, R.W.; McCarroll, R.J., **2016**. Rip current types, circulation and hazard. *Earth-Sci. Rev.* 163, 1–21. https://doi.org/10.1016/j.earscirev.2016.09.008.

Cavaleri, L.; Rizzoli, M.P., **1981**. Wind wave prediction in shallow water: Theory and applications. *J. Geophys. Res.* 86 (C11), 10961–10973. https://doi.org/10.1029/JC086iC11p10961.

Cazenave, A.; Le Cozannet, G., **2014**. Sea level rise and its coastal impacts. *Earth's Future* 2 (2), 15–34. https://doi.org/10.1002/2013EF000188.

Celata, F.; Gioia, E., **2024**. Resist or retreat? Beach erosion and the climate crisis in Italy: Scenarios, impacts and challenges. *Appl. Geog.* 169, 103335. https://doi.org/10.1016/j.apgeog.2024.103335.

Cenci, L.; Disperati, L.; Persichillo, M.G.; Oliveira, E.R.; Alves, F.L.; Phillips, M., **2017**. Integrating remote sensing and GIS techniques for monitoring and modeling shoreline evolution to support coastal risk management. *GISci. Remote Sens.* 55 (3), 355–375. https://doi.org/10.1080/15481603.2017.1376370.

Cerkowniak, G.R.; Ostrowski, R.; Wziątek, D.; Paplińska-Swerpel, B., **2015**. Wave-induced sediment motion beyond the surf zone: Case study of Lubiatowo (Poland). *Arch. Hydraul. Eng. Environ. Mech.* 62 (1–2), 27–39. https://doi.org/10.1515/heem-2015-0017.

Chatzipavlis, A.; Trogu, D.; Ruju, A.; Montes, J.; Usai, A.; Porta, M.; Coco, G.; De Muro, S.; Ciavola, P., **2025**. Development and validation of an early warning system for coastal flooding on a Mediterranean urban beach. EGUsphere [preprint]. https://doi.org/10.5194/egusphere-2025-2292.

Chawalit, C.; Boonpook, W.; Sitthi, A.; Torsri, K.; Kamthonkiat, D.; Tan, Y.; Suwansaard, A.; Nardkulpat, A., **2025**. Geoinformatics and machine learning for shoreline change monitoring: A 35-year analysis of coastal erosion in the upper Gulf of Thailand. *ISPRS Int. J. Geo-Inf.* 14 (2), 94. https://doi.org/10.3390/ijgi14020094.

Chefaoui, R.M.; Duarte, C.M.; Serrão. E.A., **2018**. Dramatic loss of seagrass habitat under projected climate change in the Mediterranean Sea. *Glob. Change Biol.* 24 (10), 4919–4928. https://doi.org/10.1111/gcb.14401.

Chew, S.Y.; Wong, P.P.; Chin, K.K., **1986**. Beach development between headland breakwaters in a low wave energy environment, Pasir Ris, Singapore. *Coast. Eng. Proc.* 1 (20), 76. https://doi.org/10.9753/icce.v20.76.

Choi, J.; Roh, M., **2021**. A laboratory experiment of rip currents between the ends of breaking wave crests. *Coast. Eng.* 164, 103812. https://doi.org/10.1016/j.coastaleng.2020.103812.

Chowdhury, P.; Lakku, N.K.G.; Lincoln, S.; Seelam, J.K.; Behera, M.R., **2023**. Climate change and coastal morphodynamics: Interactions on regional scales. *Sci. Total Environ.* 899, 166432. https://doi.org/10.1016/j.scitotenv.2023.166432.

Cocozza, C.; Parente, A.; Zaccone, C.; Mininni, C.; Santamaria, P.; Miano, T., **2011**. Chemical, physical and spectroscopic characterization of *Posidonia oceanica* (L.) Del. residues and their possible recycle. *Biomass Bioenergy* 35 (2), 799–807. https://doi.org/10.1016/j.biombioe.2010.10.033.

Cooper, J., **2022**. Response of natural, modified and artificial sandy beaches to sea-level rise. *CIG* 48 (2), 257–266. https://doi.org/10.18172/cig.5184.

Costa, G.P.; Marino, M.; Cáceres, I.; Musumeci, R.E., **2023**. Effectiveness of dune reconstruction and beach nourishment to mitigate coastal erosion of the Ebro Delta (Spain). *J. Mar. Sci. Eng.* 11 (10), 1908. https://doi.org/10.3390/jmse11101908.

Crawford, T.W.; Islam, M.S.; Rahman, M.K.; Paul, B.K.; Curtis, S.; Miah, M.G.; Islam, M.R., **2020**. Coastal erosion and human perceptions of revetment protection in the lower Meghna Estuary of Bangladesh. *Remote Sens.* 12 (18), 3108. https://doi.org/10.3390/rs12183108.

Cucco, A.; Quattrocchi, G.; Brambilla, W.; Navone, A.; Panzalis, P.; Simeone, S., **2020**. The management of the beach-cast seagrass wracks: A numerical modelling approach. *J. Mar. Sci. Eng.* 8 (11), 873. https://doi.org/10.3390/jmse8110873.

D'Alessandro, F.; Tomasicchio, G.R.; Frega, F.; Leone, E.; Francone, A.; Pantusa, D.; Barbaro, G.; Foti, G., **2022**. Beach–dune system morphodynamics. *J. Mar. Sci. Eng.* 10 (5), 627. https://doi.org/10.3390/jmse10050627.

Dalrymple, R.A.; MacMahan, J.H.; Reniers, A.J.; Nelko, V., **2011**. Rip currents. *Annu. Rev. Fluid Mech.* 43, 551–581. https://doi.org/10.1146/annurev-fluid-122109-160733.

Daly, C.J.; Bryan, K.R.; Roelvink, J.A.; Klein, A.H.F.; Hebbeln, D.; Winter, C., **2011**. Morphodynamics of embayed Beaches: The effect of wave conditions. *J. Coast. Res.* 64, 1003–1007.

Daly. C.J.; Bryan, K.R.; Winter, C., **2014**. Wave energy distribution and morphological development in and around the shadow zone of an embayed beach. *Coast. Eng.* 93, 40–54. https://doi.org/10.1016/j.coastaleng.2014.08.003.

Davidson, M.A.; Aarninkhof, S.G.J.; Van Koningsveld, M.; Holman, R.A., **2006**. Developing coastal video monitoring systems in support of coastal zone management. *J. Coast. Res.* 39, 49–56.

Davidson-Arnott, R., **2009**. *Introduction to Coastal Processes and Geomorphology*. Cambridge University Press: Cambridge, UK.

Davies, J.L., **1980**. *Geographical Variation to Coastal Development*. 2nd ed.; Longman: New York.

Davis, R.A. Jr.; Hayes, M.O., **1984**. What is a wave-dominated coast? In: *Hydrodynamics and Sedimentation in Wave-Dominated Coastal Environments*; Greenwood, B., Davis, R.A. Jr., Eds.; *Mar. Geol.* 60 (1–4), 313–329. https://doi.org/10.1016/0025-3227(84)90155-5.

De Falco, G.; Ferrari, S.; Cancemi, G.; Baroli, M., **2000**. Relationship between sediment distribution and *Posidonia oceanica* seagrass. *Geo-Mar. Lett.* 20, 50–57. https://doi.org/10.1007/s003670000030.

De Falco, G.; Simeone, S.; Baroli, M., **2008**. Management of beach-cast *Posidonia oceanica* seagrass on the Island of Sardinia (Italy, Western Mediterranean). *J. Coast. Res.* 24, 69–75. https://doi.org/10.2112/06-0800.1.

De Falco, G.; Molinaroli, E.; Conforti, A.; Simeone, S.; Tonielli, R., **2017**. Biogenic sediments from coastal ecosystems to beach–dune systems: implications for the adaptation of mixed and carbonate beaches to future sea level rise. *Biogeosciences* 14, 3191–3205. https://doi.org/10.5194/bg-14-3191-2017.

De Leon, M.P.; Nishi, R.; Kumasak, F.; Takaesu, T.; Kitamura, R.; Otani, A., **2008**. Reef rip current generated by tide and wave during summer season: field observation conducted in Yoshiwara Coast, Ishigakijima, Okinawa, Japan. In: *Proceedings of the 11th International Coral Reef Symposium*; pp. 489–493.

De Muro, S.; De Falco, G., **2010**. *Manuale per la gestione delle spiagge. Studi, indagini ed esperienze sulle spiagge Sarde e Corse*; University Press, Scienze Costiere e Marine, CUEC: Cagliari, Italy.

De Muro, S.; Ibba, A.; Kalb, C., **2016**. Morpho-sedimentology of a Mediterranean microtidal embayed wave dominated beach system and related inner shelf with Posidonia oceanica meadows: The SE Sardinian coast. *J. Maps* 12 (3), 558–572. https://doi.org/10.1080/17445647.2015.1051599.

De Muro, S.; Porta, M.; Pusceddu, N.; Frongia, P.; Passarella, M.; Ruju, A.; Buosi, C.; Ibba, A., **2018**. Geomorphological processes of a Mediterranean urbanized Beach (Sardinia, Gulf of Cagliari). *J. Maps* 14 (2), 114–122. https://doi.org/10.1080/17445647.2018.1438931.

Dean, R.G., **1973**. Heuristic models of sand transport in the surf zone. In: *Proc. Conf. Eng. Dyn. Surf Zone* (Sydney, Australia); 208–214.

Dean, R.G., **2019**. Dynamic equilibrium of beaches. In: *Encyclopedia of Coastal Science*; Finkl, C.W., Makowski, C., Eds.; Encyclopedia of Earth Sciences Series; Springer: Cham, Switzerland. https://doi.org/10.1007/978-3-319-93806-6_129.

Dentamare, I.; Capasso, L.; Chianese, E.; Calicchio, R.; Franzese, P.P.; Grande, U.; Russo, G.F.; Buonocore, E., **2025**. Ecological implications of *Posidonia oceanica* banquette removal: Potential loss of natural capital and ecosystem services. *Water* 17 (9), 1362. https://doi.org/10.3390/w17091362.

Díaz-Almela, E.; Marbà, N.; Duarte, C.M., **2007**. Consequences of Mediterranean warming events in seagrass (*Posidonia oceanica*) flowering records. *Glob. Change Biol.* 13 (1), 224–235. https://doi.org/10.1111/j.1365-2486.2006.01260.x.

Diez-Fernández, P.; Ruibal-Lista, B.; Lobato-Alejano, F.; López-García, S., **2023**. Rip current knowledge: Do people really know its danger? Do lifeguards know more than the general public?. *Heliyon* 9 (7), e18104. https://doi.org/10.1016/j.heliyon.2023.e18104.

Dieng, H.B.; Cazenave, A.; Gouzenes, Y.; Sow, B.A., **2021**. Trends and inter-annual variability of altimetry-based coastal sea level in the Mediterranean Sea: Comparison with tide gauges and models. *Adv. Space Res.* 68 (8), 3279–3290. https://doi.org/10.1016/j.asr.2021.06.022.

Dingler, J.R., **1981**. Stability of a very coarse-grained beach at Carmel, California. *Mar. Geol.* 44 (3–4), 241–252. https://doi.org/10.1016/0025-3227(81)90052-9.

Dolan, A.H.; Walker, I.J., **2006**. Understanding vulnerability of coastal communities to climate change related risks. *J. Coast. Res.* 39, 1316–1323.

Dolan, R.; Davis, R.E., **1994**. Coastal Storm Hazards. In: *Coastal Hazards: Perception, Susceptibility and Mitigation*; Finkl, C.W. Jr., Ed.; *J. Coast. Res.* 12, 103–114.

Dronen, N.; Karunarathna, H.; Fredsoe, J.; Sumer, B.M.; Deigaard, R., **2002**. An experimental study of rip channel flow. *Coast. Eng.* 45 (3–4), 223–238. https://doi.org/10.1016/S0378-3839(02)00035-2.

Duarte, C.M., **1991**. Seagrass depth limits. *Aquat. Bot.* 40 (4), 363–377. https://doi.org/10.1016/0304-3770(91)90081-F.

Duarte, C.M., **2002**. The future of seagrass meadows. *Environ. Conserv.* 29 (2), 192–206. https://doi.org/10.1017/S0376892902000127.

Duarte, C.M.; Middelburg, J.J.; Caraco, N., **2005**. Major role of marine vegetation on the oceanic carbon cycle. *Biogeosciences* 2, 1–8. https://doi.org/10.5194/bg-2-1-2005.

Dutta, D.; Kumar, T.; Jayaram, C.; Akram, W., **2022**. Shoreline change analysis of Hooghly Estuary using multi-temporal Landsat data and Digital Shoreline Analysis System. In: *Geographic Information Systems and Applications in Coastal Studies*; Zhang, Y., Cheng, Q., Eds.; IntechOpen. https://doi.org/10.5772/intechopen.103030.

Falqués, A.; Coco, G.; Huntley, D.A., **2000**. A mechanism for the generation of wave driven rhythmic patterns in the surf zone. *J. Geophys. Res.* 105 (C10), 24071–24087. https://doi.org/10.1029/2000JC900100.

Fellowes, T.E.; Vila-Concejo, A.; Gallop, S.L., **2019**. Morphometric classification of swell-dominated embayed beaches. *Mar. Geol.* 411, 78–87. https://doi.org/10.1016/j.margeo.2019.02.004.

Fernández-Hernández, M.; Calvo, A.; Iglesias, L.; Castedo, R.; Ortega, J.J.; Diaz-Honrubia, A.J.; Mora, P.; Costamagna, E., **2023**. Anthropic action on historical shoreline changes and future estimates using GIS: Guadarmar Del Segura (Spain). *Appl. Sci.* 13 (17), 9792. https://doi.org/10.3390/app13179792.

Fernández-Torquemada, Y.; Sánchez-Lizaso, J.L., **2005**. Effects of salinity on leaf growth and survival of the Mediterranean seagrass *Posidonia oceanica* (L.) Delile. *J. Exp. Mar. Biol. Ecol.* 320 (1), 57–63. https://doi.org/10.1016/j.jembe.2004.12.019.

Ferrara, C.; Palmerini, V., **1974**. Indagine sedimentologica sulla dinamica della linea di costa in facies sabbiosa nel settore centrale del Golfo di Cagliari. *Boll. Soc. Sarda Sci. Nat.* 14, 55–76.

Ferrarin, C.; Bellafiore, D.; Sannino, G.; Bajo, M.; Umgiesser, G., **2018**. Tidal dynamics in the inter-connected Mediterranean, Marmara, Black and Azov seas. *Prog. Oceanogr.* 161, 102–115. https://doi.org/10.1016/j.pocean.2018.02.006.

Feyssat, P.; Certain, R.; Robin, N.; Barusseau, J.P.; Lamy, A.; Raynal, O.; Hebert, B., **2024**. Morphodynamics of two Mediterranean microtidal beaches presenting permanent megacusps under the influence of waves and strong offshore winds. *Cont. Shelf Res.* 272, 105160. https://doi.org/10.1016/j.csr.2023.105160.

Fisichelli, N.A.; Schuurman, G.W.; Hoffman, C.H., **2016**. Is 'Resilience' maladaptive? Towards an accurate lexicon for Climate Change adaptation. *Environ. Manag.* 57, 753–758. https://doi.org/10.1007/s00267-015-0650-6.

Fornes, A.; Basterretxea, G.; Orfila, A.; Jordi, A.; Álvarez, A.; Tintoré, J., **2006**. Mapping *Posidonia oceanica* from IKONOS. *ISPRS J. Photogramm. Remote Sens.* 60 (5), 315–322. https://doi.org/10.1016/j.isprsjprs.2006.04.002.

Foti, G.; Barbaro, G.; Barillà, G.C.; Mancuso, P., **2023**. Shoreline changes due to the construction of ports: Case study - Calabria (Italy). *J. Mar. Sci. Eng.* 11 (12), 2382. https://doi.org/10.3390/jmse11122382.

Foti, G.; Barbaro, G.; Barillà, G.C.; Mancuso, P.; Puntorieri, P., **2022a**. Shoreline erosion due to anthropogenic pressure in Calabria (Italy). *Eur. J. Remote Sens.* 56 (1). https://doi.org/10.1080/22797254.2022.2140076.

Foti, G.; Barbaro, G.; Barillà, G.C.; Mancuso, P.; Puntorieri, P., **2022b**. Shoreline evolutionary trends along Calabrian coasts: Causes and classification. *Front. Mar. Sci.* 9, 846914. https://doi.org/10.3389/fmars.2022.846914.

Franco-Ochoa, C.; Zambrano-Medina, Y.; Plata-Rocha, W.; Monjardín-Armenta, S.; Rodríguez-Cueto, Y.; Escudero, M.; Mendoza, E., **2020**. Long-term Analysis of wave climate and shoreline change along the Gulf of California. *Appl. Sci.* 10 (23), 8719. https://doi.org/10.3390/app10238719.

Francour, P.; Ganteaume, A.; Poulain, M., **1999**. Effects of boat anchoring in *Posidonia oceanica* seagrass beds in the Port-Cros National Park (north-western Mediterranean Sea). *Aquat. Conserv. Mar. Freshwat. Ecosyst.* 9 (4), 391–400. https://doi.org/10.1002/(SICI)1099-0755(199907/08)9:4<391::AID-AQC356>3.0.CO;2-8.

Funedda, A.; Oggiano, G., **2009**. Outline of the Variscan basement of Sardinia. *Rend. Soc. Paleontol. Ital.* 3, 23–35.

Gacia, E.; Duarte, C.M., **2001**. Sediment retention by a Mediterranean *Posidonia oceanica* meadow: the balance between deposition and resuspension. *Estuar. Coast. Shelf Sci.* 52 (4), 505–514. https://doi.org/10.1006/ecss.2000.0753.

Gaglianone, G.; Brandano, M.; Mateu-Vicens, G., **2017**. The sedimentary facies of *Posidonia oceanica* seagrass meadows from the central Mediterranean Sea. *Facies* 63, 28. https://doi.org/10.1007/s10347-017-0511-2.

Gallop, S.L.; Kennedy, D.M.; Loureiro, C.; Naylor, L.A.; Muñoz-Pérez, J.J.; Jackson, D.W.T.; Fellowes, T.E., **2020**. Geologically controlled sandy beaches: Their geomorphology, morphodynamics and classification. *Sci. Total Environ.* 731, 139123. https://doi.org/10.1016/j.scitotenv.2020.139123.

Gama, C.; Coelho, C.; Baptista, P.; Albardeiro, L., **2011**. Equilibrium configuration of sandy embayed beaches from the Southwest Portuguese rocky coast. *J. Coast. Res.* 64, 2037–2041.

Gattuso, J.-P.; Gentili, B.; Duarte, C.M.; Kleypas, J.A.; Middelburg, J.J.; Antoine, D., **2006**. Light availability in the coastal ocean: Impact on the distribution of benthic

photosynthetic organisms and their contribution to primary production. *Biogeosciences* 3, 489–513. https://doi.org/10.5194/bg-3-489-2006.

Genz, A.S.; Fletcher, C.H.; Dunn, R.A.; Frazer, N.; Rooney, J.J., **2007**. The predictive accuracy of shoreline change rate methods and alongshore beach variation on Maui, Hawaii. *J. Coast. Res.* 231, 87–105. https://doi.org/10.2112/05-0521.1.

Gharnate, A.; Taouali, O.; Mhammdi, N., **2024**. Shoreline change assessment of the Moroccan Atlantic coastline using DSAS techniques. *J. Coast. Res.* 40 (2), 418–435. https://doi.org/10.2112/JCOASTRES-D-23-00013.1.

Ginesu, S.; Carboni, D.; Marian, M., **2012**. Coastline modifications in Sardinia starting from archaeological data: A progress report. *Procedia Environ. Sci.* 14, 132–142. https://doi.org/10.1016/j.proenv.2012.03.013.

Gleason, M.G.; Reynolds, M.D.; Heady, W.N.; Easterday, K.; Morrison, S.A., **2023**. The importance of identifying and protecting coastal wildness. *Front. Conserv. Sci.* 4, 1224618. https://doi.org/10.3389/fcosc.2023.1224618.

Gobert, S.; Cambridge, M.T.; Velimirov, B.; Pergent, G.; Lepoint, G.; Bouquegneau, J.-M.; Dauby, P.; Pergent-Martini, C.; Walker, D.I., **2006**. Biology of Posidonia. In: *Seagrasses: Biology, Ecology and Conservation*; Larkum, A.W.D., Orth, R.J., Duarte, C.M., Eds.; Springer: Dordrecht, The Netherlands; pp. 387–408. https://doi.org/10.1007/978-1-4020-2983-7_17.

Gomez, C.; Hart, D.E.; Wassmer, P.; Kenta, I.; Matsui, H.; Shimizu, M., **2019**. Coastal evolution, geomorphic processes and sedimentary records in the Anthropocene. *Forum Geogr.* 33 (1), 1–24. https://doi.org/10.23917/forgeo.v33i1.7551.

Goodess, C.M., **2013**. How is the frequency, location and severity of extreme events likely to change up to 2060?. *Environ. Sci. Policy* 27, S4–S14. https://doi.org/10.1016/j.envsci.2012.04.001.

Gourlay, M.R., **1968**. Beach and dune erosion tests. Delft Hydraulics Laboratory, Report No. M935/M936.

Green, D.; Woodroffe, C.; Evelpidou, N.; Delgado-Fernandez, I.; Karkani, A.; Ciavola, P., **2023** Coastal systems: The dynamic inter-face between land and sea. In: *Research Directions, Challenges and Achievements of Modern Geography*. 1st ed.; Bański, J., Meadows, M., Eds.; Advances in Geographical and Environmental Sciences (AGES); Springer: Singapore; pp. 207–229. https://doi.org/10.1007/978-981-99-6604-2_11.

Grilliot, M.J.; Walker, I.J.; Bauer, B.O., **2019**. The role of large woody debris in beach-dune interaction. *J. Geophys. Res. Earth Surf.* 124 (12), 2854–2876. https://doi.org/10.1029/2019JF005120.

Haas, K.A.; Svendsen, I.A., **2002**. Laboratory measurements of the vertical structure of rip currents. *J. Geophys. Res. Oceans* 107 (C5), 15–1. https://doi.org/10.1029/2001JC000911.

Haas, K.A.; Svendsen, I.A.; Haller, M.C., **1998**. Numerical modeling of nearshore circulation on a barred beach with rip channels. In: *Proceedings of Coastal Engineering*; pp. 801–814. https://doi.org/10.1061/9780784404119.059.

Haller, M.C.; Dalrymple, R.A.; Svendsen, I.A., **2002**. Experimental study of nearshore dynamics on a barred beach with rip channels. *J. Geophys. Res.* 107 (C6), 3061. https://doi.org/10.1029/2001JC000955.

Harley, M.D.; Andriolo, U.; Armaroli, C.; Ciavola, P., **2014**. Shoreline rotation and response to nourishment of a gravel embayed beach using a low-cost video monitoring technique: San Michele-Sassi Neri, central Italy. *J. Coast. Conserv.* 18, 551–564. https://doi.org/10.1007/s11852-013-0292-x.

Hasselmann, K.; Barnett, T.P.; Bouws, E.; Carlson, H.; Cartwright, D.E.; Enke, K.; Ewing, J.A.; Gienapp, H.; Hasselmann, D.E.; Kruseman, P.; Meerburg, A.; Müller, P.; Olbers, D.J.; Richter, K.; Sell, W.; Walden, H., **1973**. Measurements of wind-wave growth and swell decay during the Joint North Sea Wave Project (JONSWAP). *Ergänzungsheft zur Deut. Hydrogr. Z.* 8 (12).

Hasselmann, S.; Hasselmann, K., **1985**. Computations and parametrizations of the nonlinear energy transfer in a gravity-wave spectrum. Part I: A new method for efficient computations of the exact nonlinear transfer integral. *J. Phys. Oceanog.* 15, 1369–1377. https://doi.org/10.1175/1520-0485(1985)015<1369:CAPOTN>2.0.CO;2.

Hayes, M.O., **1979**. Barrier island morphology as a function of tidal and wave regime. In: *Barrier Islands*; Leatherman, S.P., Ed.; Academic Press: New York; pp. 1–27.

Hemer, M.; Fan, Y.; Mori, N., **2013**. Projected changes in wave climate from a multi-model ensemble. *Nat. Clim. Change* 3, 471–476. https://doi.org/10.1038/nclimate1791.

Hemminga, M.; Duarte, C.M., **2000**. *Seagrass Ecology*; Cambridge University Press: Cambridge, UK.

Hermand, J.P.; Nascetti, P.; Cinelli, F., **1998**. Inversion of acoustic waveguide propagation features to measure oxygen synthesis by *Posidonia oceanica*. In: *IEEE Oceanic Engineering Society. OCEANS'98. Conference Proceedings*; Nice, France; Vol. 2, pp. 919–926. https://doi.org/10.1109/OCEANS.1998.724372.

Himmelstoss, E.A.; Henderson, R.E.; Kratzmann, M.G.; Farris, A.S., **2021**. Digital Shoreline Analysis System (DSAS) version 5.1 user guide. U.S. Geological Survey, Open-File Report (No. 2021–1091). https://doi.org/10.3133/ofr20211091.

Hinkel, J.; Nicholls, R. J.; Tol, R.S.J.; Wang, Z.B.; Hamilton, J.M.; Boot, G.; Vafeidis, A.T.; McFadden, L.; Ganopolski, A.; Klein, R.J.T., **2013**. A global analysis of erosion of sandy beaches and sea-level rise: An application of DIVA. *Glob. Planet. Change* 111, 150–158. https://doi.org/10.1016/j.gloplacha.2013.09.002.

Ho, S.K., **1971**. Crenulate shaped bays. Master Eng. Thesis, No. 346, Asian Institute of Technology, Bangkok, Thailand.

Holman, R.A., **1986**. Extreme value statistics for wave runup on a natural beach. *Coast. Eng.* 9 (6), 527–544. https://doi.org/10.1016/0378-3839(86)90002-5.

Holman, R.A.; Guza, R.T., **1984**. Measuring run-up on a natural beach. *Coast. Eng.* 8 (2), 129–140. https://doi.org/10.1016/0378-3839(84)90008-5.

Holman, R.A.; Stanley, J., **2007**. The history and technical capabilities of Argus. *Coast. Eng.* 54 (6–7), 477–491. https://doi.org/10.1016/j.coastaleng.2007.01.003.

Hsu, J.R.C.; Silvester, R.; Xia, Y.M., **1989a**. Static equilibrium bays: New relationships. *J. Waterw. Port Coast. Ocean Eng.* 115 (3), 285–298. https://doi.org/10.1061/(ASCE)0733-950X(1989)115:3(285).

Hsu, J.R.C.; Silvester, R.; Xia, Y.M., **1989b**. Generalities on static equilibrium bays. *Coast. Eng.* 12 (4), 353–369. https://doi.org/10.1016/0378-3839(89)90012-4.

Huntley, D.A.; Hendry, M.D.; Haines, J.; Greenidge, B., **1988**. Waves and rip currents on a Caribbean pocket beach, Jamaica. *J. Coast. Res.* 4 (1), 69-79.

Husemann, P.; Romão, F.; Lima, M.; Costas, S.; Coelho, C., **2024**. Review of the quantification of aeolian sediment transport in coastal areas. *J. Mar. Sci. Eng.* 12 (5), 755. https://doi.org/10.3390/jmse12050755.

Iglesias, G.; López, I.; Castro, A.; Carballo, R., **2009**. Neural network modelling of planform geometry of headland-bay beaches. *Geomorphology* 103 (4), 577–587. https://doi.org/10.1016/j.geomorph.2008.08.002.

Inman, D.L.; Nordstrom, C.E., **1971**. On the tectonic and morphologic classification of coasts. *J. Geol.* 79, 1–21.

IPCC, **2023a**. *Climate Change 2023: Synthesis report. Contribution of Working Groups I, II and III to the Sixth Assessment Report of the Intergovernmental Panel on Climate Change*; Lee H., Romero. J., Eds.; IPCC, Geneva, Switzerland, pp. 184. https://doi.org/10.59327/IPCC/AR6-9789291691647.

IPCC, **2023b**. *Climate Change 2021 - The Physical Science Basis: Contribution of Working Group I to the Sixth Assessment Report of the Intergovernmental Panel on Climate Change*; Masson-Delmotte, V., Zhai, P., Pirani, A., Connors, S.L., Péan, C., Berger, S.,

Caud, N., Chen, Y., Goldfarb, L., Gomis, M.I., Huang, M., Leitzell, K., Lonnoy, E., Matthews, J.B.R., Maycock, T.K., Waterfield, T., Yelekçi, O., Yu, R., Zhou, B., Eds.; Cambridge University Press: Cambridge, UK. https://doi.org/10.1017/9781009157896.

Islam, M.S.; Crawford, T.W., **2022**. Assessment of spatio-temporal empirical forecasting performance of future shoreline positions. *Remote Sens.* 14 (24), 6364. https://doi.org/10.3390/rs14246364.

Johnson, D.; Pattiaratchi, C., **2006**. Boussinesq modelling of transient rip currents. *Coast. Eng.* 53 (5–6), 419–439. https://doi.org/10.1016/j.coastaleng.2005.11.005.

Kaddour, S.; Hemdane, Y.; Kessali, N.; Belabdi, K.; Sallaye, M., **2020**. Study of shoreline changes through Digital Shoreline Analysis System and wave modeling: Case of the sandy coast of Bou-Ismail Bay, Algeria. *Ocean Sci.* 57, 493–527. https://doi.org/10.1007/s12601-022-00083-x.

Kalligeris, N.; Smit, P.B.; Ludka, B.C.; Guza, R.T.; Gallien, T.W., **2020**. Calibration and assessment of process-based numerical models for beach profile evolution in southern California. *Coast. Eng.* 158, 103650. https://doi.org/10.1016/j.coastaleng.2020.103650.

Karambas, T.V., **2015**. Modelling of climate change impacts on coastal flooding/erosion, ports and coastal defence structures. *Desal. Water Treat.* 54 (8), 2130–2137. https://doi.org/10.1080/19443994.2014.934115.

Karunarathna, H.; Pender, D.; Ranasinghe, R.; Short, A.D.; Reeve, D.E., **2014**. The effects of storm clustering on beach profile variability. *Mar. Geol.* 348, 103–112. https://doi.org/10.1016/j.margeo.2013.12.007.

Kennedy, A.B.; Thomas, D., **2004**. Drifter measurements in a laboratory rip current. *J. Geophys. Res. Oceans* 109 (C8). https://doi.org/10.1029/2003JC001927.

Kennedy, D.M; Woods, J.L.D., **2012**. The influence of coarse woody debris on gravel beach geomorphology. *Geomorphology.* 159–160, 106–115. https://doi.org/10.1016/j.geomorph.2012.03.009.

Kim, K.H.; Shin, S.; Widayati, A.Y., **2013**. Mitigation measures for beach erosion and rip current. *J. Coast. Res.* 65, 290–295. https://doi.org/10.2112/SI65-050.1.

King, E.V.; Conley, D.C.; Masselink, G.; Leonardi, N.; McCarroll, R.J.; Scott, T.; Valiente, N.G., **2021**. Wave, tide and topographical controls on headland sand bypassing. *J. Geophys. Res. Oceans* 126 (8), e2020JC017053. https://doi.org/10.1029/2020JC017053.

Kirby, J.T., **2016**. Boussinesq models and their application to coastal processes across a wide range of scales. *J. Waterw. Port Coast. Ocean Eng.* 142 (6), 03116005. https://doi.org/10.1061/(ASCE)WW.1943-5460.0000350.

Klein, A.H.F.; Menezes, J.T., **2001**. Beach morphodynamics and profile sequence for a headland bay coast. *J. Coast. Res.* 17 (4), 812–835.

Klein, R.J.; Nicholls, R.J., **1999**. Assessment of coastal vulnerability to climate change. *Ambio* 28, 182–187.

Knutson, T.; Camargo, S.; Chan, J.; Emanuel, K.; Ho, C.; Kossin, J.; Mohapatra, M.; Satoh, M.; Sugi, M.; Walsh, K.; Wu, L., **2020**. Tropical cyclones and climate change assessment: Part II. Projected response to anthropogenic warming. *Bull. Am. Meteorol. Soc.* 101, E202–E322. https://doi.org/10.1175/BAMS-D-18-0194.1.

Komar, P.D.; Gaughan, M.K., **1972**. Airy wave theory and breaker height prediction. *Coast. Eng. Proceedings* 1 (13), 405–418. https://doi.org/10.9753/icce.v13.20.

Komen, G.J.; Hasselmann S.; Hasselmann, K., **1984**. On the existence of a fully developed wind-sea spectrum. *J. Phys. Oceanog.* 14 (8), 1271–1285. https://doi.org/10.1175/1520-0485(1984)014<1271:OTEOAF>2.0.CO;2.

Komen, G.J.; Cavaleri, L.; Donelan, M.; Hasselmann, K.; Hasselmann, S.; Janssen, P., **1994**. *Dynamics and modelling of ocean waves*. Cambridge University Press: Cambridge, pp. 532. https://doi.org/10.1017/CBO9780511628955.

Kuleli, T.; Guneroglu, A.; Karsli, F.; Dihkan, M., **2011**. Automatic detection of shoreline change on coastal Ramsar wetlands of Turkey. *Ocean Eng.* 38 (10), 1141–1149. https://doi.org/10.1016/j.oceaneng.2011.05.006.

Kumar, N.; Feddersen, F.; Uchiyama, Y.; McWilliams, J.; O'Reilly, W., **2015**: Midshelf to surfzone coupled ROMS–SWAN Model data comparison of waves, currents, and temperature: Diagnosis of subtidal forcings and response. *J. Phys. Oceanogr.* 45, 1464–1490. https://doi.org/10.1175/JPO-D-14-0151.1.

Kumar, B.S.; Balukkarasu, A.; Tamilarasan, K., **2019**. Coastal vulnerability mapping using remote sensing and GIS techniques in Tuticorin Coast of Tamil Nadu, India. *J. Geogr. Environ. Earth Sci. Int.* 20 (2), 1–12. https://doi.org/10.9734/jgeesi/2019/v20i230100.

Lakshmi, A., **2021**. Coastal ecosystem services & human wellbeing. *Indian J. Med. Res.* 153 (3), 382–387. https://doi.org/10.4103/ijmr.IJMR_695_21.

Laksono, F.A.T.; Borzì, L.; Distefano, S.; Czirok, L.; Halmai, Á.; Di Stefano, A.; Kovács, J., **2023**. Shoreline change dynamics along the Augusta Coast, Eastern Sicily, South Italy. *Earth Surf. Process. Landf.* 48 (13), 2630–2641. https://doi.org/10.1002/esp.5644.

Larkum, A.W.; Orth, R.J.; Duarte, C.M., **2006**. *Seagrasses*. Springer Netherlands; pp. 691.

Lawyer, C.; An, L.; Goharian, E., **2023**. A review of climate adaptation impacts and strategies in coastal communities: From agent-based modeling towards a system of systems approach. *Water* 15 (14), 2635. https://doi.org/10.3390/w15142635.

Le Cozannet, G.; Rohmer, J.; Cazenave, A.; Idier, D.; Van De Wal, R.; De Winter, R.; Pedreros, R.; Balouin, Y.; Vinchon, C.; Oliveros, C., **2015**. Evaluating uncertainties of future marine flooding occurrence as sea-level rises. *Environ. Model. Softw.* 73, 44–56. https://doi.org/10.1016/j.envsoft.2015.07.021.

Lesser, G.R.; Roelvink, J.A.; van Kester, J.A.T.M.; Stelling, G.S., **2004**. Development and validation of a three-dimensional morphological model. *Coast. Eng.* 51 (8–9), 883-915. https://doi.org/10.1016/j.coastaleng.2004.07.014.

Li, Z.; Zhu, S., **2018**. Why there are so many drowning accidents happened at Dadonghai Beach, Hainan, China: Beach morphodynamic analysis. *J. Coast. Res.* 85, 741-745. https://doi.org/10.2112/SI85-149.1.

Lin, S.; Sheng, J., **2020**. Revisiting dependences of the drag coefficient at the sea surface on wind speed and sea state. *Cont. Shelf Res.* 207, 104188. https://doi.org/10.1016/j.csr.2020.104188.

Lincke, D.; Hinkel, J., **2021**. Coastal migration due to 21st century sea-level rise. *Earth's Future* 9 (5), e2020EF001965. https://doi.org/10.1029/2020EF001965.

Lionello, P.; Bhend, J.; Buzzi, A.; Della-Marta, P.M.; Krichak, S.O.; Jansà, A.; Maheras, P.; Sanna, A.; Trigo, I.F.; Trigo, R., **2006**. Chapter 6 Cyclones in the Mediterranean region: Climatology and effects on the environment. *Dev. Earth Environ. Sci.* 4, 325–372. https://doi.org/10.1016/S1571-9197(06)80009-1.

Lippmann, T.C.; Holman, R.A., **1990**. The spatial and temporal variability of sand bar morphology. *J. Geophys. Res. Oceans* 95 (C7), 11575–11590. https://doi.org/10.1029/JC095iC07p11575.

Lippmann, T.C.; Holman, R.A., **1989**. Quantification of sand bar morphology: A video technique based on wave dissipation. *J. Geophys. Res. Oceans* 94 (C1), 995–1011. https://doi.org/10.1029/JC094iC01p00995.

Lira-Loarca, A.; Besio, G., **2020**. Future changes and seasonal variability of the directional wave spectra in the Mediterranean Sea for the 21st century. *Environ. Res. Lett.* 17, 104015. https://doi.org/10.1088/1748-9326/ac8ec4.

Liu, B.; Coulthard, T.J., **2015**. Mapping the interactions between rivers and sand dunes: Implications for fluvial and aeolian geomorphology. *Geomorphology* 231, 246–257. https://doi.org/10.1016/j.geomorph.2014.12.011.

Lotze, H.K.; Lenihan, H.S.; Bourque, B.J.; Bradbury, R.H.; Cooke, R.G.; Kay, M.C.; Kidwell, S.M.; Kirby, M.X.; Peterson, C.H.; Jackson, J.B., **2006**. Depletion, degradation, and recovery potential of estuaries and coastal seas. *Science* 312, 1806–1809. https://doi.org/10.1126/science.1128035.

Loureiro, C.; Ferreira, Ó.; Cooper, J.A.G., **2012a**. Extreme erosion on high-energy embayed beaches: Influence of megarips and storm grouping. *Geomorphology* 139–140, 155–171. https://doi.org/10.1016/j.geomorph.2011.10.013.

Loureiro, C.; Ferreira, Ó.; Cooper, J.A.G., **2012b**. Geologically constrained morphological variability and boundary effects on embayed beaches. *Mar. Geol.* 329–331, 1–15. https://doi.org/10.1016/j.margeo.2012.09.010.

Lozano, C.J.; Candela, J., **1995**. The M2 tide in the Mediterranean Sea: dynamic analysis and data assimilation. *Oceanol. Acta* 18 (4), 419–441.

Luijendijk, A.; Hagenaars, G.; Ranasinghe, R.; Baart, F.; Donchyts, G.; Aarninkhof, S.G.J., **2018**. The state of the world's beaches. *Sci. Rep.* 8, 6641. https://doi.org/10.1038/s41598-018-24630-6.

MacMahan, J.H.; Thornton, E.B.; Reniers, A.J., **2006**. Rip current review. *Coast. Eng.* 53 (2–3), 191–208. https://doi.org/10.1016/j.coastaleng.2005.10.009.

MacMahan, J.H.; Thornton, E.B.; Stanton, T.P.; Reniers, A.J., **2005**. RIPEX: Observations of a rip current system. *Mar. Geol.* 218 (1–4), 113–134. https://doi.org/10.1016/j.margeo.2005.03.019.

Manca, E.; Caceres, I.; Alsina, J.M.; Stratigaki, V.; Townend, I.; Amos, C.L., **2012**. Wave energy and wave-induced flow reduction by full-scale model *Posidonia oceanica* seagrass. *Cont. Shelf Res.* 50–51, 100–116. https://doi.org/10.1016/j.csr.2012.10.008.

Manca, E.; Pascucci, V.; Deluca, M.; Cossu, A.; Andreucci, S., **2013**. Shoreline evolution related to coastal development of a managed beach in Alghero, Sardinia, Italy. *Ocean Coast. Manag.* 85, 65–76. https://doi.org/10.1016/j.ocecoaman.2013.09.008.

Manfra, L.; Chiesa, S.; Simeone, S.; Borrello, P.; Piermarini, R.; Agaoglou, C.; Elbour, M.; Zaaboub, N.; Vandarakis, D.; Kourliaftis, I.; Scarpato, A.; Rotini, A., **2024**. Towards sustainable management of beach-cast seagrass in Mediterranean coastal areas. *Sustainability* 16 (2), 756. https://doi.org/10.3390/su16020756.

Manno, G.; Lo Re, C.; Ciraolo, G., **2017**. Uncertainties in shoreline position analysis: The role of run-up and tide in a gentle slope beach. *Ocean Sci.* 13, 661–671. https://doi.org/10.5194/os-13-661-2017.

Marbà, N.; Díaz-Almela, E.; Duarte, C.M., **2014**. Mediterranean seagrass (*Posidonia oceanica*) loss between 1842 and 2009. *Biol. Conserv.* 176, 183–190. https://doi.org/10.1016/j.biocon.2014.05.024.

Marini, A.; Murru, M., **1983**. Movimenti tettonici in Sardegna fra il Miocene superiore ed il Pleistocene. *Geografia Fisica e Dinamica Quaternaria* 6 (1), 39–42.

Marchesiello, P.; Benshila, R.; Almar, R.; Uchiyama, Y.; McWilliams, J.C.; Shchepetkin, A., **2015**. On tridimensional rip current modeling. *Ocean Model.* 96, 36-48. https://doi.org/10.1016/j.ocemod.2015.07.003.

Marriner, N.; Morhange, C.; Goiran, J.P., **2010**. Coastal and ancient harbour geoarchaeology. *Geol. Today* 26 (1), 21–27. https://doi.org/10.1111/j.1365-2451.2010.00740.x.

Marsico, A.; Lisco, S.; Lo Presti, V.; Antonioli, F.; Amorosi, A.; Anzidei, M.; Deiana, G.; De Falco, G.; Fontana, A.; Fontolan, G.; Moretti, M.; Orrù, P.E.; Serpelloni, E.; Sannino, G.; Vecchio, A.; Mastronuzzi, G., **2017**. Flooding scenario for four Italian coastal plains using three relative sea level rise models. *J. Maps* 13 (2), 961–967. https://doi.org/10.1080/17445647.2017.1415989.

Martínez-Crego, B.; Vergés, A.; Alcoverro, T.; Romero, J., **2008**. Selection of multiple seagrass indicators for environmental biomonitoring. *Mar. Ecol. Prog. Ser.* 361, 93–109. https://doi.org/10.3354/meps07358.

Masselink, G.; Hughes, M.; Knight, J., **2014**. *Introduction to Coastal Processes and Geomorphology*. 2nd ed.; Routledge. https://doi.org/10.4324/9780203785461.

Masselink, G.; Short, A.C., **1993**. The effect of tide range on beach morphodynamic sand morphology: A conceptual beach model. *J. Coast. Res.* 9 (3), 785-800.

Masselink, G.; Hughes, M., **2003**. *Introduction to Coastal Processes and Geomorphology*. Oxford University Press: Oxford, UK.

Masselink, G.; Pattiaratchi, C.B., **2001**. Seasonal changes in beach morphology along the sheltered coastline of Perth, Western Australia. *Mar. Geol.* 172 (3–4), 243–263. https://doi.org/10.1016/S0025-3227(00)00128-6.

Mateo, M.Á.; Sánchez-Lizaso, J.L.; Romero, J., **2003**. *Posidonia oceanica* 'banquettes': A preliminary assessment of the relevance for meadow carbon and nutrients budget. *Estuar. Coast. Shelf Sci.* 56 (1), 85–90. https://doi.org/10.1016/S0272-7714(02)00123-3.

Mathiesen, M.; Goda, Y.; Hawkes, P.J.; Mansard, E.; Martín, M.J.; Peltier, E.; Thompson, E.F.; Van Vledder, G., **1994**. Recommended practice for extreme wave analysis. *J. Hydraul. Res.* 32 (6), 803–814. https://doi.org/10.1080/00221689409498691.

Mayer, S.; Madsen, P.A., **2001**. Simulation of breaking waves in the surf zone using a Navier-Stokes solver. In: *Proceedings of Coastal Engineering*; pp. 928–941. https://doi.org/10.1061/40549(276)72.

Mazzella, L.; Ott, J., **1984**. Seasonal changes in some features of *Posidonia oceanica* (L.) Delile leaves and epiphytes at different depths. In: *International Workshop on Posidonia oceanica Beds*; Boudouresque, C.F.; de Grissac, A.J.; Olivier, J., Eds.; GIS Posidonie, Marseilles: France; pp. 119–127.

McCarroll, R.J.; Castelle, B.; Brander, R.W.; Scott, T., **2015**. Modelling rip current flow and bather escape strategies across a transverse bar and rip channel morphology. *Geomorphology* 246, 502-518. https://doi.org/10.1016/j.geomorph.2015.06.041.

McGlashan, D.J.; Duck, R.W.; Reid, C.T., **2005**. Defining the foreshore: Coastal geomorphology and British Laws. *Estuar. Coast. Shelf Sci.* 62 (1–2), 183–192. https://doi.org/10.1016/j.ecss.2004.08.016.

McGranahan, G.; Balk, D.; Anderson, B., **2007**. The rising tide: assessing the risks of climate change and human settlements in low elevation coastal zones. *Environ. Urban.* 19 (1), 17–37. https://doi.org/10.1177/0956247807076960.

McLachlan, A.; Brown, A.C., **2006**. *The Ecology of Sandy Shores*. 2nd ed.; Academic Press. https://doi.org/10.1016/B978-0-12-372569-1.X5000-9.

McLachlan, A.; Defeo, O., **2013**. Coastal beach ecosystems. In: *Encyclopedia of Biodiversity*. 2nd ed.; Levin, S.A., Ed.; Academic Press; pp. 128–136. https://doi.org/10.1016/B978-0-12-384719-5.00294-X.

Mei, C.C., **1989**. The applied dynamics of ocean surface waves. World Scientific.

Meli, M.; Camargo, C.M.L.; Olivieri, M.; Slangen, A.B.A.; Romagnoli, C., **2023**. Sea-level trend variability in the Mediterranean during the 1993–2019 period. *Front. Mar. Sci. 10*, 1150488. https://doi.org/10.3389/fmars.2023.1150488.

Miles, J., **1957**. On the generation of surface waves by shear flows. *J. Fluid Mech.* 3, 185-204. https://doi.org/10.1017/S0022112057000567.

Mohamed, B.; Abdallah, A.M.; Alam El-Din, K.; Nagy, H.; Shaltout, M., **2019**. Inter-annual variability and trends of sea level and sea surface temperature in the Mediterranean Sea over the last 25 years. *Pure Appl. Geophys.* 176, 3787–3810. https://doi.org/10.1007/s00024-019-02156-w.

Monnier, B.; Pergent, G.; Mateo, M.Á.; Carbonell, R.; Clabaut, P.; Pergent-Martini, C., **2021**. Sizing the carbon sink associated with *Posidonia oceanica* seagrass meadows using very high-resolution seismic reflection imaging. *Mar. Environ. Res.* 170, 105415. https://doi.org/10.1016/j.marenvres.2021.105415.

Montefalcone, M., **2009**. Ecosystem health assessment using the Mediterranean seagrass *Posidonia oceanica*: A review. *Ecol. Indic.* 9 (4), 595–604. https://doi.org/10.1016/j.ecolind.2008.09.013.

Nerves, A.; Rivera, F.D.; Blanco, A.; Tirol, Y.; Nadaoka, K., **2024**. Shoreline change analysis in New Washington, Aklan using Digital Shoreline Analysis System (DSAS). *ISPRS Ann. Photogramm. Remote Sens. Spatial Inf. Sci.* X–5–2024, 111–117. https://doi.org/10.5194/isprs-annals-X-5-2024-111-2024.

Nicholls, R. J.; Hoozemans, F.M.J., **1996**. The Mediterranean: Vulnerability to coastal implications of climate change. *Ocean Coast. Manag.* 31 (2–3), 105–132.

Nissen, K.M.; Leckebusch, G.C.; Pinto, J.G.; Ulbrich, U., **2010**. Mediterranean cyclones and windstorms in a changing climate. *Reg. Environ. Change* 14, 1873–1890. https://doi.org/10.1007/s10113-012-0400-8.

Nordstrom, K.; Psuty, N.; Carter, B., **1990**. *Coastal Dunes. Form and Process*. Wiley.

Ojeda, E.; Guillén, J., **2008**. Shoreline dynamics and beach rotation of artificial embayed beaches. *Mar. Geol.* 253 (1–2), 51–62. https://doi.org/10.1016/j.margeo.2008.03.010.

Ojeda, E.; Guillén, J.; Ribas, F., **2011**. Dynamics of single-barred embayed beaches. *Mar. Geol.* 280 (1–4), 76–90. https://doi.org/10.1016/j.margeo.2010.12.002.

Orams, M.B., **2003**. Sandy beaches as a tourism attraction: A management challenge for the 21st century. *J. Coast. Res.* 19, 74–84.

Ortega-Sánchez, M.; Bergillos, R.J.; López-Ruiz, A.; Losada, M.A., **2017**. *Morphodynamics of Mediterranean Mixed Sand and Gravel Coasts*. SpringerBriefs in Earth Sciences; Springer Cham. https://doi.org/10.1007/978-3-319-52440-5.

Orth, R.J.; Carruthers, T.J.; Dennison, W.C.; Duarte, C.M.; Fourqurean, J.W.; Heck, K.L.; Williams, S.L., **2006**. A global crisis for seagrass ecosystems. *BioScience* 56 (12), 987–996. https://doi.org/10.1641/0006-3568(2006)56[987:AGCFSE]2.0.CO;2.

Ott, J.A., **1980**. Growth and production in *Posidonia oceanica* (L.) Delile. *Mar. Ecol.* 1, 47–64.

Oyedotun, T.D., **2014**. Shoreline geometry: DSAS as a tool for historical trend analysis. *Geomorphol. Tech.* 3, 1–12.

Pang, T.; Wang, X.; Nawaz, R. A.; Keefe, G.; Adekanmbi, T., **2023**. Coastal erosion and climate change: A review on coastal-change process and modeling. *Ambio* 52, 2034–2052. https://doi.org/10.1007/s13280-023-01901-9.

Pasqualini, V.; Pergent-Martini, C.; Clabaut, P.; Pergent, G., **1998**. Mapping of *Posidonia oceanica* using aerial photographs and side-scan sonar: Application of the islands of Corsica (France). *Estuar. Coast. Shelf Sci.* 47 (3), 359–367. https://doi.org/10.1006/ecss.1998.0361.

Passarella, M., **2019**. On the prediction of swash excursion and the role of seagrass beach-cast litter: Modelling and observations. *PhD Thesis*, University of Cagliari, Cagliari, Italy.

Passarella, M.; Ruju, A.; De Muro, S.; Coco, G., **2020**. Horizontal runup and seagrass beach cast-litters: Modelling and observations. *J. Coast. Res.* 95, 143–147. https://doi.org/10.2112/SI95-028.1.

Pepe, M.; Costantino, D.; Alfio, V.S., **2023**. A GIS procedure to assess shoreline changes over time using multi-temporal maps: An analysis of a sandy shoreline in Southern Italy over the last 100 years. *Geomat. Environ. Eng.* 17 (3), 107–134. https://doi.org/10.7494/geom.2023.17.3.107.

Peregrine, D.H., **1998**. Surf zone currents. *Theor. Comput. Fluid Dyn.* 10 (1), 295–309. https://doi.org/10.1007/s001620050065.

Pérez Gómez, B.; Vilibić, I.; Šepić, J.; Međugorac, I.; Ličer, M.; Testut, L.; Fraboul, C.; Marcos, M.; Abdellaoui, H.; Álvarez Fanjul, E.; Barbalić, D.; Casas, B.; Castaño-Tierno, A.; Čupić, S.; Drago, A.; Fraile, M.A.; Galliano, D.A.; Gauci, A.; Gloginja, B.; Martín Guijarro, V.; Jeromel, M.; Larrad Revuelto, M.; Lazar, A.; Keskin, I.H.; Medvedev, I.; Menassri, A.; Meslem, M.A.; Mihanović, H.; Morucci, S.; Niculescu, D.; Quijano de Benito, J.M.; Pascual, J.; Palazov, A.; Picone, M.; Raicich, F.; Said, M.; Salat, J.; Sezen, E.; Simav, M.; Sylaios, G.; Tel, E.; Tintoré, J.; Zaimi, K.; Zodiatis, G., **2022**. Coastal sea level monitoring in the Mediterranean and Black seas. *Ocean Sci.* 18, 997–1053. https://doi.org/10.5194/os-18-997-2022.

Pergent, G.; Boudouresque, C.F.; Crouzet, A.; Meinesz, A., **1989**. Cyclic changes along *Posidonia oceanica* rhizomes (lepidochronology): Present state and perspectives. *Mar. Ecol.* 10 (3), 221–230. https://doi.org/10.1111/j.1439-0485.1989.tb00474.x.

Pergent, G.; Romero, J.; Pergent-Martini, C.; Mateo, M.Á.; Boudouresque, C.F., **1994a**. Primary production, stocks and fluxes in the Mediterranean seagrass Posidonia oceanica. *Mar. Ecol. Prog. Ser.* 106, 139–146.

Pergent-Martini, C.; Rico-Raimondino, V.; Pergent, G., **1994b**. Primary production of *Posidonia oceanica* in the Mediterranean Basin. *Mar. Biol.* 120, 9–15. https://doi.org/10.1007/BF00381936.

Pergent-Martini, C.; Boudouresque, C.F.; Pasqualini, V.; Pergent, G., **2006**. Impact of fish farming facilities on *Posidonia oceanica* meadows: A review. *Mar. Ecol.* 27 (4), 310–319. https://doi.org/10.1111/j.1439-0485.2006.00122.x.

Pergent-Martini, C.; Pergent, G.; Monnier, B.; Boudouresque, C.F.; Mori, C.; Valette-Sansevin, A., **2021**. Contribution of *Posidonia oceanica* meadows in the context of climate change mitigation in the Mediterranean Sea. *Mar. Environ. Res.* 165, 105236. https://doi.org/10.1016/j.marenvres.2020.105236.

Perry, C.T.; Beavington-Penney, S.J., **2005**. Epiphytic calcium carbonate production and facies development within sub-tropical seagrass beds, Inhaca Island, Mozambique. *Sediment. Geol.* 174 (3–4), 161–176. https://doi.org/10.1016/j.sedgeo.2004.12.003.

Phillips, J.D., **1985**. Headland-bay beaches revisited: An example from Sandy Hook, New Jersey. *Mar. Geol.* 65 (1–2), 21–31. https://doi.org/10.1016/0025-3227(85)90044-1.

Philipps, O.M., **1977**. *The dynamics of the upper ocean*. Cambridge University Press.

Piazzi, L.; Balata, D.; Ceccherelli, G., **2016**. Epiphyte assemblages of the Mediterranean seagrass *Posidonia oceanica*: an overview. *Mar. Ecol.* 37 (1), 3–41. https://doi.org/10.1111/maec.12331.

Ponte, A.L.; Cornuelle, B.D., **2013**. Coastal numerical modelling of tides: Sensitivity to domain size and remotely generated internal tide. *Ocean Model.* 62, 17–26. https://doi.org/10.1016/j.ocemod.2012.11.007.

Porta, M.; Buosi, C.; Trogu, D.; Ibba, A.; De Muro, S., **2020**. An integrated sea-land approach for analyzing forms, processes, deposits and the evolution of the urban coastal belt of Cagliari. *J. Maps* 17 (4), 65–74. https://doi.org/10.1080/17445647.2020.1719441.

Powell, E.J.; Tyrrell, M.C.; Milliken, A.; Tirpak, J.M.; Staudinger, M.D., **2019**. A review of coastal management approaches to support the integration of ecological and human community planning for climate change. *J. Coast. Conserv.* 23, 1–18. https://doi.org/10.1007/s11852-018-0632-y.

Prado, P.; Alcoverro, T.; Romero, J., **2008**. Seasonal response of *Posidonia oceanica* epiphyte assemblages to nutrient increase. *Mar. Ecol. Prog. Ser.* 359, 89–98. https://doi.org/10.3354/meps07438.

Pranzini, E., **2008**. Il colore della sabbia: Percezione, caratterizzazione e compatibilità nel ripascimento artificiale delle spiagge. *Studi Costieri* 15, 89–108.

Prasad, D.; Kumar, N., **2014**. Coastal erosion studies - A review. *Int. J. Geosci.* 5 (3), 341–345. https://doi.org/10.4236/ijg.2014.53033.

Ramesh, M.; Nair, L.S.; Ramachandran, K.K.; Prakash, T.N., **2020**. Development of video monitoring system for coastal applications. *J. Coast. Res.* 89, 118–125. https://doi.org/10.2112/SI89-020.1.

Ranasinghe, R.W.M.R.J.B., **2016**. Assessing climate change impacts on open sandy coasts: A review. *Earth-Sci. Rev.* 160, 320–332. https://doi.org/10.1016/j.earscirev.2016.07.011.

Rashid, A.H.; Razzak, I.; Tanver, M.; Hobbs, M., **2023**. Reducing rip current drowning: An improved residual based lightweight deep architecture for rip detection. *ISA Transactions* 132, 199–207. https://doi.org/10.1016/j.isatra.2022.05.015.

Reniers, A.J.H.M.; Battjes, J.A., **1997**. A laboratory study of longshore currents over barred and non-barred beaches. *Coast. Eng.* 30 (1–2), 1–21. https://doi.org/10.1016/S0378-3839(96)00033-6.

Reniers, A.J.H.M.; MacMahan, J.H.; Thornton, E.B.; Stanton, T.P.; Henriquez, M.; Brown, J.W.; Brown, J.A.; Gallagher, E., **2009**. Surf zone surface retention on a rip-channeled beach. *J. Geophy. Res.* 114 (C10). https://doi.org/10.1029/2008JC005153.

Ris, R.C.; Holthuijsen, L.H.; Booij, N., **1999**. A third-generation wave model for coastal regions: 2. Verification. *J. Geophy. Res.* 104 (C4), 7667–7681. https://doi.org/10.1029/1998JC900123.

Roelvink, D.; Reniers, A.; Van Dongeren, A.P.; De Vries, J.V.T.; McCall, R.; Lescinski, J., **2009**. Modelling storm impacts on beaches, dunes and barrier islands. *Coast. Eng.* 56 (11–12), 1133–1152. https://doi.org/10.1016/j.coastaleng.2009.08.006.

Rotini, A.; Chiesa, S.; Manfra, L.; Borrello, P.; Piermarini, R.; Silvestri, C.; Cappucci, S.; Parlagreco, L.; Devoti, S.; Pisapia, M.; Creo, C.; Mezzetti, T.; Scarpato, A.; Migliore, L., **2020**. Effectiveness of the "Ecological Beach" model: Beneficial management of Posidonia beach casts and banquette. *Water* 12 (11), 3238. https://doi.org/10.3390/w12113238.

Roukounis, C.N.; Tsihrintzis, V.A., **2022**. Indices of coastal vulnerability to climate change: A review. *Environ. Process.* 9, 29. https://doi.org/10.1007/s40710-022-00577-9.

Ruessink, G.; Ranasinghe, R., **2015**. Beaches. In: *Coastal Environments and Global Change*; Masselink, G., Gehrels, R., Eds.; Wiley; pp. 149–177. https://doi.org/10.1002/9781119117261.ch7.

Ruju, A.; Buosi, C.; Coco, G.; Porta, M.; Trogu, D.; Ibba, A.; De Muro, S., **2022**. Ecosystem services of reed and seagrass debris on a urban Mediterranean beach (Poetto, Italy). *Estuar. Coast. Shelf Sci.* 271, 107862. https://doi.org/10.1016/j.ecss.2022.107862.

Salama, N.M.; Iskander, M.M.; El-Gindy, A.A.; Nafeih, A.M.; Moghazy, H.E.D.M., **2023**. Hydrodynamic simulation of rip currents along Al-Nakheel Beach, Alexandria, Egypt: Case study. *J. Mar. Sci. Appl.* 22, 137–145. https://doi.org/10.1007/s11804-023-00320-2.

Sammari, C.; Koutitonsky, V.G.; Moussa, M., **2006**. Sea level variability and tidal resonance in the Gulf of Gabes, Tunisia. *Cont. Shelf Res.* 26 (3), 338–350. https://doi.org/10.1016/j.csr.2005.11.006.

Sarkar, N.; Rizzo, A.; Vandelli, V.; Soldati, M., **2022**. A literature review of climate-related coastal risks in the Mediterranean, a climate change hotspot. *Sustainability* 14 (23), 15994. https://doi.org/10.3390/su142315994.

Schroeder, K.; Chiggiato, J.; Josey, S.A.; Borghini, M.; Aracri, S.; Sparnocchia, S., **2007**. Rapid response to climate change in a marginal sea. *Sci Rep.* 7, 4065. https://doi.org/10.1038/s41598-017-04455-5.

Shafique, S.; Sarwar, F.; Kausar, S.; Abbas, S.; Khalid, M., **2024**. Identification of shoreline changes using Digital Shoreline Analysis System (DSAS): A case study of Karachi Coast, Sindh, Pakistan. *Pak. J. Sci.* 76 (2), 179–189. https://doi.org/10.57041/vol76iss02pp179-189.

Shepard, F.P., **1963**. *Submarine Geology*. 2nd ed.; Harper and Row: New York.

Shepherd, A.; Ivins, E.R.; A, G.; Barletta, V.R.; Bentley, M.J.; Bettadpur, S.; Briggs, K.H.; Bromwich, D.H.; Forsberg, R.; Galin, N.; Horwath, M.; Jacobs, S.; Joughin, I.; King, M.A.; Lenaerts, J.T.; Li, J.; Ligtenberg, S. R.M.; Luckman, A.; Luthcke, S.B.; McMillan, M.; Meister, R.; Milne, G.; Mouginot, J.; Muir, A.; Nicolas, J.P.; Paden, J.; Payne, A.J.; Pritchard, H.; Rignot, E.; Rott, H.; Sørensen, L.S.; Scambos, T.A.; Scheuchl, B.; Schrama, E.J.O.; Smith, B.; Sundal, A.V.; van Angelen, J.H.; van de Berg, W.J.; van den Broeke, M.R.; Vaughan, D.G.; Velicogna, I.; Wahr, J.; Whitehouse, P.L.; Wingham, D.J.; Yi, D.; Young, D.; Zwally, H.J., **2012**. A reconciled estimate of ice-sheet mass balance. *Science* 338, 1183–1189. https://doi.org/10.1126/science.1228102.

Short, A.D., **1985**. Rip-current type, spacing and persistence, Narrabeen Beach, Australia. *Mar. Geol.* 65 (1–2), 47–71. https://doi.org/10.1016/0025-3227(85)90046-5.

Short, A.D., **1996**. The role of wave height, period, slope, tide range and embaymentisation in beach classifications: A review. *Rev. Chil. Hist. Nat.* 69, 589–604.

Short, A.D., **1999**. *Beach and Shoreface Morphodynamics*; John Wiley & Sons: Chichester.

Short, A.D., **2006**. Australian beach systems – nature and distribution. *J. Coast. Res.* 221, 11–27. https://doi.org/10.2112/05A-0002.1.

Short, A.D., **2007**. Australian rip systems – friend or foe? *J. Coast. Res.* 50, 7–11. https://doi.org/10.2112/JCR-SI50-002.1.

Short, A.D., **2010**. Role of geological inheritance in Australian beach morphodynamics. *Coast. Eng.* 57 (2), 92–97. https://doi.org/10.1016/j.coastaleng.2009.09.005.

Short, A.D.; Hogan, C.L., **1994**. Rip currents and beach hazards: their impact on public safety and implications for coastal management. *J. Coast. Res.* 12, 197–209.

Short, A.D.; Masselink, G., **1999**. Embayed and structurally controlled beaches. In: *Handbook of Beach and Shoreface Morphodynamics*; Short, A.D., Ed.; John Wiley & Sons Ltd.; pp. 230–250.

Short, F.T.; Neckles, H.A., **1999**. The effects of Global Climate Change on seagrasses. *Aquat. Bot.* 63 (3–4), 169–196. https://doi.org/10.1016/S0304-3770(98)00117-X.

Simeone, S.; De Falco, G., **2012**. Morphology and composition of beach-cast *Posidonia oceanica* litter on beaches with different exposures. *Geomorphology* 151–152, 224–233. https://doi.org/10.1016/j.geomorph.2012.02.005.

Simeone, S.; De Falco, G., **2013**. *Posidonia oceanica* banquette removal: sedimentological, geomorphological and ecological implications. *J. Coast. Res.* 65, 1045–1050.

Simeone, S.; De Muro, S.; De Falco, G., **2013a**. Seagrass berm deposition on a Mediterranean embayed beach. *Estuar. Coast. Shelf Sci.* 135, 171–181. https://doi.org/10.1016/j.ecss.2013.10.007.

Simeone, S.; Palombo, L.; De Falco, G., **2013b**. Morphodynamics of a nontidal embayed beach: The case study of Is Arutas (Western Mediterranean). *J. Coast. Res.* 29 (6a), 63–71. https://doi.org/10.2112/JCOASTRES-D-12-00020.1.

Simeone, S.; Molinaroli, E.; Conforti, A.; De Falco, G., **2018**. Impact of ocean acidification on the carbonate sediment budget of a temperate mixed beach. *Clim. Change* 150, 227–242 (2018). https://doi.org/10.1007/s10584-018-2282-3.

Simeone, S.; Palombo, L.; Molinaroli, E.; Brambilla, W.; Conforti, A.; De Falco, G., **2021**. Shoreline response to wave forcing and sea level rise along a geomorphological complex coastline (Western Sardinia, Mediterranean Sea). *Appl. Sci.* 11 (9), 4009. https://doi.org/10.3390/app11094009.

Small, C.; Gornitz, V.; Cohen, J.E., **2000**. Coastal hazards and the global distribution of human population. *Environ. Geosci.* 7, 3–12.

Small, C.; Nicholls, R.J., **2003**. A global analysis of human settlement in coastal zones. *J. Coast. Res.* 19, 584–599.

Snyder, R.L.; Dobson, F.W.; Elliott, J.A.; Long, R.B., **1981**. Array measurements of atmospheric pressure fluctuations above surface gravity waves. *J. Fluid Mech.* 102, 1–59. https://doi.org/10.1017/S0022112081002528.

Spagnolo, M.; Llopis, I.A.; Pappalardo, M.; Federici, P.R., **2008**. A new approach for the study of the coast indentation index. *J. Coast. Res.* 24 (6), 1459–1468. https://doi.org/10.2112/07-0880.1.

Stanica, A.; Ungureanu, V.G., **2010**. Understanding coastal morphology and sedimentology. *Terre Environ.* 88, 105–111.

Stockdon, H.F.; Holman, R.A.; Howd, P.A.; Sallenger, A.H. Jr., **2006**. Empirical parameterization of setup, swash, and runup. *Coast. Eng.* 53 (7), 573–588. https://doi.org/10.1016/j.coastaleng.2005.12.005.

Stratigaki, V.; Manca, E.; Prinos, P.; Losada, I.J.; Lara, J.L.; Sclavo, M.; Sánchez-Arcilla, A., **2011**. Large-scale experiments on wave propagation over *Posidonia oceanica*. *J. Hydraul. Res.* 49, 31–43. https://doi.org/10.1080/00221686.2011.583388.

Stronge, W.B.; Diaz, H.F.; Bokuniewicz, H.; Inman, D.L.; Jenkins, S.A.; Hsu, J.R.C.; Kennish, M.J.; Bird, E.; Hesp, P.A.; Crowell, M.; Leatherman, S.P.; Douglas, B.; Rampino, M.R.; Healy, T.R.; Gornitz, V.; Doody, J.P.; Kelletat, D.; Scheffers, A., **2005**. E. In: *Encyclopedia of Coastal Science*; Schwartz, M.L., Ed.; Encyclopedia of Earth Science Series; Springer: Dordrecht. pp. 401–462. https://doi.org/10.1007/1-4020-3880-1_5.

Sytnik, O.; Del Río, L.; Greggio, N.; Bonetti, J., **2018**. Historical shoreline trend analysis and drivers of coastal change along the Ravenna coast, NE Adriatic. *Environ. Earth. Sci.* 77, 779. https://doi.org/10.1007/s12665-018-7963-8.

Taborda, R.; Silva, A., **2012**. COSMOS: A lightweight coastal video monitoring system. *Comput. Geosci.* 49, 248–255. https://doi.org/10.1016/j.cageo.2012.07.013.

Telesca, L., Belluscio, A., Criscoli, A., Ardizzone, G., Apostolaki, E.T., Fraschetti, S., Gristina, M., Knittweis, L., Martin, C.S., Pergent, G., Alagna, A., Badalamenti, F., Garofalo, G., Gerakaris, V., Louise Pace, M., Pergent-Martini, C., Salomidi, M., **2015**. Seagrass meadows (*Posidonia oceanica*) distribution and trajectories of change. *Sci Rep.* 5, 12505. https://doi.org/10.1038/srep12505.

Thieler, E.R.; Himmelstoss, E.A.; Zichichi, J.L.; Ergul, A., **2009**. The Digital Shoreline Analysis System (DSAS) version 4.0 - An ArcGIS extension for calculating shoreline change. U.S. Geological Survey, Open-File Report (No. 2008–1278). https://doi.org/10.3133/ofr20081278.

Thomas, T.J.; Dwarakish, G.S., **2015**. Numerical wave modelling – A review. *Aquac. Procedia* 4, 443–448. https://doi.org/10.1016/j.aqpro.2015.02.059.

Tomasello, A.; Bosman, A.; Signa, G.; Rende, S.F.; Andolina, C.; Cilluffo, G.; Cassetti, F.P.; Mazzola, A.; Calvo, S.; Randazzo, G.; Scarpato, A.; Vizzini, S., **2022**. 3D-reconstruction of a giant Posidonia oceanica beach wrack (banquette): Sizing biomass, carbon and nutrient stocks by combining field data with high-resolution UAV photogrammetry. *Front. Mar. Sci.* 9, 903138. https://doi.org/10.3389/fmars.2022.903138.

Torresan, S.; Critto, A.; Rizzi, J.; Marcomini, A., **2012**. Assessment of coastal vulnerability to climate change hazards at the regional scale: the case study of the North Adriatic Sea. *Nat. Hazards Earth Syst. Sci.* 12, 2347–2368. https://doi.org/10.5194/nhess-12-2347-2012.

Torres-Freyermuth, A.; Losada, I.J.; Lara, J.L., **2007**. Modeling of surf zone processes on a natural beach using Reynolds-Averaged Navier-Stokes equations. *J. Geophys. Res. Oceans* 112 (C9). https://doi.org/10.1029/2006JC004050.

Trogu, D., **2022**. On the role of biomass on coastal morphodynamic in natural and urban Mediterranean beaches. *PhD Thesis*, University of Cagliari, Cagliari, Italy.

Trogu, D.; Buosi, C.; Ruju, A.; Porta, M.; Ibba, A.; De Muro, S., **2020**. What happens to a Mediterranean microtidal wave-dominated beach during significant storm events? The morphological response of a natural Sardinian beach (Western Mediterranean). *J. Coast. Res.* 95, 695. https://doi.org/10.2112/SI95-135.1.

Trogu, D.; Simeone, S.; Ruju, A.; Porta, M.; Ibba, A.; De Muro, S., **2023**. A four-year video monitoring analysis of the Posidonia oceanica banquette dynamic: A case study from an urban microtidal Mediterranean beach (Poetto Beach, Southern Sardinia, Italy*). J. Mar. Sci. Eng.* 11 (12), 2376. https://doi.org/10.3390/jmse11122376.

Trogu, D.; Simeone, S.; Usai, A.; Porta, M.; De Muro, S., **2024**. On the role of wood and seagrass rests in coastal flooding events in Mediterranean microtidal beaches. In:

Coastlines under change: Proceedings from the International Coastal Symposium (ICS) 2024 (Doha, Qatar); Phillips, M.R., Al-Naemi, S., Duarte, C.M., Eds.; *J. Coast. Res.* 113, 115–119. https://doi.org/10.2112/JCR-SI113-023.1.

Usai, A.; Simeone, S.; Trogu, D.; Porta, M.; De Muro, S., **2024**. Morphometric analysis and classification of the embayed beaches on the southern coast of Sardinia Island (Western Mediterranean Sea). In: *Coastlines under change: Proceedings from the International Coastal Symposium (ICS) 2024 (Doha, Qatar)*; Phillips, M.R., Al-Naemi, S., Duarte, C.M., Eds.; *J. Coast. Res.* 113, 748-752. https://doi.org/10.2112/JCR-SI113-147.1.

Usai, A.; Simeone, S.; Trogu, D.; Porta, M.; De Muro, S., **2025a**. A morphometric analysis of embayed beaches: southern Sardinia Island. *Geomorphology* 483, 109838. https://doi.org/10.1016/j.geomorph.2025.109838.

Usai, A.; Trogu, D.; Porta, M.; Demuro, S.; Simeone, S., **2025b**. 70 years of shoreline changes in southern Sardinia (Italy): Retreat and accretion on 79 Mediterranean microtidal beaches. *Water* 17 (17), 2517. https://doi.org/10.3390/w17172517.

Vacchi, M.; De Falco, G.; Simeone, S.; Montefalcone, M.; Morri, C.; Ferrari, M.; Bianchi, C.N., **2017**. Biogeomorphology of the Mediterranean Posidonia oceanica seagrass meadows. *Earth Surf. Process. Landf.* 42 (1), 42–54. https://doi.org/10.1002/esp.3932.

Vacchi, M.; Montefalcone, M.; Bianchi, C.N.; Morri, C.; Ferrari, M., **2012**. Hydrodynamic constraints to the seaward development of *Posidonia oceanica* meadows. *Estuar. Coast. Shelf Sci.* 97, 58–65. https://doi.org/10.1016/j.ecss.2011.11.024.

Valentini, N.; Saponieri, A.; Damiani, L., **2017a**. A new video monitoring system in support of Coastal Zone Management at Apulia Region, Italy. *Ocean Coast. Manag.* 142, 122–135. https://doi.org/10.1016/j.ocecoaman.2017.03.032.

Valentini, N.; Saponieri, A.; Molfetta, M.G.; Damiani, L., **2017b**. New algorithms for shoreline monitoring from coastal video systems. *Earth Sci. Inform.* 10, 495–506. https://doi.org/10.1007/s12145-017-0302-x.

Van Dongeren, A.; Van Ormondt, M.; Sembiring, L.; Sasso, R.; Austin, M.; Briere, C.; Swinkels, C.; Roelvink, J.A.; Van Thiel de Vries, J., **2013**. Rip current predictions through model data assimilation on two distinct beaches. *Coastal Dynamics*; Bordeaux, France; pp. 1775–1786.

Venkateswarlu, C.; Surisetty, V.V.A.K.; Somani, A.; Gireesh, B.; Naidu, C.V., **2023**. Surf zone-related drownings and injuries based on lifeguard records in Goa beaches (2008-2020). *Nat. Hazards* 117, 313–337. https://doi.org/10.1007/s11069-023-05861-x.

Virdis, S.; Oggiano, G.; Disperati, L., **2012**. A geomatics approach to multitemporal shoreline analysis in Western Mediterranean: The case of Platamona-Maritza Beach (Northwest Sardinia, Italy). *J. Coast. Res.* 28, 624–640.

Von Schuckmann, K.; Moreira, L.; Cancet, M.; Gues, F.; Autret, E.; Baker, J.; Bricaud, C.; Bourdalle-Badie, R.; Castrillo, L.; Cheng, L.; Chevallier, F.; Ciani, D.; de Pascual-Collar, A.; De Toma, V.; Drevillon, M.; Fanelli, C.; Garric, G.; Gehlen, M.; Giesen, R.; Hodges, K.; Iovino, D.; Jandt-Scheelke, S.; Jansen, E.; Juza, M.; Karagali, I.; Lavergne, T.; Masina, S.; McAdam, R.; Minière, A.; Morrison, H.; Panteleit, T. R.; Pisano, A.; Pujol, M.-I.; Stoffelen, A.; Thual, S.; Van Gennip, S.; Veillard, P.; Yang, C.; Zuo, H., **2024**. The State of the Global Ocean. In: *8th Edition of the Copernicus Ocean State Report (OSR8)*; von Schuckmann, K., Moreira, L., Grégoire, M., Marcos, M., Staneva, J., Brasseur, P., Garric, G., Lionello, P., Karstensen, J., Neukermans, G., Eds.; Copernicus Publications: State Planet; Vol. 4-osr8, 1. https://doi.org/10.5194/sp-4-osr8-1-2024.

Vousdoukas, M.I.; Pennucci, G.; Holman, R.A.; Conley, D.C., **2011**. A semi automatic technique for rapid environmental assessment in the coastal zone using Small Unmanned Aerial Vehicles (SUAV). *J. Coast. Res.* 64, 1755–1759.

Vousdoukas, M.I.; Ranasinghe, R.; Mentaschi, L.; Plomaritis, T.A.; Athanasiou, P.; Luijendijk, A.; Feyen, L., **2020**. Sandy coastlines under threat of erosion. *Nat. Clim. Change* 10, 260–263. https://doi.org/10.1038/s41558-020-0697-0.

WAMDI Group, **1988**. The WAM Model - A third generation ocean wave prediction model. *J. Phys. Oceanogr.* 18, 1775–1810.

Wang, Z.Q.; Tan, S.K.; Cheng, N.S.; Goh, K.W., **2008**. A simple relationship for crenulated-shaped bay in static equilibrium. *Coast. Eng.* 55 (1), 73–78. https://doi.org/10.1016/j.coastaleng.2007.07.004.

Williams, B.A.; Watson, J.E.M.; Beyer, H.L.; Klein, C.J.; Montgomery, J.; Runting, R.K.; Roberson, L.A.; Halpern, B.S.; Grantham, H.S.; Kuempel, C.D.; Frazier, M.; Venter, O.; Wenger, A., **2022**. Global rarity of intact coastal regions. *Conserv. Biol.* 36 (4), e138374. https://doi.org/10.1111/cobi.13874.

Williams, J.J.; Esteves, L.S., **2017**. Guidance on setup, calibration, and validation of hydrodynamic, wave, and sediment models for shelf seas and estuaries. *Adv. Civil Eng. 2017*, 5251902. https://doi.org/10.1155/2017/5251902.

Woolf, D.; Wolf, J., **2013**. Impacts of climate change on storms and waves. *MCCIP Sci. Rev.* 2013, 20–26. https://doi.org/10.14465/2013.arc03.020-026.

Wright, L.D.; Short, A.D., **1984**. Morphodynamic variability of surf zones and beaches: A synthesis. *Mar. Geol.* 56 (1–4), 93–118. https://doi.org/10.1016/0025-3227(84)90008-2.

Wright, L.D.; Syvitski, J.P.M.; Nichols, C.R., **2019**. Coastal Systems in the Anthropocene. In: *Tomorrow's Coasts: Complex and Impermanent*; Wright, L., Nichols, C., Eds.; Coastal Research Library, Vol. 27; Springer: Cham. https://doi.org/10.1007/978-3-319-75453-6_6.

Wu, J., **1982**. Wind-stress coefficients over sea surface from breeze to hurricane. *J. Geophy. Res.* 87 (C12), 9704–9706. https://doi.org/10.1029/JC087iC12p09704.

Xu, J.; Yan, S.; Zou, Z.; Liu, Z.; Wang, Y.; Chang, C.; Wang, Z.; You, Z., **2024**. Flow characteristics of the rip current system adjacent to a coastal vertical structure for irregular waves. *Ocean Eng.* 312, 119128. https://doi.org/10.1016/j.oceaneng.2024.119128.

Younsi, S.E.; Bouziane, Z., **2023**. Plant diversity in Mediterranean coastal dune systems subjected to anthropogenic disturbances. *Biodivers. Res. Conserv.* 72, 25–38. https://doi.org/10.14746/biorc.2023.72.4.

Yu, J.; Slinn, D. N., **2003**. Effects of wave-current interaction on rip currents. *J. Geophys. Res. Oceans* 108 (C3). https://doi.org/10.1029/2001JC001105.

Yuan, Y.; Yang, H.; Yu, F.; Gao, Y.; Li, B.; Xing, C., **2023**. A wave-resolving modeling study of rip current variability, rip hazard, and swimmer escape strategies on an embayed beach. *Nat. Hazards Earth Syst. Sci.* 23, 3487–3507. https://doi.org/10.5194/nhess-23-3487-2023.

Zhang, C.; Wang, Y.; Du, J.; Tian, Z.; Zhong, Y., **2025**. Beach erosion characteristics induced by human activities – A case study in Haiyang, Yellow Sea. *Remote Sens.* 17 (5), 736. https://doi.org/10.3390/rs17050736.

Web Resources

Council of Europe, **1982**. *Bern Convention - Conservation of European Wildlife and Natural Habitats (82/72/EEC)*. Available online: https://www.coe.int/en/web/bern-convention (Last accessed on 31 July 2025).

Deltares, **2024a**. Delft3D-WAVE: User Manual. Deltares, Version 4.05. Available online: https://oss.deltares.nl/web/delft3d/manuals (Last accesses in January 2024).

Deltares, **2024b**. Delft3D-FLOW: User Manual. Deltares, Version 4.05. Available online: https://oss.deltares.nl/web/delft3d/manuals (Last accesses in January 2024).

EMODnet Bathymetry Consortium, **2024**. EMODnet Digital Bathymetry (DTM 2024). https://doi.org/10.12770/cf51df64-56f9-4a99-b1aa-36b8d7b743a1. Available online: https://emodnet.ec.europa.eu/geoviewer (Last accesses in July 2025).

European Commission, **1992**. *Natura 2000 Network: Europe's network of protected areas*. Available online: https://environment.ec.europa.eu/topics/nature-and-biodiversity/natura-2000_en (Last accessed on 31 July 2025).

European Council, **1992**. *Directive 92/43/EEC on the conservation of natural habitats and of wild fauna and flora (Habitats Directive)*. Available online: https://environment.ec.europa.eu/topics/nature-and-biodiversity/habitats-directive_en (Last accessed on 31 July 2025).

European Parliament and of the Council, **2000**. *Water Framework Directive - WFD (2000/60/EC)*. Available online: https://environment.ec.europa.eu/topics/water/water-framework-directive_en (Last accessed on 31 July 2025).

European Parliament and of the Council, **2008**. *Marine Strategy Framework Directive - MSFD (2008/56/EC).* Available online: https://research-and-innovation.ec.europa.eu/research-area/environment/oceans-and-seas/eu-marine-strategy-framework-directive_en (Last accessed on 31 July 2025).

European Parliament and of the Council, **2014**. *Environmental Impact Assessment Directive - EAI (2014/52/EU)*. Available online: https://environment.ec.europa.eu/law-and-governance/environmental-assessments/environmental-impact-assessment_en (Last accessed on 31 July 2025).

European Parliament and of the Council, **2014**. *Maritime Spatial Planning Directive (2014/89/EU)*. Available online: https://oceans-and-fisheries.ec.europa.eu/ocean/blue-economy/maritime-spatial-planning_en (Last accessed on 31 July 2025).

Hersbach, H.; Bell, B.; Berrisford, P.; Biavati, G.; Horányi, A.; Muñoz Sabater, J.; Nicolas, J.; Peubey, C.; Radu, R.; Rozum, I.; Schepers, D.; Simmons, A.; Soci, C.; Dee, D.; Thépaut, J-N., **2023**. ERA5 hourly data on single levels from 1940 to present. Copernicus Climate Change Service (C3S) Climate Data Store (CDS). https://doi.org/10.24381/cds.adbb2d47 (Last accesses in June 2025).

Korres, G., Ravdas, M., Denaxa, D., Sotiropoulou, M., **2021**. Mediterranean Sea Waves Reanalysis INTERIM (CMEMS Med-Waves, MedWAM3I system) (Version 1) [Data set]. Copernicus Monitoring Environment Marine Service (CMEMS). Available online: https://doi.org/10.25423/CMCC/MEDSEA_MULTIYEAR_WAV_006_012_MEDWAM3I (Accesses in April 2023; 04 July 2025).

Mediterranean Action Plan of the United Nations Environment Programme (UNEP/MAP), **1976**. *The Convention for the Protection of the Mediterranean Sea against Pollution*. Available online: https://www.unep.org/unepmap/who-we-are/barcelona-convention-and-protocols (Last accessed on 31 July 2025).

Regione Sardegna, **2013**. Programma Azione Coste Sardegna (P.A.C.) - Relazione Generale. Available online: https://portal.sardegnasira.it/strumenti-conoscitivi (Last accesses in March 2023).

Regione Sardegna, **2021**. Piano di Gestione del Rischio di Alluvioni (PGRA): Secondo Ciclo di Pianificazione. Available online: https://pianogestionerischioalluvioni.regione.sardegna.it/index.php?xsl=2425&s=435566&v=2&c=95271&t=1&tb=14006 (Lats accessed on 04 July 2025).

Regione Sardegna: WMS Service - Regione Sardegna. Available online: https://webgis.regione.sardegna.it/geoserverraster/ows?service=WMS&request=GeCapabilities (Accesses in March 2023; 27 April 2025).

Rete Ondametrica Nazionale - ISPRA (Istituto Superiore per la Protezione e la Ricerca Ambientale). Available online: https://www.mareografico.it/it/stazioni.html (Last accessed on 27 April 2025).

Sardegna Geoportale: Data download - Regione Sardegna. Available online: https://www.sardegnageoportale.it/accessoaidati/downloaddati (Accesses in March 2023; 12 July 2025).

Sardegna Geoportale: Download Raster - Regione Sardegna. Available online: https://www.sardegnageoportale.it/webgis2/sardegnamappe/?map=download_raster (Last accessed on 24 April 2025).

United Nations, **2015**. *Transforming Our World: The 2030 Agenda for Sustainable Development*; United Nations: New York, NY, USA. Available online: https://www.un.org/sustainabledevelopment/sustainable-development-goals/ (Last accessed on 31 July 2025).

Appendix A: Morphometric parameters and indices database (Chapter 4)

Table A.1

List of beaches reported in the Coastal Plan (P.A.C.) (Regione Sardegna, 2013) and new beaches identified through the analysis of aerial orthophotos (with corresponding assigned code).

ID Code	Physiographic Unit Code	Littoral Unit Code	Littoral Unit Name	Original Beach Code	New Beach Code	Original Beach Name	New Beach Name
1	8	8A	Capo Teulada - Torre di Porto Scudo	-	8A-02	-	Spiaggia di Punta Aligusta (Loc. Bocca Corti)
2	8	8A	Capo Teulada - Torre di Porto Scudo	8A-01	-	Porto Zafferano	-
3	8	8B	Torre di Porto Scudo - Porto Scudo	8B-01	-	Porto Scudo	-
4	8	8C	Porto Scudo - Punta Niedda	-	8C-02	-	Spiaggia di Porto Pirastu (Loc. Miniera M. Lapanu)
5	8	8C	Porto Scudo - Punta Niedda	-	8C-03	-	Spiaggia degli Americani (Loc. Pala di Levante)
6	8	8C	Porto Scudo - Punta Niedda	8C-01	-	Porto Tramatzu	-
7	8	8D	Punta Niedda - Torre Budello	-	8D-01	-	Spiaggia Torre del Budello (Loc. Porto di Teulada)

ID Code	Physiographic Unit Code	Littoral Unit Code	Littoral Unit Name	Original Beach Code	New Beach Code	Original Beach Name	New Beach Name
8	8	8E	Torre Budello - Capo di Piscinnì	-	8E-02	-	Spiaggia di Campionna (Loc. Porto di Campionna)
9	8	8E	Torre Budello - Capo di Piscinnì	-	8E-03	-	Spiaggia Punta Libeccio
10	8	8E	Torre Budello - Capo di Piscinnì	-	8E-04	-	Porto Larboi
11	8	8E	Torre Budello - Capo di Piscinnì	8E-01	-	Piscinnì	-
12	8	8E	Torre Budello - Capo di Piscinnì	-	8E-05	-	Spiaggia di Cala Is Crabas
13	8	8E	Torre Budello - Capo di Piscinnì	-	8E-06	-	Spiaggia della Caletta di Torre Pixinni
14	8	8F	Capo di Piscinnì - Capo Malfatano	-	8F-01	-	Spiaggia (Loc. Cala de su Senzu - 1)

ID Code	Physiographic Unit Code	Littoral Unit Code	Littoral Unit Name	Original Beach Code	New Beach Code	Original Beach Name	New Beach Name
15	8	8F	Capo di Piscinnì - Capo Malfatano	-	8F-02	-	Spiaggia (Loc. Cala de su Senzu - 2)
16	8	8G	Capo Malfatano - Isola Ferraglione	-	8G-02	-	Spiaggia di Capo Malfatano (Loc. Porto di Malfatano)
17	8	8G	Capo Malfatano - Isola Ferraglione	8G-01	-	Tuerredda	-
18	8	8G	Capo Malfatano - Isola Ferraglione	**-**	8G-03	**-**	Spiaggia di Sa Perda Longa
19	8	8G	Capo Malfatano - Isola Ferraglione	-	8G-04	-	Spiaggia di Cala de Sa Perda Longa - 1)
20	8	8G	Capo Malfatano - Isola Ferraglione	-	8G-05	-	Spiaggia di Cala de Sa Perda Longa - 2)
21	8	8G	Capo Malfatano - Isola Ferraglione	-	8G-06	-	Spiaggia dei Solitari (Loc. Punta Calarza)

ID Code	Physiographic Unit Code	Littoral Unit Code	Littoral Unit Name	Original Beach Code	New Beach Code	Original Beach Name	New Beach Name
22	8	8G	Capo Malfatano - Isola Ferraglione	-	8G-07	-	Spiaggia di Ferraglione (Fronte Isola Ferraglione)
23	8	8H	Isola Ferraglione - Cala Niedda	8H-01	-	Cala Cipolla	-
24	8	8H	Isola Ferraglione - Cala Niedda	8H-02	-	Campana Pontile - Su Giudeu - S'acqua Durci	-
25	8	8H	Isola Ferraglione - Cala Niedda	8H-03	-	Campana	-
26	8	8H	Isola Ferraglione - Cala Niedda	-	8H-06	-	Spiaggia di Cala del Morto
27	8	8H	Isola Ferraglione - Cala Niedda	8H-04	-	Bithia - Sa Colonia	-
28	8	8H	Isola Ferraglione - Cala Niedda	8H-05	-	Torre Chia - Su Cardolinu	-

ID Code	Physiographic Unit Code	Littoral Unit Code	Littoral Unit Name	Original Beach Code	New Beach Code	Original Beach Name	New Beach Name
29	8	8I	Cala Niedda - Capo di Pula	8I-01	8I-01A	Pinus Village	Pinus Village (Tratto W)
30	8	8I	Cala Niedda - Capo di Pula	8I-01	8I-01B	Pinus Village	Pinus Village (Tratto E)
31	8	8I	Cala Niedda - Capo di Pula	8I-02	-	Santa Margherita	-
32	8	8I	Cala Niedda - Capo di Pula	8I-03	-	Is Morus	-
33	8	8I	Cala Niedda - Capo di Pula	-	8I-07	-	Spiaggia (Loc. Torre di Cala d'Ostia)
34	8	8I	Cala Niedda - Capo di Pula	-	8I-08	-	Spiaggia di Cala d'Ostia (Tratto W1)
35	8	8I	Cala Niedda - Capo di Pula	-	8I-09	-	Spiaggia di Cala d'Ostia (Tratto W2)

ID Code	Physiographic Unit Code	Littoral Unit Code	Littoral Unit Name	Original Beach Code	New Beach Code	Original Beach Name	New Beach Name
36	8	8I	Cala Niedda - Capo di Pula	-	8I-10	-	Spiaggia di Cala d'Ostia (Tratto E)
37	8	8I	Cala Niedda - Capo di Pula	8I-04	-	Cala Marina	-
38	8	8I	Cala Niedda - Capo di Pula	8I-05	-	Porto d'Agumu	-
39	8	8L	Capo di Pula - Isola S. Macario	8L-01	-	Su Guventeddu - Nora	-
40	8	8M	Isola S. Macario - Punta Zavorra	8M-01	-	Su Stangioni Foxi Niedda	-
41	8	8M	Isola S. Macario - Punta Zavorra	8M-02	-	Porto Columbu - Perd'e Sali	-
42	8	8N	Punta Zavorra - Porto Canale	8N-01	8N-01A	Giorgino - La Maddalena - Frutti d'Oro	Frutti d'Oro (Tratto 1)

ID Code	Physiographic Unit Code	Littoral Unit Code	Littoral Unit Name	Original Beach Code	New Beach Code	Original Beach Name	New Beach Name
43	8	8N	Punta Zavorra - Porto Canale	8N-01	8N-01B	Giorgino - La Maddalena - Frutti d'Oro	Frutti d'Oro (Tratto 2)
44	8	8N	Punta Zavorra - Porto Canale	8N-01	8N-01C	Giorgino - La Maddalena - Frutti d'Oro	Frutti d'Oro (Tratto 3)
45	8	8N	Punta Zavorra - Porto Canale	8N-01	8N-01D	Giorgino - La Maddalena - Frutti d'Oro	Frutti d'Oro (Tratto 4)
46	8	8N	Punta Zavorra - Porto Canale	8N-01	8N-01E	Giorgino - La Maddalena - Frutti d'Oro	Spiaggia La Maddalena
47	8	8N	Punta Zavorra - Porto Canale	8N-01	8N-01F	Giorgino - La Maddalena - Frutti d'Oro	Spiaggia (Loc. La Maddalena)
48	8	8N	Punta Zavorra - Porto Canale	8N-01	8N-01G	Giorgino - La Maddalena - Frutti d'Oro	Giorgino (Tratto 1)
49	8	8N	Punta Zavorra - Porto Canale	8N-01	8N-01H	Giorgino - La Maddalena - Frutti d'Oro	Giorgino (Tratto 2)

ID Code	Physiographic Unit Code	Littoral Unit Code	Littoral Unit Name	Original Beach Code	New Beach Code	Original Beach Name	New Beach Name
50	8	8N	Punta Zavorra - Porto Canale	8N-01	8N-01I	Giorgino - La Maddalena - Frutti d'Oro	Giorgino (Tratto 3)
51	8	8N	Punta Zavorra - Porto Canale	8N-01	8N-01L	Giorgino - La Maddalena - Frutti d'Oro	Giorgino (Tratto 4)
52	8	8N	Punta Zavorra - Porto Canale	8N-01	8N-01M	Giorgino - La Maddalena - Frutti d'Oro	Giorgino (Tratto 5)
53	8	8O	Porto Canale - Torre Foxi	-	8O-03	-	Spiaggia di Cale Murru (Loc. Faro S. Elia)
54	8	8O	Porto Canale - Torre Foxi	8O-01	-	Cala Mosca	-
55	8	8O	Porto Canale - Torre Foxi	80-02	-	Poetto	-
56	8	8P	Torre Foxi - Cala Regina	-	8P-01	-	Spiaggia di Sant'Andrea - Spiaggia di Flumini - Spiaggia di Santa Luria

ID Code	Physiographic Unit Code	Littoral Unit Code	Littoral Unit Name	Original Beach Code	New Beach Code	Original Beach Name	New Beach Name
57	8	8P	Torre Foxi - Cala Regina	-	8P-02	-	Spiaggia (Loc. Marina di Capitana)
58	8	8P	Torre Foxi - Cala Regina	-	8P-03	-	Spiaggia di Capitana
59	8	8P	Torre Foxi - Cala Regina	-	8P-04	-	Spiaggia di Is Mortorius
60	8	8P	Torre Foxi - Cala Regina	-	8P-05	-	Spiaggia (Loc. Salmagi)
61	8	8Q	Cala Regina - Torre de su Fenugu	8Q-01	8Q-01A	Mari Pintau e Cala Regina	Spiaggia di Cala Regina
62	8	8Q	Cala Regina - Torre de su Fenugu	8Q-01	8Q-01B	Mari Pintau e Cala Regina	Spiaggia di Is Canaleddus
63	8	8Q	Cala Regina - Torre de su Fenugu	8Q-01	8Q-01C	Mari Pintau e Cala Regina	Spiaggia di Mari Pintau

ID Code	Physiographic Unit Code	Littoral Unit Code	Littoral Unit Name	Original Beach Code	New Beach Code	Original Beach Name	New Beach Name
64	8	8Q	Cala Regina - Torre de su Fenugu	8Q-02	-	Geremeas	-
65	8	8Q	Cala Regina - Torre de su Fenugu	8Q-03	-	Cann'e Sisa	-
66	8	8R	Torre de su Fenugu - Capo Boi	8R-01	-	Genn'e Mari	-
67	8	8R	Torre de su Fenugu - Capo Boi	-	8R-03	-	Spiaggia (Loc. Portu Perdosu)
68	8	8R	Torre de su Fenugu - Capo Boi	8R-02	-	Solanas	-
69	8	8S	Capo Boi - Capo Carbonara	8S-01	-	Porto Sa Ruxi	-
70	8	8S	Capo Boi - Capo Carbonara	8S-02	-	Capo Boi	-

ID Code	Physiographic Unit Code	Littoral Unit Code	Littoral Unit Name	Original Beach Code	New Beach Code	Original Beach Name	New Beach Name
71	8	8S	Capo Boi - Capo Carbonara	-	8S-06	-	Spiaggia di Is Piscadeddus
72	8	8S	Capo Boi - Capo Carbonara	8S-03	-	Campus	
73	8	8S	Capo Boi - Capo Carbonara	-	8S-07		Spiaggia di Cuccureddus (Loc. Punta Cuccureddu)
74	8	8S	Capo Boi - Capo Carbonara	8S-04	-	Campulongu	-
75	8	8S	Capo Boi - Capo Carbonara	8S-05	-	Spiaggia del Riso e Nuova Spiaggia del Porto	-
76	8	8S	Capo Boi - Capo Carbonara	-	8S-08	-	Spiaggia della Fortezza (Loc. Torre Vecchia)
77	8	8S	Capo Boi - Capo Carbonara	-	8S-09	-	Spiaggia di S. Stefano

ID Code	Physiographic Unit Code	Littoral Unit Code	Littoral Unit Name	Original Beach Code	New Beach Code	Original Beach Name	New Beach Name
78	8	8S	Capo Boi - Capo Carbonara	-	8S-10	-	Spiaggia (Loc. Punta S. Stefano)
79	8	8S	Capo Boi - Capo Carbonara	-	8S-11	-	Spiaggia di Cala Santa Caterina

Table A.2

Coordinates of beaches identified through the analysis of aerial orthophotos (Coordinate system: WGS84 - UTM 32N).

ID Code	Latitude (N)	Longitude (E)
1	38° 53’ 12’’	8° 38’ 53’’
2	38° 53’ 48’’	8° 39’ 05’’
3	38° 54’ 48’’	8° 39’ 54’’
4	38° 55’ 08’’	8° 41’ 37’’
5	38° 55’ 17’’	8° 42’ 22’’
6	38° 55’ 29’’	8° 42’ 40’’
7	38° 55’ 52’’	8° 43’ 11’’
8	38° 54’ 58’’	8° 46’ 05’’
9	38° 54’ 56’’	8° 46’ 32’’
10	38° 54’ 50’’	8° 46’ 42’’
11	38° 54’ 47’’	8° 46’ 52’’
12	38° 54’ 24’’	8° 46’ 47’’
13	38° 54’ 19’’	8° 46’ 45’’
14	38° 53’ 55’’	8° 47’ 06’’
15	38° 53’ 54’’	8° 47’ 11’’
16	38° 53’ 40’’	8° 47’ 55’’
17	38° 53’ 41’’	8° 48’ 47’’
18	38° 53’ 31’’	8° 49’ 20’’
19	38° 53’ 26’’	8° 49’ 20’’
20	38° 53’ 20’’	8° 49’ 46’’
21	38° 53’ 02’’	8° 49’ 47’’
22	38° 52’ 54’’	8° 49’ 46’’
23	38° 52’ 43’’	8° 51’ 16’’
24	38° 53’ 07’’	8° 51’ 47’’
25	38° 53’ 21’’	8° 52’ 16’’
26	38° 53’ 29’’	8° 52’ 28’’
27	38° 53’ 41’’	8° 52’ 43’’
28	38° 53’ 52’’	8° 53’ 13’’
29	38° 54’ 55’’	8° 54’ 36’’
30	38° 55’ 01’’	8° 54’ 41’’
31	38° 55’ 38’’	8° 55’ 24’’
32	38° 56’ 33’’	8° 56’ 45’’
33	38° 56’ 59’’	8° 57’ 26’’
34	38° 57’ 18’’	8° 57’ 50’’
35	38° 57’ 23’’	8° 57’ 60’’
36	38° 57’ 31’’	8° 58’ 15’’
37	38° 57’ 53’’	8° 58’ 41’’
38	38° 59’ 06’’	8° 59’ 43’’

ID Code	Latitude (N)	Longitude (E)
39	38° 59’ 28’’	9° 00’ 53’’
40	39° 00’ 35’’	9° 01’ 24’’
41	39° 01’ 27’’	9° 01’ 36’’
42	39° 08’ 10’’	9° 00’ 54’’
43	39° 08’ 15’’	9° 00’ 55’’
44	39° 08’ 23’’	9° 00’ 59’’
45	39° 08’ 30’’	9° 01’ 01’’
46	39° 09’ 03’’	9° 01’ 13’’
47	39° 09’ 25’’	9° 01’ 32’’
48	39° 09’ 47’’	9° 01’ 46’’
49	39° 10’ 04’’	9° 02’ 02’’
50	39° 10’ 13’’	9° 02’ 11’’
51	39° 10’ 51’’	9° 02’ 49’’
52	39° 11’ 58’’	9° 04’ 12’’
53	39° 11’ 08’’	9° 08’ 40’’
54	39° 11’ 11’’	9° 09’ 07’’
55	39° 13’ 05’’	9° 11’ 03’’
56	39° 12’ 50’’	9° 17’ 13’’
57	39° 12’ 26’’	9° 18’ 05’’
58	39° 12’ 18’’	9° 19’ 04’’
59	39° 11’ 56’’	9° 19’ 37’’
60	39° 11’ 38’’	9° 20’ 18’’
61	39° 10’ 45’’	9° 21’ 19’’
62	39° 10’ 39’’	9° 21’ 46’’
63	39° 10’ 28’’	9° 22’ 11’’
64	39° 09’ 57’’	9° 22’ 51’’
65	39° 09’ 22’’	9° 23’ 39’’
66	39° 08’ 40’’	9° 24’ 22’’
67	39° 08’ 24’’	9° 24’ 47’’
68	39° 08’ 02’’	9° 25’ 49’’
69	39° 07’ 48’’	9° 27’ 12’’
70	39° 07’ 43’’	9° 27’ 54’’
71	39° 07’ 56’’	9° 28’ 18’’
72	39° 08’ 08’’	9° 28’ 09’’
73	39° 07’ 58’’	9° 29’ 46’’
74	39° 07’ 42’’	9° 30’ 25’’
75	39° 07’ 13’’	9° 30’ 34’’
76	39° 06’ 58’’	9° 30’ 19’’
77	39° 06’ 37’’	9° 30’ 19’’
78	39° 06’ 29’’	9° 30’ 13’’
79	39° 06’ 24’’	9° 30’ 36’’

Table A.3

Values of morphometric parameters (following Bowman et al., 2009), indices and δ' calculated for each beach identified through the aerial orthophotos.

ID Code (Sector)	R_o (m)	a (m)	S_1 (m)	S_2 (m)	S_3 (%) (*Dir1*)	S_3 (%) (*Dir2*)	A_e (m^2 X10^2)	B_w (m)	I	S_2 / S_1	H_s (m)	T (s)	δ' (H_b Eq. 4.5)	δ' (H_b Eq. 4.6)
1 (1)	667	319	1541	435	94	-	1695	17	0.48	0.28			64.32	27.80
2 (1)	781	481	2204	101	21	-	3481	27	0.62	0.46			124.19	48.57
3 (1)	414	802	2282	275	51	-	2965	115	1.94	0.12			351.01	98.22
4 (1)	793	292	1761	188	0	-	1416	12	0.37	0.11			69.27	30.54
5 (1)	149	142	487	88	100	61	161	10	0.95	0.18			34.20	12.43
6 (1)	752	416	1718	472	0	-	2354	37	0.55	0.27			70.51	30.54
7 (1)	538	375	1498	147	0	-	1329	15	0.70	0.10			82.71	12.43
8 (1)	299	57	355	231	0	0	103	13	0.19	0.65	0.84	5.91	5.46	30.65
9 (1)	225	125	505	163	-	100	200	19	0.56	0.32			20.18	32.57
10 (1)	178	81	293	57	-	0	85	13	0.46	0.19			7.35	3.29
11 (1)	432	282	1313	318	-	10	1003	45	0.65	0.24			82.69	8.85
12 (1)	127	134	569	56	-	100	120	6	1.06	0.20			64.14	3.77
13 (1)	115	98	352	67	-	100	85	2	0.85	0.19			22.40	31.16
14 (1)	147	80	351	23	100	0	76	6	0.54	0.07			15.39	19.91
15 (1)	154	93	386	44	-	43	94	9	0.60	0.11			18.21	8.41

ID Code (Sector)	R_o (m)	a (m)	S_1 (m)	S_2 (m)	S_3 (%) (*Dir1*)	S_3 (%) (*Dir2*)	A_e (m^2X10^2)	B_w (m)	I	S_2 / S_1	H_s (m)	T (s)	δ' (H_b Eq. 4.5)	δ' (H_b Eq. 4.6)
16 (2)	325	140	554	346	52	-	361	23	0.40	0.62			8.10	6.54
17 (2)	1023	402	2362	437	27	-	3906	47	0.39	0.19			54.46	7.55
18 (2)	331	182	722	102	-	0	354	11	0.55	0.14			15.29	3.28
19 (2)	327	343	1667	187	-	100	1023	20	1.05	0.11	1.52	6.78	126.10	17.69
20 (2)	121	142	480	76	-	0	115	19	1.17	0.16			24.92	3.96
21 (2)	201	145	576	39	-	0	165	11	0.72	0.07			18.36	3.44
22 (2)	173	76	360	76	-	100	92	16	0.44	0.21			7.10	1.56
23 (3)	318	232	1245	131	100	88	442	70	0.73	0.11			83.44	19.32
24 (3)	1340	306	2090	1338	0	-	3383	203	0.23	0.64			35.22	12.92
25 (3)	509	156	772	431	0	-	643	82	0.31	0.56			12.48	4.64
26 (3)	262	99	639	46	0	-	135	30	0.38	0.07	1.16	6.17	21.06	6.18
27 (3)	752	280	1257	782	16	-	1639	82	0.37	0.62			23.50	8.33
28 (3)	390	210	1110	298	0	-	713	67	0.54	0.27			46.11	12.52
29 (3)	186	35	253	49	0	-	38	24	0.19	0.19			3.47	1.36
30 (3)	366	48	435	313	0	-	89	43	0.13	0.72			4.88	2.05

ID Code (Sector)	R_o (m)	a (m)	S_1 (m)	S_2 (m)	S_3 (%) (*Dir1*)	S_3 (%) (*Dir2*)	A_e (m^2 X10^2)	B_w (m)	I	S_2 / S_1	H_s (m)	T (s)	δ' (H_b Eq. 4.5)	δ' (H_b Eq. 4.6)
31 (3)	2731	179	2915	2699	0	-	3352	47	0.07	0.93			27.81	12.34
32 (3)	1366	169	1597	1159	0	-	1460	38	0.12	0.73	1.16	6.17	17.46	7.40
33 (3)	457	66	578	303	1	-	153	19	0.14	0.52			7.11	2.90
34 (4)	326	99	483	308	0	-	213	28	0.30	0.64			7.78	3.09
35 (4)	162	53	216	181	7	-	60	18	0.33	0.84			2.97	1.24
36 (4)	546	117	703	589	0	-	363	15	0.21	0.84	1.12	6.03	9.17	3.91
37 (4)	1589	82	1649	1649	0	-	914	54	0.05	1.00			15.57	7.39
38 (4)	716	526	2097	1081	33	-	3357	30	0.73	0.52			93.86	26.53
39 (5)	1326	759	2746	1480	26	N.d.	8386	67	0.57	0.54			83.16	32.75
40 (5)	1640	332	2126	1616	0	N.d.	3850	37	0.20	0.76	0.98	5.86	31.89	15.87
41 (5)	1536	384	2641	1271	10	N.d.	5477	49	0.25	0.48			60.51	26.15
42 (6)	336	55	370	227	3	N.d.	105	36	0.26	0.61			5.53	3.76
43 (6)	254	103	526	190	95	N.d.	199	31	0.41	0.36			20.26	10.05
44 (6)	208	86	377	73	100	N.d.	151	62	0.42	0.19	0.77	5.92	11.89	6.30
45 (6)	45	93	202	49	100	N.d.	21	30	2.07	0.24			24.83	8.36

ID Code (Sector)	R_o (m)	a (m)	S_1 (m)	S_2 (m)	S_3 (%) (*Dir1*)	S_3 (%) (*Dir2*)	A_e (m^2 X10^2)	B_w (m)	I	S_2 / S_1	H_s (m)	T (s)	δ' (H_b Eq. 4.5)	δ' (H_b Eq. 4.6)
46 (6)	1480	147	1610	1325	0	N.d.	1635	34	0.10	0.82			23.61	16.16
47 (6)	187	82	341	195	27	N.d.	130	22	0.44	0.57			10.85	5.74
48 (6)	1237	129	1356	1224	0	N.d.	1197	35	0.10	0.90			20.12	13.71
49 (6)	84	41	154	81	7	N.d.	30	43	0.49	0.53			4.94	2.60
50 (6)	676	72	788	685	1	N.d.	417	15	0.11	0.87	0.77	5.92	12.82	8.47
51 (6)	3116	294	3458	3043	0	N.d.	6768	31	0.09	0.88			52.26	35.40
52 (6)	1414	648	2364	821	0	N.d.	6648	33	0.46	0.35			66.06	36.46
53 (6)	127	31	148	54	100	N.d.	23	16	0.24	0.36			2.41	1.59
54 (6)	1040	482	2080	124	48	N.d.	2873	19	0.46	0.06			76.05	38.37
55 (7)	7199	2306	10987	7791	6	N.d.	145189	170	0.32	0.71	0.78	5.50	264.06	161.73
56 (8)	2277	483	2756	2301	-	2	7942	34	0.21	0.83			39.70	22.33
57 (8)	408	186	601	214	-	11	448	35	0.46	0.36			11.62	5.93
58 (8)	988	346	1432	700	-	0	2429	11	0.35	0.49	0.92	5.71	26.98	13.87
59 (8)	437	231	961	344	58	17	719	9	0.53	0.36			33.90	14.15
60 (8)	436	133	532	309	-	0	358	9	0.31	0.58			7.76	4.35

ID Code (Sector)	R_o (m)	a (m)	S_1 (m)	S_2 (m)	S_3 (%) (*Dir1*)	S_3 (%) (*Dir2*)	A_e (m^2 X10^2)	B_w (m)	I	S_2 / S_1	H_s (m)	T (s)	δ' (H_b Eq. 4.5)	δ' (H_b Eq. 4.6)
61 (8)	327	155	563	119	0	63	326	9	0.47	0.21			13.76	6.49
62 (8)	672	66	854	379	12	0	292	25	0.10	0.44			13.24	7.27
63 (8)	815	280	1143	245	-	29	1502	26	0.34	0.21	0.92	5.71	20.54	10.73
64 (8)	1660	418	2424	1456	-	0	5313	62	0.25	0.60			46.27	23.69
65 (8)	1199	591	2347	402	-	0	4953	46	0.49	0.17			69.54	30.75
66 (9)	709	393	1508	529	78	36	2057	42	0.55	0.35			41.41	13.68
67 (9)	1035	243	1541	145	-	0	1592	21	0.23	0.09	1.13	6.00	24.78	9.78
68 (9)	1455	545	2535	960	-	0	6004	63	0.37	0.38			51.61	18.83
69 (10)	1310	406	2297	714	0	25	3466	37	0.31	0.31			45.38	15.82
70 (10)	369	151	670	213	68	0	359	36	0.41	0.32			13.95	4.78
71 (10)	279	37	331	190	0	16	83	24	0.13	0.57			3.64	1.54
72 (10)	923	287	1255	759	5	21	1904	61	0.31	0.60	1.17	6.02	16.93	6.70
73 (10)	361	126	598	242	100	0	350	14	0.35	0.40			10.85	3.89
74 (10)	1302	336	1908	941	-	3	3313	19	0.26	0.49			28.80	10.98
75 (10)	294	312	1086	222	-	100	805	30	1.06	0.30			65.60	15.76

ID Code (Sector)	R_o (m)	a (m)	S_1 (m)	S_2 (m)	S_3 (%) (*Dir1*)	S_3 (%) (*Dir2*)	A_e (m^2 X10^2)	B_w (m)	I	S_2 / S_1	H_s (m)	T (s)	δ' (H_b Eq. 4.5)	δ' (H_b Eq. 4.6)
76 (10)	343	203	699	177	-	100	526	27	0.59	0.25	1.17	6.02	17.30	5.60
77 (10)	316	141	567	242	-	100	299	21	0.45	0.43			11.59	4.00
78 (10)	193	43	254	110	-	0	43	15	0.22	0.43			3.26	1.31
79 (10)	232	162	694	279	-	52	378	16	0.70	0.40			30.55	8.15

Table A.4

Values of morphometric parameters (following Fellowes et al., 2019), indices and δ' calculated for each beach identified through the aerial orthophotos.

ID Code (Sector)	R_o (m)	a (m)	S_1 (m)	S_2 (m)	S_3 (%) (*Dir1*)	S_3 (%) (*Dir2*)	A_e (m^2 X10^2)	B_w (m)	γe	S_2 / S_1	H_s (m)	T (s)	δ' (H_b Eq. 4.5)	δ' (H_b Eq. 4.6)
1 (1)	667	336	1620	484	-	94	1753	17	0.80	0.30			72.88	30.72
2 (1)	781	493	2161	107	-	22	3612	27	0.82	0.50			118.22	46.69
3 (1)	414	912	2517	482	-	52	3129	115	1.63	0.19			448.47	119.49
4 (1)	793	297	1770	182	-	0	1430	12	0.79	0.10			10.15	30.85
5 (1)	149	151	504	96	64	100	168	10	1.17	0.19			37.27	13.31
6 (1)	752	442	1834	544	-	0	2438	37	0.90	0.30			83.02	34.93
7 (1)	538	373	1577	190	-	0	1340	15	1.02	0.12			94.07	36.10
8 (1)	299	69	387	246	0	7	119	13	0.63	0.64	0.84	5.91	6.77	3.91
9 (1)	225	137	529	184	100	-	216	19	0.93	0.35			22.67	9.71
10 (1)	178	88	326	67	0	-	90	13	0.93	0.21			9.60	4.66
11 (1)	432	299	1319	380	13	-	1068	45	0.91	0.29			83.64	31.45
12 (1)	127	139	577	59	100	-	122	6	1.26	0.10			66.41	20.47
13 (1)	115	100	356	69	100	-	86	2	1.08	0.19			23.05	8.61
14 (1)	147	83	361	23	0	100	77	6	0.95	0.06			16.51	6.92
15 (1)	154	96	415	58	55	-	97	9	0.97	0.14			21.82	8.73

ID Code (Sector)	R_o (m)	a (m)	S_1 (m)	S_2 (m)	S_3 (%) (*Dir1*)	S_3 (%) (*Dir2*)	A_e (m^2 X10^2)	B_w (m)	γ_e	S_2 / S_1	H_s (m)	T (s)	δ' (H_b Eq. 4.5)	δ' (H_b Eq. 4.6)
16 (2)	325	152	591	373	-	52	392	23	0.77	0.63			9.52	2.24
17 (2)	1023	420	2425	486	-	37	4007	47	0.66	0.20			58.17	11.97
18 (2)	331	190	741	103	-	0	361	11	1.00	0.14			16.31	3.45
19 (2)	327	363	1750	232	-	100	1043	20	1.12	0.13	1.52	6.78	142.39	19.50
20 (2)	121	158	511	90	-	0	122	19	1.43	0.18			29.15	4.49
21 (2)	201	158	600	49	-	0	169	11	1.22	0.08			20.34	3.73
22 (2)	173	92	408	105	-	100	102	16	0.91	0.26			9.71	2.00
23 (3)	318	298	1407	250	100	100	517	70	1.31	0.18			113.29	24.68
24 (3)	1340	463	2797	1840	0	-	4478	203	0.69	0.66			72.97	23.15
25 (3)	509	237	1211	796	0	-	854	82	0.81	0.66			38.45	11.42
26 (3)	262	129	704	88	0	-	142	30	1.08	0.13			26.83	7.50
27 (3)	752	321	1584	1016	12	-	1909	82	0.73	0.64	1.16	6.17	41.89	13.23
28 (3)	390	259	1522	573	13	-	803	67	0.91	0.38			101.51	23.55
29 (3)	186	51	286	69	0	-	44	24	0.77	0.24			4.72	1.74
30 (3)	366	61	624	453	0	-	146	43	0.51	0.73			12.02	4.22

ID Code (Sector)	R_o (m)	a (m)	S_1 (m)	S_2 (m)	S_3 (%) (*Dir1*)	S_3 (%) (*Dir2*)	A_e (m^2 X10^2)	B_w (m)	γ_e	S_2 / S_1	H_s (m)	T (s)	δ' (H_b Eq. 4.5)	δ' (H_b Eq. 4.6)
31 (3)	2731	211	3301	3121	0	-	3960	47	0.34	0.95			37.95	15.82
32 (3)	1366	179	1778	1268	0	-	1581	38	0.45	0.71	1.16	6.17	22.84	9.17
33 (3)	457	84	620	332	2	-	183	19	0.62	0.54			8.48	3.33
34 (4)	326	119	492	298	0	-	243	28	0.76	0.61			8.15	3.21
35 (4)	162	64	270	209	20	-	79	18	0.72	0.77			5.24	1.96
36 (4)	546	129	708	594	0	-	425	15	0.63	0.84	1.12	6.03	9.34	3.97
37 (4)	1589	135	1910	1887	0	-	1267	54	0.38	0.99			22.48	9.92
38 (4)	716	511	2394	1358	35	-	3477	30	0.87	0.57			130.70	34.57
39 (5)	1326	813	3061	1783	30	N.d.	8702	67	0.87	0.58			109.10	40.70
40 (5)	1640	359	2427	1956	4	N.d.	4159	37	0.56	0.81	0.98	5.86	44.40	20.69
41 (5)	1536	402	2899	1445	10	N.d.	5632	49	0.54	0.50			76.39	31.51
42 (6)	336	76	503	334	6	N.d.	159	36	0.60	0.66			11.91	6.95
43 (6)	254	117	545	187	98	N.d.	229	31	0.77	0.34			22.14	10.79
44 (6)	208	84	483	114	100	N.d.	177	62	0.63	0.24	0.77	5.92	22.09	10.35
45 (6)	45	151	354	124	65	N.d.	42	30	2.34	0.35			100.97	25.69

ID Code (Sector)	R_o (m)	a (m)	S_1 (m)	S_2 (m)	S_3 (%) (*Dir1*)	S_3 (%) (*Dir2*)	A_e (m^2 X10^2)	B_w (m)	γ_e	S_2 / S_1	H_s (m)	T (s)	δ' (H_b Eq. 4.5)	δ' (H_b Eq. 4.6)
46 (6)	1480	186	1769	1445	0	N.d.	2013	34	0.41	0.82			29.88	19.50
47 (6)	187	100	422	235	28	N.d.	160	22	0.79	0.56			18.49	8.78
48 (6)	1237	134	1462	1306	1	N.d.	1290	35	0.37	0.89			24.28	15.94
49 (6)	84	91	276	183	5	N.d.	48	43	1.31	0.66			21.25	8.37
50 (6)	676	83	837	722	1	N.d.	486	15	0.38	0.86	0.77	5.92	14.91	9.56
51 (6)	3116	318	3522	3066	0	N.d.	7051	31	0.38	0.87			54.71	36.72
52 (6)	1414	677	2437	858	0	N.d.	6735	33	0.82	0.35			71.28	38.74
53 (6)	127	41	168	62	100	N.d.	27	16	0.78	0.37			3.30	2.05
54 (6)	1040	503	2116	154	62	N.d.	2887	19	0.94	0.07			79.39	39.71
55 (7)	7199	2372	14610	1142	7	N.d.	149362	170	0.61	0.78	0.78	5.50	538.42	285.98
56 (8)	2277	491	2957	2487	-	5	8220	34	0.54	0.84			47.34	25.71
57 (8)	408	184	656	261	-	10	487	35	0.83	0.40			14.47	7.06
58 (8)	988	349	1489	725	-	0	2461	11	0.70	0.49	0.92	5.71	29.80	15.02
59 (8)	437	238	914	354	55	20	739	9	0.88	0.39			29.91	12.80
60 (8)	436	138	562	329	-	0	378	9	0.71	0.59			8.90	4.85

ID Code (Sector)	R_o (m)	a (m)	S_1 (m)	S_2 (m)	S_3 (%) (*Dir1*)	S_3 (%) (*Dir2*)	A_e (m^2 X10^2)	B_w (m)	γ_e	S_2 / S_1	H_s (m)	T (s)	δ' (H_b Eq. 4.5)	δ' (H_b Eq. 4.6)
61 (8)	327	164	595	136	0	72	336	9	0.89	0.23			15.80	7.25
62 (8)	672	77	925	429	22	0	351	25	0.41	0.46			16.16	8.52
63 (8)	815	312	1257	345	-	34	1544	26	0.79	0.27	0.92	5.71	26.05	12.98
64 (8)	1660	482	2910	1910	-	6	5728	62	0.64	0.66			73.07	34.15
65 (8)	1199	636	2504	540	-	0	5056	46	0.89	0.22			81.75	35.01
66 (9)	709	437	1599	598	82	42	2149	42	0.94	0.37			47.94	15.38
67 (9)	1035	259	1580	161	-	0	1613	21	0.64	0.10	1.13	6.00	26.38	10.28
68 (9)	1455	605	2851	1241	-	0	6323	63	0.76	0.44			69.23	23.82
69 (10)	1310	443	2434	835	0	29	3570	37	0.74	0.34			52.45	18.76
70 (10)	369	175	736	278	71	0	396	36	0.88	0.38			17.64	5.77
71 (10)	279	64	380	235	0	32	107	24	0.62	0.62			5.14	2.03
72 (10)	923	321	1496	985	7	24	2099	61	0.70	0.66	1.17	6.02	26.26	9.52
73 (10)	361	141	652	275	100	0	370	14	0.73	0.42			13.46	4.63
74 (10)	1302	346	1007	1031	-	3	3412	19	0.59	0.51			28.80	10.98
75 (10)	294	343	1183	237	-	100	838	30	1.18	0.20			65.60	15.76

ID Code (Sector)	R_o (m)	a (m)	S_1 (m)	S_2 (m)	S_3 (%) (*Dir1*)	S_3 (%) (*Dir2*)	A_e (m^2 X10^2)	B_w (m)	γ_e	S_2 / S_1	H_s (m)	T (s)	δ' (H_b Eq. 4.5)	δ' (H_b Eq. 4.6)
76 (10)	343	209	747	208	-	100	539	27	0.90	0.28	1.17	6.02	20.43	6.39
77 (10)	316	145	661	325	-	100	319	21	0.81	0.49			17.01	5.43
78 (10)	193	50	302	136	-	0	54	15	0.68	0.45			5.03	1.86
79 (10)	232	170	760	319	-	51	329	16	0.86	0.42			38.34	9.78

Table A.5

Surf zone circulation types estimated from the obtained δ' values, using both classification approaches (Bowman et al., 2009 and Fellowes et al., 2019) and H_b formulations (Short and Masselink, 1999 and Komar and Gaughan, 1972). Circulation types: N (Normal beach circulation); T (Transitional beach circulation); C (Cellular beach circulation). The colour of the Beach ID Code indicates whether the embayment is natural (green) or artificial (red).

ID Code	δ' (H_b - Short and Masselink, 1999)		δ' (H_b - Komar and Gaughan, 1972)	
	Platform Index (I)	Embayment Morphometric Parameter (γ_e)	Platform Index (I)	Embayment Morphometric Parameter (γ_e)
1	N	N	N	N
2	N	N	N	N
3	N	N	N	N
4	N	N	N	N
5	N	N	T	T
6	N	N	N	N
7	N	N	N	N
8	C	C	C	C
9	N	N	T	T
10	C	T	C	C
11	N	N	N	N
12	N	N	N	N
13	N	N	T	T
14	T	T	C	C
15	T	N	C	T
16	T	T	C	C
17	N	N	T	T
18	N	T	C	C
19	N	N	T	N
20	N	N	C	C
21	T	N	C	C
22	C	T	C	C
23	N	N	N	N
24	N	N	T	N
25	T	N	C	T
26	N	N	C	C
27	N	N	T	T
28	N	N	T	N
29	C	C	C	C
30	C	T	C	C

ID Code	δ' (H_b - Short and Masselink, 1999)		δ' (H_b - Komar and Gaughan, 1972)	
	Platform Index (I)	Embayment Morphometric Parameter (γ_e)	Platform Index (I)	Embayment Morphometric Parameter (γ_e)
31	N	N	T	T
32	T	N	C	T
33	C	T	C	C
34	C	T	C	C
35	C	C	C	C
36	T	T	C	C
37	T	N	C	T
38	N	N	N	N
39	N	N	N	N
40	N	N	T	N
41	N	N	N	N
42	C	T	C	C
43	N	N	T	T
44	T	N	C	T
45	-	-	-	-
46	N	N	T	T
47	T	T	C	T
48	N	N	T	T
49	C	N	C	T
50	T	T	T	T
51	N	N	N	N
52	N	N	N	N
53	C	C	C	C
54	N	N	N	N
55	-	-	-	-
56	N	N	N	N
57	T	T	C	C
58	N	N	T	T
59	N	N	T	T
60	C	T	C	C
61	T	T	C	C
62	T	T	C	T
63	N	N	T	T
64	N	N	N	N
65	N	N	N	N
66	N	N	T	T
67	N	N	T	T

ID Code	δ' (H_b - Short and Masselink, 1999)		δ' (H_b - Komar and Gaughan, 1972)	
	Platform Index (I)	Embayment Morphometric Parameter (γ_e)	Platform Index (I)	Embayment Morphometric Parameter (γ_e)
68	N	N	T	N
69	N	N	T	T
70	T	T	C	C
71	C	C	C	C
72	T	N	C	T
73	T	T	C	C
74	N	N	T	T
75	N	N	T	T
76	T	N	C	C
77	T	T	C	C
78	C	C	C	C
79	N	N	T	T

Appendix B: Digital Shoreline Analysis System (DSAS) database (Chapter 5)

Table B.1

Sector 1: Values of statistical indicators (Shoreline Change Envelope - SCE; Net Shoreline Movement - NSM; End Point Rate - EPR; Weighted Linear Regression - WLR; Linear Regression Rate - LRR) using the DSAS method for each beach identified within the sector. For each indicator are reported the minimum, maximum and mean value.

Beach ID (numbers of Transects)	SCE		NSM		EPR		WLR		LRR	
	Mean	Min | Max	Mean	Min | Max	Mean	Min | Max	Mean	Min | Max	Mean	Min | Max
1 (21)	12.8	5.9 | 15.4	-2.1	-5.1 | 2.3	-0.03	-0.07 | 0.03	-0.07	-0.14 | 0.01	-0.04	-0.08 | 0.01
2 (47)	12.6	6.3 | 22.7	-6.0	-15.6 | -	-0.09	-0.23 | -	-0.11	-0.21 | 0.05	-0.11	-0.20 | 0.04
3 (12)	31.3	27.3 | 39.0	-8.4	-11.4 | -	-0.12	-0.17 | -	-0.27	-0.36 | -	-0.35	-0.43 | -
4 (11)	14.1	6.8 | 17.2	-8.6	-12.2 | -	-0.13	-0.18 | -	-0.12	-0.18 | -	-0.10	-0.16 | -
5 (5)	6.2	3.9 | 10.4	-1.2	-2.1 | -	-0.02	-0.03 | -	-0.07	-0.10 | -	-0.06	-0.08 | -
6 (24)	13.8	4.0 | 25.0	1.0	-2.4 | 5.5	0.01	-0.06 | 0.08	-0.05	-0.08 | -	-0.03	-0.07 | 0.04
7 (7)	6.0	4.4 | 10.7	2.5	-1.6 | 10.7	0.04	-0.02 | 0.16	-0.01	-0.05 | 0.08	-0.01	-0.05 | 0.08
8 (10)	4.7	3.3 | 8.0	-3.3	-5.9 | -	-0.05	-0.09 | -	-0.06	-0.10 | -	-0.06	-0.10 | -
9 (8)	11.5	5.9 | 15.2	-6.2	-8.3 | -	-0.09	-0.12 | -	-0.13	-0.17 | -	-0.13	-0.17 | -
10 (2)	4.7	3.9 | 5.5	-0.9	-1.7 | -	-0.01	-0.02 | -	-0.03	-0.04 | -	-0.03	-0.04 | -
11 (16)	25.9	5.3 | 34.1	-5.2	-12.1 | 3.4	-0.08	-0.18 | 0.5	-0.11	-0.19 | 0.01	-0.11	-0.19 | 0.01
12 (2)	8.5	7.9 | 9.0	-1.3	-1.6 | -	-0.02	-0.02 | -	-0.06	-0.06 | -	-0.05	-0.05 | -
13 (3)	6.3	4.5 | 8.0	-3.3	-4.9 | -	-0.05	-0.07 | -	-0.07	-0.09 | -	-0.06	-0.08 | -
14 (1)	6.1	6.1 | 6.1	-2.4	-2.4 | -	-0.03	-0.03 | -	-0.06	-0.06 | -	-0.07	-0.07 | -
15 (2)	4.3	3.8 | 4.7	-1.1	-1.1 | -	-0.02	-0.02 | -	-0.03	-0.04 | -	-0.04	-0.04 | -

Beach ID (numbers of Transects)	SCE		NSM		EPR		WLR		LRR	
	Mean	Min | Max	Mean	Min | Max	Mean	Min | Max	Mean	Min | Max	Mean	Min | Max
16 (18)	12.6	5.0 | 19.1	-10.4	-18.3 | 1.7	-0.15	-0.27 | 0.02	-0.14	-0.27 | 0.01	-0.14	-0.27 | 0.01
17 (21)	18.5	6.6 | 28.9	2.7	-6.7 | 16.5	-0.03	-0.13 | 0.24	0.04	-0.1 | 0.01	-0.04	-0.09 | 0.06
18 (4)	3.7	1.8 |5.6	-1.3	-2.0 | -	-0.01	-0.02 | -	-0.02	-0.03 | 0.02	-0.01	-0.03 | 0.01
19 (10)	7.0	1.9 | 14.2	-0.9	-3.7 | 0.5	-0.03	-0.08 | 0.01	-0.03	-0.21 | 0.03	-0.04	-0.11 | 0.02
20 (3)	11.3	9.6 | 13.3	0.7	- | 1.4	-0.04	-0.06 | 0.02	0.01	-0.04| 0.01	-0.02	-0.04 | -
21 (2)	3.6	2.9 | 4.3	-1.1	-3.0 | 0.9	-0.02	-0.04 | 0.01	-0.02	-0.04 | -	-0.02	-0.04 | -
22 (3)	5.1	3.8 | 6.2	-3.0	-4.2 | 19.2	-0.05	-0.06 | -	-0.04	-0.06 | -	-0.04	-0.06 | -

Table B.2

Sector 2: Values of statistical indicators (Shoreline Change Envelope - SCE; Net Shoreline Movement - NSM; End Point Rate - EPR; Weighted Linear Regression - WLR; Linear Regression Rate - LRR) using the DSAS method for each beach identified within the sector. For each indicator are reported the minimum, maximum and mean value.

Beach ID (numbers of Transects)	SCE		NSM		EPR		WLR		LRR	
	Mean	Min | Max	Mean	Min | Max	Mean	Min | Max	Mean	Min | Max	Mean	Min | Max
23 (6)	29.2	26.0 | 32.0	0.9	-7.8 | 19.2	0.02	-0.12 | 0.32	0.02	-0.12 | 0.33	0.02	-0.13 | 0.31
24 (65)	50.8	34.3 | 68.0	7.3	-6.8 | 32.0	0.11	-0.10 | 0.47	-0.01	-0.25 | 0.31	0.17	-0.02 | 0.39
25 (24)	22.6	3.5 | 34.9	5.9	-0.7 | 13.2	0.09	-0.01 | 0.19	-0.03	-0.13 | 0.05	0.03	-0.04 | 0.01
26 (2)	16.8	14.5 | 19.2	9.0	- | 9.9	0.13	- | 0.15	0.02	- | 0.03	0.01	- |0.02
27 (40)	22.2	7.6 | 38.8	3.4	- | 8.9	0.05	-0.06 | 0.30	-0.03	-0.09 | 0.08	0.01	-0.01 |0.07
28 (15)	9.4	2.9 | 27.4	-0.7	-8.7 | 8.1	-0.01	-0.13 | 0.12	-0.04	-0.15 | 0.01	-0.04	-0.09 | 0.01
29 (2)	15.5	14.7 | 16.4	4.1	-1.4 | 9.6	0.07	-0.02 | 0.16	0.18	- | 0.21	0.15	- | 0.20
30 (16)	22.0	5.0 | 38.8	-6.9	-26.2 | 5.2	-0.07	-0.38 | 0.40	-0.10	-0.43 | 0.35	-0.05	-0.33 | 0.34
31 (143)	20.5	2.5 | 35.4	-1.0	-15.7 | 14.0	-0.02	-0.68 | 0.22	-0.04	-0.64 | 0.26	0.01	-0.68 | 0.27
32 (56)	13.2	5.6 | 32.2	-4.0	-11.3 | 4.1	-0.06	-0.17 | 0.06	-0.10	-0.30 | 0.01	-0.08	-0.22 | 0.04
33 (16)	5.0	3.4 | 7.7	1.7	-2.9 | 5.4	0.02	-0.06 | 0.08	-0.02	-0.08 | 0.04	-0.01	-0.09 | 0.05
34 (14)	7.4	4.6 | 11.6	-6.6	-11.6 | -	-0.10	-0.17 | -	-0.08	-0.11 | -	-0.08	-0.12 | -
35 (9)	11.3	8.7 | 14.5	-8.3	-11.6 | -	-0.12	-0.17 | -	-0.10	-0.16 | -	-0.12	-0.18 | -
36 (28)	11.2	4.1 | 17.4	-6.5	-13.3 | -	-0.10	-0.20 | -	-0.09	-0.18 | -	-0.11	-0.18 | -
37 (125)	12.0	2.6 | 22.4	-2.9	-12.3 | 5.6	-0.04	-0.18 | 0.08	-0.01	-0.18 | 0.14	-0.02	-0.16 | 0.12

Beach ID (numbers of Transects)	SCE		NSM		EPR		WLR		LRR	
	Mean	Min | Max	Mean	Min | Max	Mean	Min | Max	Mean	Min | Max	Mean	Min | Max
38 (59)	16.6	9.0 | 26.4	-9.5	-17.9 | 9.4	-0.14	-0.28 | 0.14	-0.14	-0.35 | 0.38	-0.14	-0.30 | 0.27
39 (73)	9.5	3.3 | 16.5	-2.0	-9.8 | 5.5	-0.03	-0.39 | 0.08	-0.03	-0.43 | 0.06	-0.01	-0.41 | 0.10
40 (83)	14.5	4.0 | 45.0	3.8	-8.4 | 28.6	0.06	-0.12 | 0.42	0.01	-0.11 | 0.37	0.01	-0.11 | 0.39
41 (83)	28.8	4.9 | 68.8	-18.2	-46.2 | 57.4	-0.30	-1.25 | 0.84	-0.13	-0.22 | 1.19	-0.20	-1.30 | 1.17

Table B.3

Sector 3: Values of statistical indicators (Shoreline Change Envelope - SCE; Net Shoreline Movement - NSM; End Point Rate - EPR; Weighted Linear Regression - WLR; Linear Regression Rate - LRR) using the DSAS method for each beach identified within the sector. For each indicator are reported the minimum, maximum and mean value.

Beach ID (numbers of Transects)	SCE		NSM		EPR		WLR		LRR	
	Mean	Min | Max	Mean	Min | Max	Mean	Min | Max	Mean	Min | Max	Mean	Min | Max
42 (13)	27.3	19.2 | 35.7	-13.5	-23.7 | -	-0.20	-0.35 | -	-0.08	-0.34 | 0.12	-0.17	-0.35 | -
43 (11)	79.6	56.0 | 94.8	-61.3	-94.1 | -	-0.96	-1.42 | -	-0.78	-1.23 | -	-0.99	-1.39 | -
44 (6)	97.1	87.9 | 105.1	-87.8	-96.1 | -	-1.44	-1.56 | -	-1.32	-1.46 | -	-1.51	-1.62 | -
45 (4)	64.7	53.4 | 79.3	-58.5	-79.3 | -	-0.87	-1.22 | -	-0.70	-0.99 | -	-0.82	-1.12 | -
46 (68)	44.6	13.6 | 85.1	-16.1	-84.7 | 22.1	-0.24	-1.24 | 0.32	-0.13	-0.77 | 0.34	-0.16	-0.96 | 0.34
47 (8)	116.3	106.2 | 135.4	-114.8	-132.2 | -	-1.69	-1.94 | -	-1.45	-1.59 | -	-1.64	-1.76 | -
48 (61)	30.0	12.7 |41.8	7.2	-11.2 | 19.0	0.10	-0.25 | 0.28	-0.09	-0.47 | 0.23	-0.02	-0.38 | 0.23
49 (4)	26.8	23.4 | 31.3	4.4	- | 9.3	0.06	- | 0.14	0.11	- | 0.16	0.11	- | 0.16
50 (34)	34.6	19.9 | 54.0	26.5	-6.2 | 54.0	0.39	-0.09 | 0.79	0.35	-0.16 | 0.88	0.38	-0.14 | 0.87
51 (149)	41.6	19.6 | 75.7	3.4	-32.8 | 73.3	0.05	-0.48 | 1.08	-0.02	-0.74 | 1.27	-0.03	-0.66 | 1.21
52 (58)	48.5	29.8 | 93.4	44.1	- | 90.8	0.65	- | 1.33	0.66	- | 1.36	0.57	- | 1.26
53 (3)	7.1	4.3 | 9.7	-3.8	-5.5 | -	-0.08	-0.12 | -	-0.06	-0.12 | -	-0.06	-0.11 | -
54 (7)	6.2	3.3 | 7.9	-0.2	-7.9 | 4.6	-0.02	-0.18 | 0.10	0.03	-0.18 | 0.12	0.01	-0.19 | 0.10
55 (401)	33.1	6.8 | 84.8	10.2	-18.3 | 83.6	0.15	-0.27 | 1.23	0.17	-0.43 | 0.86	0.20	-0.25 | 1.01

Table B.4

Sector 4: Values of statistical indicators (Shoreline Change Envelope - SCE; Net Shoreline Movement - NSM; End Point Rate - EPR; Weighted Linear Regression - WLR; Linear Regression Rate - LRR) using the DSAS method for each beach identified within the sector. For each indicator are reported the minimum, maximum and mean value.

Beach ID (numbers of Transects)	SCE		NSM		EPR		WLR		LRR	
	Mean	Min | Max	Mean	Min | Max	Mean	Min | Max	Mean	Min | Max	Mean	Min | Max
56 (119)	14.0	6.7 | 32.8	-3.2	-15.8 | 8.5	-0.05	-0.23 | 0.12	-0.05	-0.25 | 0.09	-0.03	-0.23 | 0.07
57 (21)	15.2	6.6 | 44.6	-6.6	-16.5 | 24.7	-0.21	-0.59 | 0.36	-0.14	-0.56 | 0.60	-0.18	-0.63 | 0.59
58 (42)	6.8	0.7 | 12.5	-4.4	-12.5 | 2.6	-0.06	-0.18 | 0.06	-0.06	-0.22 | 0.09	-0.06	-0.17 | 0.06
59 (18)	7.5	1.6 | 20.0	-4.7	-13.4 | 4.3	-0.07	-0.20 | 0.06	-0.07	-0.19 | 0.14	-0.07	-0.20 | 0.14
60 (17)	6.5	3.0 | 11.0	-4.7	-8.5 | -	-0.07	-0.13 | -	-0.03	-0.08 | 0.01	-0.04	-0.08 | 0.01
61 (6)	3.8	3.5 | 4.3	-0.4	-1.6 | 0.6	-0.01	-0.02 | 0.01	-0.03	-0.04 | -	-0.03	-0.04 | -
62 (19)	6.3	4.0 | 11.4	3.0	-0.4 | 8.0	0.04	-0.01 | 0.12	-0.02	-0.09 | 0.05	0.01	-0.07 | 0.08
63 (13)	4.9	2.9 | 6.0	-1.0	-4.9 | 4.2	-0.01	-0.07 | 0.06	0.01	-0.05 | 0.05	0.01	-0.05 | 0.05
64 (76)	41.2	24.7 | 55.9	-28.8	-55.9 | 19.9	-0.42	-0.82 | 0.29	-0.12	-0.52 | 0.22	-0.23	-0.57 | 0.09
65 (21)	31.4	21.8 | 47.3	-28.4	-46.6 | -	-0.42	-0.75 | -	-0.21	-0.35 | -	-0.29	-0.48 | -
66 (27)	19.2	10.2 | 24.6	-16.0	-21.0 | -	-0.24	-0.31 | -	-0.11	-0.18 | -	-0.15	-0.22 | -
67 (7)	4.8	4.2 | 5.1	-1.5	-2.0 | -	-0.02	-0.03 | -	-0.03	-0.05 | -	-0.03	-0.05 | -
68 (49)	33.3	19.3 | 47.0	-25.0	-47.0 | -	-0.37	-0.69 | -	-0.17	-0.33 | -	-0.23	-0.38 | -
69 (35)	12.3	7.2 | 20.2	-2.9	-9.8 | 3.4	-0.04	-0.14 | 0.05	-0.06	-0.19 | 0.06	-0.04	-0.14 | 0.09
70 (10)	11.0	6.5 | 16.1	-7.3	-14.7 | -	-0.11	-0.22 | -	-0.12	-0.16 | -	-0.12	-0.16 | -

Beach ID (numbers of Transects)	SCE		NSM		EPR		WLR		LRR	
	Mean	Min | Max	Mean	Min | Max	Mean	Min | Max	Mean	Min | Max	Mean	Min | Max
71 (9)	17.7	8.7 | 21.5	1.1	- | 2.2	0.02	- | 0.03	-0.07	-0.14 | -	-0.02	-0.09 | 0.02
72 (39)	15.3	3.5 | 25.7	3.3	-7.9 | 16.4	0.05	-0.12 | 0.24	0.01	-0.08 | 0.19	0.01	-0.03 | 0.20
73 (11)	14.4	5.4 | 21.0	-1.3	-6.1 | 3.2	-0.02	-0.09 | 0.05	-0.13	-0.15 | -	-0.10	-0.13 | -
74 (55)	9.3	2.6 | 19.9	-4.5	- | 2.6	-0.06	-0.22 | 0.19	-0.08	-0.27 | 0.03	-0.09	-0.26 | 0.02
75 (24)	23.1	2.1 | 119.9	5.0	-33.7 | 108.1	0.01	-0.50 | 1.59	0.04	-0.73 | 1.94	0.03	-0.69 | 1.58
76 (7)	4.0	2.3 | 7.2	-1.7	-6.9 | 1.2	-0.02	-0.10 | 0.02	-0.02	-0.04 | 0.01	-0.02	-0.06 | 0.01
77 (13)	6.1	3.4 | 9.1	1.4	-4.3 | 3.4	0.02	-0.08 | 0.05	-0.02	-0.07 | 0.01	-0.01	-0.08 | 0.01
78 (5)	7.2	4.9 | 9.6	-1.0	-2.1 | 1.0	-0.02	-0.03 | 0.01	-0.01	-0.06 | 0.03	-0.03	-0.08 | 0.02
79 (12)	9.1	4.3 | 13.8	-6.7	-13.6 | -	-0.10	-0.20 | -	-0.06	-0.13 | 0.02	-0.08	-0.15 | -

Table B.5

Overview of the main types of potential anthropogenic impacts identified on the studied beaches: **(I)** Dune system impacts; **(II)** Use of heavy vehicles on the beach, for example: removal of *Posidonia oceanica* banquettes during "beach cleaning" operations; military exercises; **(III)** Coastal infrastructures and operations within the beach system, including **(III-1)** coastal engineering structures (e.g., breakwaters, groynes, etc.), **(III-2)** artificial structures (e.g., tourist facilities and buildings) and **(III-3)** coastal protection measures (e.g., beach nourishment); **(IV)** Artificial structures located inland of the beach system (e.g., dams); **(V)** Impacts on the upper limit of the *Posidonia oceanica* meadow. The table presents the data as follows: Impact absent (A), impact present (X) or not defined (Nd) (data from [1] Sardegna Geoportale: Data Download; [2] Biondo et al., 2020; [3] De Muro et al., 2018; [4] Regione Sardegna, 2021; [5] Carlini, 2024); Impact presumed absent (PA), impact presumed present (PP) or not defined (Nd) (data from the analysis of aerial orthophotos from the WMS of "Regione Autonoma della Sardegna").

Beach ID (Sector)	(I)	(II)	(III)		(IV)	(V)
			(III-1) and (III-2)	(III-3)		
1 (1)	PA	Nd	PA	PA	Nd	Nd
2 (1)	X [4]	X [4]	A [4]	A [4]	Nd	A [4]
3 (1)	X [4]	X [4]	A [4]	A [4]	Nd	A [4]
4 (1)	PP	Nd	PA	PA	Nd	Nd
5 (1)	PP	Nd	PA	PA	Nd	Nd
6 (1)	X [4]	Nd	A [4]	X [4]	Nd	A [4]
7 (1)	PP	X [5]	PP	PA	Nd	Nd
8 (1)	PP	Nd	PA	PA	Nd	Nd
9 (1)	PP	Nd	PA	PA	Nd	Nd
10 (1)	Nd	Nd	PA	PA	Nd	Nd
11 (1)	X [4]	Nd	A [4]	X [4]	Nd	A [4]
12 (1)	Nd	Nd	PA	PA	Nd	Nd
13 (1)	Nd	Nd	PA	PA	Nd	Nd
14 (1)	Nd	Nd	PA	PA	Nd	Nd
15 (1)	Nd	Nd	PA	PA	Nd	Nd
16 (1)	PP	X [5]	PA	PP	Nd	Nd
17 (1)	X [4]	Nd	A [4]	X [4]	Nd	A [4]
18 (1)	PP	Nd	PA	PA	Nd	Nd
19 (1)	Nd	Nd	PA	PA	Nd	Nd
20 (1)	PP	Nd	PA	PA	Nd	Nd
21 (1)	PA	Nd	PA	PA	Nd	Nd
22 (1)	PP	Nd	PA	PA	Nd	Nd
23 (2)	X [4]	Nd	A [4]	A [4]	Nd	A [4]
24 (2)	X [4]	Nd	A [4]	X [4]	Nd	A [4]

Beach ID (Sector)	(I)	(II)	(III)		(IV)	(V)
			(III-1) and (III-2)	(III-3)		
25 (2)	X [4]	Nd	A [4]	X [4]	Nd	A [4]
26 (2)	PP	Nd	PA	PA	Nd	Nd
27 (2)	X [4]	Nd	A [4]	X [4]	X [1]	A [4]
28 (2)	X [4]	Nd	A [4]	X [4]	Nd	A [4]
29 (2)	X [4]	X [5]	PA	PA	Nd	A [4]
30 (2)	X [4]	X [5]	A [4]	X [4]	Nd	A [4]
31 (2)	X [4]	X [5]	PA	X [4]	X [1]	A [4]
32 (2)	ND [4]	X [5]	A [4]	X [4]	Nd	A [4]
33 (2)	PP	Nd	PA	PA	Nd	Nd
34 (2)	PP	Nd	PA	PA	Nd	Nd
35 (2)	PP	Nd	PA	PA	Nd	Nd
36 (2)	PP	Nd	PA	PA	Nd	ND
37 (2)	X [4]	X [5]	A [4]	X [4]	X [1]	Nd [4]
38 (2)	X [4]	Nd	PP	X [4]	Nd	Nd [4]
39 (2)	X [4]	X [5]	A [4]	X [4]	Nd	A [4]
40 (2)	X [4]	Nd	PP	X [4]	X [1]	Nd [4]
41 (2)	X [4]	X [5]	X [4]	X [4]	Nd	A [4]
42 (3)	X [4]	Nd	X [4]	X [4]	X [1]	X [3, 4]
43 (3)	X [4]	Nd	X [4]	X [4]	Nd	X [3, 4]
44 (3)	X [4]	Nd	X [4]	X [4]	Nd	X [3, 4]
45 (3)	X [4]	Nd	X [4]	X [4]	Nd	X [3, 4]
46 (3)	X [4]	X [5]	X [4]	X [4]	Nd	X [3, 4]
47 (3)	X [4]	X [5]	X [4]	X [4]	Nd	X [3, 4]
48 (3)	X [4]	Nd	X [4]	X [4]	X [1]	X [3, 4]
49 (3)	X [4]	Nd	X [4]	X [4]	Nd	X [3, 4]
50 (3)	X [4]	Nd	X [4]	X [4]	X [1]	X [3, 4]
51 (3)	X [4]	Nd	X [4]	X [4]	X [1]	X [3, 4]
52 (3)	X [4]	Nd	X [4]	X [4]	Nd	X [3, 4]
53 (3)	PP	Nd	PP	PP	Nd	Nd
54 (3)	ND [4]	Nd	A [4]	X [4]	Nd	A [4]
55 (3)	X [4]	X [2, 5]	X [4]	X [4]	X [1]	X [3, 4]
56 (4)	PP	Nd	PP	PP	X [1]	Nd
57 (4)	PP	Nd	PP	PP	Nd	Nd
58 (4)	Nd	Nd	PA	PP	X [1]	Nd
59 (4)	Nd	Nd	PP	PP	Nd	Nd
60 (4)	PP	Nd	PA	PP	Nd	Nd
61 (4)	X [4]	Nd	A [4]	PA	Nd	A [4]
62 (4)	X [4]	Nd	A [4]	X [4]	Nd	A [4]

Beach ID (Sector)	(I)	(II)	(III)		(IV)	(V)
			(III-1) and (III-2)	(III-3)		
63 (4)	X [4]	Nd	A [4]	X [4]	Nd	A [4]
64 (4)	X [4]	X [5]	A [4]	X [4]	Nd	A [4]
65 (4)	X [4]	X [5]	A [4]	X [4]	Nd	Nd [4]
66 (4)	X [4]	Nd	A [4]	X [4]	Nd	A [4]
67 (4)	Nd	Nd	PA	PA	Nd	Nd
68 (4)	X [4]	Nd	A [4]	X [4]	Nd	A [4]
69 (4)	X [4]	Nd	A [4]	X [4]	Nd	A [4]
70 (4)	X [4]	X [5]	A [4]	X [4]	Nd	Nd [4]
71 (4)	PP	Nd	PA	PA	Nd	Nd
72 (4)	X [4]	Nd	A [4]	X [4]	Nd	X [4]
73 (4)	PA	Nd	PA	PP	Nd	Nd
74 (4)	X [4]	X [5]	A [4]	X [4]	Nd	Nd [4]
75 (4)	X [4]	Nd	X [4]	X [4]	Nd	Nd [4]
76 (4)	PP	Nd	PP	PA	Nd	Nd
77 (4)	PP	Nd	PA	PP	Nd	Nd
78 (4)	PP	Nd	PA	PP	Nd	Nd
79 (4)	PP	Nd	PA	PP	Nd	Nd

Appendix C: Wave and Wind data from CMEMS and ERA5 (Chapter 7)

Table C.1

Wave Data (significant wave height - H_s; peak wave period - T_p; mean wave period - T_m; wave direction - *Dir*) from CMEMS (Korres et al., 2021) used to numerical modelling (from 27 to 30 October 2018).

Data	Time	H_s (m)	T_p (s)	T_m (s)	*Dir* (°)
27 October 2018	00:00	0.26	5.21	3.11	149.87
27 October 2018	01:00	0.30	5.21	3.41	146.71
27 October 2018	02:00	0.34	5.21	3.68	144.37
27 October 2018	03:00	0.39	5.73	3.95	142.26
27 October 2018	04:00	0.44	5.73	4.24	140.20
27 October 2018	05:00	0.52	6.30	4.52	138.39
27 October 2018	06:00	0.64	6.30	4.97	137.27
27 October 2018	07:00	0.69	6.30	5.05	136.95
27 October 2018	08:00	0.73	6.30	5.12	137.01
27 October 2018	09:00	0.83	6.93	5.18	137.46
27 October 2018	10:00	0.87	6.93	4.41	139.79
27 October 2018	11:00	0.95	6.93	3.95	144.25
27 October 2018	12:00	1.06	6.93	3.89	149.33
27 October 2018	13:00	1.17	6.93	3.94	154.06
27 October 2018	14:00	1.24	6.93	4.09	157.87
27 October 2018	15:00	1.27	6.93	4.25	159.89
27 October 2018	16:00	1.27	6.93	4.41	160.50
27 October 2018	17:00	1.24	6.93	4.53	160.23
27 October 2018	18:00	1.06	6.30	4.36	159.46
27 October 2018	19:00	1.04	6.93	4.61	157.32
27 October 2018	20:00	1.02	6.93	4.88	153.70
27 October 2018	21:00	1.01	7.63	5.08	149.10
27 October 2018	22:00	1.07	7.63	5.03	144.00
27 October 2018	23:00	1.17	8.39	4.80	141.81
28 October 2018	00:00	1.31	8.39	4.60	143.18
28 October 2018	01:00	1.46	8.39	4.73	145.32
28 October 2018	02:00	1.59	8.39	4.93	147.61
28 October 2018	03:00	1.68	8.39	5.08	149.81
28 October 2018	04:00	1.72	8.39	5.11	152.34
28 October 2018	05:00	1.73	8.39	5.09	155.10
28 October 2018	06:00	1.73	7.63	5.13	157.25
28 October 2018	07:00	1.69	7.63	5.25	157.89
28 October 2018	08:00	1.63	7.63	5.39	157.31
28 October 2018	09:00	1.57	7.63	5.38	156.60
28 October 2018	10:00	1.52	7.63	5.21	156.55
28 October 2018	11:00	1.49	7.63	4.98	157.65
28 October 2018	12:00	1.47	7.63	4.90	158.33

Data	Time	H_s (m)	T_p (s)	T_m (s)	*Dir* (°)
28 October 2018	13:00	1.44	7.63	4.98	158.48
28 October 2018	14:00	1.41	7.63	5.09	158.45
28 October 2018	15:00	1.36	7.63	5.35	157.78
28 October 2018	16:00	1.30	7.63	5.66	156.93
28 October 2018	17:00	1.23	7.63	5.81	156.12
28 October 2018	18:00	1.04	6.93	5.51	155.64
28 October 2018	19:00	1.00	6.93	5.50	154.72
28 October 2018	20:00	0.97	6.93	5.12	152.98
28 October 2018	21:00	0.96	6.93	4.66	150.17
28 October 2018	22:00	1.02	7.63	4.69	146.79
28 October 2018	23:00	1.09	7.63	4.57	147.79
29 October 2018	00:00	1.23	7.63	4.63	147.86
29 October 2018	01:00	1.39	7.63	4.84	146.50
29 October 2018	02:00	1.49	7.63	5.07	145.68
29 October 2018	03:00	1.55	7.63	5.14	146.07
29 October 2018	04:00	1.76	7.63	5.05	149.74
29 October 2018	05:00	2.25	7.63	5.17	153.65
29 October 2018	06:00	2.33	7.63	5.21	153.66
29 October 2018	07:00	2.59	8.39	5.64	151.61
29 October 2018	08:00	2.63	8.39	5.94	149.22
29 October 2018	09:00	2.85	9.23	6.44	147.28
29 October 2018	10:00	2.66	9.23	6.35	147.47
29 October 2018	11:00	2.53	9.23	5.87	151.27
29 October 2018	12:00	2.54	9.23	5.26	162.34
29 October 2018	13:00	2.59	9.23	4.99	176.56
29 October 2018	14:00	2.50	9.23	4.98	184.39
29 October 2018	15:00	2.40	9.23	4.93	188.10
29 October 2018	16:00	2.35	9.23	5.01	189.28
29 October 2018	17:00	2.35	9.23	5.10	190.20
29 October 2018	18:00	2.31	10.15	5.21	189.75
29 October 2018	19:00	2.21	10.15	5.39	188.07
29 October 2018	20:00	2.15	10.15	5.51	187.53
29 October 2018	21:00	2.12	10.15	5.52	187.66
29 October 2018	22:00	2.05	10.15	5.51	186.54
29 October 2018	23:00	1.99	10.15	5.53	186.09
30 October 2018	00:00	1.97	10.15	5.37	187.10

Table C.2

Wave Data (significant wave height - H_s; peak wave period - T_p; mean wave period - T_m; wave direction - *Dir*) from CMEMS (Korres et al., 2021) used to numerical modelling (from 19 to 22 January 2020).

Data	Time	H_s (m)	T_p (s)	T_m (s)	*Dir* (°)
19 January 2020	00:00	0.22	4.74	2.50	209.33
19 January 2020	01:00	0.20	4.74	2.44	206.29
19 January 2020	02:00	0.19	4.31	2.38	203.93
19 January 2020	03:00	0.19	4.31	2.39	201.51
19 January 2020	04:00	0.18	3.91	2.51	198.90
19 January 2020	05:00	0.17	3.91	2.69	196.34
19 January 2020	06:00	0.17	3.91	2.83	193.86
19 January 2020	07:00	0.16	3.56	2.85	191.28
19 January 2020	08:00	0.16	10.15	2.66	188.35
19 January 2020	09:00	0.18	9.23	1.61	178.34
19 January 2020	10:00	0.26	1.83	1.74	139.35
19 January 2020	11:00	0.32	2.21	1.87	137.97
19 January 2020	12:00	0.35	2.43	1.88	140.13
19 January 2020	13:00	0.48	2.94	2.19	138.75
19 January 2020	14:00	0.58	3.23	2.41	138.08
19 January 2020	15:00	0.66	3.56	2.56	137.81
19 January 2020	16:00	0.75	3.91	2.69	136.55
19 January 2020	17:00	0.83	4.31	2.81	134.39
19 January 2020	18:00	1.05	4.74	3.27	133.29
19 January 2020	19:00	1.06	5.21	3.31	133.14
19 January 2020	20:00	1.11	5.73	3.37	132.70
19 January 2020	21:00	1.17	5.73	3.50	133.01
19 January 2020	22:00	1.23	5.73	3.59	133.94
19 January 2020	23:00	1.30	5.73	3.71	134.96
20 January 2020	00:00	1.36	5.73	3.82	135.79
20 January 2020	01:00	1.43	5.73	3.92	136.58
20 January 2020	02:00	1.47	6.30	4.04	137.47
20 January 2020	03:00	1.52	6.30	4.10	138.40
20 January 2020	04:00	1.55	6.30	4.17	139.39
20 January 2020	05:00	1.59	6.30	4.22	140.41
20 January 2020	06:00	1.63	6.30	4.32	141.50
20 January 2020	07:00	1.68	6.30	4.39	142.31
20 January 2020	08:00	1.75	6.30	4.43	142.42
20 January 2020	09:00	2.19	6.93	4.96	141.70
20 January 2020	10:00	2.21	6.93	5.01	141.56
20 January 2020	11:00	2.29	7.63	5.16	140.67
20 January 2020	12:00	2.39	7.63	5.23	138.76

Data	Time	H_s (m)	T_p (s)	T_m (s)	*Dir* (°)
20 January 2020	13:00	2.48	7.63	5.33	136.66
20 January 2020	14:00	2.51	7.63	5.50	135.29
20 January 2020	15:00	2.55	8.39	5.58	134.41
20 January 2020	16:00	2.57	8.39	5.64	133.92
20 January 2020	17:00	2.59	8.39	5.70	133.63
20 January 2020	18:00	2.59	8.39	5.75	133.53
20 January 2020	19:00	2.59	8.39	5.79	133.57
20 January 2020	20:00	2.58	8.39	5.80	133.78
20 January 2020	21:00	2.53	8.39	5.73	134.00
20 January 2020	22:00	2.57	8.39	5.75	134.26
20 January 2020	23:00	2.60	8.39	5.81	134.54
21 January 2020	00:00	2.63	8.39	5.86	134.65
21 January 2020	01:00	2.62	8.39	5.88	135.00
21 January 2020	02:00	2.61	8.39	5.88	135.29
21 January 2020	03:00	2.60	8.39	5.87	135.60
21 January 2020	04:00	2.61	8.39	5.87	135.93
21 January 2020	05:00	2.64	8.39	5.90	136.28
21 January 2020	06:00	2.81	9.23	6.14	136.48
21 January 2020	07:00	2.81	8.39	6.17	137.12
21 January 2020	08:00	2.86	9.23	6.22	137.53
21 January 2020	09:00	2.75	8.39	6.08	137.59
21 January 2020	10:00	2.77	9.23	6.08	137.00
21 January 2020	11:00	2.75	9.23	6.04	136.6
21 January 2020	12:00	2.73	8.39	5.99	136.26
21 January 2020	13:00	2.70	8.39	5.94	136.02
21 January 2020	14:00	2.68	8.39	5.90	135.89
21 January 2020	15:00	2.59	8.39	5.65	135.85
21 January 2020	16:00	2.60	8.39	5.63	135.82
21 January 2020	17:00	2.66	8.39	5.69	136.23
21 January 2020	18:00	2.77	8.39	5.81	136.75
21 January 2020	19:00	2.86	8.39	6.01	137.71
21 January 2020	20:00	2.90	8.39	6.18	138.90
21 January 2020	21:00	2.89	8.39	6.28	139.76
21 January 2020	22:00	2.83	8.39	6.31	140.29
21 January 2020	23:00	2.75	8.39	6.30	140.66
22 January 2020	00:00	2.65	8.39	6.28	140.97

Table C.3

Wind Data (U_{10} - wind speed; Dir_w - wind direction) from ERA5 (Hersbach et al., 2023) used to numerical modelling (from 27 to 30 October 2018; from 19 to 22 January 2020).

Data	Time	U_{10} (m/s)	Dir_w (°)	Data	Time	U_{10} (m/s)	Dir_w (°)
27 October 2018	00:00	1.41	178.41	19 January 2020	00:00	8.63	300.90
27 October 2018	01:00	1.54	221.11	19 January 2020	01:00	7.62	300.37
27 October 2018	02:00	1.71	243.52	19 January 2020	02:00	6.75	300.98
27 October 2018	03:00	1.37	253.39	19 January 2020	03:00	6.42	301.02
27 October 2018	04:00	1.13	238.28	19 January 2020	04:00	5.70	298.89
27 October 2018	05:00	1.14	226.79	19 January 2020	05:00	5.06	292.80
27 October 2018	06:00	1.62	219.25	19 January 2020	06:00	5.33	286.52
27 October 2018	07:00	2.23	202.03	19 January 2020	07:00	5.84	284.28
27 October 2018	08:00	3.50	186.30	19 January 2020	08:00	6.29	284.03
27 October 2018	09:00	5.36	186.24	19 January 2020	09:00	7.11	288.12
27 October 2018	10:00	5.94	186.54	19 January 2020	10:00	5.87	270.94
27 October 2018	11:00	6.67	185.51	19 January 2020	11:00	6.69	271.79
27 October 2018	12:00	7.41	185.41	19 January 2020	12:00	7.11	267.79
27 October 2018	13:00	7.78	191.46	19 January 2020	13:00	7.33	262.68
27 October 2018	14:00	7.61	200.92	19 January 2020	14:00	7.36	257.13
27 October 2018	15:00	6.97	200.30	19 January 2020	15:00	7.59	255.05
27 October 2018	16:00	6.61	198.15	19 January 2020	16:00	7.54	252.55
27 October 2018	17:00	5.92	196.80	19 January 2020	17:00	7.61	257.24
27 October 2018	18:00	4.98	198.24	19 January 2020	18:00	6.12	251.95
27 October 2018	19:00	3.04	194.10	19 January 2020	19:00	5.95	252.85
27 October 2018	20:00	2.43	161.81	19 January 2020	20:00	6.88	258.29
27 October 2018	21:00	3.03	157.55	19 January 2020	21:00	7.16	259.69
27 October 2018	22:00	6.09	172.41	19 January 2020	22:00	8.52	265.63
27 October 2018	23:00	8.82	202.46	19 January 2020	23:00	7.44	266.39
28 October 2018	00:00	8.87	208.62	20 January 2020	00:00	6.19	266.06
28 October 2018	01:00	7.79	195.25	20 January 2020	01:00	5.11	266.70
28 October 2018	02:00	8.34	187.93	20 January 2020	02:00	4.74	254.68
28 October 2018	03:00	8.57	183.88	20 January 2020	03:00	5.79	251.69
28 October 2018	04:00	8.68	187.19	20 January 2020	04:00	6.57	262.95
28 October 2018	05:00	9.15	197.52	20 January 2020	05:00	6.49	271.47
28 October 2018	06:00	8.05	214.94	20 January 2020	06:00	6.32	273.31
28 October 2018	07:00	7.02	221.97	20 January 2020	07:00	6.36	273.42
28 October 2018	08:00	6.18	217.26	20 January 2020	08:00	6.66	276.74
28 October 2018	09:00	6.87	216.32	20 January 2020	09:00	7.03	281.74
28 October 2018	10:00	7.29	212.57	20 January 2020	10:00	7.26	291.34
28 October 2018	11:00	7.85	228.22	20 January 2020	11:00	7.32	301.85
28 October 2018	12:00	7.00	237.57	20 January 2020	12:00	6.78	301.16

Data	Time	U_{10} (m/s)	Dir_w (°)	Data	Time	U_{10} (m/s)	Dir_w (°)
28 October 2018	13:00	6.60	241.33	20 January 2020	13:00	6.72	298.16
28 October 2018	14:00	5.62	245.68	20 January 2020	14:00	6.89	299.70
28 October 2018	15:00	3.84	236.42	20 January 2020	15:00	7.15	299.16
28 October 2018	16:00	1.97	192.51	20 January 2020	16:00	7.07	297.28
28 October 2018	17:00	2.48	121.79	20 January 2020	17:00	6.59	296.65
28 October 2018	18:00	4.06	104.06	20 January 2020	18:00	6.38	300.26
28 October 2018	19:00	5.95	105.75	20 January 2020	19:00	5.91	303.29
28 October 2018	20:00	5.94	110.25	20 January 2020	20:00	5.00	305.32
28 October 2018	21:00	8.09	155.91	20 January 2020	21:00	4.29	307.76
28 October 2018	22:00	5.69	167.02	20 January 2020	22:00	4.06	319.02
28 October 2018	23:00	6.78	162.99	20 January 2020	23:00	3.64	330.06
29 October 2018	00:00	7.19	145.29	21 January 2020	00:00	3.03	337.78
29 October 2018	01:00	8.15	135.26	21 January 2020	01:00	2.51	342.94
29 October 2018	02:00	7.14	136.58	21 January 2020	02:00	2.15	4.49
29 October 2018	03:00	9.96	168.06	21 January 2020	03:00	2.39	50.69
29 October 2018	04:00	12.82	171.55	21 January 2020	04:00	2.84	82.84
29 October 2018	05:00	12.98	166.92	21 January 2020	05:00	2.94	108.21
29 October 2018	06:00	12.39	167.41	21 January 2020	06:00	2.90	131.45
29 October 2018	07:00	11.37	174.70	21 January 2020	07:00	2.59	144.58
29 October 2018	08:00	9.56	190.62	21 January 2020	08:00	3.05	151.44
29 October 2018	09:00	9.77	219.30	21 January 2020	09:00	3.39	151.94
29 October 2018	10:00	11.29	234.78	21 January 2020	10:00	4.39	150.07
29 October 2018	11:00	15.05	230.26	21 January 2020	11:00	4.50	156.65
29 October 2018	12:00	15.20	231.49	21 January 2020	12:00	4.12	158.56
29 October 2018	13:00	14.64	243.16	21 January 2020	13:00	3.70	156.59
29 October 2018	14:00	13.21	240.94	21 January 2020	14:00	3.82	152.32
29 October 2018	15:00	14.15	238.45	21 January 2020	15:00	4.41	150.38
29 October 2018	16:00	14.31	236.61	21 January 2020	16:00	3.84	153.37
29 October 2018	17:00	14.47	240.11	21 January 2020	17:00	2.94	161.17
29 October 2018	18:00	13.25	245.96	21 January 2020	18:00	2.06	177.69
29 October 2018	19:00	12.62	242.22	21 January 2020	19:00	2.10	200.47
29 October 2018	20:00	12.93	236.58	21 January 2020	20:00	2.67	231.21
29 October 2018	21:00	12.15	237.64	21 January 2020	21:00	2.93	248.30
29 October 2018	22:00	10.48	236.34	21 January 2020	22:00	3.13	239.87
29 October 2018	23:00	11.96	232.17	21 January 2020	23:00	3.46	244.64
30 October 2018	00:00	12.45	235.93	22 January 2020	00:00	3.75	242.98

This thesis was produced while attending the PhD programme in INNOVATION SCIENCE AND TECHNOLOGY at the University of Cagliari, Cycle XXXVIII, with the support of a scholarship financed by the Ministerial Decree no. 351 of 9th April 2022, based on the NRRP - funded by the European Union - NextGenerationEU - Mission 4 "Education and Research", Component 1 "Enhancement of the offer of educational services: from nurseries to universities" - Investment 3.4 "Advanced teaching and university skills".